Statistical Analysis of Coherent Monostatic and Bistatic Radar Sea Clutter

Matthew. A. Ritchie

A thesis submitted to the University of London for the degree of Doctor of Philosophy in Electronic Engineering

Department of Electronic and Electrical Engineering

University College London

June 2013

Abstract

Radar sea clutter analysis has been an important area of radar research for many years. Very limited research has been carried out on coherent monostatic sea clutter analysis and even less on bistatic sea clutter. This has left a significant gap in the global scientific knowledge within this area.

This thesis describes research carried out to analyse, quantify and model coherent sea clutter statistics from multiple radar sources. The ultimate goal of the research is to improve maritime radars' ability to compensate for clutter and achieve effective detection of targets on or over the sea surface.

The first analyses used monostatic data gathered during the flight trials of the Thales Searchwater 2000 AEW radar. A further sea clutter trials database from CSIR was then used to investigate the variation of clutter statistics with look angle and grazing angle. Finally simultaneous monostatic and bistatic sea clutter data recorded in South Africa using the S-band UCL radar system NetRAD were analysed. No simultaneous monostatic and bistatic coherent analysis has ever been reported before in the open literature. The datasets recorded included multiple bistatic angles at both horizontal and vertical polarisations.

Throughout the analysis real data have been compared to accepted theoretic models of sea clutter. An additional metric of comparison was investigated relating to the area of information theoretic techniques. Information theory is a significant subject area, and some concepts from it have been applied in this research.

In summary this research has produced quantifiable and novel results on the characteristics of sea clutter statistics as a function of Doppler. Analysis has been carried out on a wide range of monostatic and bistatic data. The results of this research will be extremely valuable in developing sea clutter suppression algorithms and thus improving detection performance in future maritime radar designs.

I, Matthew Andrew Ritchie, confirm that the work presented in this thesis is my own. Where information has been derived from other sources, I confirm that this has been indicated in the thesis.

Acknowledgements

Firstly I would like to thank my supervisors Dr. Karl Woodbridge and Dr. Andy Stove. Karl, your support and advice has been incredible throughout my EngD, many thanks for this. Andy, thank you so much for your infinite patience in discussing my research and for you inventive input, which made all of this possible. I would like to express my upmost gratitude to Prof. Simon Watts for his invaluable help, without his expertise and guidance I would not have achieved my goals. My thanks also go to Prof. Hugh Griffiths, his guidance during my EngD has been very valuable.

This work would not have been possible without the data that I have worked on. Firstly a special thanks must go to Thales UK and the EPSRC for their funding and support towards this project. I also am very grateful for the data I have received from the CSIR South Africa as well as the support from US Office of Naval Research Global (ONRG). Lastly the measurement campaign by the UCL and UCT team was critical to my research. From this particular thanks go to Dr. Waddah Al-Ashwal, Stephan Sandenbergh and William Micelli for their hard work during this time, it was all worth it!

My family and friends have been through this with me. Without the unflinching support from my parents and sister I would certainly not have been able to achieve this alone, thank you so much. To my friends I thank you for your continued support and for your distractions from all things Radar. In particular Simon Bozzoli, Robin Burgess, Sam Collard, Lindsey Groh, Charlie Howarth, Mark Hymers, Laura James, Rich Lake, Dave Robinson and Ben Waller. Thanks guys. To Jen thank you for listening to my endless radar conversations and for distracting me from all of this in the best possible way.

Finally I would like to thank all the members of the UCL radar group past and present that I have had the pleasure to work with. You have made the work environment such a pleasant place to be and have created many interesting discussions on radar and other subjects. In particular I would like to thank Dr. Waddah Al-Ashwal, Dr. Matt Ash, Dr. Alessio Balleri, Dr. James Brown, Dr. Alex Charlish, Dr. Kevin Chetty and Dr. Raimund Mueckstein.

Contents

List of Figures

List of Tables

List of Symbols and Abbreviations

Symbols

α_i	Incidence angle
α_c	Critical angle
α_{KS}	KS test significant level
β	Bistatic angle
δ	Difference in time taken by signal
$\Delta\Theta_R$	3dB beamwidth of receiver
$\Delta\Theta_T$	3dB beamwidth of transmitter
$\Delta\mathrm{R}$	Range resolution
$\Delta\mathrm{T}$	Difference in threshold
Δx	Full width of Gaussian
η_w	Weibull shape parameter
$\Gamma(.)$	Gamma function
λ	Wavelength
λ_t	Likelihood ratio threshold level
λ_w	Wavelength of sea wave
λ_{w_c}	Wavelength of capillary sea waves
$\Lambda(z)$	Likelihood ratio
ν	K-distribution shape parameter
ν_b	Brag wave speed frequency
ν_{boat}	Velocity of boat
ν_c	Velocity of current
ν_G	Gamma distribution shape parameter
ν_p	Gravity wave speed frequency
ν_w	Velocity of wave
μ_{LN}	Log-Normal mean
Φ	Phase
ϕ	Angle with respect to plane of bistatic measurement
ϕ_a	The two-way 3dB azimuth beamwidth
Ψ	Angle between target velocity vector and radar line of sight
$\Psi_B(\nu)$	Bragg component of Doppler spectra
$\Psi_H(\nu)$	Vertically polarised Doppler spectra

$\Psi_S(\nu)$	Spike component of Doppler spectra
$\Psi_V(\nu)$	Vertically polarised Doppler spectra
$\Psi_W(\nu)$	Whitecap component of Doppler spectra
σ	Radar cross section
σ^0	Normalised radar cross section
σ_b	Bistatic radar cross section
σ^0_{HH}	Horizontally polarised normalised radar cross section
σ^2_{LN}	Log-Normal variance
σ^2_s	Variance of the spectrum width
σ^0_{VV}	Horizontally polarised normalised radar cross section
σ_w	Weibull scale parameter
τ	Pulse length
θ	Grazing angle
θ_i	Angle of incidence
θ_T	Angle of transmitter to target
θ_R	Angle of receiver to target
θ_s	Angle of scattering
θ_{SW}	Aspect angle with respect to swell
a_n	Individual scatterer contribution
A_c	Monostatic clutter cell area
$(A_C)_b$	Bistatic clutter cell area - Beamwidth limited case
$(A_C)_r$	Bistatic clutter cell area - Range gate limited case
A_e	Effective aperture
A_i	Interference factor
A_u	Upwind / Downwind factor
A_w	Wind speed factor
b	K-distribution scale parameter
B	Bandwidth
B_{earing}	Azimuth bearing
BW	Beamwidth
c	Speed of electromagnetic wave propagation
C	Channel capacity
c_{gw}	Speed of gravitational sea wave
c_p	Speed of scatterer on surface
d	Depth of water
D^*	Kolmogorov-Smirnov Statistic
$D(p\|\|q)$	Kullback Leibler Divergence of p(x) and q(x)
E	Scattering field
E_i	Energy reflected
E_p	Expectation value for p(x)

E_r	Energy reflected
f_c	Frequency of carrier
f_d	Doppler frequency
F_i	Doppler frequency of Doppler bin i
f_{PRF}	Pulse repetition frequency
f_r	Receive antenna pattern factor
f_t	Transmit antenna pattern factor
F_n	Noise figure
g	Gravitational constant
G	Antenna gain
G_r	Receiver Gain
G_{sim}	Simulated Gamma Doppler texture
G_t	Transmitter Gain
$h_{\frac{1}{3}}$	Significant wave height
h_{av}	Average wave height
H	Entropy
H_n	Hermite polynomial
I	In-phase component
k	Wavenumber
K	Proportionality constant
k_B	Boltzmann's constant (1.38×10^{-23} JK^{-1})
k_{pol}	Polarisation parameter
k_{w_c}	Capillary wavenumber
L	Loss factor
L_b	Bistatic baseline
L_p	Processing loss factor
M_2	2nd order intensity moment
m_f	Centre of gravity of Doppler spectra
M_n	Nth moment of PDF
$M_{n(norm)}$	Normalised Nth moment of PDF
m_s	Mean Doppler spectrum width
M_{S_n}	Nth moment of scatterer
N	Pulse compression factor
P_A	PDF of clutter background with no target present
P_D	Detection probability
P_{FA}	Probability of false alarm
P_n	Noise power
P_t	Transmit power
P_T	PDF of signal with target present
P_r	Received power

PSD_i	PSD sample value
Q	Quadrature component
$Q_{dist}(.)$	Complementary quantile function
R	Range
R_R	Range to receiver
R_T	Range to transmitter
$R_{unambiguous}$	Unambiguous Range
R_x	Receiver
$\dot{R}$	Rate of change in the relative radial distance
s	Standard deviation width of the Doppler spectra
S_{min}	Minimum detectable signal
T	Temperature
T_x	Transmitter
V_w	Wind speed
x	Power of sea returns
x_{CoG}	PSD Centre of Gravity
X_K	Frequency domain output of DFT
x_n	Time domain input of DFT
z	Intensity of sea returns

Abbreviations

ACF	Auto Correlation Function
AEW	Airborne Early Warning
AEW&C	Airborne Early Warning and Control
CDF	Cumulative Density Function
CFAR	Constant False Alarm Rate
CNR	Clutter to Noise Ratio
CSIR	Council for Scientific and Industrial Research
CW	Continuous Wave
EM	Electromagnetic
EW	Electronic Warfare
FFT	Fast Fourier Transform
FIAC	Fast Inshore Attack Craft
FM	Frequency Modulation
GIT	Georgia Institute of Technology
GPS	Global Positioning Satellite
GPSDO	Global Positioning Satellite Disciplined Oscillator
GUI	Graphical User Interface
HPA	High Power Transmitter

IFFT	Inverse Fast Fourier Transform
KLD	Kullback Leibler Divergence
KS	Kolmogorov-Smirnov test
LIDAR	LIght Detection and Ranging
LOS	Line of Sight
MNLT	Memoryless Non-Linear Transform
MR	Maritime Reconnaissance
NRCS	Normalised Radar Cross Section
ONR	Office of Naval Research
PDF	Probability Density Function
PM	Phase Modulation
PRF	Pulse Repetition Frequency
PRI	Pulse Repetition Interval
RAM	Radar Absorbent Material
RCS	Radar Cross Section
RF	Radio Frequency
RMSE	Root Mean Square Error
RTI	Range Time Intensity
SCR	Signal to Clutter Ratio
SNR	Signal to Noise Ratio
SS2 - SS6	Sea State 2 - 6
SSD	Sum Square Difference
SSE	South South East
SW2000	SearchWater 2000 radar system
SWH	Significant Wave Height
UCL	University College London
UCT	University Cape Town

Chapter 1

Introduction

1.1 Context of Research

Sea clutter has been studied for many years due to its significance to maritime radar systems. The extent of activity in this area demonstrates the complexity and range of phenomenological effects that sea clutter as an area of research presents. The many important scenarios and applications that require reliable and effective operational maritime radars have been the driving force behind much of this work.

For effective operation, maritime radar systems require the ability to dynamically compensate for the effects of sea clutter. The sea's surface presents a constantly changing clutter background that requires complex models to accurately describe the interaction with radar transmissions. This makes the task of distinguishing between small maritime targets and sea clutter a complex one. In order to be able to accurately predict and enhance the performance of an operational radar in a real maritime environment it is therefore essential to understand the behaviour of sea clutter. Due to the significant range of environmental and radar parameters that need to be considered, the study of sea clutter aims to characterise the clutter behaviour across as many scenarios as possible. The principal reason behind the study and modelling of sea clutter is to enable a better compensation for the clutter and improve the effective detection of targets on or near the sea surface.

In most scenarios the limiting factor for reliable detection of small RCS (Radar Cross Section) targets in the maritime environment is the level of sea clutter returns. Other possible limiting factors, for example receiver noise, do not reduce the detection capability of a radar system to the same extent as sea clutter. In general the thermal noise floor of the system should be much lower than the clutter returns, especially in high sea states.

Developing a comprehensive understanding of sea clutter returns is critical to drive improvements in signal processing algorithms, for clutter suppression and hence the continued enhancement of maritime radar performance. Due to the improvements in hardware and understanding of the characteristics of sea clutter over the past 20 years, modern radar systems now have a better prospect than ever before of efficiently compensating for sea clutter.

Modelling is a very important aspect of sea clutter research and subsequent radar development. Through both empirical models based on existing recorded data and EM scattering theory models, there have been many different attempts to describe the radar returns from the sea surface. Empirical models have been defined by analysing the clutter statistics, and the variation of these with selected parameters, from recorded datasets. Due to the significant number of environmental conditions and radar system variables involved, prior work has only examined part of the possible range of environmental and radar variables.

Constant false alarm (CFAR) algorithms are commonly used to set adaptive detection threshold levels with the knowledge from developed sea clutter models, [1]. This results in the suppression of the sea clutter and a reduction in the false alarm rate. The sea clutter model used directly defines these adaptive threshold levels. Misestimation between these models and the real sea clutter result directly in the overloading of a radar with false alarms. This demonstrates the importance of good sea clutter models to the performance of maritime radar.

Modern radar systems have the ability to use coherent processing to reject the bulk of the sea clutter when searching for low flying aircraft or for fast-moving ships. This raises a new area of research into understanding the behaviour of the sea clutter in the Doppler domain. Some research into the variation of Doppler with sea clutter amplitude distributions has been reported but there are still many areas that have not been fully explored.

Some key areas of sea clutter research which required further exploration are highlighted within [2] and are grouped into the following topics:

- Modelling of the Doppler spectrum of sea clutter.
- Characterisation of sea clutter spikes.
- Doppler processing for detection of slow-moving targets in sea clutter
- EM modelling of amplitude statistics and Doppler spectrum, in open seas and littoral waters.

In addition to the sea clutter specific research areas the topic of bistatic radar is of significant importance a large section of the work presented in this thesis. The very first radars were bistatic due to the inability to use a single antenna for reception and transmission. Since then bistatic radar research has gone through a number of resurgences, [3]. The latest resurgence in the area of bistatic radar development has been driven by a number of factors. A major contributing factor has been access to global positioning satellite facilities that can be used for unified timing, as well as accurate atomic clocks on a chip. In the context of maritime radar very few bistatic radar experimental campaigns have been generated for the purpose of studying the sea's surface. This leaves considerable gaps in the scientific knowledge of how the scattering varies with the significant number of variables. In [4] it is stated that future bistatic systems will increase the accuracy with which ocean wave information can be obtained through remote sensing. This improvement in understanding of the sea's interaction with radar signals, along with the additional advantages of bistatic systems seen in section 2.1.8, clearly shows the great potential for future bistatic maritime radar systems.

1.2 Aims and Objectives

The main aim of the work reported in this thesis has been the statistical study, characterisation and modelling of radar sea clutter using a number of different data sources covering a range of different environments. The objective has been to improve the understanding of sea clutter and optimise the design of maritime radar systems, allowing an improvement of detection of low RCS targets in sea clutter. The main objectives of the work towards this over-arching aim are outlined below:

- Analyse the amplitude statistics of the sea clutter returns by fitting clutter models to the observed amplitude distributions of real sea clutter from recorded data.
- Develop the understanding of the relationships between sea clutter distributions and Doppler. The area of Doppler analysis is defined as a important area of clutter research in [2] and hence is an important part of sea clutter research.
- Define the variation of these sea clutter characteristics as a function of different geometries and environmental conditions
- Utilise information theoretic measures in a novel way to improve the characterisation of sea clutter.

These objectives have been achieved through the analysis of both monostatic and bistatic radar data. The study of monostatic radar sea clutter statistics is a mature area of radar research. Numerous papers and books have been published on the empirical analysis of monostatic sea clutter data over many years. Despite this, the novel parts of the monostatic analysis that have been achieved in this work are of more immediate practical importance to operational coherent monostatic systems. The outputs of the analysis can be utilitised now to improve the way in which current monostatic maritime radar system operate.

The bistatic analysis of sea clutter is a more novel area of research as very few bistatic sea clutter datasets exist, none of which analyse the coherent properties of bistatic clutter in comparison to monostatic. The implication of this work is equally important for bistatic radar systems as it is for monostatic, but fewer operational bistatic systems exist. Hence the direct influence of the bistatic component of the work is more long term for the future generation of potential bistatic maritime systems.

This work has the potential to further optimise maritime radar system capabilities and help open up a new area of bistatic maritime radar. By characterising bistatic sea clutter, future bistatic systems can be developed to adapt to the behaviour of bistatic sea clutter and therefore maximise detection performance in these complex systems and geometries.

The importance of effective sea clutter modelling is described in great detail within [5]. A practical radar system requires effective modelling throughout the lifecycle of the radar. If the wrong models are used in the performance analysis and prediction stages, incorrect conclusions may be drawn prior to developing the radar. This generates false expectations for the user of a radar system and on delivery of the system it will not operate at it's specified required level. As contracts to provide radar's are based on strict performance criteria it is clear the modelling of sea clutter and a radars ability to compensate for it is an extremely important part of practical radar engineering.

Information theory is a well establish area of applied mathematical research that has the aim of quantifying information as well as optimising its use. This wide area of research has been applied in many fields from data compression, communications and cryptography. Little prior work from this field has been applied to any radar applications. The objective of the work included in this thesis is to use an information theory metric when quantifying real clutter data in comparison to established clutter models. This novel application in the quantification of the effectiveness of clutter models is a new proposed way of assessing how well the model is representing the clutter itself. The concept of applying the selected information theory metric was initially suggested by A. Charlish and resulted in a joint publication, [6] listed in Section 1.6 (which demonstrated the concept).

1.3 Importance of Maritime Radar

Maritime radar is of as much great civil and military importance now as it has been since its invention. Some of the applications of modern maritime radar include search and rescue, collision avoidance, port security, remote sensing, as well as Airborne Early Warning (AEW) used in civil and military scenarios. As well as these well known applications more recently a resurgence in modern day piracy and human trafficking has brought more demand for effective maritime radar systems. In the modern world these applications are as important as ever. Thanks to radar engineering research, contemporary radar systems are constantly pushing the boundaries of their capabilities to effectively succeed in these tasks.

The very first application of radar was a maritime radar created by Christian Hülsmeyer used to detect ships for collision avoidance in low visibility conditions [7]. This was tested in 1904 in Cologne and successfully detected an approaching ship whilst located on a bridge. This shows that from the very beginnings of radar maritime applications have been a key application of the technology.

A few examples of modern maritime radars are presented here to give insight into the current systems that work in this complex environment. In the area of maritime reconnaissance examples of current radar are the SearchWater 2000, Sharpeye, Erieye, and Seaspray; seen in Fig. 1.1, 1.2, 1.3 and 1.4 respectively.

Figure 1.1: Searchwater 2000 on Sea King Mk7

SearchWater was originally developed by EMI which later became Thales UK. The first system was used for maritime reconnaissance (MR) applications and was located on the British Royal Air Force Nimrod aircraft. The next iteration of the system, the MK2, was adapted to be located on to a Sea King Mk7 helicopter as seen in Fig. 1.1 for airborne early warning (AEW) applications. This adaptation occurred due to the Falklands War and a demand for AEW presence during the conflict. The systems key advantages are its long range, and good range resolution the combination of which makes it one of the most effective modern maritime radar systems.

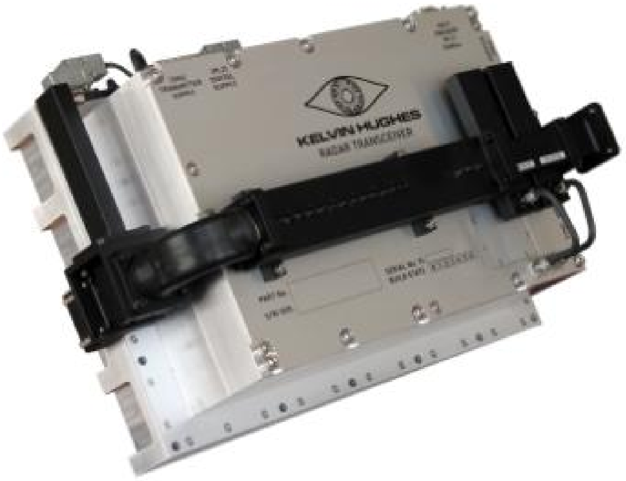

Figure 1.2: SharpEye radar

The SharpEye system is a solid state radar that has been developed by Kelvin Hughes Marine Systems. This system claims to be the world's first solid state civil maritime radar system, [8]. This fully coherent system is aimed at the civil maritime market and boasts high reliability due to the use of a solid state transmitter instead of a less reliable, but more powerful and cheaper magnetron.

Figure 1.3: Erieye radar

The Erieye radar system was first developed in 1985. It is an AEW and control (AEW&C) radar that is manufactured by Ericsson Microwave Systems (now Saab Electronic Defense Systems) Sweden, [9, 10]. Examples of the aircraft that used this system include the Saab2000 and the Embraer EMB-145. The radar employs an electronic array system with 192 individual transmit and receive modules. This array allows for electronic beam steering as opposed to physical mechanical steering of the direction of the radar beam.

Figure 1.4: Seaspray 7500E radar mounted in U.S Coast Guard HC-130 Hercules

The Seaspray 7500E is another example of an electronically steered active array maritime radar, developed by Selex Galileo. This system uses a composite scanning method of an electronically and mechanically steered main beam. Selex defines the system as a multi-mode surveillance radar which is capable of detecting even small targets such as fast inshore attack craft (FIAC).

The understanding of clutter amplitude statistics is clearly important for these radars as they are required to operated in the complex environment the sea represents. From these examples of maritime radars SW2000, Sharpeye and Seaspray 7500E are all coherent systems. Therefore the additional understanding of the coherent characteristics of sea clutter is critical for these systems to maximise the added ability that coherence gives them. By effectively using the coherence of a maritime radar it can increase detection probabilities and reduce false alarm rates in comparison to non-coherent systems.

1.4 Thesis Structure

The thesis has been organised in the following way:

This chapter introduces the background aims and goals of this work, along with a brief overview of real radar systems that are used in this area of work.

Chapter 2 begins with radar fundamentals including sections on radar equation, clutter, Doppler and bistatic radar concepts. An overview of the theory behind sea clutter is then included. The area of information theory is then introduced and the concepts linked to radar statistics information are discussed. A comprehensive literature review of prior research into different aspects on sea clutter then follows.

Chapter 3 describes each of the datasets used for analysis in this thesis. Initially each dataset is described in detail along with the radar system used to generate it. The pre-processing analysis techniques applied to all datasets are then described which enable the data to be brought to a point that statistical analysis can be performed.

Chapter 4 follows this with the comprehensive statistical analysis of all of the datasets. In each case the non-coherent data is analysed then the Doppler data characteristics are analysed. This chapter contains the bulk of the practical analysis of real data.

Chapter 5 introduces a model of sea clutter, first developed by S. Watts, and applies it to multiple datasets. The simulation results are discussed and compared with the real dataset characteristics that were defined in Chapter 3.

Chapter 6 discusses the information theoretic work that has been applied to sea clutter analysis. The relevance of the applied methods are discussed and then their results of are shown.

Chapter 7 summarises the findings of the research and highlights the key result. Possible future work is discussed detailing areas where potential gains could be made through a continuation of research.

1.5 Novel Aspects

The novel aspects of this thesis are contained in Chapters 4-7. These can be summarised as:

- Characterisation of Sea clutter Doppler amplitude statistics as a function of Doppler frequency. This has been completed by using both the sum square difference fitting approach and the method of moments. The fitting methods were applied between raw data and the Compound-K, Weibull and Gaussian distributions.

- First publication of the analysis of bistatic sea clutter Doppler amplitude statistics. The NetRAD sea clutter dataset has allowed for the analysis of bistatic sea clutter Doppler statistics. Analysis of data from multiple bistatic angles and geometries in both horizontal and vertical polarisations has been performed.

- Application of newly developed coherent clutter model to simulate bistatic and monostatic sea clutter Doppler spectra. The model was originally introduced by S. Watts [11], the novel aspects of this work are:
  - The application to further datasets generated from a different radar that the model was original tested with.

  - The establishment of relationships between the model parameters and physical parameters, as well as new relationships between parameters within the model itself.

- The application of the information theory metric Kullback Leibler Divergence (KLD) to sea clutter. The metric was used as a measure of goodness of fit of sea clutter model and raw data. The applicability of the KLD metric in sea clutter analysis was demonstrated through testing a clutter model's ability to represent real data distributions, as well as being able to define the performance of a model in representing raw data distributions as a function of Doppler.

1.6 Publications

The following list of publication have been generated during the work towards this EngD:

- M. A. Ritchie, A. G. Stove, S. Watts, K. Woodbridge and H. D Griffiths, Application of a New Sea Clutter Doppler Model, *Submitted to International Radar Conference Australia*, 9-12 Sept 2013

- M. Inggs, A. Balleri, W. A. Al-Ashwal, K. D Ward, K. Woodbridge, M. A. Ritchie, W. Miceli, R. J. A. Tough, C. J. Baker, S. Watts, R. Harmann, A. G. Stove, S. Sandenbergh, and H. D. Griffiths, NetRAD Multistatic Sea Clutter Database, *IEEE International Geoscience and Remote Sensing Symposium (IGARSS)*, pp.2937-2940, 22-27 July 2012

- M. A. Ritchie, W. A. Al-Ashwal, A. G. Stove, K. Woodbridge, and H. D. Griffiths, Analysis of simultaneously recorded monostatic and bistatic sea clutter generated at separate significant bistatic angles, *IET International Radar Conference*, 2012.

- M. A. Ritchie, W. A. Al-Ashwal, A. G. Stove, K. Woodbridge, and H. D. Griffiths, Statistical analysis of monostatic and bistatic sea clutter Doppler spectrum, *CIE International Conference on Radar*, Chengdu, China, pp.816-820, 24-27 Oct. 2011

- M. A. Ritchie, A. Charlish, K. Woodbridge, and A. G. Stove, Application of Kullback-Leibler divergence to sea clutter estimation, *IEEE International Radar Conference*, Kansas City, USA, May 2011.

- W. A. Al-Ashwal, A. Balleri, J. P. Browning, H. D. Griffiths, R. Harmanny, M. Inggs, W. Miceli, M. A. Ritchie, S. Sandenbergh, A. G. Stove, R. J. A. Tough, K. D. Ward, S. Watts, and K. Woodbridge, Measurements of Bistatic Radar

Sea Clutter, *IEEE International Radar Conference*, Kansas City, USA, May 2011.

- W. A. Al-Ashwal, C. J. Baker, A. Balleri, H. D. Griffiths, R. Harmanny, M. Inggs, W. Miceli, M. A. Ritchie, J. Sandenbergh, A. G. Stove, R. J. A. Tough, K. D. Ward, S. Watts, and K. Woodbridge, Statistical analysis of simultaneous monostatic and bistatic sea clutter at low grazing angles, *Electronics Letters*, Vol. 47 No. 10, 12th May 2011

- Ritchie, M.A.; Woodbridge, K.; Stove, A.G., Analysis of sea clutter distribution variation with Doppler using the compound k-distribution, *IEEE International Radar Conference*, Washington D.C, pp.495-499, 10-14, May 2010

Chapter 2

Background

This chapter starts by introducing the relevant aspects of radar and sea clutter theory. A brief introduction to the subject area is given with an overview of general radar theory highlighting basics such as the radar equation and RCS. The mathematical background of information theory is then discussed. The chapter then goes on to review prior literature in the area of monostatic sea clutter research, bistatic radar, bistatic sea clutter and finally reviews information theory literature. In the review of monostatic sea clutter literature the various models for sea clutter that have been developed are defined and analysed.

2.1 Radar Fundamentals

This section introduces some of the key performance metrics that have to be considered when analysing any aspect of radar. The necessary background knowledge required will be introduced here to build on the more advanced research which is discussed in later sections.

Firstly the term Radar is an acronym which comes from *RAdio Detection And Ranging.* In [12] radar is defined as a system that,

operates by radiating electromagnetic energy and detecting the presence and character of the echo returned from reflecting objects.

The ability of radar to detect a returned signal depends on the capacity of an EM wave to propagate to a object, be reflected by the object and to propagate back to a receiver antenna. The target may be approximated by a point scatterer such as a small aircraft or an extended scatterer such as an illuminated area of land or sea. It is the interaction of radar with the extended surface of the sea, over a range of circumstances, which is the focus of interest for this work.

Radar systems are defined by a number of characteristics but a key factor is the frequency of operation. The range of frequencies that modern radars are capable of operating at is large, extending from hundreds of mega-Hertz to giga-Hertz. An example of a very high frequency radar system would be an automobile radar system that can operate at $\approx$ 80 GHz, while over-the-horizon radars for example utilise some of the lowest radar frequencies, 3-30 MHz. The characteristics, including polarisation, of the transmitted waveform is also an important factor. Examples of the main waveform types are continuous wave, pulse and chirp. There are also many other parameters of importance, which will be discussed subsequently. Similar techniques to radar do exist, for example systems at optical frequency (LIDAR) and other systems that use acoustics, although the latter does not use EM radiation and neither of these propagate the long distances that is characteristic of microwave radars.

The enormous range of applications of radar systems as well as the significant variation in the characteristics of radars has been a key driver behind the extensive research in radar systems. Understanding the interactions of the radiated signal with both the desired target and the background clutter is therefore of upmost importance especially since these interactions vary greatly for different scenarios and signals.

The basic steps involved in monostatic radar operation is the emission then reception of a EM signal from and then back to an antenna. During the signal's propagation across the environment it interacts with the environment via various scattering mechanisms. Due to backscattering from the environment and targets, a fraction of the emitted signal returns to the reciever antenna. This received signal then undergoes signal processing to extract information from it, most commonly desired information is the range and bearing, hence giving the location, as well as the Doppler of any present targets.

The following sections describe the key fundamental concepts behind radars and the propagation of their electromagnetic waves. Core texts that summarise this area well are [1, 12–14].

2.1.1 Radar Equation

The radar equation is the most fundamental equation for predicting the power received by a radar system, and depends on a number of important variables. It can take many forms that range in complexity, although the underlying physics is the same for all forms. For a monostatic pulsed radar a basic form for the radar equation, in free space, is defined as:

$$P_r = \frac{P_t G^2 \sigma \lambda^2}{(4\pi)^3 R^4 L} \tag{2.1}$$

where P_r is the power received by the antenna given a transmit power P_t and G is the antenna gain, σ is the target RCS, λ is the wavelength of signal, R is the range to the target from antenna, and L is a loss factor. The loss factor in this case is ≥ 1 as it is on the denominator. The RCS term relates to the power reflected from a target and is defined further in section 2.1.4.

The power terms in Eqn. (2.1) are related to the absolute values that are transmitted and received by the front end of the radar system. The gain is related to the effective aperture A_e by:

$$G = \frac{4\pi A_e}{\lambda^2} \tag{2.2}$$

the effective aperture of the radar antenna is defined by the product of its physical aperture and its efficiency.

The loss factors represented by L include, for example, receiver losses, beamshape losses and atmospheric losses.

Eqn. (2.1) only takes into account the significant factors that affect the received power of the system and hence the performance. There are a large number of additional variables that can cause the real life performance of a radar system to differ from this predicted value, but they have not been considered in this simplified case.

As well as the received power from the returned radar signal, receiver noise is present within the signal. To calculate the signal to noise ratio at the radar receiver requires the receiver noise power, P_n, to be evaluated:

$$P_n = k_B T_0 B F_n \tag{2.3}$$

k_B is Boltzmann's constant (1.38×10^{-23} JK^{-1}), T_0 is the absolute temperature of the receiver defined as 290k, B is the bandwidth and F_n is the noise figure. The noise power P_n represents the thermal noise of the environment and system. Due to the defined temperature T the factor $k_B T$ is -174 dBmHz^{-1} [15].

Using Eqn. (2.1) and (2.3) it is possible to define the signal to noise ratio (SNR) for the radar receiver.

$$SNR = \frac{P_t G^2 \lambda^2 \sigma}{(4\pi)^3 R^4 k_B T B F_n L} \tag{2.4}$$

The signal to noise ratio is literally the ratio of the power of the received desired signal (often the selected target) and the noise level present within the signal. Using the equations presented so far it is now possible to define the minimum signal that a radar can detect, as follows,

$$S_{min} = P_n(SNR) \tag{2.5}$$

This shows only a simple theoretical equation that describes the minimum detectable signal given the environmental thermal noise and added noise of the system, $k_B T B F_n$. It does not define the practical required signal needed to detect a target at a given range. In reality this is affected by a number of factors, of which clutter is the most important.

2.1.2 Pulse Compression

Pulse compression is a technique which attempts to enhance the detection range as well as the range resolution of a radar signal. This is achieved by applying a form of modulation to the transmitted signal. In radar systems the most commonly used form of modulation is frequency modulation (FM), although it is also possible to apply phase modulation (PM).

Frequency modulation applies a linear increase or decrease to the frequency of the transmitted signal as a function of time lag. When this transmitted signal is then received a filter introduces a time lag that decreases or increases linearly with frequency at the same rate it was applied to the transmitted signal.

The resulting output signal has much higher amplitude over a shorter period of time, as the time lag has overlapped the signal onto one location in time, or compressed the signal. Hence giving the system a finer range resolution, but still maintaining a long duration pulse. The long duration pulse allows a greater incident power onto a given target, compared to a short pulse, which increases the maximum detection range. This is explained in detail within Chapter 13 of [1]. Equation (2.1) shows that power received from a given target is directly proportional to the pulse compression gain factor, N, that is applied to the signal.

Figure 2.1, from [1], shows a diagram of a linearly stepped frequency pulse with a pulse length of τ as an input to a receiver filter. The filter then applies the process described above and produces the output signal which is much higher in amplitude. The output is also compressed to a pulse length that is a 1/6th of the original length, due to the six frequency steps in the input signal.

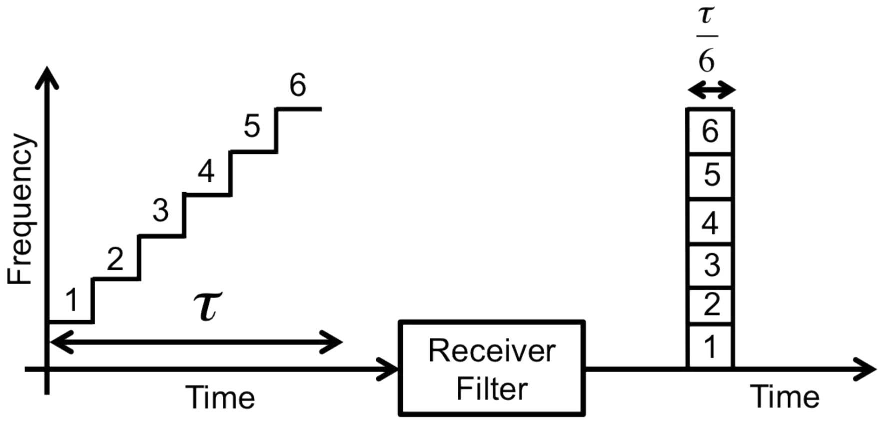

Figure 2.1: Pulse compression diagram

The disadvantages of introducing pulse compression is that is increases the minimum range of the radar system, and it also produces range sidelobes. Using pulse compression is a trade off between these disadvantages and the important advantages of increasing both power incident on target while maintaining enhanced range resolution.

2.1.3 Clutter

In radar the term clutter is defined in [13] as,

a radar return from an object or objects that is of no interest to the radar mission

Examples of these objects that are cited include precipitation, vegetation, soil, rocks and the sea. As well as these natural existing examples, man-made objects can also be considered clutter and will generate their own distinct signals. A topical example of a modern man-made clutter object is a wind turbine. These represent large objects with fast moving turbine blades that will give high amplitude and Doppler returns to a radar system that are generally unwanted. All of these examples have the potential to cause reflections back to the radar which will be included within the signal along with the desirable components such as targets.

Clutter, like thermal noise, is an unwanted component of the radar signal, and can be defined in terms of a clutter to noise ratio (CNR). Unlike thermal noise, which will often have a constant mean amplitude within a received signal, clutter returns follow an amplitude variation that is related to distance in the same way as the returned radar signal, see Eqn. (2.1). The samples of thermal noise are also normally distributed and statistically independent between received pulses, whereas clutter returns can be highly correlated between pulses and follow a wide range of statistical distributions. The characterisation of these type of distributions is of great importance when compensating for these clutter effects.

It is more often the case that the limiting factor for detection in a practical radar system is the signal to clutter ratio (SCR), not the SNR. This demonstrates the importance of understanding the clutter returns. In cluttered environments the detection process of small difficult to detect targets is heavily dependent on SCR.

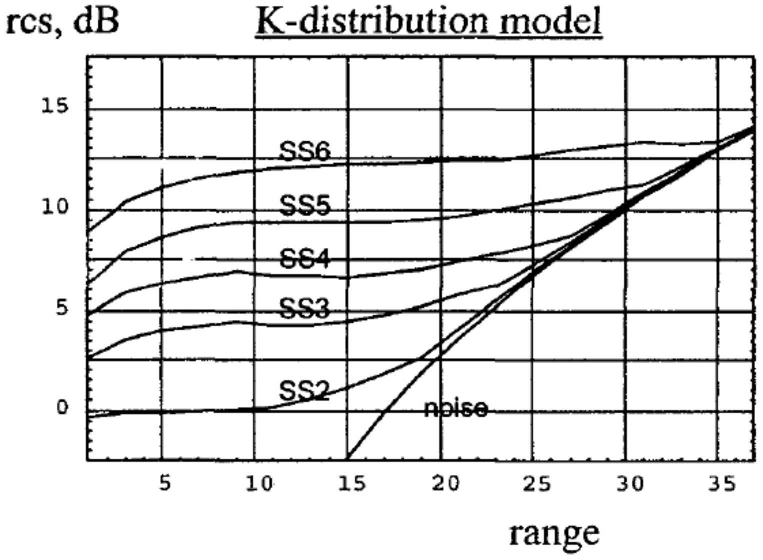

Figure 2.2: Clutter limited and thermal noise limited minimum RCS vs. range (miles)

Figure 2.2 taken from [?] shows an example plot of the simulated minimum RCS of a detectable target as a function of range. The lines labelled SS2 - SS6 refer to clutter conditions at sea states 2 to 6, see section 2.2, and the line labelled noise refers to the thermal noise limited case. In the clutter limited cases at low ranges a significantly higher RCS is required to detect a given target compared to a thermally noise limited system, which is to be expected. At a certain range each sea state clutter limited case reaches the same required minimum RCS for detection. This demonstrates the difference in clutter limited detection and thermally noise limited detection over a range of conditions.

2.1.4 Radar Cross Section (RCS)

This section introduces the concept of RCS and its relation to scattering theory. The RCS, σ, of a target is effectively a metric that is related to the power that a object will return to the receiving antenna, as a fraction of the power incident on the target. The RCS value depends on an objects ability to reflect signals, and is a measure of power scattered per steradian (unit of solid angle). The ratio of the power intercepted by a target to backscattered density is used to calculate the RCS.

The RCS of a target behaves differently to the manner in which visible light produces a perceived image of an object. An RCS is often larger than the geometric cross section of the object. This is due to the distinct way EM waves interact with each target. As the wavelength of the signal used approaches the size of the object, it is attenuated during the reflection, which results in a received power signal that does not represent the exact physical size.

RCS is a product of three factors; Projected Cross Section, Reflectivity and Directivity. The projected cross section is simply the two dimensional image of the object, as seen from the point of view of the antenna. Reflectivity is the percentage of intercepted power that is redirected (scattered) by the object. The Directivity is a measure of the power reflected back to the receive antenna as a fraction of isotropic (equal in all directions) scattering.

The RCS factor seen in Eqn. (2.1) and Eqn. (2.4) is given by (Chapter 27 [12]):

$$\sigma = \frac{\text{Power reflected towards radar per unit solid angle}}{\left(\frac{\text{Incident power density}}{4\pi}\right)} = \lim_{R \to \infty} 4\pi R^2 \left| \frac{E_r}{E_i} \right|^2 \tag{2.6}$$

where σ is the RCS, E_r is the electric field strength of the scattered EM wave received by the radar, and E_i is the electric field strength of the incident EM wave on the target, and R is the distance from the target to the radar antenna.

A target's RCS is a basic representation of the complex scattering mechanisms that occur with the interaction of the radar signal with the target. It can vary significantly with orientation of the target with respect to the incoming signal. This is primarily due to how the signals reflected from various components of the target combine.

Stealth technologies aim to reduce the RCS of a target as much as possible. This is achieved by using materials that absorb the EM radiation, Radar Absorbent Material (RAM), minimising the physical size of the targets, and by designing the structure to reflect back the EM waves in a different direction than its origin. An examples of a aircraft that uses RAM material are the U-2 and B-2 while a example of a platform that uses directivity in its design is the F-117 jet.

Bistatic radar systems have potential counter-stealth capability due to their multi perspective on the target increasing detection of waves scattered in different directions, see section 2.1.8.

2.1.5 Radar Range Resolution

In a radar the returned target signal delay is directly proportional to the range of the target. Range resolution is defined as the minimum distance possible between two separate targets at which it is still possible to independently resolved each target. In a simple pulsed radar system this is a function of the pulse length that is transmitted:

$$\Delta R = \frac{c\tau}{2} \tag{2.7}$$

where ΔR is the range resolution, c is the radar pulse speed (which is assumed as speed of light in free space) and τ is the pulse length.

This shows that range resolution is directly proportional to the length of the pulse used. An issue with reducing the pulse length to enable finer range resolution is that this will reduce the amount of EM energy incident on a given target. This will lead to a reduction in the signal level received by a radar. A method to enhance the resolution whilst keeping a long pulse is pulse compression which has been discussed within section 2.1.2.

Pulse length has an inverse relationship with the bandwidth of the pulse, [1]. To produce very short square pulses a very large pulse bandwidth is needed. This is due to short temporal signals having very wide frequency outputs after Fourier transform. Hence the range resolution is also linked to the pulse bandwidth:

$$\Delta R = \frac{c}{2B} \tag{2.8}$$

Where B is the Pulse bandwidth.

2.1.6 Doppler Theory

In coherent radar systems it is possible to measure the Doppler of the returned signal. This is a measurement of the frequency shift of the returned signal from the original centre frequency that was transmitted. The extent of this shift is directly proportional to the relative radial velocity of the target or clutter that is being illuminated. The Doppler phenomenon is very important to radar systems as the ability to measure the relative speed of a target gives radars an almost unique input into the targets characteristics that other sensors require further steps to evaluate.

A coherent system has the ability to measure the phase Φ of the returned signal, any change in phase is assumed to be due to the relative motion of the target or clutter. The phase of the signal, measured in radians, is defined as:

$$\Phi = -\frac{2R(2\pi)}{\lambda} \tag{2.9}$$

The Doppler frequency, in Hertz, is defined as the rate of change in phase, which is the derivative of Eqn. (2.9):

$$\dot{\Phi} = -\frac{2\dot{R}}{(2\pi)\lambda} = f_d \tag{2.10}$$

Where f_d is the Doppler frequency, $\dot{R}$ is the rate of change in the relative radial distance and λ is the radar signal wavelength. The factor of 2 is due to the radar signal travelling the two way distance to the target/clutter. The negative sign is used it is convention that a decreasing relative range gives a positive Doppler frequency, e.g the frequency is increased from that transmitted. Using the relationship between wavelength and frequency it is possible to also relate the Doppler frequency to the transmitted frequency of the radar system,

$$f_d = -2\frac{\dot{R}f_c}{c} \tag{2.11}$$

As previously noted the velocity vector $\dot{R}$ is the relative radial velocity of the target with respect to the radar. In the case where a radar is tracking a moving aircraft target the component of the aircraft's velocity with respect to the ground based radar is proportional to $cos\Psi$ where Ψ is the angle between the aircraft velocity vector and the radar's line of sight (LOS), [13]. This gives,

$$f_d = \frac{2V}{\lambda}cos\Psi \tag{2.12}$$

The characteristics of sea clutter Doppler spectra returns are discussed later in section 2.3.3.

2.1.7 Range and Doppler ambiguities

Pulsed Doppler radar systems operate at a single or changing (agile) pulse repetition frequency (PRF). This represents the frequency at which the pulses emitted are repeated at. Within the gaps between pulses the radar detects the returned signal. The time between pulses is the inverse of the PRF and is commonly known as the pulse repetition interval (PRI).

Operational radars in practice can use PRFs of the order of a few hundreds of Hz up to 100's kHz. The selection of the PRF of a radar is an important decision and is tightly linked to the applications that the radar is designed for. The balance between a high or low PRF will define the ambiguities that will be present in range and Doppler.

Range ambiguous measurements occur when the returned signal is not from the pulse directly preceding the measurement, but from any number of pulses prior to it. Often there is no method of identifying which pulse a given return originated from. Thus the range at which that pulse has returned from is ambiguous.

As the power of the returned signal is related to R^{-4}, Eqn. (2.1), then returns from more than a couple of pulses preceding the detection are normally not detected due to the significant reduction of power at long ranges. The unambiguous range of a radar is as follows:

$$R_{\text{unambiguous}} = \frac{c}{2PRF} \tag{2.13}$$

By operating at a low PRF a significant amount of time is left between receiving pulses. Thus the vast majority of returns are unambiguous as the ambiguous returns will occur from such long ranges that they will most likely not be detected. The disadvantage of this is that the frequency of updates from the scene is lowered, which may result in lost information, target detections or target track losses. High PRF radars obtain more frequent returns from a given target, but limit their maximum unambiguous range. To overcome this issue it is possible to introduce a changing PRF. By altering the PRF between pulses it is possible to observe if a target is at an ambiguous range. An ambiguous range target will shift its distance by a value related to the change in the PRF. The change in distance due to the PRF shift can be used to locate the target at its true unambiguous range but still operate at a high PRF.

The effect of an ambiguous detection can be seen in Fig. 2.3, where target (A) is unambiguous in range at 20 km, while target (B) is either at a distance of 10 km after pulse 2 or 40 km after pulse 1 making it ambiguous in range.

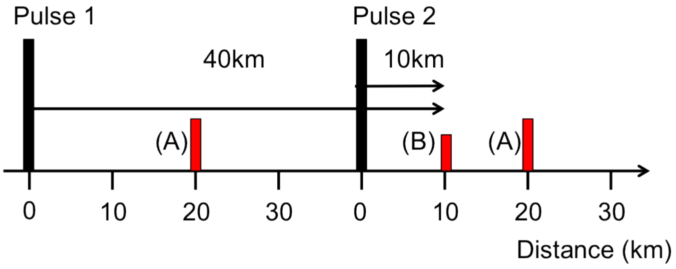

Figure 2.3: Diagram of ambiguous target measurement

As well as range ambiguities it is also possible for radar returns to be ambiguous in Doppler. In the reception and filtering of the returned signal the resulting signal has sideband frequencies that are separated from the main carrier frequency by ± PRF (Hz). The resulting Doppler of a target will wrap around in the Doppler domain to be confined within ± PRF (Hz). Hence a target with a Doppler frequency greater than the PRF, for example $W.PRF + X$ where W is an integer, will be located at X in the Doppler domain making it ambiguous.

Therefore it is advantageous to have a high PRF, as this increases the size of the unambiguous Doppler space. When detecting targets using Doppler processing it is very easy to achieve a successful detection if the target Doppler is located separately from the background clutter spectrum. If the system is operating with a large PRF the target's Doppler return resides within the unambiguous Doppler region. If a low PRF is selected then it is very possible that the target's Doppler return will wrap into the background clutter and be much more difficult to detect, due to it coexisting with the clutter spectra, see Fig. 2.4.

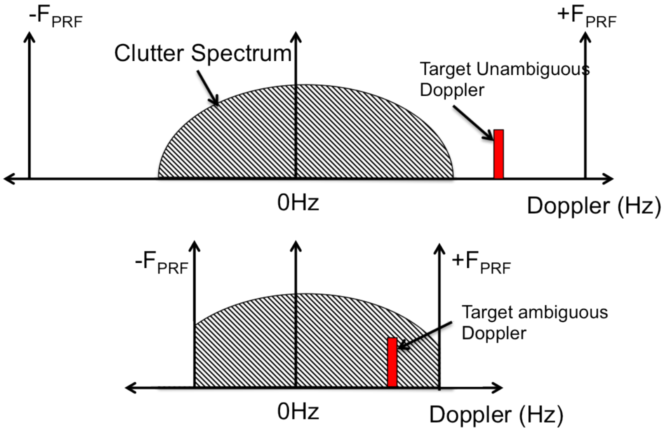

Figure 2.4: Diagram of Doppler unambiguous and ambiguous target measurement

This shows that a careful selection of the PRF is required to maximise either the unambiguous range or unambiguous Doppler spectrum, or attempt to obtain a balance between the both of these parameters that satisfies the requirements of the radar system.

2.1.8 Bistatic Radar

So far all the discussion has been focused on monostatic radar systems, where the transmit and receive antenna are the same or co-located. This section will introduce the key theoretical components associated with bistatic radar systems including the advantages of such systems, the definition of bistatic geometries, bistatic radar equation and bistatic RCS.

A bistatic radar system is defined as having its transmit and receive antennas at different positions [12]. A clear and full overview of the area of bistatic radar can be found in [3, 14, 16], as well as Chapter 36 in [12].

Bistatic radars can either use dedicated radar transmitters or non-radar transmissions (for example FM radio or TV transmissions). The majority of the work in this thesis discusses the configuration when a monostatic radar is used as the transmitter for the bistatic receiver, which is known as a hitchhiker setup.

There are many advantages of a bistatic radar system. The key ones are:

- Anti-stealth capability due to the bistatic geometry. The re-radiated energy does not have to return to its source, as in monostatic systems. Therefore the stealth design that reduces reflection that are directed back to the origin can be countered by bistatic systems.

- Increased RCS of target when it is close to or on the bistatic baseline. This is due to Babinet's principle, where the same scattering occurs for a perfectly absorbing target and a infinity conducting sheet with hole the same shape as the target. Therefore a target on the baseline between the transmitter and receiver antennas will have a significantly increased RCS, in comparison to the same target at an equivalent distance.

- Increased coverage, particularly useful in extending coverage into existing monostatic radar blackspots. For example a monostatic system may not be able to detect targets behind a mountainous area because of shadowing by the mountains. The used of a bistatic system could allow for detections within this previously non-illuminated region.
- Covert operation. By using a system in a passive mode it is receive only, therefore significantly more difficult to detect by EW devices.
- Increased resilience to EW counter measures. This is because in receive only operation the location of the receiver cannot be determined by any EM emissions, and hence can not be jammed by a directional jammer.

A representation of the bistatic geometry can be see in Fig. 2.5. L_b is the baseline length which is the separation between the transmitter (T_x) and the receiver (R_x), R_T and R_R are the range of the transmitter and receiver from the target, β is the bistatic angle, and θ_T and θ_R are the angle between North and the receiver / transmitter azimuth.

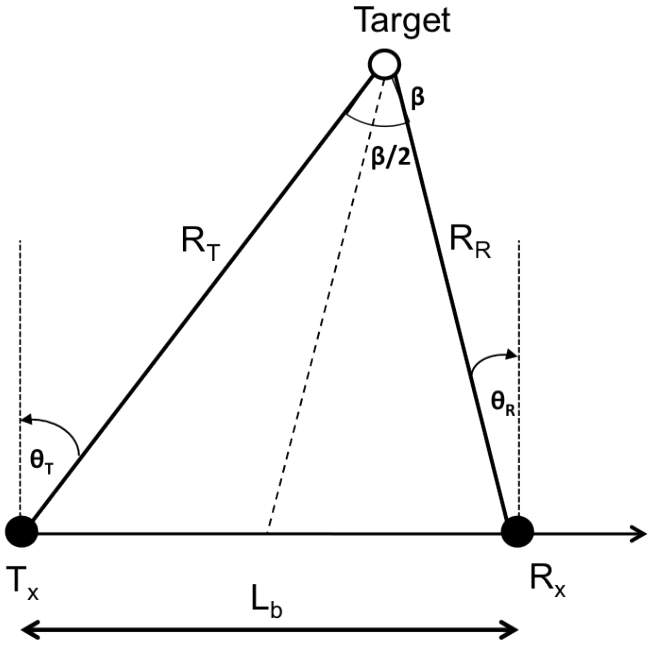

Figure 2.5: Bistatic geometry convention

As bistatic systems have a complex geometry compared to monostatic systems there is a different definition for the range and a different range equation is required.

Some of the literature uses the defines bistatic range as $R_R + R_T - L_b$, another definitions is $R_R + R_T$, for the rest of this work the latter will be used.

Bistatic radar systems range contours are defined by ovals of Cassini. The ellipses are quadratic curves which are described by a point that the product of the distances from two fixed points a distance $2a$ apart is a constant b^2. The characteristics shape of the curves are defined by the ratio of b/a. As the ratio decreases the shape moves from a oval to a figure of eight shape then eventually two separate loops exist if $a > b$. In polar co-ordinates ovals of Cassini follow as:

$$r^4 + a^4 - 2a^2r^2[1 + \cos 2\Theta] = b^4 \tag{2.14}$$

Where r and Θ are the distance and angle to the co-ordinate on a specific oval of Cassini. The points along an oval of Cassini are all loci that conform to the condition that they all have the same values for the sum of the two sides of a triangle (R_T and R_R), where the third side is fixed as the baseline (L_b). These lines mark out lines of constant SNR for a fixed baseline L_b. A plot showing examples of ovals of Cassini with varying parameters can be seen in Fig. 2.6, where a is set to 5 and the ratio of a/b is varied from 1 to 1.5.

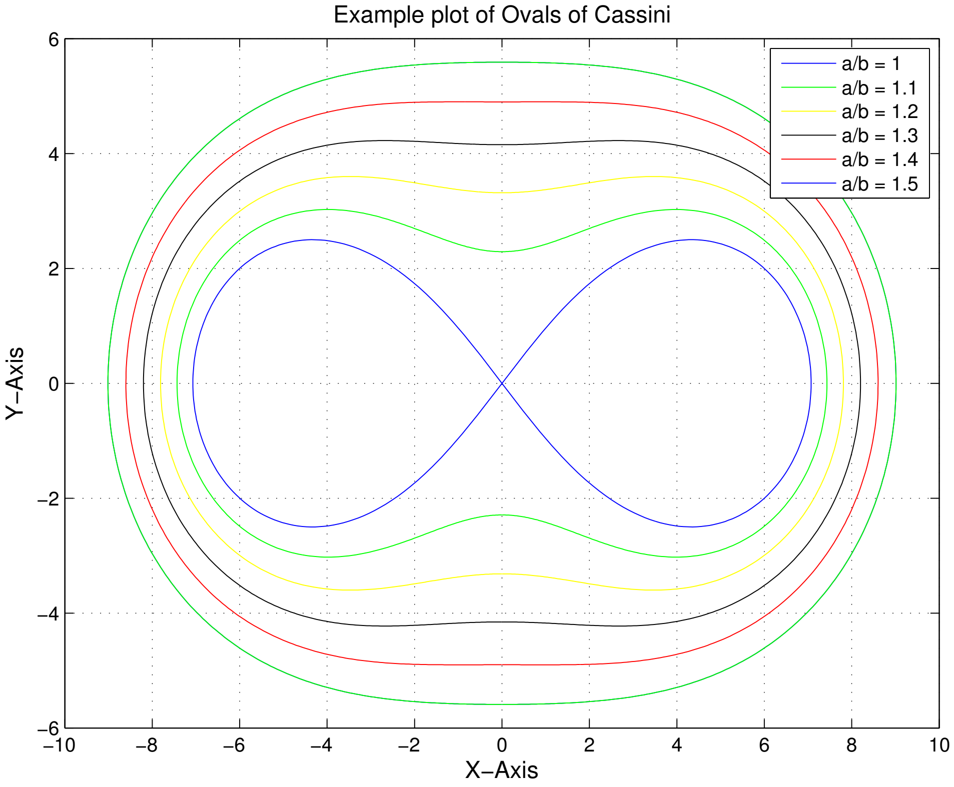

Figure 2.6: Example plot showing ovals of cassini

The bistatic range equation is:

$$P_r = \frac{P_t G_t G_r \lambda^2 \sigma_b L_p}{(4\pi)^3 R_T^2 R_R^2 k_B T_0 B F_n} \tag{2.15}$$

where P_r is the power received, P_t is the transmit power, G_t and G_r are the transmitter and receiver antenna respective gains, λ is the wavelength, σ_b is the bistatic target RCS, L_p is a system loss, and F_n is the noise figure.

The bistatic clutter cell will obviously not be equal to a monostatic radar equivalent clutter cell. It is defined to be an intersection of the range cell, Doppler cell and main beam footprint. The clutter cell can either be defined as being beam width-limited, range-limited or Doppler-limited, [14]. The Doppler-limited case has not been considered within this work.

In the beamwidth-limited case the clutter cell area $(A_c)_b$ can be approximated at small grazing angles by [14],

$$(A_C)_b \approx \frac{(R_R \Delta\Theta_R)(R_T \Delta\Theta_T)}{\sin\beta} \tag{2.16}$$

where $\Delta\Theta_T$ and $\Delta\Theta_R$ are the 3dB widths of the transmit and receive beams, $R_T\Delta\Theta_T$ and $R_R\Delta\Theta_R$ are the transmit and receive cross range at the intersection of the two beams.

The range gate limited clutter area, $(A_C)_r$, is always smaller than the beamwidth-limited case and defined as,

$$(A_C)_r \approx \frac{c\tau R_R \Delta\Theta_R}{2\cos^2\frac{\beta}{2}} \tag{2.17}$$

The beamwidth limited and range gate limited cases are shown as the shaded regions in Fig. 2.7 (a) and (b) respectively. This diagram uses the assumption that the beamwidth shape is square making a quadrilateral shape, while in reality the beam will have a fan like shape.

The equations given for the clutter cell areas use assumptions to simplify their evaluation. Prior work has also been completed into numerical integration methods to evaluate the areas in [17], which is not covered in this thesis.

As a bistatic receiver observes a different target aspect angle in comparison to an equivalent monostatic system the bistatic and monostatic RCS can vary greatly. Early work by [18] defined an RCS equivalent for bistatic systems as the sum of the transmit and receive vector aspect angles. This uses the assumption of a simple geometric target and a small wavelength in comparison to the target. The theory has now been expanded by classifying three separate regions pseudo-monostatic, bistatic and forward scatter. The current region of a system is dependent on the bistatic angle of the geometry.

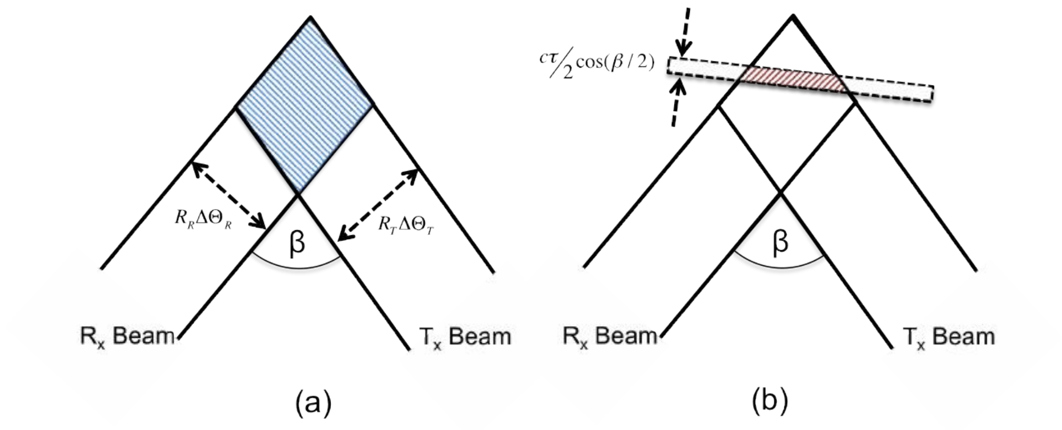

(a)

(b)

Figure 2.7: (a) Beamwidth limited bistatic clutter cell (b) Range gate limited bistatic clutter cell

In the first region the RCS of a target can be assumed to be the monostatic equivalent value if a monostatic radar was located at the central point of the baseline between transmitter and receiver. This equivalence can be used only up to a given bistatic angle, which depends on the target and wavelength of the system. The example given in [14, 19] shows that for a large sphere the pseudomonostatic assumption works within 3dB up to $\beta = 100°$ whereas a smaller sphere this region only extends to $\beta = 40°$.

The next bistatic RCS region as β increases is defined as the bistatic region, this is where it is no longer possible to utilise a monostatic equivalent for the bistatic RCS. The key reasons for this break down of the equivalence method are, changes in relative phase between individual separate scattering centres on the target, change in the characteristics of the radiation from these discrete scattering centres and lastly the change in the scattering centres themselves (removal of previous and generation of new scatterers).

Early work showing the ratio of monostatic RCS to bistatic RCS of real targets can be seen in [20]. The conclusions from this research was that on average the bistatic RCS is less than the monostatic. The trend of a decrease in the ratio of bistatic RCS to monostatic RCS as a function of increasing bistatic angle was also shown. Exceptions to this trend were shown for a few data values recorded at bistatic angles that were less than 5°.

The work completed within [20] is now greater than 30 years old, naval ship design has changed considerably since then. There is now a greater consideration taken into the resulting monostatic RCS of modern naval ships. Hence the absolute monostatic RCS of modern ships would have reduced in comparison to these earlier ship models. The bistatic RCS potentially may not be reduced by the same amount, meaning that the conclusions from the [20] work would no longer be valid on modern ships.

The final region of bistatic RCS is the forward scattering regime, which occurs as β

approaches 180°. At these angles the transmitter boresight is aimed almost directly at the receiver antenna's boresight. At exactly $\beta = 180°$ it is possible to apply the Babinet's principle which has its basis within optical physics. This principle states that the forward scattering pattern of a emission that is diffracted through an aperture and the pattern of the same emission which is diffracted by a shape which is the complimentary of that aperture are identical. This gives a significant gain in the received energy at the receiver in the true forward scattering case of $\beta = 180°$. As β is reduced from this value the bistatic RCS reduces from this peak. The behaviour of this change requires numerical evaluation for all targets other than simplistic geometric shapes.

2.2 Characterisation of the Sea

Before understanding the way that radar signals interact with the surface of the sea it is important to understand the characteristics of the sea itself. Oceanography is an extensive subject area and has many technical expressions and terms used to describe the characteristics of the sea. Some of these which are introduced in this section in order to facilitate the understanding of sea clutter backscatter in section 2.3. The terms described here are given in [12, 23]

Sea State: The Douglas Sea State is a metric commonly used to characterise the sea conditions. It was devised in the 1920s by Captain H. P. Douglas CMG, RN who was a Hydrographer for the Royal Navy. The wave height are used to break up the sea state in to a range from 0 to 9. Table 2.1, [23], demonstrates each sea state with its corresponding wave height and description. As well as the Douglas scale the Beaufort wind scale can also be used to describe the seas' condition. This relates the state of the sea directly to the wind speed instead of wave height, Table 2.2 [?].

Sea State	Wave Height $h_{\frac{1}{3}}$ (ft)	Description
0	0	Calm, glassy
1	0 - $\frac{1}{3}$	Calm, rippled
2	$\frac{1}{3}$ - 2	Smooth, wavelets
3	2 - 4	Slight
4	4 - 8	Moderate
5	8 - 13	Rough
6	13 - 20	Very rough
7	20 - 30	High
8	30 - 45	Very High
9	> 45	Phenomenal

Table 2.1: Douglas sea states

Beaufort Number	Wind Speed (Knots)	Description
0	< 1	Calm
1	1-3	Light air
2	4 - 6	Light breeze
3	7 - 10	Gentle breeze
4	11 - 16	Moderate breeze
5	17 - 21	Fresh breeze
6	22 - 27	Strong breeze
7	28 - 33	Near gale
8	34 - 40	Gale
9	41 - 47	Strong gale
10	48 - 55	Storm
11	56 - 63	Violent storm
12	> 64	Hurricane

Table 2.2: Beaufort scale

Significant Wave Height, $h_{\frac{1}{3}}$: Due to the fact that at any one time there is a range of wave heights present within an area of sea an accepted term is used to define a single overall height that can be used for comparison. $h_{\frac{1}{3}}$ is defined as the average of the highest third of the waves present.

Fetch: This is an area of the sea surface over which seas are generated by a wind having a constant direction and speed

Duration: In the context of oceanography duration describes the length of time that winds blows in the same direction over a fetch.

Developed/Un-Developed Sea : The sea can be described as either being a fully developed sea or an un developed sea. It is fully developed when the ocean waves have reached the maximum height which they can be generated by a given wind force blowing over a sufficient fetch. This is regards of the duration that the wind had been blowing. In this state all possible wave components are present and have a maximum amount of spectral energy.

Swell: This is made by ocean waves that have travelled out of the area they were generated. Swell is characteristically regular with longer periods and flatter peaks than waves generated within their fetch.

2.3 Monostatic Radar Sea Clutter Theory

2.3.1 Sea clutter NRCS

As opposed to point targets like ground vehicles or aircraft, sea clutter represents a return from an extended surface area. Therefore to define a comparable RCS to a individual target, section 2.1.4, its RCS must be defined differently. The reflectivity of the sea surface is a complex result of the interaction between the EM wave and the dynamic sea surface. The average reflectivity parameter used for sea clutter RCS is a normalised RCS (NRCS), σ^0 given by:

$$\sigma^0 = \frac{\sigma}{A_c} \tag{2.18}$$

This normalises the measured returned power from the sea clutter with respect to an area, or Clutter Cell. The area A_c is the footprint of the radar signal on the sea surface defined as:

$$A_c = \left(\frac{Rc\tau}{2}\right)(\phi_a sec\theta) \tag{2.19}$$

where R is the range of the clutter patch from the antenna, c is the speed of light, τ is the width of the pulse used, ϕ_a is the two-way 3dB azimuth beamwidth (in radians) and θ is the grazing angle.

This relationship assumes a low grazing angle with respect to the sea surface, and a relatively narrow azimuth beam width.

Sea clutter reflectivity is a function of a large number of variables, both environmental and radar related. Many models have been developed to describe how it varies with some of these parameters. Sea clutter NRCS values are generally lower than land clutter NRCS, but they have the added complexity of the dynamic nature of the sea, making it much more complex to analyse and model. A review of the prior research into the links between sea clutter reflectivity and some of these parameters is included in Sections 2.5.1, 2.5.4 and 2.5.5.

2.3.2 Sea clutter scattering components

Research utilising EM scattering theory and empirical analysis of radar data has shown sea clutter, as seen by non-coherent radar, to have a compound distribution. This can be attributed to the different scattering components within the signal. The three main components [21] [22] [23] within the clutter are defined in general as:

- Bragg scattering: This is an important physical scattering phenomenon when considering sea clutter returns. It is caused by the interaction of the signal with the local wind generated capillary waves on top of the modulated longer gravity waves. The statistics for this component is Gaussian in nature as predicted by the central limit theorem due to the large quantity of scatterers contributing to the Bragg returns. Vertically polarised Bragg scattering is found to be consequently greater in amplitude than horizontally polarised [24].

- Long Duration Spikes (Whitecap): This component is directly related to the physical effect of waves breaking. This effect lasts for time frames of order ∼1s. The returns are noise-like fluctuations, with high mean power, that decorrelate over ∼1ms. The contribution from this component is not polarisation dependent. Their Doppler spectrum is relatively extensive, with a centre around the main gravity wave phase velocity.

- Short Duration Spikes (Bursts): Burst scattering is generated by the rough surface on the crest of gravity waves that is generated just prior to the waves breaking. This component is much larger in amplitude in horizontal polarisation than vertical. The lifetime of these effects is shorter than the whitecap component, although they are coherent throughout their duration. Therefore they do not decorrelate when frequency agility is applied to the radar signal from burst to burst.

Both Bursts and Whitecap effects are referred as spikes, despite being two clearly different phenomena. The two key characteristics of these spike returns are high polarisation ratio and Doppler velocity in comparison to the Bragg scattered returns, this is illustrated in [24] [25] [26] [27].

The empirical models that have been developed for sea clutter attempt to include each of these key scattering components. Each of these individual components must be considered when analysing sea clutter data in terms of the how spiky the amplitude statistics are as well as the coherence of the spikes present. The separate scattering components within recorded data can be identified by their polarisation dependence and the length of time they exist.

2.3.3 Doppler spectra of Sea clutter

Sea clutter returns have a constant dynamic motion associated with them, due to the nature of the fluctuating motion of the sea surface. This makes the Doppler spectra of the clutter more complex and difficult to characterise. It is of great importance to understand components behind the generated spectra and quantitatively characterise its behaviour. Modern Doppler radars are capable of Doppler processing techniques that allow for easy detection of fast moving targets outside of the spectra of the clutter present. This is not the case for slower moving targets that are located in the clutter dominated section of the Doppler spectra, potentially masking the target return.

When considering the velocity components of the sea surface its total spectra contains contributions from the motion of the components described within 2.3.2. The key velocity components include the main gravity waves and the wind speed induced capillary surface waves. These two factors induce the main components of the motion of the sea surface, the large scale wave motion, and the small scale motion that is superimposed on top of this. Wind generated sea waves and swell are both considered to by gravity waves. The gravity wave phase velocity is defined as:

$$c_{gw} = \sqrt{\frac{g\lambda_W}{2\pi} \tanh \frac{2\pi d}{\lambda_W}} \tag{2.20}$$

where c_{gw} is the speed of the gravitational wave, g is the gravitational constant, λ_W is the wavelength, and d is the depth of the water. In the case of deep water, $d >> \lambda_W$ [12], this simplifies to:

$$c_{gw} = \sqrt{\frac{g\lambda_W}{2\pi}} \tag{2.21}$$

These equations are valid in medium to deep water conditions. Different effects are generated within very shallow waters but these are not discussed here. This can be related to the Doppler frequency of the gravity waves using the Bragg scattering equation:

$$\lambda = 2\lambda_W \cos\phi \tag{2.22}$$

where ϕ is the angle of the direction of wave propagation with respect to the radar, and λ is the radar signal wavelength. Using Eqn. (2.20) and (2.22) it is possible to define the gravity wave Doppler frequency as:

$$f_d = \pm\sqrt{\frac{g\cos\phi}{\pi\lambda}} \tag{2.23}$$

Capillary waves are also generated by wind, but their restoring force is the water's surface tension, not the Earth's gravitational field. Waves of a length of less than ~ 3 cm are considered capillary waves, [12]. The have much shorter wavelengths and last for shorter periods of time. Hence if the wind speed drops considerably the capillary waves will cease significantly before the swell reduces.

Quantifying the relative importance and effect of these two factors has been the topic of many research projects over many years. This research has been mainly directed at understanding the effect of these as well as other variables influence on the observed sea clutter distributions. It is the differences in the spectra seen in vertical and horizontal polarisation as well as variations with grazing angle that are of interest to radar engineers. The selection of polarisation is one of the few parameters that radar engineers have control over that effects the characteristics of the returned clutter, unlike the uncontrollable parameters such as geometry or metreological conditions. Prior literature on sea clutter Doppler characteristics is reviewed in section 2.5.7.

2.3.4 Sea clutter amplitude statistical models

As well as the average reflectivity sea clutter by nature is fluctuating in amplitude with time from a single location. The characteristics of this fluctuation is described by the temporal amplitude statistics of the clutter. This section introduces some of the models, which have been developed over many years of sea clutter research, that are used represent the amplitude statistics of sea clutter. Only the core well known models that have been shown to accurately represent sea clutter distributions are discussed here. Additional models have been applied previously, but this is often with limited success or little reasoning behind their methodology.

2.3.4.1 Gaussian model

One of the simplest models that can be used to define the observed statistics of the sea clutter returns distribution is the Gaussian model. It has been shown, under certain conditions, that this model can be applied effectively. These conditions include observations of clutter over short time scales, of approximately 0.1 seconds, medium to high grazing angles and use of a radar system with low spatial range resolution. If these conditions are met then it is possible to assume many scatterers inside the resolution cell contribute equally to the returned signal. The number of scatterers can be assumed to tend towards a significant number, therefore it is possible to apply the central limit theorem and the amplitude of the net backscattered signal will have a Gaussian distribution.

The theory states that the sea surface can be described as a scattering field, E, that is represented by the complex contributions from a number of independent scatterers,

$$E = \sum_{n=1}^{N} a_n \tag{2.24}$$

If it is assumed that N is a large number then for this case it is possible to define the predicted scattering statistics. Using an assumed characteristic function of the summed individual components it can be shown that the model for a large number of identical scatters simplifies to a Rayleigh envelope, where the Probability Density Function (PDF) of the in-phase and quadrature components are represented by,

$$P(E_I, E_Q) = \frac{1}{\pi x} exp\left(\frac{-E_I^2 + E_Q^2}{x}\right); -\infty \leq E_I, E_Q \leq \infty \tag{2.25}$$

After envelope detection of these Gaussian components the exponential intensity distribution is given by:

$$P(z) = \frac{1}{z} exp\left(-\frac{z}{x}\right); z = E^2; 0 \leq z \leq \infty \tag{2.26}$$

The single parameter exponential model for the intensity is defined by x which represents the mean clutter return which in turn is directly proportional to the clutter power received by the radar system.

It is important to note that the Gaussian model has been found to be inadequate at describing the backscatter from the sea surface, at low grazing angles, high resolutions and longer timescales ($\approx$ 10s). The number of scatterers in these situations is greatly reduced, and hence the central limit theorem assumption is no longer valid. It is explained in [23] that in these conditions the statistics of the sea clutter has a large number of high returns, producing longer tailed distributions to which a Gaussian model cannot be fitted. The failure of the Gaussian clutter model to represent sea clutter drove numerous other models to be applied to clutter in an effort to improve upon the Gaussian model.

Although over shorter time scales of $<<$ 1 sec the sea clutter distribution due to the underlying gamma distribution remaining approximately constant over this time. Therefore only the speckle component of the clutter is sampled which will give a Gaussian return, see section 2.3.4.4 for the K-distribution that applied a compound structure to sea clutter.

2.3.4.2 Weibull distribution

The Weibull model was developed by Waloddi Weibull, and was initially used to model material varying material strength with size [28]. It was then applied to ground clutter in [29], and since there are many examples of it being applied to both land and sea clutter. The model is popular as it is described as being analytically tractable in [23], although it does not have a compound nature like the K distribution model.

The PDF of the Weibull distribution is given by, [30]:

$$p(x) = \frac{\eta_w}{\sigma_w}\left(\frac{x}{\sigma_w}\right)^{\eta_w - 1} \exp\left(-1\left(\frac{x}{\sigma_w}^{\eta_w}\right)\right), x > 0, \sigma_w > 0, \eta_w > 0 \tag{2.27}$$

where σ_w and η_w are the scale and shape parameters respectively. The Rayleigh PDF is a particular case of the Weibull PDF when $\eta_w = 2$. With the intensity moments being defined as:

$$\langle z^n \rangle = \sigma_w \Gamma\left(\frac{n}{\eta_w} + 1\right) \tag{2.28}$$

Some example plots of the Weibull PDF distribution with a fixed scale parameter of 1 and a varying shape parameter can be seen in Fig. 2.8.

Farina et al [31] produced a coherent Weibull clutter model, which was then expanded on within [32]. This results in temporally correlated in-phase and quadra-

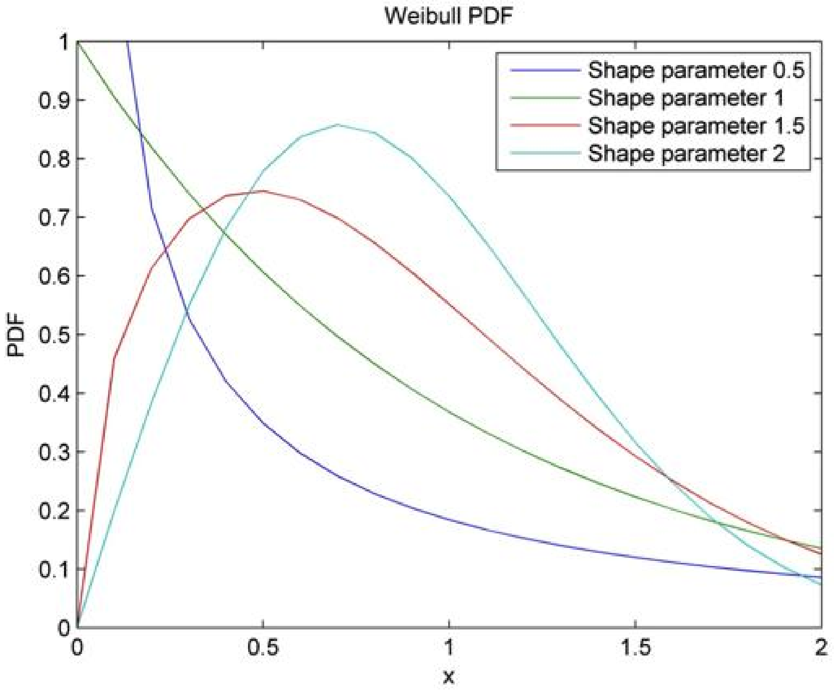

Figure 2.8: Example Weibull function PDF plots with varying shape parameters

ture components with Weibull distributions which are generated using a nonlinear memoryless transform.

2.3.4.3 Log Normal Distribution

The Log-normal distribution is only dependent on two key parameters, the mean μ_{LN} and variance σ^2_{LN}. The form of the distribution is a similar to a Gaussian distribution but contains a logarithmic component within the exponential,

$$P(x) = \frac{1}{x\sigma_{LN}\sqrt{2\pi}} \exp \frac{-(ln(x) - \mu_{LN})^2}{2\sigma^2_{LN}} \tag{2.29}$$

This has been used previously to model the amplitude distribution of sea clutter returns. It was first applied to sea clutter analysis in [33] and can also be seen being used to compare against real data distributions with recent research [34]. Figure 2.9 shows a plot of three separate log normal distribution PDFs all with $\mu_{LN} = 0$, but varying values of σ_{LN}.

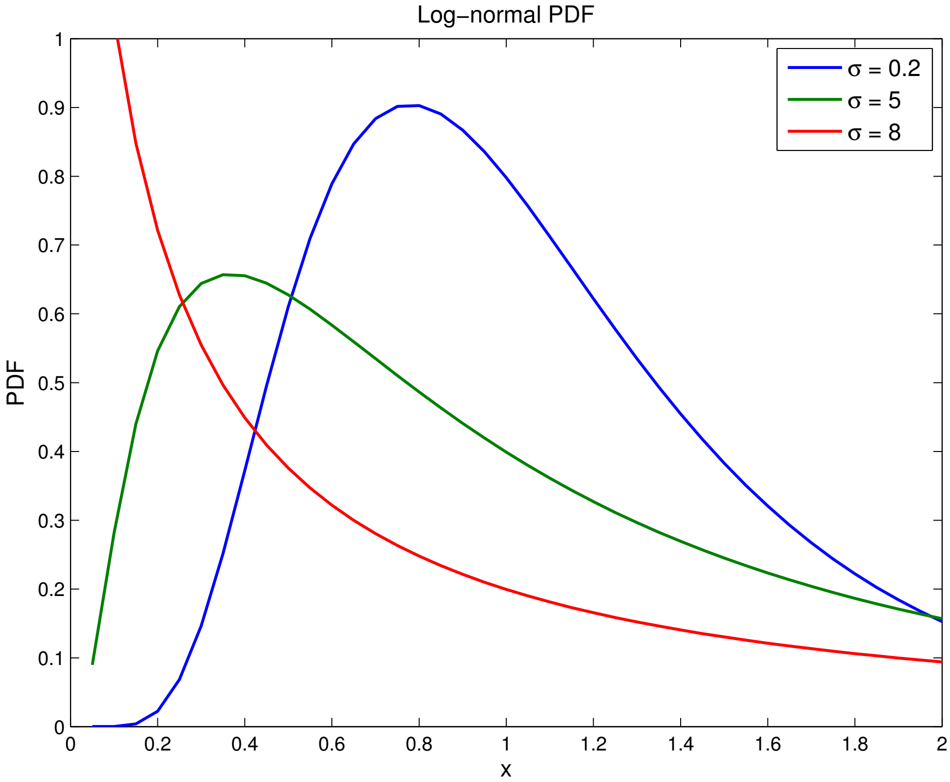

Figure 2.9: Example log-normal distribution PDF plots with varying shape parameters

2.3.4.4 K-distribution

The compound K-distribution model is a well established model that was developed by Jakeman and Pusey in [35] and was found to effectively model sea clutter [36] [37]. The compound model takes into account both the long modulation of the gravity waves and the additional non-Bragg scattered speckle component. The key strengths of the model are that it is has been proven to fit well to sea clutter from multiple datasets as well as being grounded within a logical physical representation of the sea surface.

A Gamma distributed variant is used to represent the slower fluctuating local mean power component. The theoretical logic behind the use of a Gamma variable for the mean power fluctuation is reinforced by a number of points. As the shape parameter of the Gamma distribution tends to ∞ the PDF of the distribution trends to a Dirac delta function. The implication of this is that the compound K-distribution will revert to a Rayleigh distribution. Allowing the K-distribution to well represent a thermal noise power distribution for this limiting special case. In addition to this the Gamma distribution has been shown to well represent the approximate solution for the intensity distribution of a sum of a number of random vectors. This was applied to terrain scatterers and complex targets using a random vector model within [38]. It should therefore be possible to extend this assumption to be applied to the sea clutter distribution case.

In addition to this experimental results have also shown it to be a valid assumption. When using a frequency agile system it is possible to obtain independent samples, due to decorrelation of returns between each pulse. To estimate the local power component it is possible to average these returns. Using this method to estimate the local power it has been shown that it follows a Gamma distribution, [23]. Therefore within the compound K-distribution a Gamma distribution is used to represent the local power. As follows:

$$P_c(x) = \frac{b^\nu}{\Gamma(\nu)} x^{\nu-1} \exp(-bx); 0 \leq x \leq \infty \tag{2.30}$$

where x is the local power, ν is the shape parameter, and b is the scale parameter. This local power is then combined with the speckle component represented by a rapidly fluctuating random Rayleigh distributed variable.

The speckle component of the clutter is assumed to be Rayleigh distributed for a number of reasons. The first is that the contributing scattering components generating the speckle are believed to be the fine structure on the surface of the sea, the ripples on top of the larger gravity waves. As many of these scatters will reside within a single range gate the conditions of the central limit theorem can be assumed hence Rayleigh envelope statistics are a valid assumption. In addition to this experimental results shows that the speckle is well represented by a Rayleigh distributed, and can be assumed to be statistically indistinguishable when measured, [37].

$$P(E) = 2E \int_0^\infty \frac{dx}{x} \exp\left(-\frac{E^2}{x}\right) P_c(x) \tag{2.31}$$

where E is the sea clutter energy. Combining Eqn. (2.30) and Eqn. (2.31) gives the compound form:

$$P(E) = \frac{2Eb^\nu}{\Gamma(\nu)} \int_0^\infty dx x^{\nu-2} \exp\left(-bx - \frac{E^2}{x}\right) \tag{2.32}$$

Eqn. (2.32) represents the K-distribution in a form that does not take into account thermal noise. This allows for a closed form solution for the intensity PDF:

$$P(z) = \frac{2b^{\frac{\nu+1}{2}} z^{\frac{\nu-1}{2}}}{\Gamma(\nu)} K_{\nu-1}\left(2\sqrt{bz}\right) \tag{2.33}$$

where $z = E^2$ is the intensity, $\Gamma(.)$ is a Gamma function, and $K_{\nu-1}(.)$ is a modified Bessel function of the second kind with order $\nu - 1$ (which gives the K-distribution its name).

The K-distribution shape parameter is linked to the spikiness of the sea clutter;

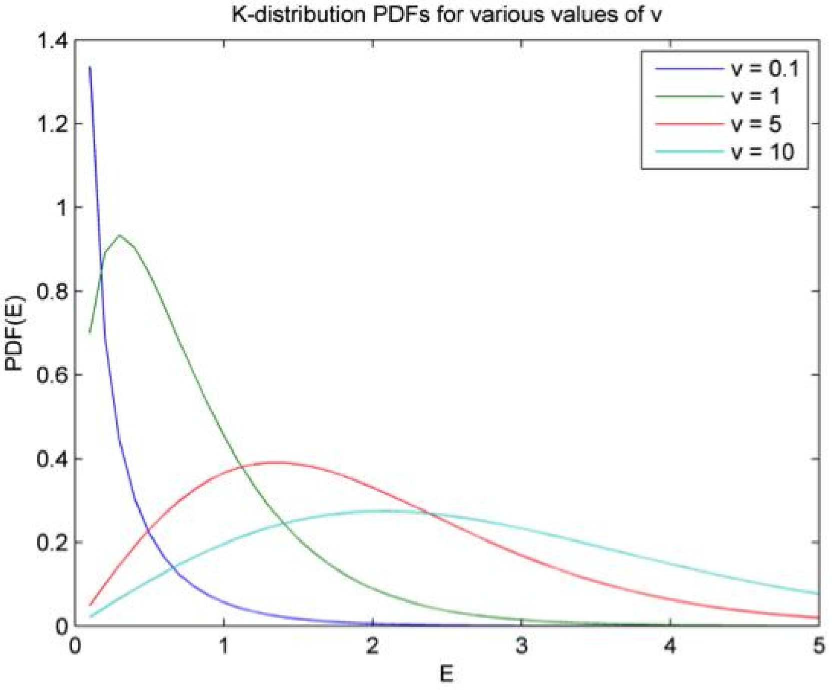

Figure 2.10: K-distribution PDFs for varying values of ν

it can, in practice, take values between $0.1 \leq \nu \leq \infty$. When $\nu \leq 1$ the distribution is defined as being very *spiky*, and when the shape parameter tends to ∞ the distribution become a Rayleigh distribution. The term *spiky* refers to data that has a large number of isolated high level returns from individual range gates. The cause of this effect is generally accepted to be Bragg scattering from resonant capillary waves and whitecap scattering.

Figure 2.10 shows a series of K-distribution PDF plots with varying shape parameter values. This clearly demonstrates that as the shape parameter reduces the proportion of the distribution above a given amplitude increases.

The form of the K-distribution that has been presented so far does not consider the influence of thermal noise on the amplitude distribution statistics. When the influence of thermal noise is included, the local clutter power becomes:

$$P(E \mid p_n, x) = \frac{2E}{x + p_n} \exp(-\frac{E}{x + p_n}) \tag{2.34}$$

This then needs to be integrated over a gamma distribution as completed in the previous steps for the model that did not take into account thermal noise. The resultant PDF of the K-distribution + thermal noise is:

$$P(E \mid p_n, b, \nu) = \frac{2Eb^{\nu}}{\Gamma(\nu)} \int_0^{\infty} \frac{x^{\nu-1}\exp(-bx)}{x + p_n} \exp(-\frac{E^2}{x + p_n}) dx \tag{2.35}$$

This form of the K-distribution has not been shown to have a closed form solution and therefore requires numerical integration methods to evaluate its solution.

As well as the direct distribution comparison it is possible to use moments to compare sea clutter data with a model. The first three intensity moments of the K-distribution with noise have defined solutions seen respectively below:

$$\langle z \rangle = \frac{\nu}{b} + p_n \tag{2.36}$$

$$\langle z^2 \rangle = \frac{2\nu(\nu+1)}{b^2} + \frac{4p_n\nu}{b} + 2p_n^2 \tag{2.37}$$

$$\langle z^3 \rangle = \frac{6\nu(\nu+1)(\nu+2)}{b^3} + \frac{18p_n\nu(\nu+1)}{b^2} + \frac{18p_n^2\nu}{b} + 6p_n^3 \tag{2.38}$$

These moments can be used in the fitting process when comparing real data moments with the compound K distribution. It is also seen in section 3.2 that additional fitting methods can be applied by comparing the probability of false alarm of data and model.

Knowledge of the variation of P_{FA} distributions allows CFAR processing techniques to define the correct threshold levels to produce the required performance level for a radar system. Hence allowing the radar system to effectively detect targets using Doppler filtering taking account of the sea clutter in the target Doppler bin.

In a noise-free case, the false alarm probability, P_{FA}, is defined as the probability of the returned clutter signal existing above a set threshold E_T. Making use of the compound K distribution and assuming a square law detector, the false alarm is given by:

$$P_{FA} = \frac{2}{\Gamma(\nu)}(\nu a)^{\frac{\nu}{2}} K_\nu(2(\nu a)^{\frac{1}{2}}) \tag{2.39}$$

where ν is the shape parameter of the distribution, a is the threshold level and K_v is the modified Bessel function of the second kind.

2.3.5 Clutter Probability of False Alarm Distributions

The scattering models discussed so far can all be compared to real data using the P_{FA} curves generated from sea clutter. Evaluating these curves makes it possible to define the false alarm rate a radar system will have for a given operating threshold level. This relates to the radars sensitivity to the sea clutter and is used for CFAR processing. An example plot showing $\log_{10}(P_{FA})$ against threshold (dB) from real data, can be seen in Fig. 2.11 generated using CSIR data seen in [86].

The behaviour of the tail of the P_{FA} distribution is important to radar systems, as to operate effectively they require low P_{FA} levels. For example, if the radar has a million range/bearing 'cells' a false alarm probability of 10^{-6} corresponds to one

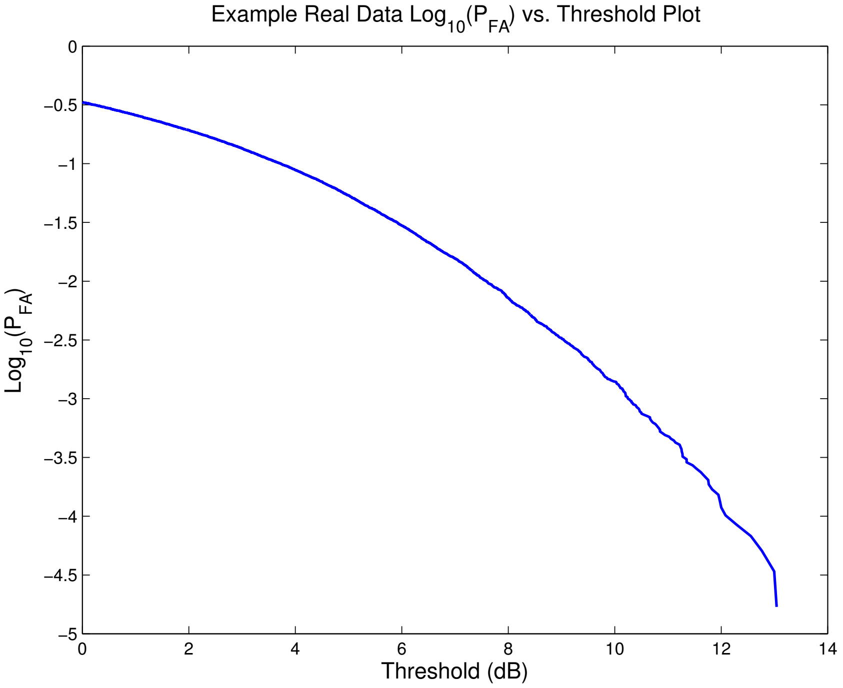

Figure 2.11: Example sea clutter $log_{10}(P_{FA})$ vs. threshold plot (generated using data from the CSIR 2007 database)

false alarm per scan. This is equivalent to probabilities of the order of 10^{-4} to 10^{-3} (which is -4 and -3 within the $\log_{10}(P_{FA})$ domain) per range/Doppler cell per burst of pulses, once account is taken of the post-detection processing in the radar.

If the P_{FA} is too high the radar system will be overloaded with false targets and this will hinder processing such as tracking. Hence to achieve low P_{FA} levels, using optimum CFAR threshold values, the tail of the distributions of sea clutter statistics need to be fully understood.

The majority of historical research into the nature of sea clutter statistics has been with non-coherent data and there has been little prior work on the analysis of the P_{FA} tail distributions across the Doppler spectrum. Fitting of the raw data to distribution models at the tail of the P_{FA} distributions could lead to an understanding of the behaviour of the sea clutter in the area applicable to an operating maritime radar system.

An issue with analysing the shape and fit of $\log_{10}(P_{FA})$ curves is that the number of components within the whole data set that contribute to the curve at a given point is proportional to the location on the curve. For example at $\log_{10}(P_{FA}) = -3$ only 0.1% of the dataset contributes to the curves location at this point. This means that the fractional error introduced by the reducing sample size increases with decreasing $\log_{10}(P_{FA})$. It is important to note therefore that at low P_{FA} levels if a curve generated from raw data deviates from a given distribution, this may be due to the curve not defining the clutter behaviour correctly, or due to having a limited number of samples. It is therefore important to ensure that if the P_{FA} has to be defined to a certain level then the amount of samples used is large enough to produce a acceptably small error at that level.

2.4 Information Theory

Information theory is the study of quantifying the transfer and storage of information. It is used in many applied disciplines from communications, to mathematics, physics, statistics, computer science and economics. The study of information theory often focuses on the optimum information that can be transferred or obtained from a given data source or signal. As radar involves significant signal processing elements information theory has great potential to provide solutions to obtaining the optimum information from the signals analysed. An excellent review of this subject area is presented within [39].

In information theory the metric of quantifiable measures of information used are bits. These represent singular digits of data in their most basic form of either 1 or 0. To measure the amount of information that is stored or transferred a value of bits is defined. This is seen in the size of a hard drives storage capacity which is often measured in gigabytes which represents 8589934592 bits.

A crucial figure of early information theory research, who is often cited as the founder of the subject, was Claude Elwood Shannon. His key papers on the subject are presented within [40].

Shannon's law [41–43] is an important hypothesis that defines the maximum error free transfer rate possible for a given channel. The theorem relates the capacity of a given data channel to its bandwidth, the average thermal noise power and the signal to noise ratio of a signal passed through the channel. As follows:

$$C = B\log_2(1 + SNR) \tag{2.40}$$

where C is the channel capacity in bits/sec, B is the bandwidth and SNR is the signal to noise ratio of a given signal. This defines the upper limit on the amount of bits per second that can be transfer through a channel. This shows that C is directly proportional to the bandwidth and the log_2 of the SNR. This relates directly to radar signals as systems have a given bandwidth over which they operate and receive signals with a defined SNR, and hence they possess a given channel capacity.

In addition to defining a theoretical limit on the capacity of a given information transfer channel Shannon also linked the concept of entropy from thermodynamics to the area of information theory. Entropy is defined as a quantitate way of measuring the uncertainty of a given variable. As follows:

$$H(X) = -\sum_{x} p(x) \log_2 p(x) \tag{2.41}$$

where H is the entropy, X is a random variable with possible states x which have a PDF $p(x)$. The logarithm is to the base 2 so that the output entropy is measured in bits. It should be noted that the entropy of a variable is only a function of its probability distribution, not the values the random values can take. Entropy can be interpreted as a metric that quantifies that amount of information on average required to describe a random variable.

The entropy of a random variable can also be defined as:

$$H(X) = E_p \log \frac{1}{p(x)} \tag{2.42}$$

where E_p is the expectation value for $p(x)$. This formulation for entropy is commonly used within thermodynamics. It is clear from this form of entropy that is must alway take a non-zero value as by definition $p(x)$ takes values between 0 and 1, hence $log\frac{1}{p(x)} \geq 0$.

As well as individual probabilities and entropy it is possible to define conditional probabilities that involve two or more variables and their respective probability distributions. The entropy of multiple variates can be either a joint entropy or a conditional entropy.

The joint entropy of a distribution with an overall PDF of p(x,y) is:

$$H(X|Y) = -\sum_{x \epsilon \chi} \sum_{y \epsilon \chi} p(x,y) \log p(x,y) \tag{2.43}$$

A conditional entropy between a pair of discrete random variables (X,Y) is presented as:

$$H(Y|X) = \sum_{x \epsilon \chi} p(x) H(Y|X=x) = -E \log p(Y|X) \tag{2.44}$$

where $H(Y|X)$ represents the conditional entropy of Y conditioned on X, and $p(Y|X)$ represents the probability distribution of Y conditioned on X.

As well as conditional and joint entropy measurements between two random variables an additional expression labelled relative entropy, $D(p||q)$, also exists. Relative entropy is also know as Kullback-Leibler Divergence (KLD), [44, 45]. This measures the distance between two PDFs. It can be interpreted as the error introduced when one variable PDF was assumed and it was in fact another. As follows:

$$D(p||q) = \sum_{x \epsilon \chi} p(x) \log \frac{p(x)}{q(x)} \tag{2.45}$$

where $p(x)$ and $q(x)$ are the two PDFs under test. It is normally setup such that $q(x)$ is the assumed distribution for a given variable and $p(x)$ is the actual. The KLD is always non-negative, asymmetric, non-commutative and reduces to zero when $p(x) = q(x)$. The KLD metric is shown as an integral of the log-likelihood ratio of the two distributions.

2.4.1 Detection Theory

In general the main purpose of maritime radar is the detection of targets within a background of sea clutter. In section 2.3 the statistics and characteristics of this background is discussed, using this a priori knowledge detection methods can be applied in a effective way. Information theory has a connection to the decision making processing of target detection, this section discusses the application of this knowledge to radar systems.

A radar signal which includes a target will produce an increase within the amplitude of the signal within the time or spatial domain. It is this increase in the amplitude of the signal that needs to be highlighted in an automated way and declared as a detection. A detection is a binary result from the test of two hypotheses, that a target is present, or a target is not present.

A detection has two possible error types, a false alarm where a target is declared as present when it is not commonly know as a type I error; and a false dismissal which is missing a target detection when one it present commonly known as a type II error. The detection probability, P_D, is defined as follows [23]:

$$P_D = \int_Z^\infty P_T(z)dz \tag{2.46}$$

where P_T is the PDF of a returned signal which has a target present within it and z is the threshold set for detection. The probability of detection P_D can also be interpreted as one minus the probability of dismissal. The probability of a false alarm, P_{FA} is as follows:

$$P_{FA} = \int_Z^\infty P_A(z)dz \tag{2.47}$$

where P_A is the PDF of a clutter background with no target present. Equation (2.46) and (2.47), show that a reduction in the threshold z produces an increase in detection probability, but also increases the probably of false alarm.

Figure 2.12, from [?], shows a diagram of two separate distributions, a Rayleigh and a Rice distribution. The Rayleigh distribution represents the PDF for a thermally noise dominated receiver, see Eqn. (2.26) and (2.25) in section 2.3.4.1. The Ricean distribution, [?] has been shown to represent a coherent signal embedded within thermal noise [23], in this case it has a SNR of 10dB. Where the Ricean distribution PDF is as follows:

$$P_T(E|A) = \frac{2E}{x}\exp\left(-\frac{E^2+A^2}{x}\right)I_0\left(\frac{2EA}{x}\right) \tag{2.48}$$

where A is the coherent signal amplitude, E is the signal envelope, I_0 is the modified Bessel function of the first kind with zero order and x is the mean thermal noise intensity.

Two example threshold levels are marked on the diagram with the relevant P_D and P_{FA} noted next to them. The lower amplitude threshold level achieves a P_{FA} of 10^{-1} and a P_D of > 0.95, when this is increased the P_{FA} decreases to 10^{-4} but the P_D also decreases to 0.6. This clearly demonstrates the problem of threshold level setting as the goal of increasing the detection probability is also linked to increasing the probability of false alarm.

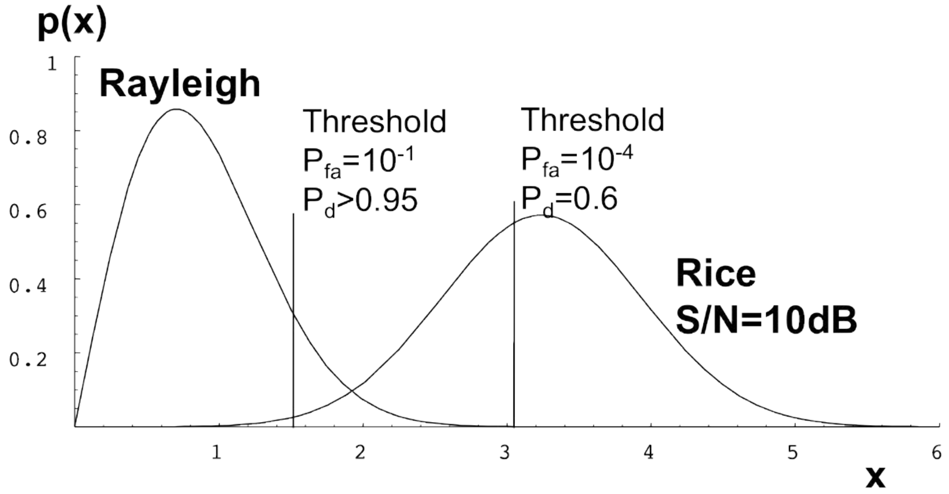

Figure 2.12: Diagram of Rayleigh clutter and Rice target PDFs with two separate threshold levels

The method for optimisation of detection thresholding uses the maximum likelihood test [46]. This test maximises the detection probability for a fixed probability of false alarm, by applying the Neyman-Pearson lemma [47, 48]. This lemma is as follows:

$$\Lambda(z) = \frac{P_T(z)}{P_A(z)} > \lambda_t \tag{2.49}$$

Where Λ is the likelihood ratio and λ_t is the threshold level. The value of λ_t is dependent on the SNR of the target and needs to be varied to achieve a fixed P_{FA} for a given SNR. It is also commonly shown as a log-likelihood ratio:

$$\log \frac{P_T(z)}{P_A(z)} > \log \lambda_t \quad (2.50)$$

Using a the results from a log likelihood ratio it is possible to define the signal to noise ratio to achieve a given probability of detection and probability of false alarm. This analysis of the relationship between both the P_D and P_{FA} is commonly plotted as a receiver operating curve (ROC), see Fig 2.13.

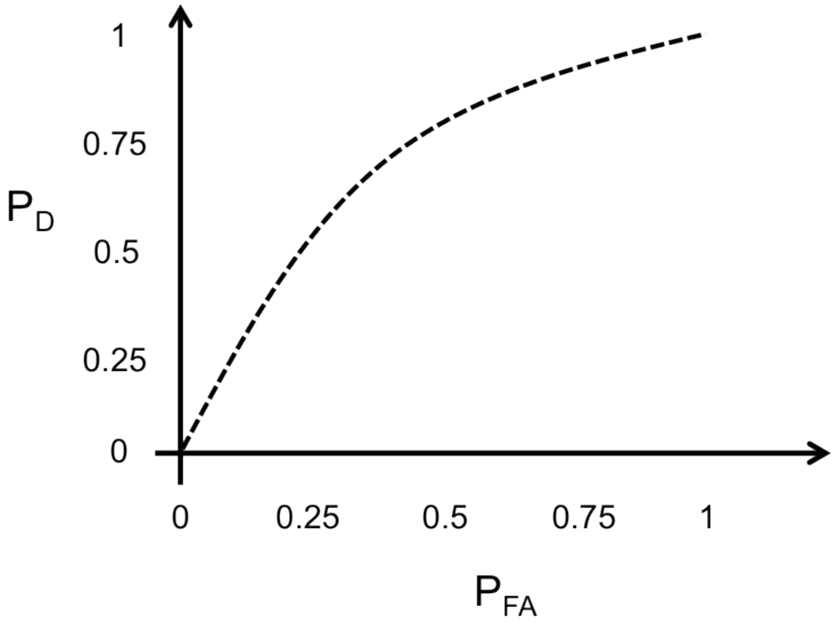

Figure 2.13: Example ROC curve example

It is clear that the log likelihood ratio is related to the KLD Eqn. (2.45) seen in section 2.4 which includes the log of the ratio of two PDFs. Where P_A and P_T represent $p(x)$ and $q(x)$ respectively. The difference being that the KLD is the product of the log likelihood ratio and the numerator PDF integrated over all threshold values.

2.5 Literature Review

2.5.1 Sea clutter NRCS

The analysis of sea clutter mean NRCS has been the key aim of many experimental trial campaigns, resulting in the production of numerous papers and a number of chapters in books focusing on this research topic. This section reviews development of the prior literature on sea clutter NRCS from its beginnings to the most recent research on the subject.

Some of the early work on sea clutter scattering was completed on the analysis of the capillary wave component of sea clutter reflections in [49]. This work applied the scattering theory that had been previously developed by [50] and [51] to the backscattering response from sea clutter capillary waves. The conclusions of the research showed that Bragg scattering effects enhanced the response from sea clutter returns to be a maximum when the Bragg equation is satisfied,

$$k_{w_c} = 2k\cos\theta \tag{2.51}$$

where k_{w_c} and k correspond to $\frac{2\pi}{\lambda_{w_c}}$ and $\frac{2\pi}{\lambda}$ respectively, and λ_{w_c} is the capillary wavelength, and λ is the radar signal wavelength. The measurements made showing these Bragg effects were between 4° and 80° grazing angle at X-band. The comparison to the theoretical scattering amplitudes as a function of grazing angle showed good agreement between 4° and $\approx 20°$, after which both vertical and horizontal polarised amplitudes were shown to be less than that predicted by the theoretical models used.

One of the most comprehensive collections of the variation of NRCS, with a range of parameters, from 60 difference experimental references was collated by Nathanson [52], an updated version also exists [53]. This is a very useful resource for radar engineers evaluating the predicted performance across a range of conditions. The data presented includes both horizontal and vertical polarisation, grazing angles from 0.1° to 30° and a range of frequencies from 0.5 GHz to 35 GHz, as well as a range of sea states at which the data were recorded. Although the information available is extensive it is by no means exhaustive.

Using the collected data empirical models have been developed relating the variation of individual parameters to the NRCS. Extrapolating these trends enables the ability of predicting NRCS across a range of parameters that aren't necessary covered in the current recorded datasets. The key trends that were noted from this range of data were:

- Vertical polarisation will return equal or higher NRCS values. This is enhanced even more at low grazing angles ($\leq 1°$) and lower frequencies.
- NRCS increases with grazing angle from 0 to 20°.
- NRCS increases with sea state. This change is noted to be up to 10 dB per sea state increase (at low sea states and frequencies).

Nathanson [52] stated that the uncertainties within the database increase at low carrier frequency and low grazing angle. The values in the datasets were shown to be larger than predicted by models. A number of explanations were given for why this occurred:

- These values were recorded on less sensitive older radar systems.
- The experimentalists only recorded points that were noted above the norm. These could have been induced by an increase in the wind speed or wave height.

- Ducting events have been noted to increase the σ^0 values. This variation can be up to 10dB at 0.1° grazing angle.

Other restrictions of modelling recorded data and following a specific model is caused by the averaging that occurs when recording/processing the data. When generating the distributions of the sea clutter the data must be averaged over a finite length of time and from a discrete number of range gates. This averaging possibly removes or masks some of the subtle variations that may exist.

The most prevalent of empirical models for NRCS is the Georgia Institute of Technology (GIT) model [54]. The model evaluates the parameter σ^0 by defining it as a product of three variables, multi path, sea direction and wind speed. It has been shown to be a close match to the variation of the NRCS over a range of conditions and is often used as the base model to fit a variation of NRCS with a single parameter. The model defines mean σ^0_{HH} values for horizontally polarised returns with a frequency from 1-10 GHz,

$$\sigma^0_{HH} = 10\log[3.9 \times 10^{-6}\lambda\alpha_i^{0.4}A_iA_uA_w] \tag{2.52}$$

For the mean vertically polarised returns, σ^0_{VV}, there are two solutions one for the region 1-3 GHz and another for 3-10 GHz, seen in Eqn. (2.53) & Eqn. (2.54) respectively, [54].

$$\sigma^0_{VV} = \sigma^0_{HH} - 1.73\ln(h_{av} + 0.015) + 3.76\ln(\lambda) + 2.46\ln(\alpha_i + 0.0001) + 22.2 \tag{2.53}$$

$$\sigma^0_{VV} = \sigma^0_{HH} - 1.05\ln(h_{av} + 0.015) + 1.09\ln(\lambda) + 1.27\ln(\alpha_i + 0.0001) + 9.70 \tag{2.54}$$

where σ^0_{HH} and σ^0_{VV} are the horizontally and vertically polarised NRCS respectively, λ is the radar wavelength, α_i is the incidence angle, A_i is the Interference factor, A_u is the upwind/downwind factor, A_W is the wind speed factor and h_{av} is the average wave height.

The factors A_i, A_u, and A_W, included in the vertically and horizontally polarised NRCS values are defined below.

$$A_i = \frac{(\sigma_\phi^4)}{(1+\sigma_\phi^4)} \tag{2.55}$$

σ_ϕ^4 is a variable dependent on wave height, grazing angle and signal wavelength,

$$\sigma_\phi = (14.4\lambda + 5.5)\alpha_i\frac{h_{av}}{\lambda} \tag{2.56}$$

A_u is a function of look angle ϕ, signal wavelength and grazing angle,

$$A_u = \exp(0.2\cos\phi(1 - 2.8\alpha_i)(\lambda + 0.015)^{-0.4}) \tag{2.57}$$

In the GIT model only a single direction, the look angle, is used. The model does not take into account differences between the wind and swell vectors with respect to the look direction. It is noted that the emphasise should be placed on the actual wave propagation vector not the wind vector.

The wind speed factor, A_w, only depends on the wind speed, V_w, and wavelength,

$$A_w = \left(\frac{1.94V_W}{1 + \frac{V_W}{15.4}} \right)^{\frac{1.1}{(\lambda+0.015)^{0.4}}} \tag{2.58}$$

The relationship of σ^0 is more closely tied to wind speed than wave height. Linear relationships have been shown between σ^0 and log wind speed. Although in a fully developed sea the relationship between wind speed and wave height is,

$$V_W = 8.67h_{av}^{0.4} \tag{2.59}$$

The characteristics of σ^0 are defined to fall into two separate regions, low grazing angle and a plateau region. Within the low grazing angle region σ^0 depends strongly on the angle, unlike in the plateau region where σ^0 can be assumed to be independent of grazing angle. The dividing point between these two regions is marked by the critical angle α_c. This critical angle is defined as being proportional to wavelength and inversely proportional to the average wave height,

$$\alpha_c = \frac{\lambda}{Kh_{av}} \tag{2.60}$$

where K is a proportionality constant. This constant is predicted to take the value 4 if interpolated to the location between the two regimes, and experimental results for S and X band radars have given the values of 6.3, [54].

This model has shown a close match to the variation of the NRCS over a range of conditions and is often used as the base model to fit a variation of NRCS with a single parameter. Although the GIT does by no means provide a complete description of the true relationship. An obvious restriction is that it is limited to small grazing angles ($\leq 10°$) and hence fails to predict the NRCS correctly for medium to large grazing angles.

Some discrepancies between the GIT model and the data in [52] do exist. This was particularly true at low grazing angles, when short pulses were used or the data statistics were particularly spiky. Horst et al [54] commented that the effects of heavy averaging of the Nathanson collection of data gave a α_i^{-2} rather than the predicted α_i^{-4} relationship for small grazing angles beyond the critical angle.

Further work by Ward [23] using electromagnetic modelling shows a closer agreement with the GIT model than the results shown in the Nathanson datasets.

2.5.2 Amplitude Distributions

As well as the study of the NRCS of the sea clutter many previous research papers have focused on understanding the characteristics of the amplitude distributions exhibited by sea clutter returns.

As described in section 2.3.4 the key models that have been applied are the Gaussian, Weibull, Log-normal and K-distribution. The early assumed model of a simple Gaussian distribution fails to represent the sea surface under key conditions. It is at these key challenging conditions of low grazing angle, high resolution, high sea state that a complete separation from Gaussian assumed statistics occur. The main focus of this section is describing the empirical results from the prior literature on sea clutter amplitude distributions.

Wright [55] described a compound model made up of the scattering from both the capillary waves and the large scale gravitational waves. This helped explain the non-Gaussian nature that was observed within the clutter recording but did not explain the occurrence of large amplitude spikes within the recordings.

An early experiment to characterise sea clutter RCS variations was completed by Guinard and Daley, [56]. This also used a composite model of Rice scattering proposed in [50] superimposed onto a larger swell structure. This was show to effectively represent the scatter only within the wind speed range of 3.5 ms^{-1} to 6 ms^{-1}. It was advised that the assumption of a vanishing RCS as grazing angle reduces was inadvisable.

Leading on from this work Valenzuela and Laing completed amplitude statistics analysis [57]. This analysis used real sea clutter data to test the amplitude distributions. A Kolmogorov-Smirnov test was applied to the data and showed that for calm seas and small sample sizes the cumulative distributions exhibited a good fit to exponential or log-normal distributions. The Kolmogorov-Smirnov test does not give an absolute solution to the agreement between the distributions tested and in the information theory research section it is shown that other tests may be more relevant to radar signal processing.

It was shown that for for large sample sizes, > 30 seconds, the data no longer can be assumed to be an acceptable fit to the exponential or log-normal distribution. This may be because only at sample sizes greater than 30 seconds was enough samples available to characterise the actual distribution of the clutter present. A more significant deviation was shown at C and X band compared to P and L band. It was also shown that the vertically polarised data was better represented, in general, by the exponential or log-normal model in comparison to horizontally polarised data.

Trunk, [58], detailed that sea clutter observed at low-grazing angles with high resolutions has a non-Rayleigh distribution. This work built on previous work completed in [33]. This key point has led to many researchers exploring and characterising sea clutter due to its non-simplistic gaussian model. A Ricean model was proposed as a suitable fit to the observed distributions. Again vertically polarised data were shown to be more Rayleigh distribution when compared to their horizontally polarised counterparts. It was also shown that up/down wind measurements had a much larger spread in amplitude values compared to crosswind data.

Fay et al. [59] completed analysis using an X-band using both horizontal and vertical polarisation. This was the first practical application of the Weibull distribution in sea clutter analysis. This analysis showed that the clutter amplitude distributions were represented very well by the Weibull distribution while the log normal and Rayleigh failed to effectively model the distributions. The meteorological conditions recorded during the experiments showed wind speeds of 10-15 knots.

A key difference between horizontal and vertical polarisation was shown in the experimental results seen in [60]. The observations made in this report showed that HH polarised data was not well represented by the Weibull distribution especially when the intensity of the clutter returns were large. This was not noted within the vertically polarised data.

Jakeman and Pusey introduced optical scattering theory to radar sea clutter within [35], which was followed up by Jakeman and Tough in [61]. In this work the K-distribution family was first introduced to sea clutter distributions. The characteristics of the K-distribution, seen in Section 2.3.4, are such that it reduces to the exponential distribution case when the number of contributing scatterers tends to infinity. Which is linked to the case of low resolution medium grazing angle clutter returns. The K-distribution applied to real sea clutter data by Ward in [36]. This work showed a very good fit of the K-distribution to sea clutter recorded using an airborne X-band radar at a low grazing angle of $0.75°$ and reasonable sea state of 3. Through the use of frequency agility it was qualitatively shown that the amplitude returns are much less spiky when applying this technique. These results agree with the two component scattering correlation times, showing that the speckle component is uncorrelated when frequency agility is applied. Leaving a distribution that is close to the Gamma distribution, which is the assumed large scale structure distribution within this model. Since then it has become a very popular distribution to use when modelling sea clutter amplitude distributions.

The work in [37] analysed the statistics of high-resolution ($\approx$ 4m) X-band radar sea clutter. This research included by incoherent and coherent statistical analysis, showing locally Rayleigh distributed speckle and a mean Gamma distributed component. Therefore agreeing with the structure of the compound K-distribution formulation. Where a local illuminated patch has many scatters which leads to the central limit theorem and a Rayleigh distribution. It is suggested that non-Rayleigh distributions are produced by "bunching" of scatterers rather than a lack of scatterers to allow for the central limit assumption. The suitability of the Gamma distribution to high resolution scattering modelling is also explained using moments analysis. It is suggested that the moments of the reflectivity PDF could be expressed in terms of each scatterers moment along with a probability of the scatterer existing within an area.

$$M_n = pM_{S_n} \tag{2.61}$$

where M_n is the nth moment of the reflectivity PDF, M_{S_n} is the nth moment of a typical scatterer and p is the probability of there being a scatterer within an area. This alters to the following when evaluating the normalised moments,

$$M_{n(norm)} = M_{S_{n(norm)}} p^{1-n} \tag{2.62}$$

These moments are then compared to the Gamma distribution normalised moments,

$$M_{n(norm)} = \frac{\Gamma(\nu + n)}{\nu^n \Gamma(\nu)} \simeq (n-1)! \nu^{1-n} \tag{2.63}$$

where ν is the Gamma shape parameter, and n is the moment order. It should be noted that Eqn. 2.63 is valid for small values for ν. The relationship between Eqn. 2.62 and Eqn. 2.63 can then be used to argue that the dominance of the p^{1-n} or ν^{1-n} terms suggest that the Gamma distribution is a suitable one for very high resolution reflectivity.

The results of [37] also showed that Horizontally polarised clutter was shown to be significantly more spiky in nature compared to vertically polarised data recorded in the same conditions, although the horizontal data deviated away more from the K-distribution (seen in the moment analysis) compared to the vertical. This agrees with the analysis of large number of datasets from different radars and conditions.

Stehwien evaluated the statistics observed within sea clutter data recorded using an X-band radar, [62]. It was concluded that the sea clutter was well represented by the Weibull, log-normal and K-distribution. Although the log-normal was shown to be effective in all wind directions, while the Weibull distribution was most effective in crosswind and the K-distribution in downwind direction.

Recent empirical research evaluated the relationship between sea clutter NRCS and compound K distribution shape parameter variation with grazing angle is presented, in Section 8 of [23]. This shows that the relationship between shape parameter and grazing angle (from $0.1^\circ < 10^\circ$), as well as various other parameters, was found to empirically follow,

$$\log_{10}(\nu) = \frac{2}{3}\log_{10}(\phi^0_{gr}) + \frac{5}{8}\log_{10}(A_c) - k_{pol} - \frac{\cos(2\theta_{SW})}{3} \tag{2.64}$$

where ν_G is the shape parameter, θ is the grazing angle, A_c is the area of the radar resolution cell, k_{pol} is a polarisation dependent parameter (1.39 for VV and 2.09 for HH), θ_{SW} is the aspect angle with respect to the swell direction. Verifying and expanding the work on relating the distribution shape parameter to external factors such as those in Eqn. (2.64) as others is an area of sea clutter research that is of active interest [2].

A high resolution radar system was recently used to establish if the observed amplitude distribution at higher frequency, Ka-band, are similar to those at S-band and X-band, [63,64]. This work was also accompanied by additional studies of target detection within the sea clutter, [65,66]. A collection of models were fitted to the real sea clutter data; the Rayleigh, Weibull, log-normal, K-distribution, K-distribution + thermal noise, generalised K-distribution with generalised gamma texture and the generalised K-distribution with log-normal texture. From both square difference fitting and methods of moments it was shown that the best fitting distribution was the generalised K-distribution with log-normal texture. The speckle components of the clutter were also confirmed to still maintain Gaussian distributions even for range resolutions of a few centimetres.

Additional distribution have also been applied to sea clutter modelling and analysis. The Pareto distribution [67] is an example of one such new distribution to this area of research. In some cases this did show smaller errors when fitting to real sea clutter data. The issue with applying this distribution to sea clutter is that it is less analytically tractable back to the physical phenomena occurring. A key advantage of the K-distribution in comparison is that its structure can be linked directly to the physical scattering mechanisms occurring. The two components are representative of both the large scale gravity waves and the small speckle component from ripples on the surface.

2.5.3 Key Sea Clutter Datasets

In order to stimulate research into sea clutter analysis some recorded datasets have been made openly available to the research community. When describing the prior literature existing on sea clutter distribution analysis it is important to introduce these openly available datasets. The first modern day radar dataset made available was the McMaster University Canada IPIX radar datasets from 1993 and 1998. These datasets were generated using a X-band, coherent, ground based pulsed radar system. These datasets have produced over 31 publications between them, some of which can be seen here [34,68–84]. Between them they represents a significant contribution to sea clutter research.

The second significant sea clutter datasets that is available to researchers was produced by CSIR (Council for Scientific and Industrial Research) in South Africa. Two datasets are available for analysis from the 2006 and 2007 sea clutter trials. The publications resulting from these sea clutter and small boat trials are [85–87]. The analysis of this dataset is a key component of the research within this Thesis and will be defined in detail within later chapters.

2.5.4 Variation with grazing angle

The behaviour of sea clutter reflectivity with grazing angle has been analysed in many datasets. Early work [88] defined a critical angle after which the reflectivity dropped off very quickly with decreasing grazing angle. This critical angle was shown to be inversely proportional to frequency, in that it decreased with increasing frequency. The received power was defined as varying as R^{-3} up to a certain range (and hence grazing angle), then the relationship clearly change to R^{-7} above this critical angle.

Further work has expanded on this and established a three region model, [89]. Figure 2.14, from [23], shows the clear relationship between the reflectivity, σ^0, and the grazing angle within these regions.

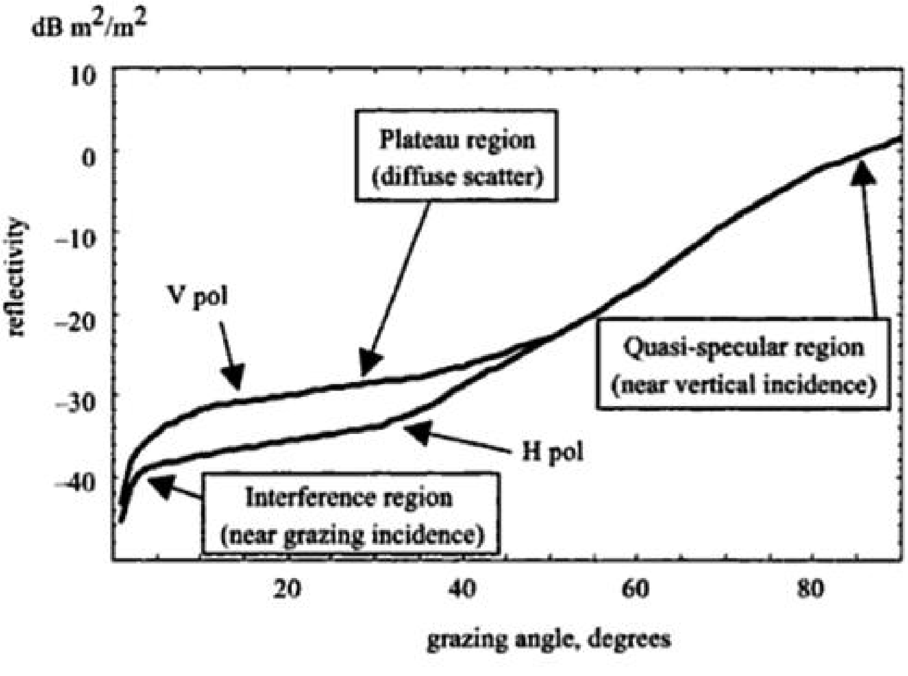

Figure 2.14: Reflectivity variation with grazing angle

When the grazing angle is close to incidence the backscatter is considered to be specular. As the grazing angle moves away from 90° the log reflectivity is shown to decrease quickly with grazing angle from the peak at 90° incidence. The behaviour is then seen to transition between three separate regions with their own distinct behaviour [23]. The regions are named:

- Quasi-specular region, at high grazing angles. The reflectivity is found to reduce steadily with grazing angle for both vertical and horizontal polarisation.
- Plateau region where diffuse scattering dominates, medium grazing angles. The rate of reduction of reflectivity is found to reduce within the Plateau region, with vertical polarisation maintaining a higher level than horizontal polarisation.
- Interference region at low grazing angles. Within this region the reflectivity drops quickly with decreasing grazing angle. It is believed that this effect is due to increased shadowing at this geometry and multipath effects.

There is a clear separation of the reflectivity coefficient from horizontal and vertical polarisation within the Plateau region. Yet in both the interference and Quasi-specular region the behaviour of both polarisations is very comparable.

The location of the division between the Plateau region and the interference region is defined by the critical angle. The critical angle can shift significantly and depends on the conditions of the sea clutter and other radar system variables, [23].

The very low reflectivity coefficient at small grazing angles shows that the returned power from a unit clutter area at these grazing angles is very small. At first glance this would give the impression that due to the low CNR level the issue of compensating for the clutter is reduced at these geometries. This isnt true and in fact it is the low grazing angle sea clutter reflections that are particularly difficult to deal with. This is because in these conditions the clutter cell sizes are much larger.

A reason for the added complexity for compensating low grazing angle clutter is that the NRCS is only tells us the mean backscatter level. Defining statistical variations requires more information. The nature of the statistical fluctuations changes at low grazing angles and therefore so does the requirements for the models.

At low grazing angles the returned sea clutter is removed significantly from a simple Gaussian amplitude return model. The majority of the EM wave is forward scattered and not returned to the radar at all [21], and the component of the signal that is backscattered has a longer tailed amplitude distribution. This is particularly true for horizontal polarised signals. These issues are discussed in later sections of this chapter but are clear examples of the complicated scattering interactions generated by sea clutter returns.

2.5.5 Polarisation variation

Empirical analysis of sea clutter data has shown a number of differences that have been documented between vertically and horizontally polarised clutter returns. The overall characteristics of sea clutter returns are clearly dependent on the polarisation used, as the key contributing effects are themselves polarisation dependent, see section 2.3.2.

Horizontally polarisation sea clutter returns include a great deal more high amplitude spiky returns. These alter the amplitude statistics significantly. This is in contrast to the less spiky vertically polarised returns which have higher mean amplitude; as predicted by the NRCS seen in Fig. 2.14.

The cross polarised returns are much reduced in amplitude, as expected. Also due to the reciprocal EM scattering theory the VH and HV returns are equal (in the monostatic case). It was noted in [90] that the cross polarised speckle component is very small. In comparison the cross polarised spike/mean ratio were shown to be relatively larger, with on average 7dB more amplitude.

Farina et al. [34] showed in the analysis of X-band sea clutter data that the vertically polarised data was well represented by the K-distribution. The horizontal and cross polarised datasets failed to be represented well by the K-distribution and were shown to be exhibiting distributions closer to the log-normal distribution.

D. Walker, [22], completed analysis on the Doppler spectra of both polarisations and noted the differences present within the recorded data. The non-Bragg scatterers that are present within the HH polarisation cause HH to have a higher peak Doppler frequency. Whereas VV polarisation was shown to have a bi-modal behaviour. The higher frequency non-Bragg effects have been shown to have larger amplitude in HH confirming their increased dominance within this polarisation. The reverse is true at the lower frequency peak of the VV polarised returns which is many dBs larger than the HH returns, emphasising the dominance of the Bragg returns within the VV clutter.

The level of the offset of the sea clutter central Doppler frequency is linked to the speed of the waves, which is closely related to the wind speed. Both polarisations were shown to have an increase shift in Doppler with wind speed, although this is seen to be exaggerated in HH polarisation, this is due to the HH having a larger non-Bragg component present.

2.5.6 Sea clutter correlation properties

The discussion of the characteristics of sea clutter so far has been independent of the temporal or spatial correlation properties of the clutter itself. Some simple models treat the clutter as an independent stationary process with no correlation in time or space. As has been previously discussed the more advance sea clutter models utilise a compound form which takes into account the large scale and small scale structure of the sea surface and the effect it has on the scattered EM wave. The components of the clutter were discussed in Section 2.3.2 and 2.3.4.4. These models can be enhanced further by applying the correlation properties of the clutter.

Jakeman and Pusey's work on non-Rayleigh sea clutter scattering showed that there was two clear components of the backscatter that each had different decorrelation time scales, [35]. This introduced the concept of two or more characteristics time lengths for the correlation of scattering events.

The separate components of the clutter, the texture and speckle, possess different temporal correlation characteristics, [34]. These separate components are assumed to be uncorrelated. It was shown in [91, 92] that it is possible to define the over all Auto Correlation Function (ACF) of the clutter as the product of the two individual correlations of these components.

It is important to understand the time scales of the decorrelation of these components to appreciate the temporal behaviour of sea clutter. This understanding helps in the analysis of data and contributes towards developing radar algorithms what need to compensate for their individual effects. The speckle component of the clutter has a fast decorrelation time of the order of milliseconds. While the component representing the large scale structure of the sea surface has been defined as having longer decorrelation time of the order of seconds, [23, 34, 93].

When analysing the texture component of the clutter a window of samples has to be chosen to evaluate the ACF over. Using the knowledge that the texture and speckle have very different decorrelation times, approximately 10ms and 5 seconds respectively [23, 37], a window length can be defined. The window is long enough to allow the speckle to decorrelate over its length, but small enough to ensure that assumption of non-stationarity of the texture is maintained.

Davidson, [94, 95], completed a simulation process in which the correlation properties that have been observed within sea clutter were imparted on simulated clutter returns. The process applies a Memoryless Non-Linear Transform (MNLT) which is seen in Section 5 of [23] and [96], it is also discussed further in Chapter5. This method allows for the gamma texture to be correctly temporally correlated.

2.5.7 Sea Clutter Doppler

The majority of prior sea clutter research has been focused on incoherent analysis, making sea clutter Doppler a relatively new research area. Despite this there is still a reasonable amount of work which has now established a reasonable understanding of the key effects.

Some of the very early work on sea clutter was completed by V. W. Pidgeon. He was first to note that there is a separation in the peak amplitude values in horizontal and vertical polarisation within the Doppler spectra, [97]. This early work was expanded on by G. R. Valenzuela [98] who analysed the variation of the clutter spectra with frequency, polarisation and grazing angle. In this work the bandwidth of the spectra was shown to broaden with lower frequencies (frequencies P, L, C and X were used). The separation of the peak in the spectra, and the difference in this from both polarisations, was also analysed. It showed that the clutter spectra present were clearly bi-modal and the relative amplitudes of the two peaks varied between horizontal and vertical polarisation.

The importance of modelling not only the average power of the Doppler spectrum was emphasised in [99]. Analysis is undertaken into the characteristics of the more detailed fluctuations in power, spectral shape and Doppler offset. The research showed the variation of the centre of the Doppler spectra as a function of into/across the wind/swell environmental conditions. Only a simple relationship was demonstrated but it is an important documentation of this link. As well as this the non-Gaussian nature of the clutter-dominated sections of the spectra was shown, and emphasis was placed on it requiring further research to understand its characteristics to allow for optimised detection processing. Continuing on from this work it was shown that the K-distribution was also suitable to represent the Doppler amplitude statistics as well as the temporal statistics, [100].

Lee et al collected and analysed sea clutter using an X-band system [101]. The aim of the work to was to collect sea clutter data at varying grazing angles using a dual-polarised system. The results showed fast and slow components within the spectrums, generating a bi-modal distribution, as had previously been reported in [98]. In some scenarios, particularly at low grazing angles, a single peak dominated in each polarisation and a clear separation existed between them. Also at low grazing angles and in horizontal polarisation spiking events were found to contribute significantly to the recorded data. These observed spiking events were linked to, but not limited to, breaking wave events.

A basic equation that can be used as an initial estimate for the obtained Doppler frequency obtained from an individual small scatterer component of the surface of the sea is:

$$f_D = \frac{2cos\theta}{\lambda}(\nu_{boat} \pm \nu_w \pm \nu_c \pm c_p) \tag{2.65}$$

where θ is the grazing angle, λ is the wavelength, ν_{boat}, ν_w, ν_c and c_p refer to the velocity of the boat (from which the data is being taken), wind drift, sea current, and the speed of the scatterer on the surface. This does not take into account tilt and the vertical motion of the scatterer.

Ward et al. [37] showed some of the first analysis of the mean Doppler of sea clutter as a function of geometry. This included a simple figure showing 5 samples taken from up/down wind positions as well as cross swell and into swell geometries. The mean Doppler of the clutter was shown to vary from $\approx +64$Hz to ≈ -64Hz. Both vertical and horizontal data values are shown, of which the horizontal data gave a larger variation in mean Doppler values.

A significant section of research of sea clutter Doppler analysis was established by D. Walker in [22] and [24]. This work consists of analysis and modelling of actual data collected from both a wind-wave tank and the seas surface, recorded with 6 GHz and 9.75 GHz radars respectively. The Doppler clutter spectra present is shown as well as a model developed for the spectra. This model uses three components, each represented by a weighted Gaussian. These components are directly linked to those defined in section 2.3.2, hence there is a separate Gaussian to represent each component; Bragg, whitecap and spike (burst).

The models equations for vertical and horizontal polarisation respectively are given by the two equations below:

$$\Psi_V(\nu) = B_V \Psi_B(\nu) + W\Psi_W(\nu) \tag{2.66}$$

$$\Psi_H(\nu) = B_H \Psi_B(\nu) + W\Psi_W(\nu) + S\Psi_S(\nu) \tag{2.67}$$

.

where the subscripts H and V refer to the polarisation, while B, W, and S identify the component inducing that part of the Doppler the spectra (Bragg, whitecap and spike). The key difference between the two polarisations Doppler spectra is that the horizontal polarised model contains three components while the vertically polarised model only has two. The Gaussian representing each of the three components are defined as:

$$\Psi_B(\nu) = exp\frac{-(\nu - \nu_B)^2}{W_B^2} \tag{2.68}$$

$$\Psi_w(\nu) = exp\frac{-(\nu - \nu_p)^2}{W_W^2} \tag{2.69}$$

$$\Psi_S(\nu) = exp\frac{-(\nu - \nu_p)^2}{W_S^2} \tag{2.70}$$

the values ν_B and ν_P represent the Bragg resonant wave speed frequency and the gravity wave phase speed frequency. The model uses these components with different weighting values which can then be fitted to the observed Doppler spectra.

This model was found to be a good fit to both polarisations in the recorded Doppler spectra. Although at the edge of the spectra where the clutter returns merge with the noise floor of the system the model did depart from the recorded data as noise is unaccounted for within this model.

Non-stationarity as a term have been used to describe sea clutter Doppler spectra , [102–105]. In the context of this area of research non-stationarity describes a changing PSD, shape parameter and mean intensity of the clutter over time. It is observed through the changing shape and intensity of a Doppler spectrogram over time. This moving, expanding/contracting spectra is very much characteristics of coherent sea clutter returns within high Doppler resolution radar systems.

Recent work by G. Davidson [95] shows a method of simulating coherent K-distributed sea clutter with the aim of generating large quantities of simulated data over a range of variables, which is based on the smaller amount of real data that has been recorded. The key parameters from the data are the Doppler, temporal correlation and non-coherent signal statistics. This is completed in a non-stationarity way, in that the Doppler shape and amplitude vary over time. The simulation of the data successfully replicated the Doppler characteristics observed in the data, although it was noted that additional Doppler characteristics that occasionally occur could not be included in this model.

2.5.8 Bistatic Sea Clutter

Very little research has been completed into collecting and analysing bistatic sea clutter measurements. The majority of the few trials that have been completed are summarised in Chapter 9 of [14], [3], as well as [53].

The first recorded bistatic sea clutter measurements are discussed by Pidgeon in [106]. This was completed with a ground based C-band CW transmitter and an airborne receiver. During the experiment the bistatic angle was altered by changing the transmitter depression angle, an increase in depression angle resulted in a decrease in the bistatic angle for the geometry used. This gave values for the bistatic NRCS for a range of transmitter depression angles from 0.2° to 2° over sea states 1, 2 and 3. The results showed that there is an increase in sea clutter σ_B^0 with the increase in depression angle from 0.2° to 2°. This increase was shown to be greater in the car of horizontal polarisation, but in general the horizontal σ_B^0 was less than the vertical polarised σ_B^0. A few issues with these results are that the σ_B^0 values for sea state 3 was shown to be lower than sea state 1 and the data compares downwind and crosswind results which can not be necessarily directly related. Although the general trend of an increase in σ_B^0 with the decrease in β over these small angle changes.

This work was followed by Domville's work [107] and [108] which covered bistatic measurements of both various types of land and the sea. This consisted of in-plane measurements of the sea surface using a X-band receiver and transmitter on two separate airborne platforms; both horizontal and vertical polarised data were collected. As described in section 2.1.8 the bistatic RCS was shown to be have a equivalent monostatic region and a forward scattering region. The bistatic RCS region is not defined in the plots shown, but will exist in the intermediate area that was not as well defined. Plots of σ_B^0 vs. θ_i and θ_s using vertical polarisation and horizontal polarisation are shown in the paper can be seen in Fig. 2.15, from [107].

Particular interest was paid to low incident and reflection as well along the region called the specular ridge, $\theta_i = \theta_s$, as well as forward scattering experiments. The results were presented as a gradient map of the σ_B^0 values as a function of θ_i and θ_s, using the data that was collected and interpolating between to fill the entire space of $0° \leq \theta_i, \theta_s \leq 90°$. Domville's results showed a reasonable agreement with Pidgeon's

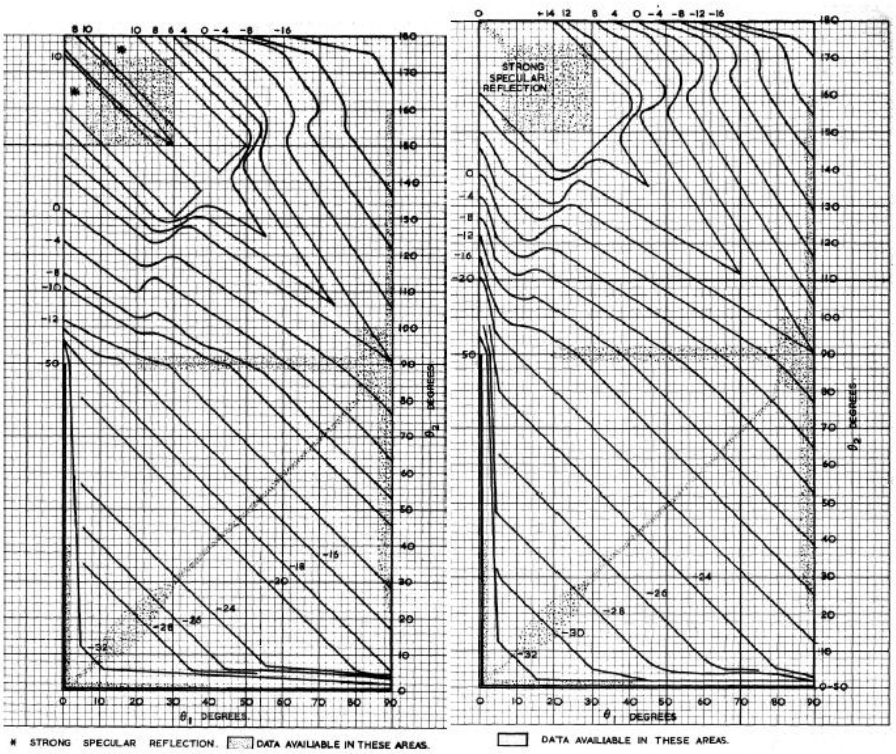

(a) Vertically polarised

(b) Horizontally polarised

Figure 2.15: Bistatic σ_B^0 variation with θ_i and θ_s angles

work with approximately ±5dB difference over the small range of angles Pidgeon had collected data. A key limitation of Domville's work was that no sea state was recorded during the experiments, this is vital when comparing these results to other datasets and as seen in Pidgeon's work [106] a difference in sea state from 1 to 3 can cause $\approx$ 10dB's difference in the σ_B^0 values obtained.

Iterating Pidgeon's results the horizontal polarised σ_B^0 values were shown to be less than the vertically polarised with a difference seen between $\approx 1-5$dB. The issue with this measurement difference is that it is actually smaller than the fluctuation in the results ($\approx$ 10dB) or potential changes due to the current sea state.

Kochanski et al. [109] experiments used a ground based transmitter and a airborne platform as a receiver, like Pidgeon's bistatic in-plane work [106]. The results agreed with Domville's results which demonstrated that σ_B^0 is not sensitive to a change in receiver angle over a large range of angles, as well as agreeing on an approximate average value for σ_B^0 of -45dB. This data was very limited in terms of the range of sea conditions it was collected in and only a small set of receive and transmit angles were used.

The measurements described in this section so far a have all been in-plane bistatic measurements where within the 3D geometry of a bistatic system the angle $\phi = 0°$. Even less experimental results exist for out of plane bistatic sea clutter data. The earliest work showing out of plane data was completed by Ewell. His bistatic research into this area started with bistatic measurements of ships, [20], then developed into the measurement and study of out of plane bistatic sea clutter, [110, 111]. Small grazing angles were used to record simultaneously monostatic and bistatic NRCS values, and the resulting ratio of σ_B^0/σ^0 were evaluated. It is stated that the NRCS values are used to compare the monostatic and bistatic clutter reflections as they compensate for the difference in clutter cell size. The monostatic clutter cell was defined as,

$$\text{Monostatic Area} = kR(\frac{c\tau}{2})(BW) \tag{2.71}$$

where k is a constant related to beam shape (usually close to unity), BW is the 3dB beam width. The more complex bistatic clutter cell was evaluated using a numerical integral defined as,

$$\text{Bistatic Area} = R_T^2 R_R^2 \int \Delta \frac{f_t(\alpha_E - \theta_1)}{r_1^2} \frac{f_r^2(\beta_E - \theta_2)}{r_2^2} \mathrm{dA} \tag{2.72}$$

where f_t and f_r are antenna patterns factors, R_T and R_R are vectors from the transmitter and receiver respectively to the intersection point, Δ is a factor that is 1 if the following inequality is satisfied and 0 otherwise,

$$c(\delta - \tau) < r_1 + r_2 - L_b < c\delta \tag{2.73}$$

δ is the difference in time taken by the signal that travels from transmitter to target to receiver compared to the signal that travels from transmitter directly to receiver along the baseline L_b,

$$\delta = \frac{1}{c}(R_T + R_R - L_b) \tag{2.74}$$

The factors r_1, r_2, α_E and β_E are factors all related to the geometry used for the numerical integral,

$$\begin{aligned} r_1 &= ((x - \tfrac{L_b}{2})^2 + y^2)^{\frac{1}{2}} \\ r_2 &= ((x - \tfrac{L_b}{2})^2 + y^2)^{\frac{1}{2}} \\ \alpha_E &= tan^{-1}(\tfrac{y}{(x - \frac{L_b}{2})}) \\ \beta_E &= tan^{-1}(\tfrac{y}{(x + \frac{L_b}{2})}) \end{aligned} \tag{2.75}$$

The bistatic angles that data were recorded over ranges from 23° to 85°. The results showed that the σ_B^0 values were consistently less than the monostatic equivalent. Ranging from a minimum difference of ≈ -5dB at around $\beta = 30°$ to a peak difference of ≈ -25dB at $\beta = 60°$. The trend showed a inverse relationship of σ_B^0/σ^0

with increasing β, but no data was gather for angles above 85°, so the relationship beyond this point is unknown.

Since these early bistatic experimental campaigns very little work has been completed in this area. A recent campaign completed by UCL in collaboration with University of Cape Town, Thales UK, Thales Netherlands and the ONR Global is the most recent published bistatic clutter measurements, [112,113]. The focus of this trials campaign was to address the lack of knowledge and classification of bistatic sea clutter, which has been described above within this section, over a range of geometries and meteorological conditions. The analysis of this data collected from those trials is a key part of this thesis.

Chapter 3

Data Collection and Pre-Processing

3.1 Data

This chapter focuses on introducing the individual real sea clutter datasets and the radar systems that were used to generate them. The radars that are defined are the SearchWater 2000, the CSIR MerCORT radar and the UCL NetRAD system. Each of the three radars are characterised in terms of their specifications and the RF parameters they are capable of. The datasets generated by each radar that are analysed in this thesis are discussed at the end of each radars subsection.

There are two SW2000 datasets, four CSIR datasets and finally 6 NetRAD datasets (with both monostatic and bistatic for each). The location of each experiment along with meteorological conditions, if recorded, have been defined. Following the detailed introduction of the radars and each of the datasets selected is a pre-processing section. This includes a description of all the pre-processing techniques that have been applied across every datasets to bring the data to a level that it can begin to be analysed. Then a description of the statistical analysis techniques and fitting methods is included to explain how information on the behaviour of the clutter present was extracted.

Access to multiple datasets has allowed for comparative analysis of the sea clutter present within each of the databases generated by separate radars. Using common processing and statistical analysis techniques makes it possible to directly compare the results and clutter behaviour across dataset to evaluate trends and relationships produced by the sea clutter itself, independent of the radar system. Due to the extensive quantities of data available and the significant processing steps applied only the high level plots of comparative statistics between datasets are shown in the later part of the analysis on the data from each radar.

3.1.1 Thales SW2000 Datasets

The first datasets analysed were recorded during the development trials of a variant of the Thales UK SW2000 radar system. This radar was briefly introduced in section 1.3, it is designed primarily for airborne early warning (AEW) applications in the maritime environment. In this application sea clutter compensation is a vital aspect of the data processing within the radar, making the analysis of the sea clutter statistics present within the data recorded of practical radar engineering significance as well as a relevant research opportunity.

The SW2000 system is a X-band (c.a. 9 GHz frequency), coherent radar that was located on a moving airborne platform during these experiments. The grazing angles covered from the look angle of the system range from $< 1°$ to $7°$. The two datasets analysed for this work are labelled 612 V and 612 H, where 612 V is vertically polarised and 612 H is horizontally polarised. These measurements were taken consecutively so allow for the direct comparison of the two polarisation. Although are not as ideal as a simultaneously recorded dual polarisation measurement. A list of the radar parameters used can be seen in Table 3.1.

Table 3.1: SW2000 Radar specifications

Parameter	Value
PRF	$\approx$ 3kHz, Agile
RF	$\approx$ 9GHz, Agile
Bandwidth	10 MHz
Duty Cycle	3%
Range Resolution	$\approx$ 20m
Polarisation	VV and HH. Not simultaneously

The pulse repetition frequency (PRF) used during the experiments was sufficiently high enough to allow for the data to be unambiguous in Doppler. As the clutter spectrum only extended over a fraction of the full Doppler dynamic range, leaving the rest of the Doppler spectra only limited by the thermal noise of the system. The disadvantage of this is that ambiguities are introduced within the range domain, see Section 2.1.7. The ambiguities within the data, in both Doppler and range, are discussed in depth later on within this chapter.

Both the PRF and RF used by the radar system are agile, with the PRF set at approximately 3 kHz. This agility generates significant issues when integrating multiple bursts to generate a single sea clutter distribution. After each group of 32 pulses the data changes RF and PRF, it is this group of 32 pulses that will be defined as a burst when describing the analysis of the SW2000 data. Due to the changes in PRF the number of unambiguous range gates of data varies, from approximately 2500 to 3000. The methodology used to overcome these effects is described in Section 4.1.2.

A diagram showing the geometry of the air platform and radar look direction can be seen in Fig. 3.1. The antenna tilt is shown with the 3dB beamwidth located either side of the declined main lobe.

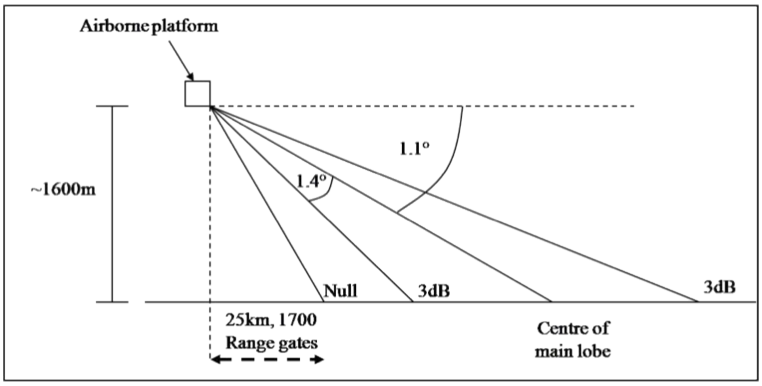

Figure 3.1: Geometry of SW2000 trials

Limited sea conditions characteristics (sea state and wind direction) were recorded during the trials from the observations on the day. This information along with the look angle of the radar can be used to approximately define whether the data being analysed was acquired while looking up/down/cross wind.

Using the notes recorded during the flight trials it is possible to assume a sea state 3 with a northernly wind direction and a swell from 280°N. Using the depression angle at the centre of the beam, 1°, i.e. about 50km range. The expected K-distribution shape parameter for H pol is 7.7 and in V-pol it is 39 using incoherent processing. In addition to this for the assumed sea state 3 the expected CNR for V and H polarisation would be 29dB and 28dB respectively, Chp 3. [23].

3.1.2 CSIR 2007 Datasets

These datasets were generated by the Radar and Electronic Warfare Systems division of the South African institute the Council for Scientific and Industrial Research (CSIR). The data were recorded on the coast of South Africa in 2007 using a ground based, staring, X-band, monopulse radar system. An image of the radar system can be seen in Fig. 3.2, from [86].

The aim of this experimental campaign was to collect sea clutter measurements as well as small boat targets data. As a portion of the trials were designed specifically for the collection of sea clutter, the data is very suitable for the analysis goals of this thesis. Another key reason for the suitability this data for sea clutter analysis is the fixed PRF and RF during the experiments, unlike the SW2000 data. This means that the artefacts introduced by RF and PRF agility do not have to be compensated for unlike the SW2000 data.

Figure 3.2: CSIR radar

Figure 3.3: CSIR plan image of radar location

The 2007 datasets were recorded on Signal Hill close to Cape Town South Africa, see Fig. 3.3, from [86], and Table 3.2 for full location details. The geometry used meant that the shortest distance to the sea was 1250m at a bearing of 288°N from the radar location. Grazing angles of 0.3° to 10° were possible from the site while using a maximum instrumented range of 60km.

Table 3.2: 2007 Database Location parameters

Parameter	Value
Latitude	33°55’15.62 S
Longitude	18°23’53.76” E
Height above sea level	308m
Distance to sea	1250m
Range of grazing angles	10° (Coastline) - 0.3° (Max Range)

A key advantage of the CSIR dataset is the comprehensive documentation of the environmental conditions and geometries used during the experiments. An example section of the trials summary from one of the datasets is seen in Fig. 3.4, from [85]. These clear recordings of both the environmental conditions and exact radar parameters contributes greatly to the usefulness for the data when relating phenomena to the recorded conditions.

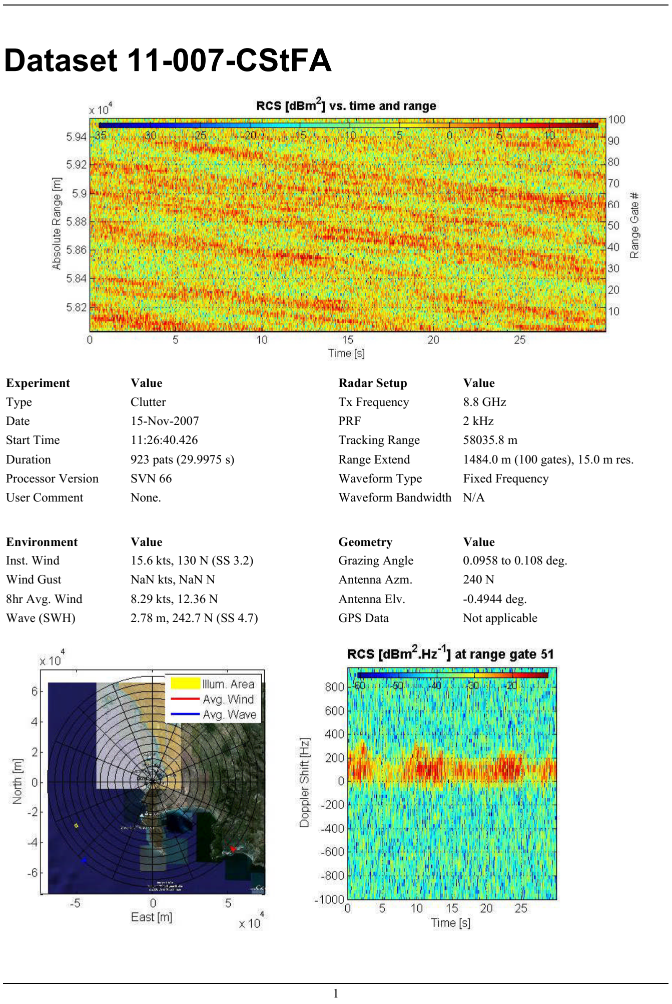

Dataset 11-007-CStFA

Experiment	Value	Radar Setup	Value
Type	Clutter	Tx Frequency	8.8 GHz
Date	15-Nov-2007	PRF	2 kHz
Start Time	11:26:40.426	Tracking Range	58035.8 m
Duration	923 pats (29.9975 s)	Range Extend	1484.0 m (100 gates), 15.0 m res.
Processor Version	SVN 66	Waveform Type	Fixed Frequency
User Comment	None.	Waveform Bandwidth	N/A

Environment	Value	Geometry	Value
Inst. Wind	15.6 kts, 130 N (SS 3.2)	Grazing Angle	0.0958 to 0.108 deg.
Wind Gust	NaN kts, NaN N	Antenna Azm.	240 N
8hr Avg. Wind	8.29 kts, 12.36 N	Antenna Elv.	-0.4944 deg.
Wave (SWH)	2.78 m, 242.7 N (SS 4.7)	GPS Data	Not applicable

Figure 3.4: Example CSIR 2007 dataset summary sheet

From the large quantity of CSIR data available for analysis, four datasets were selected. These are labelled 11-007-CStFA, 11-010-CStFA, 11-012-CStFA and 11-015-CStFA, and were all recorded on 15th November 2007. For ease of reference from this point onwards in this thesis the datasets will be referred to as dataset 07, 10, 12 and 15. In addition to these four main datasets three secondary datasets, 11-008-CStFA, 11-009-CStFA and 11-01-CStFA (now labelled 08, 09 and 11), were selected for use during the simulation and modelling component of this work. The secondary datasets were selected to allow for a better relationship between modelling parameters and azimuth, this is discussed later in Section. 5.

The radar and geometry parameters for each dataset is shown in Table 3.3, from [?], along with the details of the secondary datasets parameters in Table 3.4. All of these datasets were recorded over a duration of $\approx$ 30 seconds, with vertical polarisation, at a frequency of 8.8 GHz and a PRF of 2kHz.

These four specific datasets were selected as they were recorded for the purposes of sea clutter analysis not target tracking. Therefore no CSIR controlled targets were present within any of the range gates of data during these recordings. As well as this the sea conditions on the day of recording represented some of the greater wave heights and wind speeds of all the days of the experimental campaign. This ensures that the sea clutter present would have a high CNR as well as significant Doppler speeds, in the context of sea clutter. The datasets represent a matrix of 2 azimuth angles (240N and 307.5N) and different 2 ranges (58,036m and 39,449m). Two of the azimuth angles are directed approximately into the swell (datasets 07 and 12) while the alternate pair (datasets 10 and 15) have an azimuth directed across the swell present. This allow for the comparison of the statistical variation of the clutter present with swell direction, which is a key factor in the characteristics of sea clutter.

Table 3.3: CSIR radar 2007 datasets parameters

Parameter	Dataset			
	07	10	12	15
Time of recording	11:26:40	11:30:59	11:33:37	11:36:41
Duration of recording (seconds)	29.9975	29.9975	29.9975	29.9975
Frequency (GHz)	8.8	8.8	8.8	8.8
PRF (kHz)	2	2	2	2
Range of first range gate (m)	58035.8	58035.8	39448.7	39448.7
Range gates	100	100	101	101
Range Extend (m)	1484	1484	1499	1499
Grazing Angles (Degrees)	0.0958 - 0.108	0.0958 - 0.108	0.293 - 0.314	0.293 - 0.314
Antenna Azimuth (Bearing)	240° N	307.5° N	240° N	307.5° N
Antenna Elevation (Degrees)	-0.4944	-0.4944	-0.5712	-0.5693

Table 3.4: CSIR radar 2007 secondary datasets parameters

Parameter	Dataset		
	08	09	11
Time of recording	11:27:64	11:28:40	11:31:46
Duration of recording (seconds)	29.9975	29.9975	29.9975
Frequency (GHz)	8.8	8.8	8.8
PRF (kHz)	2	2	2
Range of first range gate (m)	58035.8	58035.8	58035.8
Range gates	100	100	100
Range Extend (m)	1484	1484	1484
Grazing Angles (Degrees)	0.0958 - 0.108	0.0958 - 0.108	0.0958 - 0.108
Antenna Azimuth (Bearing)	262.5° N	284.5° N	330° N
Antenna Elevation (Degrees)	-0.4944	-0.4944	-0.4944

The location of the radar along with the overlay of the range swath on a map of datasets 07, 10, 12 and 15 can be seen in Fig. 3.5 and 3.6 . The range swath of recorded data is shown in yellow, while the recorded wind direction is a red arrow and the wave direction a blue arrow.

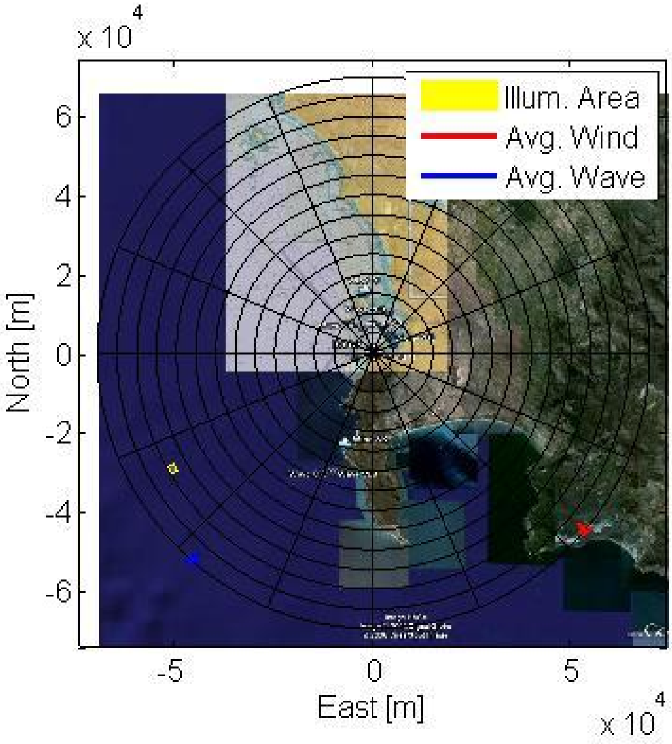

(a) Dataset 07

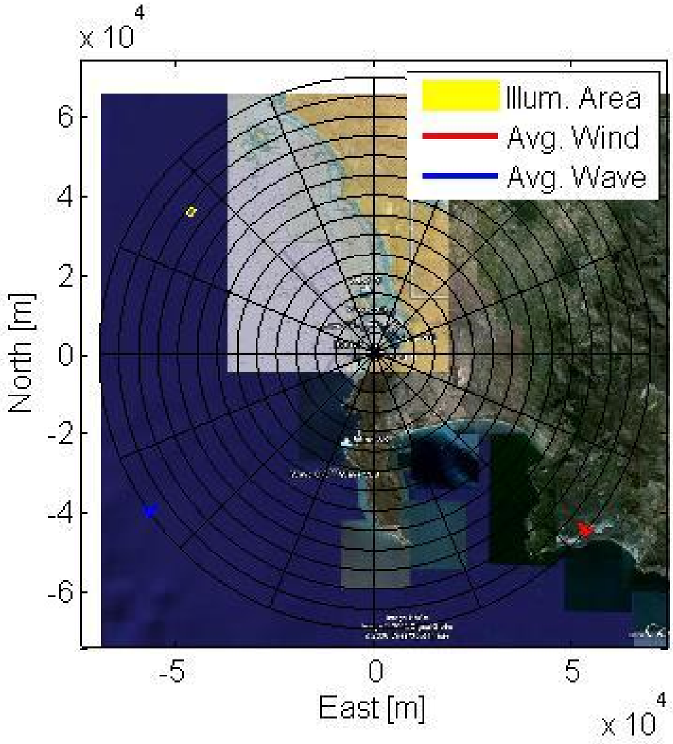

(b) Dataset 10

Figure 3.5: CSIR datasets geometry (a) 07 (b) 10

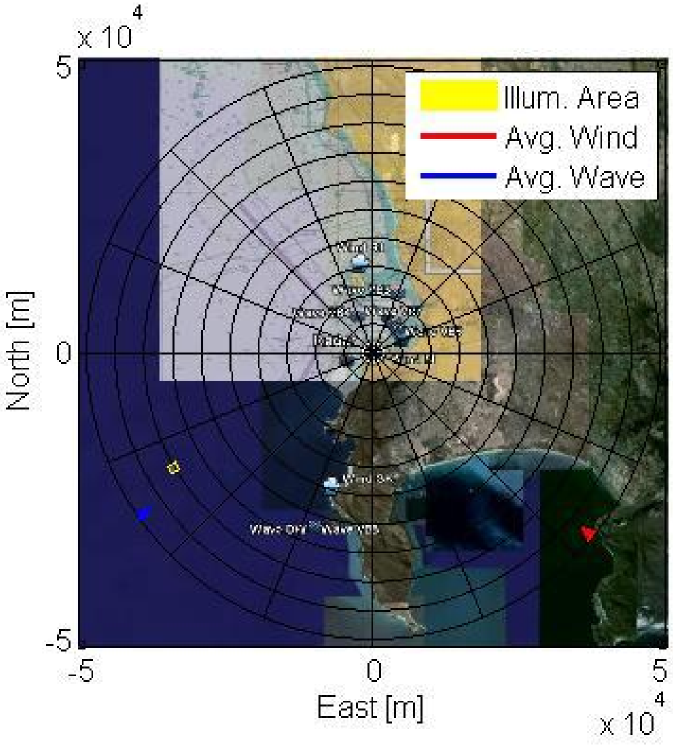

(a) Dataset 12

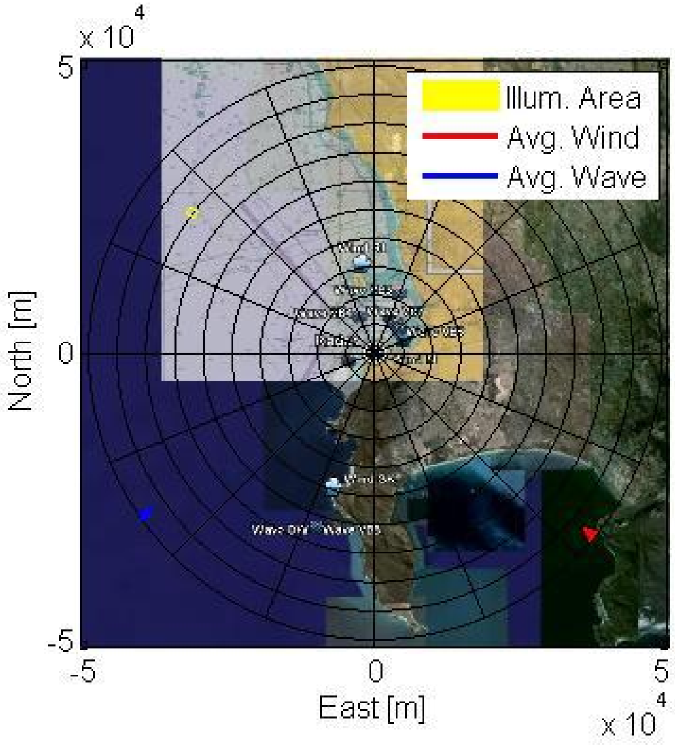

(b) Dataset 15

Figure 3.6: CSIR datasets geometry (a) 12 (b) 15

The record of meteorological conditions during the experiments on 15th November 2007 can be seen in Table 3.5, from [**?**]. The local wave conditions were measured using a wave sensor on the seabed located at Camp's Bay, which is approx 33°57'04 S and 18°22'42 E, and a wave buoy located at Cape Point. The wind conditions recorded were measured at the radar location.

Table 3.5: CSIR Radar 2007 datasets meteorological conditions parameters

Parameter	Value
Inst. Wind	15.6 kts, 130 N (SS 3.2)
8hr Avg. Wind	8.29 kts, 12.36 N
Wave (SWH)	2.48 m, 245.3 N (SS 4.4) Except Dataset 07 2.78 m, 242.7 N (SS 4.7)

Archived meteorological conditions recorded on the weather database website Weather Underground gave a hourly recorded wind speed measurement, see Table3.6. This shows the weather conditions from 2hr30mins either side of the experimentation recordings between ≈11:26am and ≈11:36am.

Table 3.6: CSIR radar 2007 datasets meteorological conditions [1]

Time	Wind speed (km/h)	Direction
9:00am	31.5	SSE
9:30am	37	SSE
10:00am	33.3	SSE
10:30am	33.3	SSE
11:00am	35.2	SSE
11:30am	33.3	SSE
12:00pm	33.3	SSE
12:30pm	33.3	SSE
1:00pm	33.3	SSE
1:30pm	33.3	SSE
2:00pm	38.9	SSE

3.1.3 NetRAD Radar and South Africa trials data 2010

NetRAD is a netted, multistatic, pulsed, S-band (2.4 GHz) radar system that has been developed at University College London over a number of years. The system was initially developed to be a low power, coherent system, which was capable of recording simultaneous monostatic and bistatic data, by T. Derham and S. Doughty [114–116]. It was then further developed to allow the system to be capable of recording multi static sea clutter data by Waddah Al-Ashwal [117] and Stephan Sandenbergh. The key upgrades to the system to enable sea clutter measurements were:

---

[1] Obtained from website www.wunderground.com

- Higher power transmitter (HPA)
- Wireless operation between nodes for increased maximum baseline
- Antenna improvements - More robust and improved directional control
- Software upgrades

The initial transmit power low at 200mW per radar node. The power of the system was then significantly increased by integrating a new external HPA. The main HPA has an output of 450W (Microwave Amplifiers Ltd. AM85-2.45S-57-57) and the backup amplifier has 200W peak power (Microwave Amplifiers Ltd. AM82-2.5S-45-53), see Table 3.7 from [117].

Table 3.7: NetRAD radar parameters

Parameter	Main HPA	Backup HPA
Output power	57.7 dBm	54.3 dBm
Input power for rated output	5 dBm	10 dBm
Control signal	TTL	TTL
Control pulse rise time	5μs	10μs
Control pulse fall time	5μs	10μs
Positive bias	12V	12V
Negative bias	-12V	-12V
Peak positive supply current	120A	60A
Standby current	1400mA	183mA
Maximum duty cycle	10%	10%

Prior to the sea clutter trials the timing of the radar system was changed completely from a shared wired communicated clock for synchronisation to a wireless GPS Disciplined Oscillators (GPSDO) system [118, 119] . This provided a coherent clock reference signal and time synchronisation that could be operated wirelessly. The hardware and software upgrades to implement this core change to the radar system were conducted by Waddah Al-Ashwal and Stephan Sandenbergh.

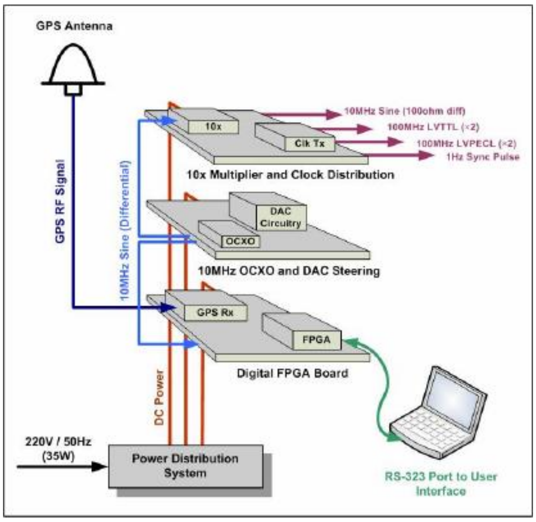

Figure 3.7: GPSDO schematic diagram

A GPSDO is a clock that uses a combination of a stable oscillator and GPS signals to increase the overall accuracy of its timing signal. This is completed by implementing a phase lock between the GPS signal and the clock using a tracking loop. Within the GPSDO clocks used with the NetRAD system the 1 Hz GPS signal has been phase locked to a oven controlled crystal oscillator that operates at 10 MHz. This signal is itself multiplied up to the 100MHz reference signal required for the radar system. A schematic diagram showing the setup of the GPSDOs can be seen in Fig. 3.1.3. The clocks were integrated completely with the NetRAD operational GUI to allow control over their parameters. The images in Fig. 3.1.3 (a) and (b) show a GPSDO without its external house and then it with its external housing and connected to a NetRAD node respectively. The GPSDO can be used to trigger the radar via the user inputing a given time for the transmission to occur in the future, as the carrier is synchronised exactly with GPS at this time a trigger pulse is sent to NetRAD to initiate the transmission.

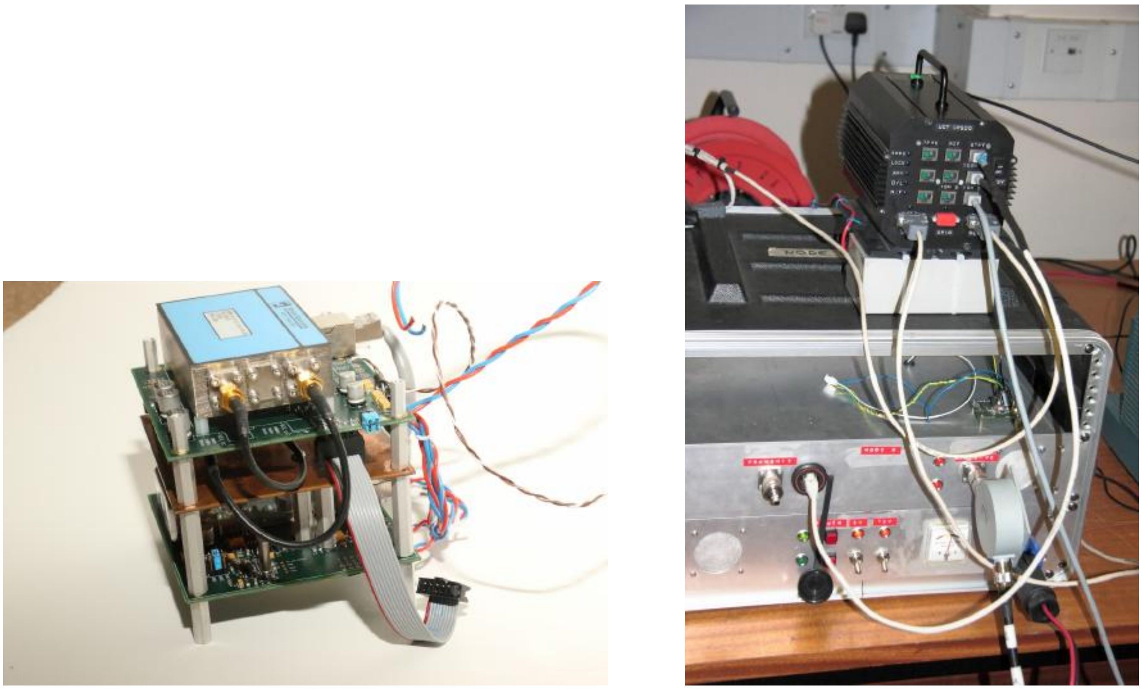

(a)

(b)

Figure 3.8: Images of GPSDO (a) Internal components (b) Device connected to NetRAD Node

For the transmission of the data and commands between nodes wireless links were used. These devices, Ubiquiti “bullet” data links, were connected to 20dBi patch antennas (L-Com HG5158-23P), see Fig. 3.9. These devices allowed a separations of radar nodes up to 5km, with line of sight. They operate around 5GHz, which sufficiently separate from the 2.4 GHz operational frequency of the radar to not cause any interference with its operation.

Figure 3.9: Wireless bullet and patch antenna

The antennas selected for use with the radar were the Poynting K-GRID-003-05 grid antennas. Their gain, beamwidth and ruggedness, meant that they were well suited the experiments planned. The specification data from the manufacturer on the antennas can be seen in Table 3.8.

Table 3.8: NetRAD antennas specifications

Parameter	Value
Electrical Frequency	2.4 - 2.5 GHz
Gain (max)	27dBi (±0.5 dB)
VSWR	$< 2.0 : 1$
E-plane 3 dB beamwidth	11° (± 2 dB)
H-plane 3 dB beamwidth	8° (± 2 dB)
All sidelobes	< -20dB
Nominal input impedance	50 Ohm
Polarisation	Linear (Vertical or Horizontal)

During performance evaluation of the antennas it was found that the antenna gain values were 23.7 dB, and the beamwidth values were 11.23° x 8.97° (E and H respectively). These gain and beamwidth values gave sufficient power to be able to measure returns at monostatic ranges of $\approx$ 3 km while maintaining a cross range resolution of the order of $\approx$ 450m.

The antennas were set up on variable height tripods with a custom built mounting bracket to attach them and set the azimuth and elevation angles, see Fig. 3.1.3 (b). A rotational stage for azimuth positioning was fitted to the mounting structure with a vernier to allow angle measurements to be set with a 0.2° accuracy. During experimentation this angular accuracy was not possible due to wind conditions therefore the accepted accuracy is given as ±1°, this was also assumed as the elevation accuracy error.

(a) (b)

Figure 3.10: NetRAD antenna and setup

The NetRAD data analysed in this thesis was collected during a series of trials completed in 2010. The trial campaign was located on the coast of South Africa and organised in collaboration with the University of Cape Town, Thales UK, Thales Netherlands and the US Office of Naval Research Global. The main campaign was completed over a period of three weeks, with a team of researchers from UCL travelling with the radar to South Africa to work with the university of Cape Town team. The aim of the trials was to collect simultaneous recorded coherent monostatic and bi-static sea clutter, as well as data on small maritime targets. This was to be achieved using the NetRAD system operating over significant baseline distances (> 1km) wirelessly with GPSDOs and wireless network links. The radar parameters used for the experimental campaign can be seen in the Table 3.9.

Table 3.9: NetRAD radar parameters

Parameter	Value
Carrier Frequency	2.4 GHz
Transmitter Power (HPA)	57.7 dBm
Max range over which data is recorded	3 km
Bandwidth	50 MHz
Range Resolution	3 m
Pulse Length	0.1 - 10 μs
PRF	50 Hz - 3 kHz

During this campaign only two nodes were used, meaning that a monostatic measurement and a single bistatic measurement could be recorded for each experiment. This limitation was because the third GPSDO was not available at the time.

Multiple geometries were tested while recording simultaneous bistatic and monostatic clutter. The datasets selected for analysis all used a horizontal plane separation geometry between nodes, the difference in height of the nodes above sea level was kept to a minimum. The practical separation was limited by suitable location for experiments as well as the requirement for direct line of sight between radar nodes for the wireless communications links to work.

The changes in bistatic geometries were achieved by maintaining the baseline between the monostatic and bistatic nodes and changing the azimuth angle of the antennas at each node. Therefore an Isosceles triangle was established between the intersection point of the two beams and the two nodes. This shift in azimuth angle allowed for multiple bistatic angle measurements to be taken without the labour intensive action moving the radar nodes to new location to shift bistatic angle. A problem associated with this method was that in changing the bistatic angle the illuminated area of sea that resides at the intersection between the two beams is no longer the same area of sea prior to the angle change. It was decided that this is an acceptable experimental method as the shift in area of sea should not be significant with respect to the expected changes in sea clutter phenomenology.

The datasets selected for analysis were all generated on 10th October 2010 at a site on the western side of Cape Point named Scarborough. The exact locations of the two nodes was recorded using the GPS positioning signals from the GPSDO clocks after setting up the nodes, see Table 3.10. Note that the height values are taken using the WGS84 ellipsoid which was set $\approx$30 m below the actual sea level. In this geometry the horizontal separation was 1827m the vertical separation was 14.17m and the baseline 1827.05m. Plan images showing the locations of the two nodes can be seen in Fig. 3.1.3 (a) and (b).

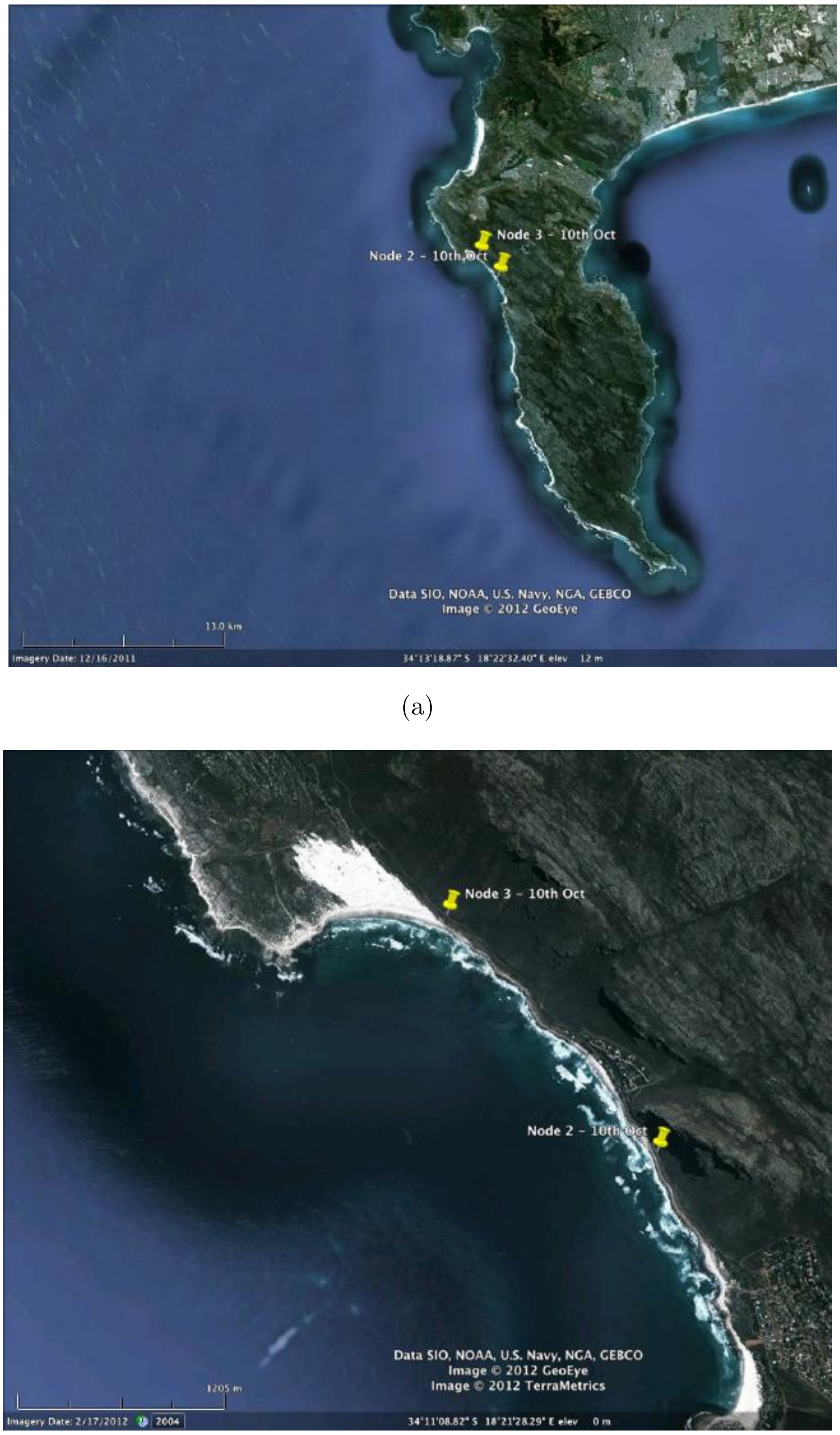

(a)

(b)

Figure 3.11: Image of locations used for sea clutter data collection on Cape Point (a) Full view (b) Zoomed view

Table 3.10: NetRAD datasets location

Bistatic Node			Monostatic Node		
Latitude (°)	Longitude (°)	Height (m)	Latitude (°)	Longitude (°)	Height (m)
-34.189073	18.366482	65.4	-34.176775	18.353305	79.57

In total 6 datasets have been selected from all those recorded on 10th October 2010, these include 3 bistatic angles and 2 polarisations, with a monostatic and bistatic recording for each, see Table 3.11. All of these experiments are out-of-plane geometry bistatic measurements, in that the monostatic and bistatic nodes are horizontally separated and not transmitting in the same plane. These 6 measurements are the focus of all the data analysis from the NetRAD trial campaign as they were recorded on the same day allowing for a direct comparison between bistatic angles and polarisation from what can be assumed to be the "same sea".

Table 3.11: NetRAD datasets

Dataset Label	Bistatic Angle	Polarisation	Pulse Length (μs)
1233	60	Horizontal	3
1244	90	Horizontal	2.2
1253	120	Horizontal	1.8
1551	60	Vertical	3
1603	90	Vertical	2.2
1617	120	Vertical	1.8

Meteorological conditions relating to wave and wind conditions were obtained during the trials by CSIR, Table 3.12, Originally shown in [117], this has been collected on behalf of the Transnet National Port Authority.

Table 3.12: NetRAD data meteorological conditions obtained by CSIR

Dataset	Wind speed (ms^{-1})	Wind Direction	Period (s)	Wave Direction	$H_{1/3}$ (m)
1233	10.15	North	7.1	289	3.28
1244	10.37	North	7.7	279.5	3.48
1253	10.8	North	8.3	270	3.67
1551	11.55	North	8.3	283	3.89
1603	11.55	North	8.3	283	3.89
1617	12.3	North	8.65	276	4.02

In addition to this the trials logs themselves contained basic qualitative observations and the weather web database www.wunderground.com was also used for information, see Table 3.13.

Table 3.13: NetRAD data meteorological conditions

Property	Value (km/h)	Value (ms^{-1})
Wind Speed	24 km/h	6.67 m/s
Max Wind Speed	63 km/h	17.5 m/s
Max Gust Speed	82 km/h	22.78 m/s

3.2 Pre-processing

This section describes the general pre-processing techniques applied to all the datasets analysed. This processing was required to bring that data to the point that statistical analysis could be applied to characterise the sea clutter present. In each case the reason for each processing step is explained, along with how they were applied.

The pre-processing description starts with the methods used to produce the short-time Doppler spectra as well as range-Doppler spectra from the data. Range-Doppler processing is relevant to the SW2000 data and the short-time Doppler processing relates to the CSIR and NetRAD data. Following this the statistical analysis applied to each dataset is defined in detail, stating each model and how it was fitted or compared to the data.

3.2.1 General Pre-processing and Doppler Processing

The programming tool used for the majority of the analysis was the Matlab software package including the signal processing, statistical and parallel computing toolboxes. All of the data was post processed after it was recorded using this software, as this research did not consider realtime processing of the data.

The first steps for analysing the data was to ensure that it was in a readable format for the software to be able to input the recorded values. This usually resulted in converting the binary files values into the raw ADC output voltages if the data is non-coherent and complex values I and Q for coherent data.

To produce the Doppler spectra from the coherent data then either a long-time or a short-time discrete FFT (Fast Fourier Transform) was performed on the data, Eqn 3.1.

$$X_k = \sum_{n=0}^{N-1} x_n e^{-i2\pi kn/N} \tag{3.1}$$

where n = 0,..., N-1, x_n is the input time series of length N and X_k is the output frequency domain signal. A weighting window is applied to the data prior to input into the discrete FFT in each case a -55dB Dolph-Chebshev window was used. see example in Fig. 3.12. This was generated using a Matlab in built function. This sidelobe weighting function as it gives equal sidelobes that can be a defined level below the main lobe. The -55dB level was chosen as any values below that level will most likely be limited by thermal noise.

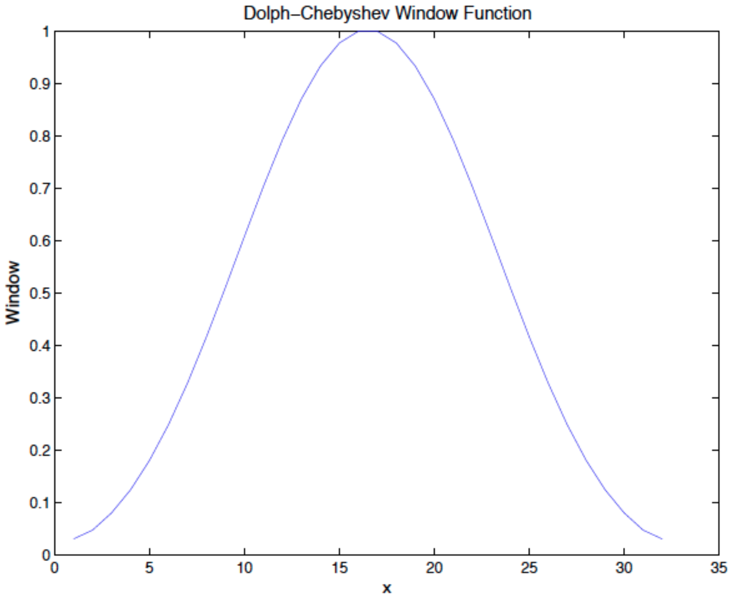

Figure 3.12: Dolph-Chebshev window function of length 32 with -55dB sidelobes

The short-time FFT performs the Fourier transform on consecutive samples within an individual range gate producing Doppler-time data from within that specific range gate. This technique was used on the staring radar data generated by CSIR and NetRAD.

A long-time FFT involves completing the Fourier transform on groups of Range-time samples, where consecutive pulses are selected and then Fourier transformed. This technique has been used for the scanning radar data recorded using the SW2000 radar. The difference between the long-time FFT and the short-time FFT is that the Fourier transform output of the former is arranged as Range-Doppler from all range gates. Whereas in the short-time FFT only the output from a single range gate is concatenated together with many other FFT outputs.

From the datasets that have been analysed the SW2000 data was processed using long-time FFTs. This is because the mechanically steered radar changes angle with respect to the sea surface and wind direction. Therefore data from a single range gate changes physical location over the duration of the recording. So producing the Doppler spectrogram for a single range gate would involve joining data from a variation of physical locations and not allow for characterisation of statistical behaviour with swell direction or wind direction.

The CSIR and NetRAD recordings were analysed using short-time FFTs as both systems were setup on land staring into the sea from a fix angle. Hence over the duration of the recording a range gate still represents the same physical location and a short-time FFT shows the progression of the Doppler spectra at this location over this duration.

3.2.2 Generation of data PDFs and P_{FA} curves from data

To characterise and compare to existing sea clutter models the discrete data must be assigned a representative continuous PDF. As the data is real discrete samples then there is no absolute solution for the PDF that represents the data. Therefore the representative PDF generated for the data is only an approximation. The accuracy of this approximation increases as the number of samples used to generate it increases as well as using more advanced techniques to generate the PDF.

Initial methods used to define the PDF of the amplitude statistics of the clutter involved generating a histogram. This allocated each data sample to a given histogram bin based on the amplitude value, generating a discrete PDF in both bin locations and quantity within each histogram bin. The bins were defined as fixed number of locations spread from the minimum to the maximum values within the data passed to it. The characteristics of this discrete histogram PDF method is dependent on the range and size of histogram bins used. This introduces sampling noise errors to the PDF amplitude values equal to ± of the histogram bin width.

To overcome the issues of a histogram PDF generation an improved method was applied to generate PDF curves from the data. This method uses each sample's amplitude value as a singular incremental value to the CDF and then normalises the CDF curve with the sum total of samples used to generate it. Ensuring the values obtained are bounded between 0 to 1, as required for an CDF. This does not have any sampling noise associated with it as each sample is located at its exact amplitude. This also give much greater detail in the shape of the higher values of the distribution unlike the histogram method. For sea clutter distribution analysis it is important to characterise the behaviour of the high values amplitudes.

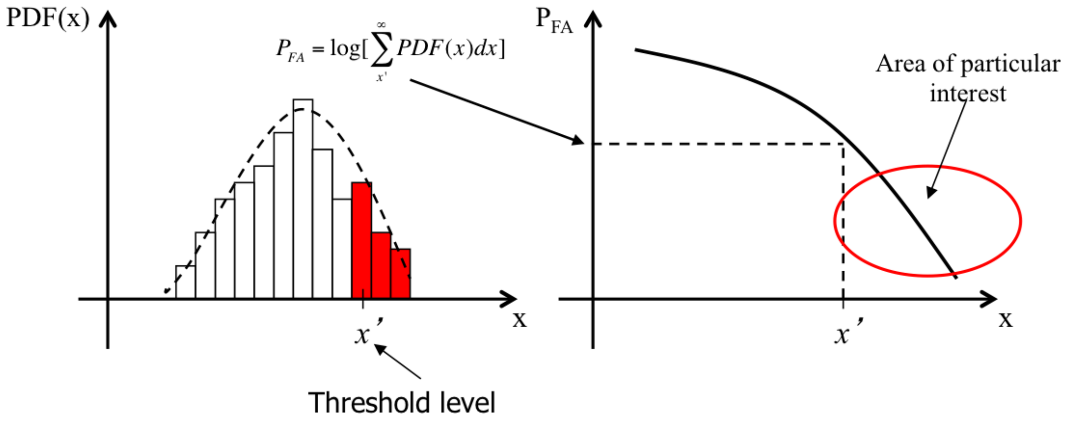

Figure 3.13: P_{FA} to PDF diagram from histogram PDF

The generation of P_{FA} plots from the first method using a histogram was completed by applying a summation of the PDF from each applied threshold level, see diagram in Fig. 3.13. The second method uses the relationship,

$$CDF = 1 - P_{FA} \tag{3.2}$$

to generate P$_{FA}$ curves from the CDF.

A comparison between the histogram and single value CDF methods can be seen in the resulting log(P_{FA}) curves seen in Fig. 3.14. This figure was generated by using simulated K-distribution samples as an input to both the histogram PDF method and the single value CDF method. The outputs were then used to produce a log(P_{FA}) curves from the same data. The tail end of the log(P_{FA}) curve has been shown in this figure as this is where the differences in the two curves are enhanced. The CDF generated log(P_{FA}) curve shows much more detail with over 3500 samples defining the log(P_{FA}) curve over this range, while the histogram generated curve has only 10 samples.

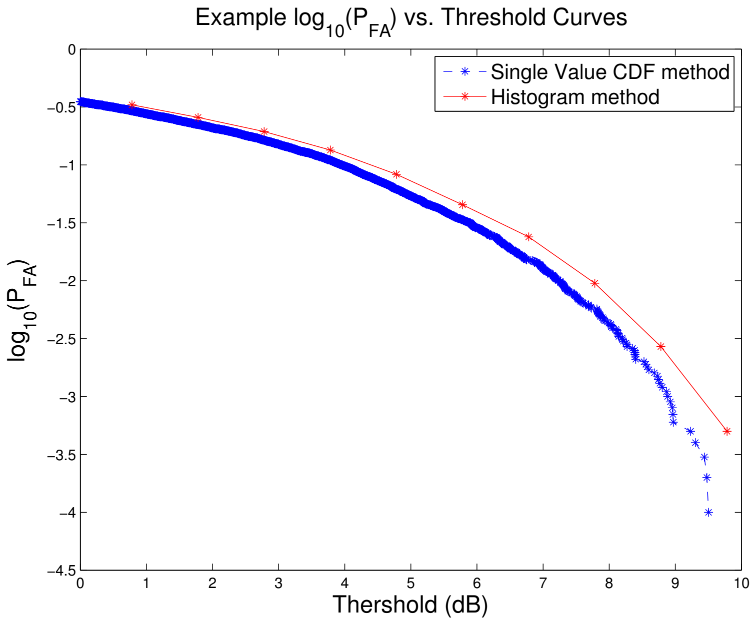

Figure 3.14: Example $log_{10}(P_{FA})$ vs. threshold (dB) curves generated using two different methods

3.2.3 Fitting methods

It is important to be able to now compare the real clutter measurement distribution to accepted models for sea clutter. In this thesis two methods have been used to fit sea clutter models to real data. The first is completed in the log(P_{FA}) domain using a sum squared difference (SSD) fit and the second uses the normalised amplitude moments of the data. The method of moments compares the normalised moments with predicted moments from given amplitude models.

The SSD fit to the data curves uses the log(P_{FA}) curve and evaluates the summation of the square difference between the data $\log(P_{FA})$ curve and a series of theoretic curves generated from the model that is being fitted. This fitting was completed on values of the threshold above 0 dB, therefore focusing on the tail end of the $\log(P_{FA})$ curve, which is of particular interest when evaluating sea clutter. The $\log(P_{FA})$ curve for a given model was evaluated at each of the $\log(P_{FA})$ sample locations. This results in a net squared vertical difference between curves being evaluated which establishes the difference between data and model. A set of model curves were used each with a different parameter, the curve with the least sum square difference was declared as the best fitting curve for that model to the data. For the K-distribution the set of curves used to compare to the raw data curves used shape parameters varying from 0.1 to 10 in steps of 0.1, with an additional curve with a shape parameter of 100 which represents thermal noise like distributions.

Examination of the characteristics of the K-distribution suggests that shape parameters of less than 0.1 would be very unlikely for non-coherent processing of the data, [23]. If a fitting was found to suggest a shape parameter less than 0.1 then it is likely that the data is not well characterised by the K-distribution. It will also be seen from empirical results, Section 4, that they are not expected with coherent processing either.

The K-distribution P_{FA} was been defined in Eqn. 2.39 and requires the use of both a gamma function and a modified Bessel function. For the numerical analysis completed in this work these functions were approximated using the respective inbuilt function within the program Matlab. The Matlab gamma function interpolates the integer solutions from:

$$\Gamma(n) = (n - 1)! \tag{3.3}$$

for the input variable n. The derivation of the exact methods used to evaluate the Gamma function can be found in [120]. A plot of integer solutions to Eqn. 3.3 as well as the non-interger interpolate solutions from the Matlab Gamma function for $n = 0$ to 5 in steps of 0.1 are shown in Fig. 3.15.

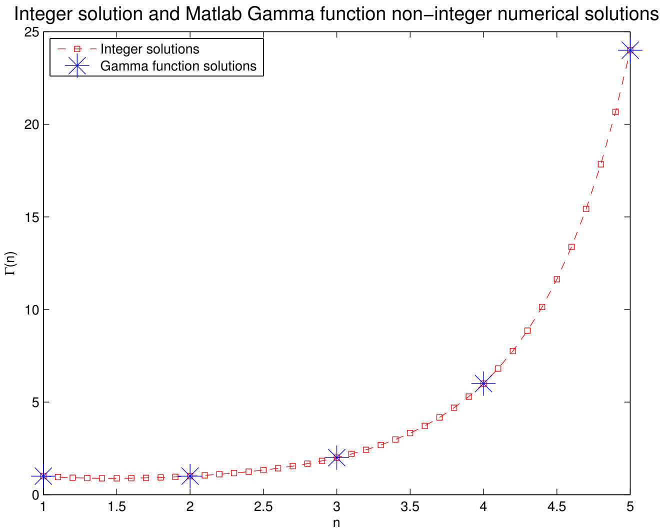

Figure 3.15: Integer solutions and Gamma function non-integer solutions to Eqn. 3.3

The Bessel function of the second kind in Matlab solves the modified Bessel differential equation [121]:

$$z^2 \frac{d^2y}{dz^2} + z\frac{dy}{dz} = (z^2 + v^2)y = 0 \tag{3.4}$$

where v is a real constant and the solution of this differential equation are named Bessel functions. The second order solution is:

$$K_\nu(z) = \left(\frac{\pi}{2}\right) \frac{I_{-\nu}(z) - I_\nu(z)}{\sin(\nu\pi)} \tag{3.5}$$

where ν is the shape parameter, and $I_\nu(z)$ and $I_-\nu(z)$ are fundamental sets of solutions to the modified Bessel equation for non-integer ν:

$$I_\nu(z) = \left(\frac{z}{2}\right)^\nu \sum_{k=0}^{\infty} \frac{\left(\frac{z^2}{4}\right)^k}{k!\Gamma(\nu + k + 1)} \tag{3.6}$$

where Γ is the Gamma function. Example plots of the numerical solutions obtained from the modified Bessel function of the 2nd order with varying shape parameter can be seen in Fig. 3.16.

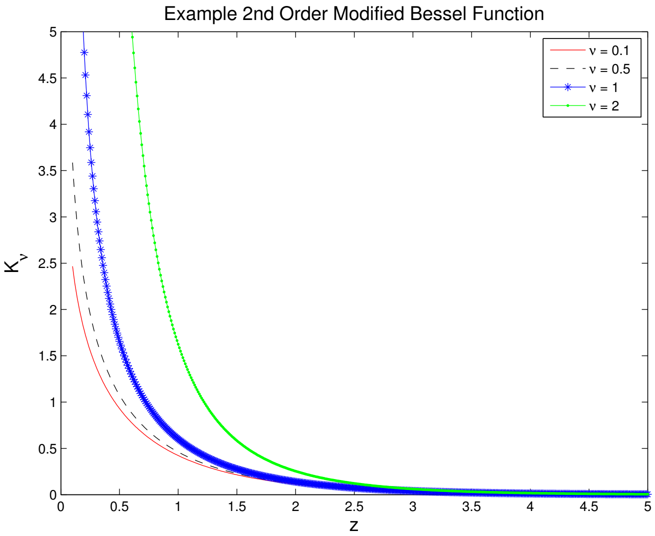

Figure 3.16: Example modified Bessel function of the second order plots

The second fitting method applied was the comparison of amplitude moments of the data with the predicted theoretic intensity moments of a model. Then the shape parameter of the data using this relationship is defined. This is called Method of Moments fitting. The relationship between the K-distribution shape parameter and the 2nd order intensity moment is defined as:

$$\nu = \frac{1}{\frac{M_2}{2} - 1} \tag{3.7}$$

where M_2 is the 2nd order intensity moments and ν is the shape parameter. Moments are defined as follows,

$$M_n = \frac{\sum \frac{X^n}{N}}{\bar{X}} \tag{3.8}$$

where n is the order of the moment, and X is the samples being evaluated and $\bar{X}$ is the mean of the samples in X.

In the case of a Gamma distribution the relationship between the Gamma shape parameter, ν_G and the 2nd order intensity moment is as follows:

$$\nu_G = \frac{1}{M_2 - 1} \tag{3.9}$$

The first three intensity moments of the K-distribution + thermal noise were previously shown in Eqn. 2.36, 2.37 and 2.38. To relate the K-distribution + thermal noise first two moments to shape parameter the following equation can be used:

$$\nu = \frac{2(M_1 - P_n)^2}{M_2 - 2M_1^2} \tag{3.10}$$

The advantage of this method is that if a simple relationship exists between the moments and shape parameter is it easy to evaluate the data shape parameter. Its disadvantage is that it does not show how close to the assumed distribution that the data is. Therefore when analysing each dataset care must be taken to evaluate if the data is well represented by the assumed distribution before using Method of Moments fitting.

Chapter 4

Data Analysis

This chapter presents extensive analysis of each dataset defined in Chapter 3. The data from each radar is first analysed using non-coherent processing, where the correlation and statistical distributions in the time domain are investigated. This validates that clutter is present with the data and quantifies its behaviour in the time domain.

This is followed by coherent processing, where the unique challenges faced in processing each dataset are initially described. Statistical analysis techniques are then applied using the methods defined in Section 3.2. The results within individual Doppler bins are defined first, this is followed by characterising the distribution as a function of Doppler in multiple datasets. Finally the characteristic behaviour of the clutter with Doppler is discussed and compared between datasets and radars.

The overall main aim of this analysis is to characterise statistically the behaviour of sea clutter as a function of Doppler within multiple dataset and radars. This characterisation will then be used to draw links between the behaviour of the clutter and the conditions of the dataset or the radar parameters used. The SW2000 data analysis provides the initial tests to establish the amplitude statistics of sea clutter in the Doppler domain. The CSIR data analysis expands this to observe how the clutter statistics change with azimuth with respect to wind and wave direction. Finally the NetRAD data analysis also provides information on clutter behaviour with look angle, but uniquely it directly relates monostatic and bistatic clutter.

During the majority of steps in the process example figures are given to demonstrate typical characteristic plots from the data. In the coherent processing initial example range-Doppler (SW2000 data) or time-Doppler (CSIR and NetRAD data) figures are provided. Due to a significant number of possible plots that can be generated only a single dataset or range gate from a data was selected to to generate the example plots for most of the stages. Plot from every dataset available were only generated for the high level statistical comparative plots, which are used to compare results between datasets and radars.

4.1 Thales SW2000 Analysis

This section describes the analysis and results obtained from the processing completed on the non-coherent and coherent SW2000 data. The non-coherent data analysis is shown first showing example distributions and detailing any variation of the statistics with range. This is followed by the coherent data analysis focusing on the variation of sea clutter statistics with Doppler.

All of the standard pre-processing methods detailed in section 3.2 were applied to the SW2000 dataset prior to the statistical analysis of the amplitude values. In addition to this pre-processing Doppler re-sampling was also completed on the coherent data.

Example results and plots from individual pulses, bursts and range gates of data are initially shown to demonstrate the characteristic values and shapes of the data. All of these were generated using a single datasets, trial 612 vertical polarisation. Following this the high level results showing the variation of the statistics with range or Doppler are then shown for both the trial 612 vertical and horizontal polarisation datasets.

4.1.1 SW2000 Non-Coherent data analysis

As detailed in the literature review section on sea clutter, section 2.5, non-coherent sea clutter has been extensively analysed in the prior research literature. Although this area of research is therefore less novel in its contribution to radar sea clutter research it does establish the characteristics of the non-coherent data. These can then be compared and contrasted with the more novel analysis of the coherent data, section 4.1.3. In addition to this the method used for fitting the non-coherent data to the assumed distributions is the same as those used for the coherent data, hence it also provides a check that these fitting methods are providing valid results within both domains.

Figure 4.1 shows a flow diagram of the major processing steps completed during the non-coherent data analysis. Examples from these processing steps completed on trial 612 vertical polarisation can be seen below. Only the final statistical results are shown for both datasets, as these are the most relevant when comparing datasets.

As previously described, section 3.2, the initial method of PDF generation from the discrete data samples used the histogram method, later a single value sampled CDF method was also applied. Both distribution characterisation methods are shown in this analysis. The amplitude values of the SW2000 non-coherent data was first analysed using the amplitude distributions from the sea clutter present within the data within a single pulse. The normalised power data, it's PDF and the P_{FA} from a single example pulse within a burst from dataset 612 vertical polarisation can be seen in Figures. 4.2, 4.3 and 4.4 respectively.

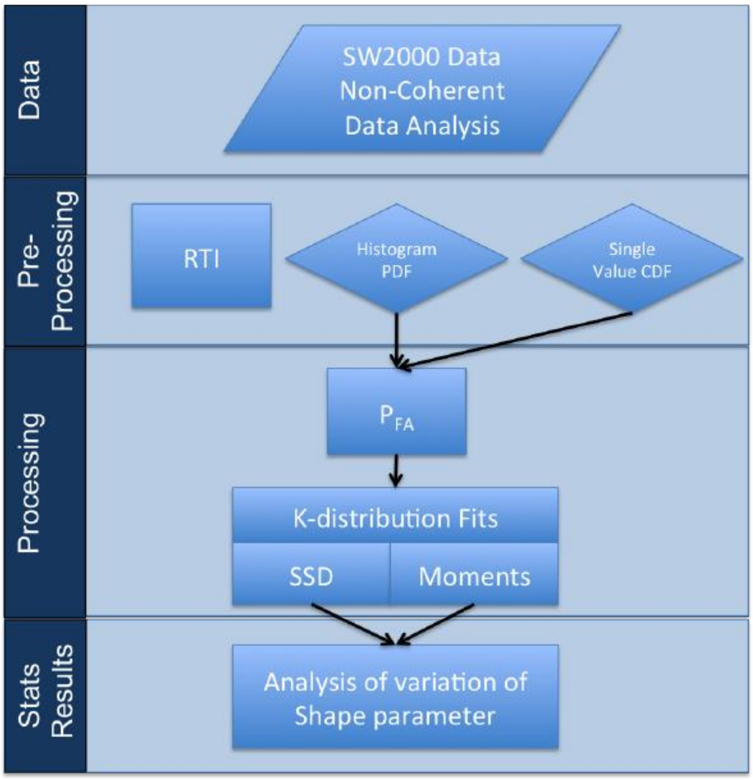

Figure 4.1: Non-coherent data analysis flow diagram

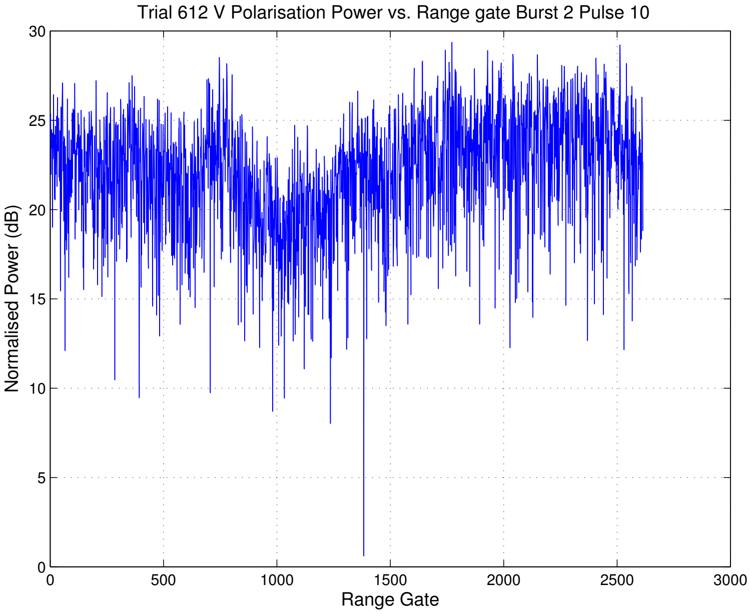

Figure 4.2: SW2000 data normlised power vs. range gate - single pulse

In Fig. 4.2 a clear reduction in the power levels exists between range gates ≈750-1250. This behaviour shows that the data is dominated by a single range ambiguity. If multiple range ambiguities were present within the data then the profile of the mean power levels would be more linear without this dip in power. This is because the sum of the multiple ambiguities would flatten out the profile removing any dip in power levels.

The single dominate ambiguity is fortunate for the analysis performed here as when selected segments of the data is it possible to confirm that the samples will be from the single ambiguity. If multiple ambiguities were present the clutter data would originate from many different ranges and this is an added complication when defining its characteristics.

As the data selected has been taken from a wide selection of range gates it is likely to be spatially non-homogenous. The behaviour of the clutter across the swath of selected data will vary and can not be considered the same. Hence the overall bulk distribution generated from these samples will be a superposition of the many varying location clutter distributions.

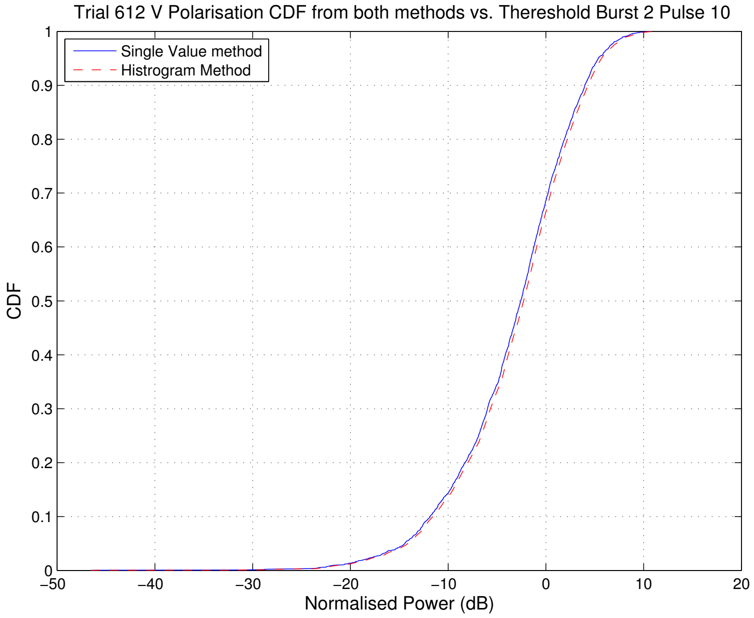

Figure 4.3: SW2000 data CDF comparison - single pulse

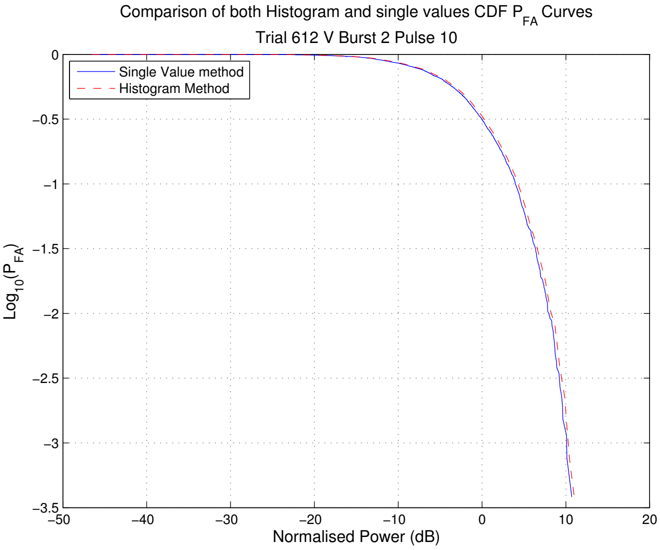

Figure 4.4: SW2000 data P_{FA} comparison - single pulse

These plots were all generated using a single pulse of data from a selected burst; as described in section 3.1.1 there is 32 pulses in each burst with each pulse having between 2500 and 3000 range gates. It is therefore possible to join 32 consecutive pulses without the need for any corrective processing to take into account any PRF or RF changes. It is possible to join multiple pulses of data without any corrective processing to produce single PDFs, CDFs and P_{FA} plots, similar to those shown from a single pulse. The joining of the data is simply concatenating the data from each selected pulse into a single array. Figures 4.5 4.6 and 4.7 show the sample number against amplitude from a joint array of 32 pulses, the joint CDF and P_{FA} respectively. All these plots were generated using the same dataset 612 V polarised.

A clear difference between the P_{FA} plots from a single pulse, Fig. 4.4, and 32 joint pulses, Fig. 4.7, is the extent to which the curves go in negative $\log(P_{FA})$. As the dataset used has 32 times more samples within it the $\log(P_{FA})$ curve is able to extend to $\approx$ -4 for the histogram method and $\approx$ -4.9 for the single sample method. Whereas in the single pulse case the $\log(P_{FA})$ curve only extended to $\approx$-3.4. This is an important extension to this $\log(P_{FA})$ curve as the area of interest for a radar engineer is the tail end of the P_{FA}. An operational radar will be specified to have a typical $\log(P_{FA})$ of *approx* -4 or less as discussed in section 4.1.2.

The single sample method is also shown to extend further into negative $\log(P_{FA})$ in comparison to the histogram method in Fig. 4.7. This is due to the nature of how this curve is defined, instead of a set range of fixed width histogram bins the single sample method used each sample location as a point on the $\log(P_{FA})$ curve. This extension in the curve is an advantage of this method, although the associated disadvantage is that the sample error increases with decreasing $\log(P_{FA})$ as less sample contributed to the curve as the low P_{FA} levels. It is the behaviour of these few large samples that is of particular interest to sea clutter research as their departure from Gaussian model predicted behaviour means predicted false alarms rates, for a given threshold, are much higher. By increasing the understanding of the large intensity samples in different conditions methods for threshold level setting can be improved.

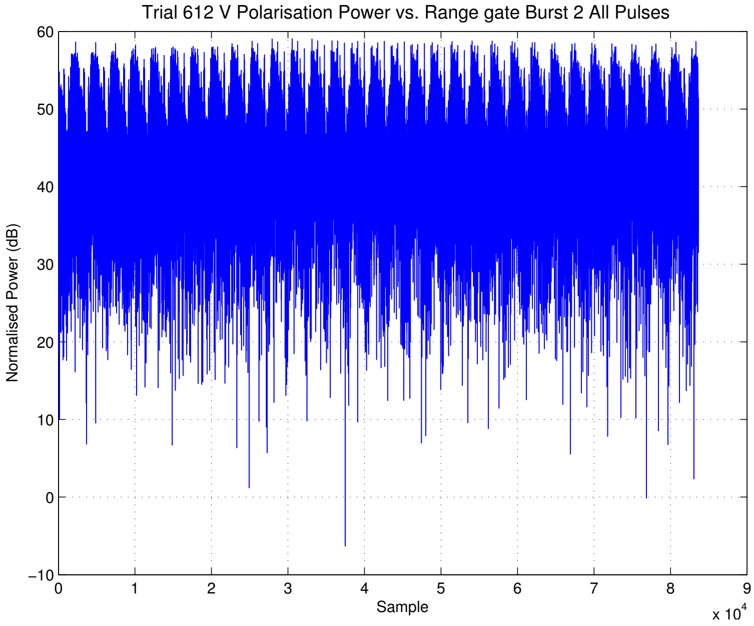

Figure 4.5: SW2000 data normlised power vs. range gate - 32 joint pulses

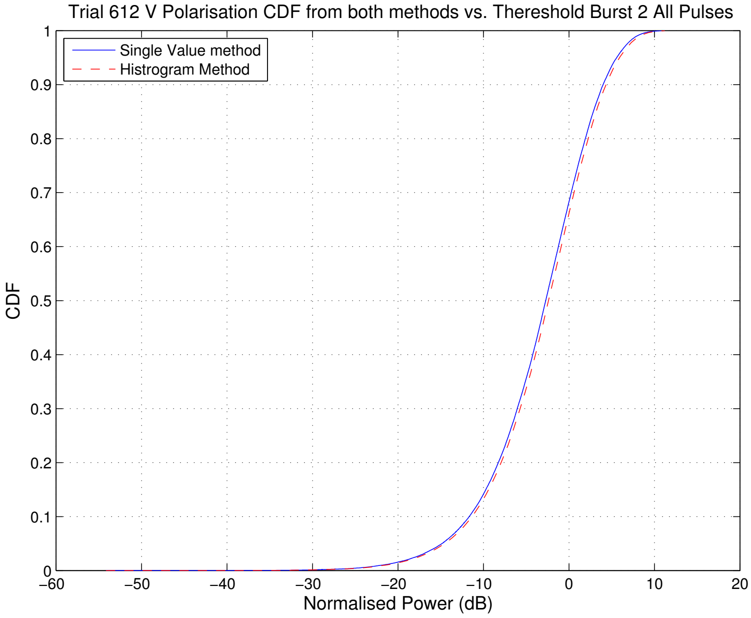

Figure 4.6: SW2000 data CDF comparison - 32 joint pulses

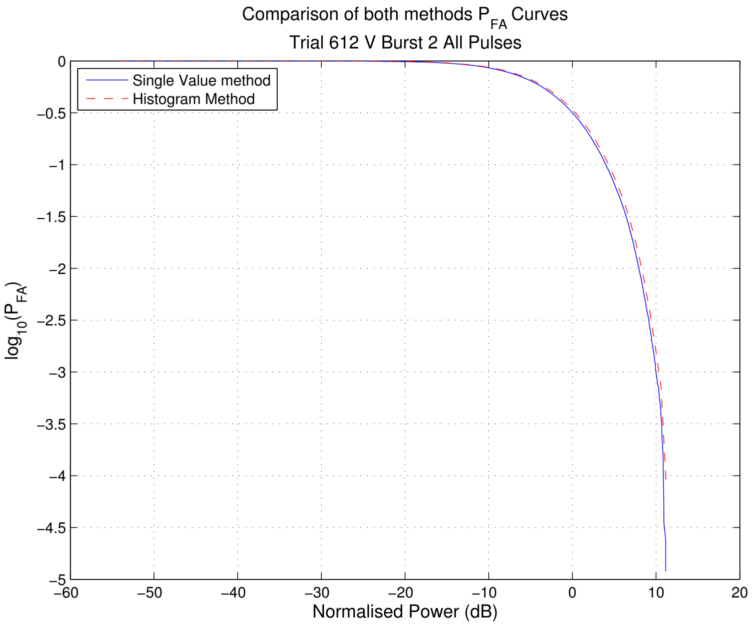

Figure 4.7: SW2000 data P_{FA} comparison - 32 joint pulses

From the data $\log(P_{FA})$ curves that were generated the K-distribution was fitted to establish the shape parameter of the clutter present within the data and how this varied within a dataset and between datasets. A SSD fit of the K-distribution to the $\log(P_{FA})$ curves generated by a single pulse and a joint distribution of 32 pulses can be seen in Fig. 4.1.1 (a) and (b) respectively. The fitted shape parameter to the single pulse was found to be 3 and the joint distribution was fitted to 2.8. The fitting was completed on the section of the positive dB component of the $\log(P_{FA})$ curve as the area of interest is the tail end of the curve. In the joint distribution fit the theoretical K-distribution curve is shown to follow the data distribution very closely up to $\approx$ 9dB. After this point the data has a lower P_{FA} level, but still maintains a close fit to the distribution except for the last value. The single pulse $\log(\mathrm{P}_{FA})$ fit also shows the K-distribution curve to follow the data distribution closely and over estimate the P_{FA} for threshold values $>$ 8dB by $\approx 0.1 \log(\mathrm{P}_{FA})$.

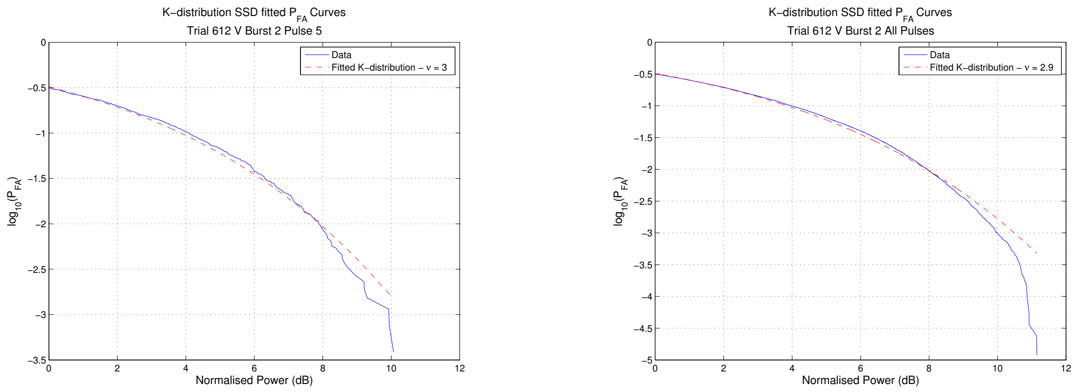

(a) (b)

Figure 4.8: SW2000 data - K-distribution SSD fitted P_{FA} - (a) Single pulse (b) 32 joint pulses

The SSD and moment fitted shape parameters from both datasets using the individual distributions of each pulse from the first 10 successive bursts of data can be seen in Fig. 4.9. The mean values from these fits are shown in Table 4.1. The horizontally polarised data is shown to have a larger value in both the SSD and moment fitted values. This disagrees with prior research showing that horizontal polarised amplitude statistics show a more spiky distribution compared to vertical polarisation. The disagreement may be due to using a too small a sample set, or because of the large increase in shape parameter shown in the fits to pulse numbers > 250 which would have significantly increased the average.

Table 4.1: Non-Coherent data Fitted shape parameters

	Mean SSD fitted ν	Mean Moment fitted ν
V pol	2.3	2.4
H pol	3.4	3.5

This shows the importance of sample group size when analysing amplitude statistics present with a dataset. The variations in shape parameter for the K-distribution only produce small differences, $\approx$ 0.3 dB, in the threshold at a log(P$_{FA}$) = -3. Although at lower shape parameter values closer to 0.1 the same absolute difference in shape parameter would produce a much more significant difference in threshold sensitivity of the order of a few dB's.

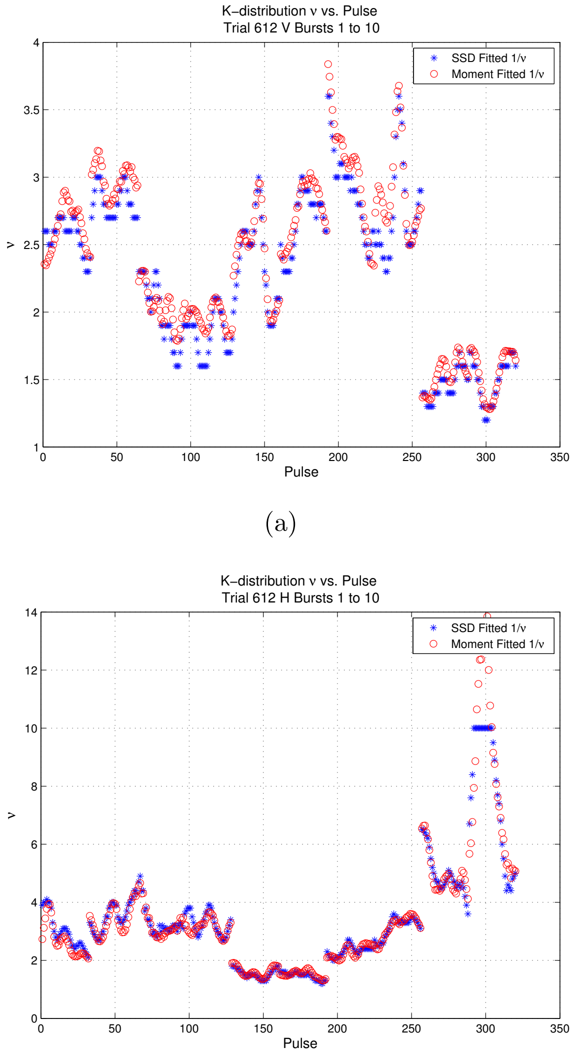

(a)

(b)

Figure 4.9: SW2000 Data - K-distribution SSD and moment fitted (a) Vertical polarisation, (b) Horizontal polarisation

The Weibull distribution was additionally fitted to the non-coherent data using the SSD method. A plot showing the Log(P_{FA}) curve of data, SSD fitted K-distribution and SSD fitted Weibull distribution can be seen in Fig. 4.10. Although the fit to the Weibull distribution looks superficially acceptable, the closest fitting Weibull log(P_{FA}) curve was found to have an average square difference of 66 dB^2 per sample in comparison to 0.56 dB^2 for the K-distribution. This result was calculated by averaging the SSD values for the fitted distribution for each pulse in the first burst of the Trial 612 V polarisation dataset. It clearly shows that the K-distribution represents the amplitude statistics of the sea clutter present much more closely, and that the difference in this goodness of fit is significant. Therefore the Weibull distribution was not fitted to any further non-coherent SW2000 data.

Figure 4.10 states normalised power on the x-axis. This is because the data was normalised with respect to the mean of the power, such that 0dB is the mean. Data from these distributions does exist at values below 0dB but throughout this thesis the plots will only show 0dB onwards. This is because the study of sea clutter has particular interest in the behaviour of the tail end of the clutter distributions. By fitting and studying from the mean 0dB onwards this focuses the analysis on the component of the data that is of interest to this research.

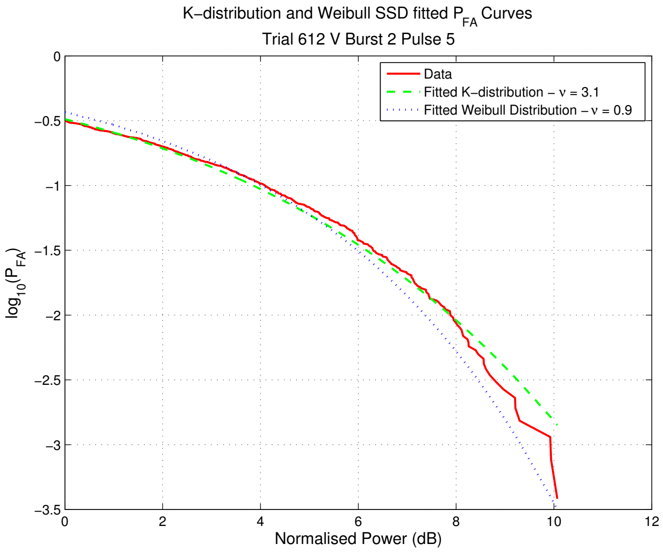

Figure 4.10: SW2000 data - K-distribution and Weibull Distribution SSD fitted P_{FA} - Burst 2 Pulse 5

Analysis using additional distributions was not performed on the SW2000 data as the CSIR and NetRAD datasets are from instrumented radar systems that are more suited to the study of sea clutter data. Hence the characterisation of the clutter with multiple distributions is will be completed with these other datasets. The SW2000 data issues of RF and PRF agility as well as a rotating airborne antenna mean that the characterisation of sea clutter statistical behaviour with weather, sea or geometry conditions (except changes in polarisation) are very difficult and sub optimal.

4.1.2 PRF resampling

In this section the methods applied specifically to the SW2000 data to correct for the agile PRF between pulses prior to producing joint distributions from multiple bursts of data are described.

To perform valid analysis of sea clutter statistics significant quantities of samples are required. To ensure that a sufficient data is used to generate a representative distribution it was required to join consecutive pulses into a single distribution. The key issue with joining multiple bursts when using the SW2000 data is the agility of the PRF. The agility of the PRF means that within the Doppler domain the dynamic range of the Doppler spectra as well as the sample locations of the Doppler bins are not equal when comparing bursts of data. To overcome this, a method was used to resample the data and limit the unambiguous dynamic range of the Doppler to the lowest PRF. This made it possible to join the Doppler samples from multiple bursts, and generate distributions of the amplitude statistics within each Doppler bin with an order of magnitude more samples.

The data recorded using the SW2000 radar is also RF agile between bursts of pulses. This agility could potentially effect the statistics of each burst as the RF emissions with different frequency interact with the sea surface in a different way. For this research it is assumed that the relatively small shift in frequency has an insignificant affect on the statistics of the individual bursts. This is deemed a valid assumption as the shift in frequency is a small fraction of the main frequency of the radar $\approx$ 9GHz and therefore will not affect the amplitude statistics of the clutter returns significantly. Using this assumption it is possible to then concatenate adjacent bursts (with different RF) to obtain enough samples to complete a valid statistics characterisation. If this assumption was not used it would introduce significant delays between bursts that could be selected as every Nth burst with the same frequency could only be used when joining the data. The introduction of this delay between selected bursts would influence the characterisation of the data, due to the mechanically steered antenna, every Nth burst will be significantly separated spatially.

Maritime radars are required to operate with a give specified false alarm rates that are caused by sea clutter returns. An acceptable rate for a coherent maritime radar would be of the order of 1x10^{-4}, meaning that 1 in every 10,000 returns produce a false alarm. If an radar system has 2000 range gates and operates at 3kHz a false would be required to occur every 5 bursts which is 1 every 0.0017 seconds. To characterise the P_{FA} curves of the statistics of the clutter present at least 10 samples at the 1x10^{-4} level are required, meaning 10^5 samples. If it is assumed that 2000 range gates can be selected from each burst this requires 50 bursts of data to be joined to produce a single P_{FA} distribution.

The lowest PRF data has the smallest unambiguous Doppler spectra width and the finest Doppler resolution. As the unambiguous Doppler range is directly proportional to the PRF and there is the same number of pulses within each given PRF. Therefore the same number of samples cover a smaller dynamic range in Doppler giving a finer Doppler resolution. To correct the Doppler spectra of each group of pulses with a given PRF the dynamic range of all the spectra produced was limited to that of the smallest PRF. Then the samples within that limited Doppler spectra were interpolated onto a uniform grid with the same sample locations as the highest PRF spectra. This can be seen in Fig 4.11 where in part (A) the low PRF data is interpolated and in (B) the high PRF data has its Doppler dynamic range limited. The resulting spectra can then be directly compared with one another and therefore joined to allow for the production of probability distributions from each corresponding uniform Doppler bins.

The interpolation used on each of the lower PRF bursts was a 2D spline interpolation on the amplitude values of the range Doppler data. The interpolation algorithm took the input values within each range gates Doppler spectra and evaluated the interpolated value at a fixed uniform Doppler sampling grid that all bursts have been interpolated onto.

The disadvantage of this processing is that the Doppler dynamic range is limited by the lowest PRF, and the resolution is limited to the length of the shortest burst, i.e. that with the highest PRF. The down sampling method is still used instead of up sampling because the generation of artefacts can be reduced in down sampling in comparison to possible generation of artefacts when generating new sampling locations in Doppler.

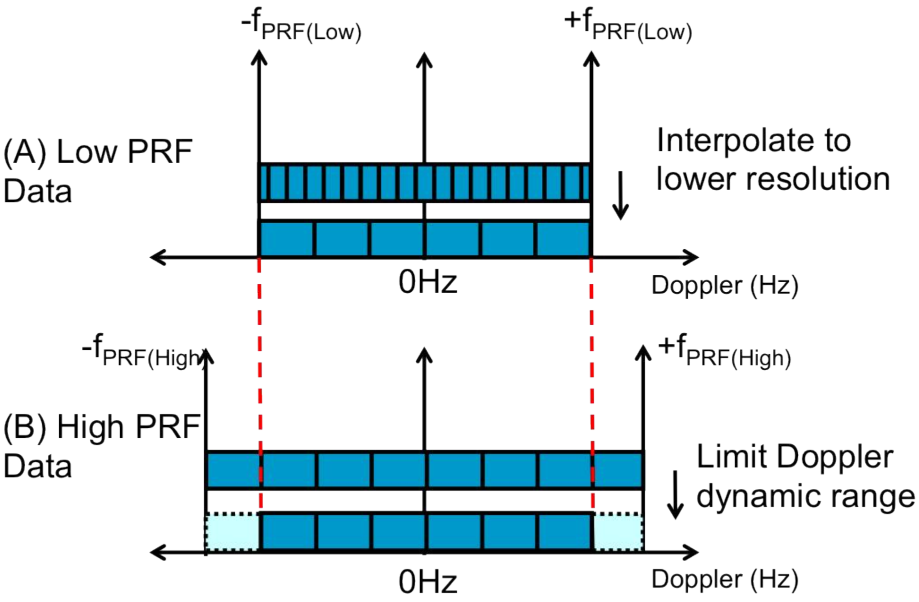

Figure 4.11: Resampling in Doppler domain diagram

The key reason for this PRF resampling is to combine multiple consecutive bursts of data. When doing this the assumption is made that the sea clutter statistics are at some level consistent from burst to burst. This is believed to be a legitimate assumption for a limited number of bursts. As the SW2000 recordings were made with a rotating antenna the patch of sea that is being accumulated to produce a single observed distribution grows with each burst added. The limitation of joining the bursts will be when the antenna has significantly changed angle with respect to factors such as swell, and wind direction. This is dependent on the rotational rate of the mechanically steered radar, hence pulse groups were not collected from a significant number of bursts that cover a large cross range physical area that has a substantial change in azimuth angle across it's width.

4.1.3 SW2000 Data Doppler Analysis

The statistical analysis performed on the coherent SW2000 radar data is reviewed in this section. The Doppler data was generated using the pre-processing techniques described within section 3.2, then similar statistical analysis seen in the non-coherent analysis section have been applied. Example plots of distributions and fits are shown only for the Trial 612 V polarisation. While the results showing the variation of the amplitude statistics as a function of Doppler are shown from both datasets. The key processing steps of the analysis completed in this section have been summarised in Fig. 4.12.

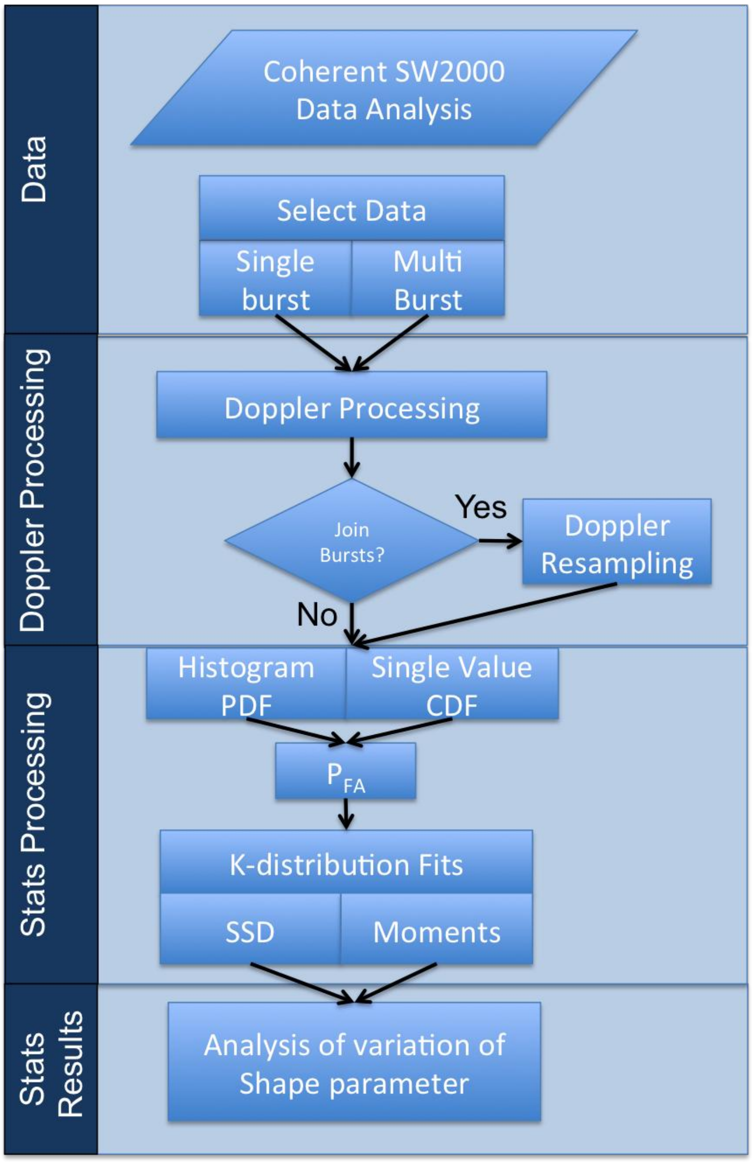

Figure 4.12: Coherent data analysis flow diagram

The Doppler pre-processing applied to the data gave complex range Doppler data from each burst, an example range-Doppler normalised power plot is shown in Fig. 4.13. The central Doppler sea clutter column is shown to extend from ≈ -200 to +350

Hz, outside of this region the data is shown to be thermally noise dominated. This demonstrates clearly the difficulty of detecting slow moving targets within the maritime environment. Fast moving targets with Doppler shifts in the noise dominated region can be easily detected, as the detection of the target return is only limited by the noise floor of the system. Whereas in the clutter dominated region there is an increase of up to ≈ 50 dB in interference from the clutter which could easily result in a missed detection.

The length of the FFT used was 32 points, this was selected mainly due to the PRF agility. The additional reason for this short length FFT was because a shorter length FFT captures the quick changing affects within the clutter spectra and results in more samples per Doppler bin for amplitude statistics analysis.

Note that the CNR and K-distribution shape parameter estimates from the non-coherent data are approximately what would be expected. Therefore this data can be assumed to be atypical example sea clutter measurements. Using this assumption it is possible to infer that the new novel Doppler results reported here, regarding the statistics, can be thought of as broadly typical for sea clutter. Although through the use of further dataset the characterisation and variation in the behaviour is explored further.

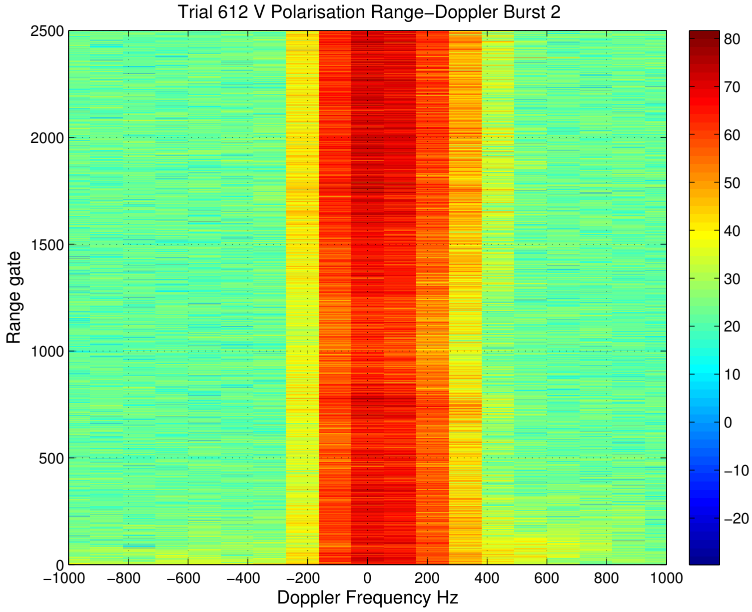

Figure 4.13: SW2000 data range-Doppler burst 2

Figure 4.13 shows that the clutter spectra has an approximately fixed mean width and CNR which do not vary significantly with range. The structure of the individual clutter spectra appear to be a single Gaussian, each with small variations in width, CNR and centre of gravity. The 32 point FFT gives a low resolution for characterising the detail of the individual Doppler spectra, but the compromise on this resolution is counterbalanced by the quantity of samples needed to produce the spectra.

The clutter spectra shown has maintains a bulk central structure with no discernible fast moving components. Additional trials with the ARTIST system observing sea clutter show fast moving individual components that may be attributed to sea clutter, [122]. These are not present here and the spectra is shown to be much more predictable. There is some departure from the main body of the clutter spectra in the lower range gates, 0-300, on the positive Doppler side of the spectra. This isn't small individual components though and doesn't show similar characteristics to the effects seen in [122].

In addition to Fig. 4.13 a plot of multiple overlaid Doppler spectra of 20 adjacent range gates, 1001 to 1020, is shown in Fig. 4.14. This demonstrates the consistency of the single Gaussian structure of the clutter spectra from range gate to range gate, as well as the consistency noise floor level. The sample locations of each of the spectra differ due to the PRF agility but qualitative observations of each PSD is still valid, see section 4.1.2.

These observations differ in some degree from the D. Walker measurements and model, [22,24], which uses a three component Gaussian form for the sea clutter. The difference may be due to the Doppler resolution of this data, which may limit the ability to observe the independent components within the Doppler PSD. A small number of the spectra do shift their central Doppler frequency, which may be an additional fast moving Gaussian component being present or a shift of the total single Gaussian spectra itself.

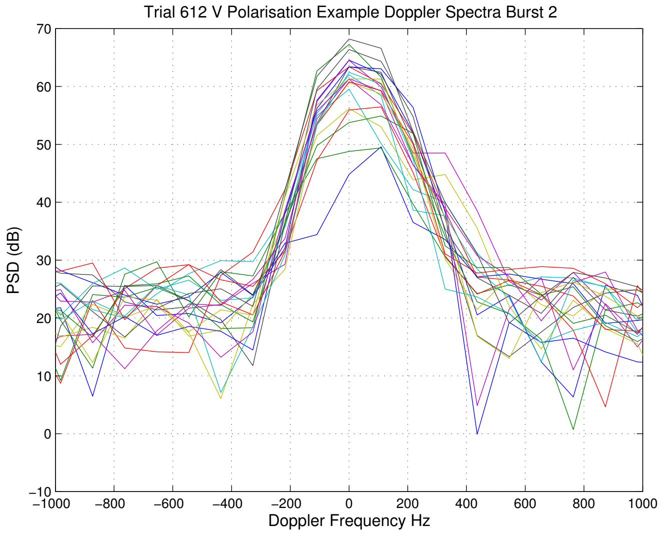

Figure 4.14: SW2000 data - 20 example Doppler spectra burst 2

It is the characterisation of the sea clutter amplitudes statistics as a function of Doppler that is of critical importance for the effective operation of coherent maritime radars. Figure 4.13 shows the increase in power of the sea clutter within the central Doppler bins, but it does not give any information on changes in the statistics behaviour of the clutter as a function of Doppler. To characterise the amplitude statistics as a function of Doppler the same methods used on the non-coherent data in Section 4.1.1 have been applied. The $\log(P_{FA})$ curves have been evaluated using the amplitude values within each Doppler bin, then SSD fitted to the K-distribution.

The data and SSD fitted curves from two example Doppler bins that are clearly sea clutter dominated can be seen in Fig. 4.15. The two plots show that the amplitude statistics of the data within these two Doppler bins is well represented by the K-distribution. An important difference between the two plots is the significant change in the K-distribution shape parameter despite the Doppler bins being adjacent, from $\nu = 2$ in Doppler bin 19 and $\nu = 0.7$ in Doppler bin 20. This shows that the amplitude statistics for the clutter clearly change from one Doppler bin to another and that the change can be dramatic. This is an important novel discovery of the variation of the sea clutter amplitudes statistics and the following work aims to characterise this variation further.

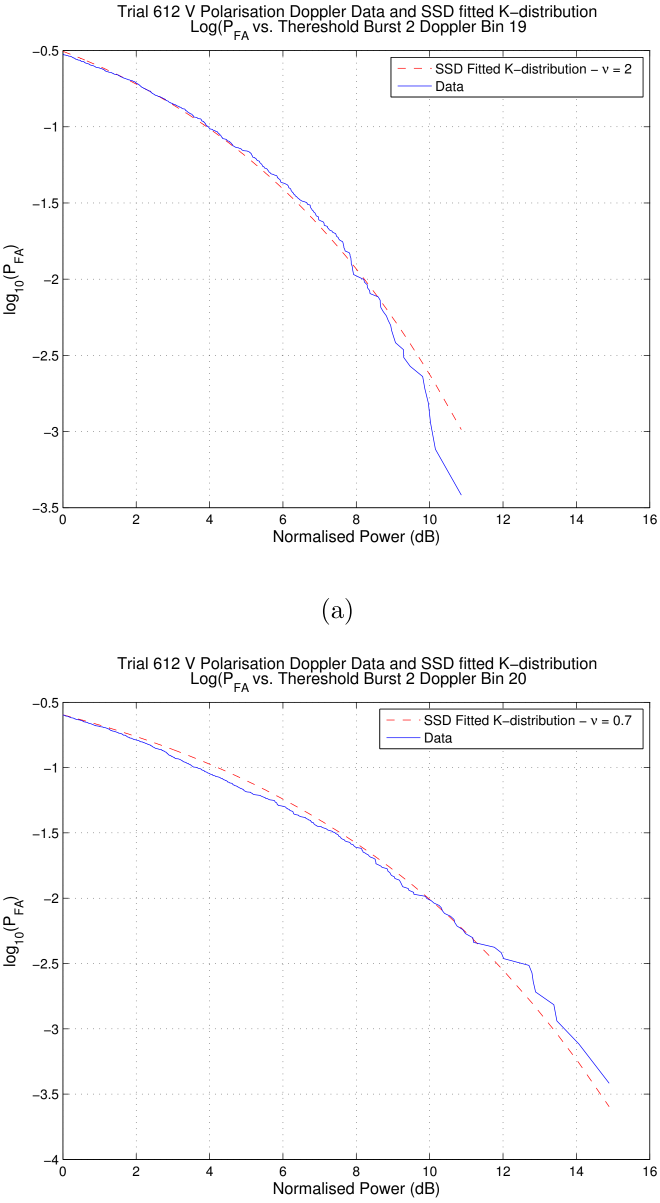

(a)

(b)

Figure 4.15: SW2000 data - Doppler burst 2 - log(P_{FA}) vs. threshold (dB) and K-distribution SSD fitted curve (a) Doppler bin 19, (b) Doppler bin 20

The SSD fitted log(P_{FA}) curves from the noise dominated section of the Doppler spectra did not show the expected shape parameters, which for thermal noise tend towards infinity but as the SSD fitting method uses a maximum possible ν of 100 the outer Doppler bins should be fitted to 100. Figure 4.16 shows Doppler bin 5 fitted and its SSD fitted K-distribution curve. This figure is unlike the previous two Doppler bin plots, Fig. 4.15, as the data distribution is not well represented by the closest fitting K-distribution, which was in fact a very spiky value of 0.3. The data log(P_{FA}) curve has a uncharacteristic concave shape, for thermal noise, which shows that the data from this Doppler bin does not contain just thermal noise. Additional outer Doppler bins that should have been thermally noise dominated showed similar non-thermal noise behaviour. The interference within these Doppler bins removed the ability to effectively compare the sea clutter amplitude distributions with the outer Doppler bins.

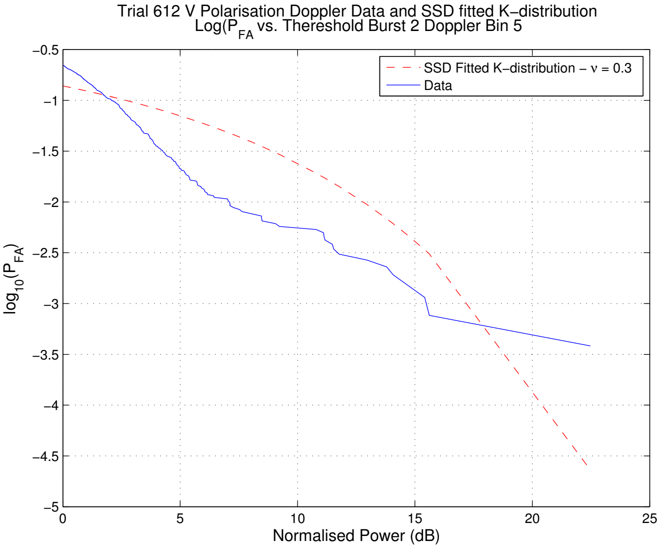

Figure 4.16: SW2000 data - Doppler burst 2 - log(P_{FA}) vs. threshold (dB) and K-distribution SSD fitted curve Doppler bin 5

Further observations of the range-Doppler plots of the data from this burst showed interference in the outer Doppler bins within the first ≈ 500 range gates. By removing the data from these range gates the outer Doppler bin amplitude distributions then displayed the expected thermal noise limited characteristics, and fitted to the largest shape parameter available in the fitting process, 100, see Fig. 4.17.

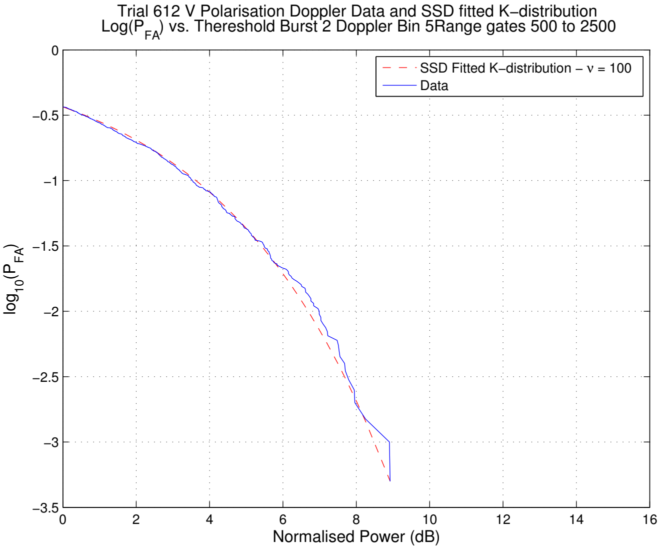

Figure 4.17: SW2000 data - Doppler burst 2 - log(P_{FA}) vs. threshold and K-distribution SSD fitted curve Doppler bin 5 - range gates 500 to 2500

This range gate selection was then applied to the data across all Doppler bins to allow for the comparison of the SSD and moment fitted shape parameters as a function of Doppler bin. The inverse shape parameter obtained from SSD fitting to the range gate limited data across each Doppler bin from burst a single burst can be seen in Fig. 4.18. The average Doppler power from the range gate limited data is also plotted along side the inverse shape parameter to allow a comparison of where the clutter power is in comparison to the changes in statistics. The inverse value of the SSD fitted ν values was plotted as this gives a clearer visual representation of the variation in shape parameter than plotting the ν value itself. For consistency, throughout the rest of the analysis included the standard representation will be the inverse fitted shape parameters, unless otherwise stated. The maximum values possible for the inverse shape parameter through SSD fitting is 10 due to the fixed grid of tested solutions having a minimum of $\nu = 0.1$, see Section 3.2.3.

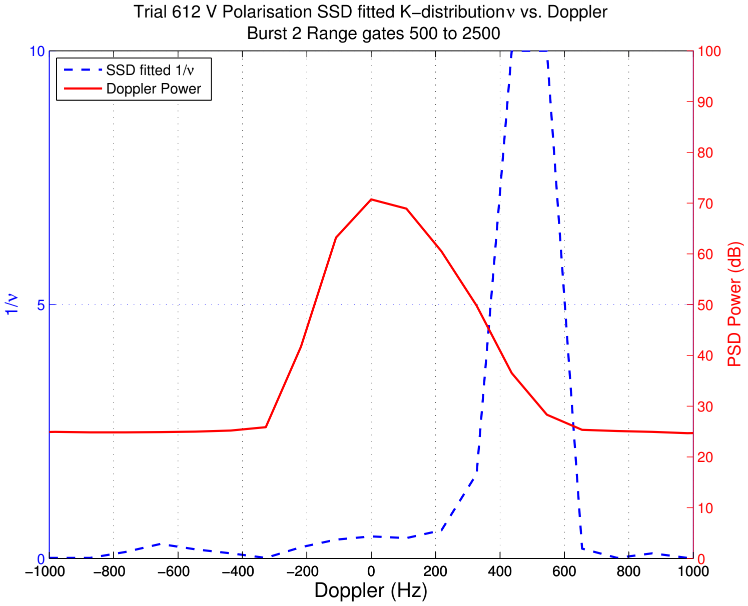

Figure 4.18: SW2000 data - Doppler burst 2 - SSD fitted $\frac{1}{\nu}$ vs. Doppler - range gates 500 to 2500

In Fig. 4.18 the SSD fitted inverse shape parameters were shown to increase to a maximum of 10 ($\nu = 0.1$) on the leading possible Doppler edge of the clutter spectra present. This marked increase in shape parameter was found to only occur at this frequency within the spectrum. In comparison at the peak CNR only a relatively small increase in the $1/\nu$ was shown. This is a very important result for coherent sea clutter analysis. Firstly the clutter clearly shows a marked variation in its amplitude statistics as a function of Doppler which would effect greatly any CFAR algorithms operating on this Doppler data. Secondly the most spiky amplitude distribution was shown not to be at the peak of the clutter power, but offsest at the leading Doppler edge of the clutter. A plot comparing the two SSD fitted theoretical K-distribution curves at the maximum CNR, $\nu = 2.3$, and the max $1/\nu$ can be seen in Fig. 4.19. The difference in threshold required to produce a false alarm rate of 10^{-2} between the two distributions is significant, $\approx$ 4.6dB. If the clutter statistics at the peak CNR were assumed across the Doppler distribution then a marked increase in false alarms would be obtain in the peak $1/\nu$ Doppler bins, a shift from log(P_{FA}) from -2 to -1.425 in this example.

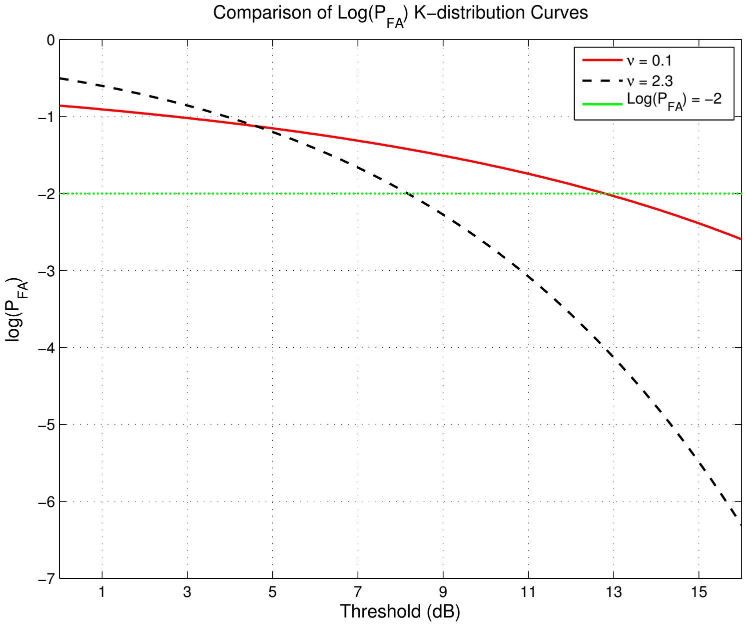

Figure 4.19: K-distribution log(P_{FA}) vs. threshold for $\nu = 2.3$ and $\nu = 0.1$

The variation of shape parameter with Doppler, seen in Fig. 4.18, was repeated for consecutive bursts of data to analyse the consistency of the observed characteristic variation with Doppler. It is important to define whether the phenomenon of the variation of statistics is seen within multiple bursts and the extend of variation between bursts and datasets. The extent to which valid information is gained by producing joined distributions from multiple bursts can also be established by analysing the variation of statistics from individual bursts. This was tested by plotting both the average power and inverse SSD fitted ν values from bursts 1 to 10 in Fig. 4.20. The average power is shown to be consistent in shape, a single Gaussian, and peak CNR, $\approx$ 45 dB, over the 10 bursts of data shown. The inverse shape parameter from all bursts showed the same increase centred around 500 Hz, located on the leading positive Doppler edge of the clutter spectra. On the negative Doppler side of the spectra 4 of the 10 bursts exhibited a marked increase in the inverse ν value located around $\approx$ -500 Hz. As well as this a clear sloped increase in the inverse shape parameter is centred around the peak of the CNR at 0 Hz. The variation of shape parameters evaluated at 0 Hz ranged from $\nu = 1.2$ to $\nu = 2.6$.

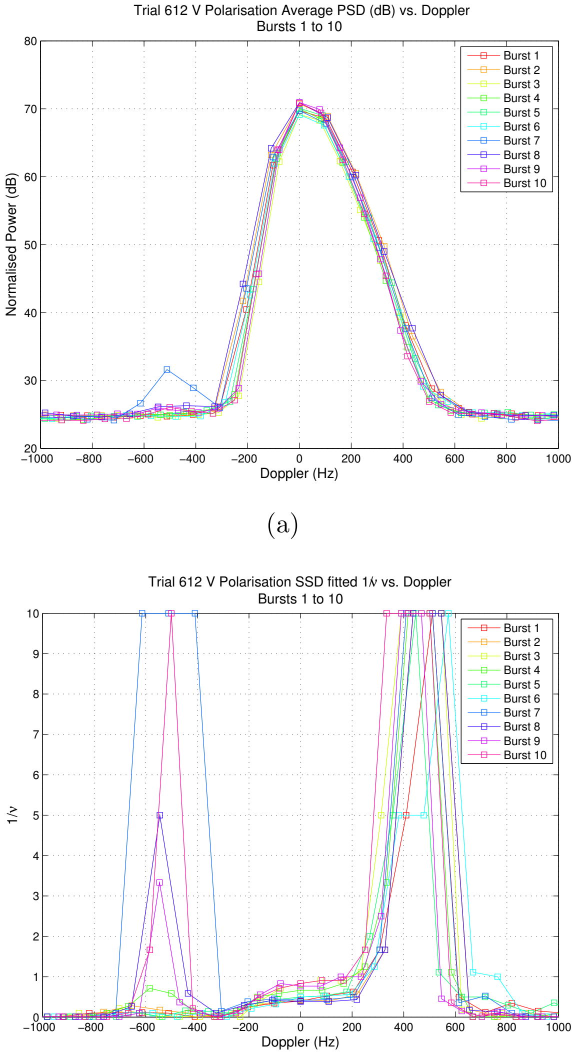

(a)

(b)

Figure 4.20: SW2000 data - trial 612 V pol - Doppler bursts 1 to 10 - (a) Average PSD vs. Doppler (dB), (b) SSD fitted $1/\nu$ vs. Doppler

This analysis was repeated for the trial 612 horizontal polarised data, using the same processing methods. The resulting average power and $1/\nu$ plotted against Doppler from bursts 1 to 10 are shown in Fig. 4.21. The averaged power spectra show a CNR that is comparable, but slightly less at 40 dB, than the vertically polarised data. The inverse shape parameter results confirm that the consistently spiky section of the Doppler spectra is focused on the leading positive edge of the clutter distribution at ≈+500 Hz within the horizontal data also. The negative Doppler side of the spectrum shows much more variation in its distribution characteristics in comparison to the vertical polarised results in Fig 4.20 (b). High inverse shape parameter values exist at frequencies well into the thermal noise floor of the Doppler spectra, these are likely to be caused by effects other than sea clutter. A small number of high amplitude returns from small targets would alter the statistics greatly in a thermal noise dominated Doppler bin, an effect that is discussed later in this section.

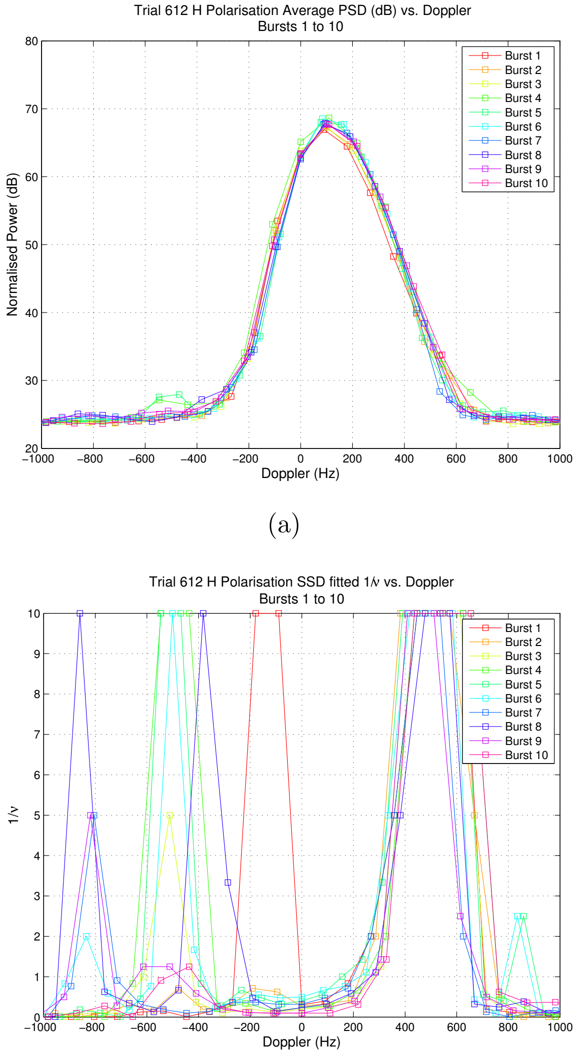

(a)

(b)

Figure 4.21: SW2000 data - trial 612 H pol - Doppler bursts 1 to 10 - (a) Average PSD vs. Doppler (dB), (b) SSD fitted $1/\nu$ vs. Doppler

As previously discussed, due to PRF agility each burst is sampled at slightly different locations in Doppler. This therefore makes a direct comparison of the statistics at a given exact Doppler frequency impossible. Despite this before resampling is applied it has still been possible to qualitatively compare the general structure observed within the Doppler spectra of each burst, see Fig. 4.20 and 4.21.

The next step in the analysis was undertaken to overcome the difference in sample locations for each burst, see section 4.1.2. After this processing a single distribution can be generated for each Doppler bin by joining multiple bursts of data. This allows a single characterisation of the variation in $1/\nu$ with Doppler using a much greater number of samples. The first 10 bursts were joined using these techniques and Fig. 4.22 shows the resulting average PSD (dB) and SSD fitted inverse shape parameter. The inverse shape parameter increased at both $\pm \approx 500$ Hz, with the positive Doppler edge increasing to 5 and the negative Doppler increasing to 10.

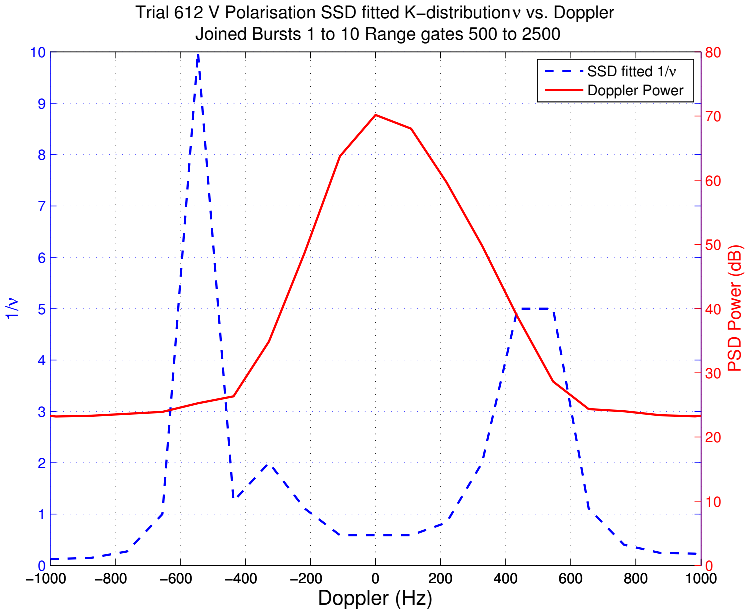

Figure 4.22: SW2000 data - trial 612 V pol - joint distribution bursts 1 to 10 average PSD and SSD fitted K-distribution vs. Doppler

The moment fitting method was then also applied to the same joint distribution generated from bursts 1 to 10, Fig. 4.23 (a). This fitting method gave extreme values for the inverse shape parameter, peaking at $1/\nu \approx 150$, that disagreed with the SSD fitted results and are well above the possible solutions for the K-distribution. This issue was resolved by removing the 5 largest amplitude samples within each Doppler bin prior to evaluating the moments within each Doppler bin. The removal of 5 samples from the total set of 20,010 (2001 x 10 bursts) in each Doppler bin made a significant difference to the moment fitted shape parameters, see Fig. 4.23 (b), but only reduced the size of the dataset analysed by 0.0002498%. These samples were therefore almost certainly either interference from other radars or small targets, which were too weak to be visible in the power spectrum but had a considerable effect on the CDF. These assumption make it valid to remove these data points to ensure the analysis performed is focused on sea clutter and not other external effects.

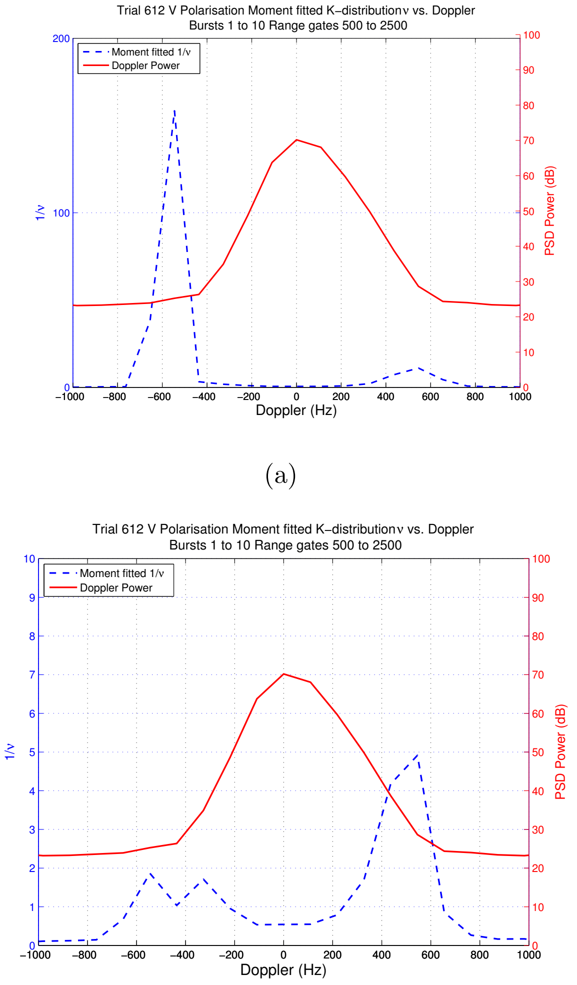

(a)

(b)

Figure 4.23: SW2000 data - trial 612 V pol - joint distribution bursts 1 to 10 average PSD and moment fitted K-distribution vs. Doppler (a) All samples (b) 5 largest amplitude samples removed

The same reduced size dataset from each Doppler bin was then processed using the SSD method to allow for a direct comparison of the variation of the inverse shape parameter, for both H and V polarisation Fig. 4.24 and 4.25 respectively. These two plots shows that the SSD and moment fitting method closely agreed on the best fitting shape parameter K-distribution curve. With the exception of a single Doppler bin in Fig. 4.24 where the SSD fit gave a fit value of $1/\nu = 10$ and the moment fit gave 1.86. The dual peak shown in the negative doppler region of -650 to -200 Hz may be indicating a multiple Gaussian structure within the faster moving components moving out of the main Gaussian causing increased spiky distributions at these locations.

The inverse shape parameter axis was limited to a maximum of 10 for Fig. 4.25 despite the moment fitted parameters taking values greater than this. The axis were limited to allow for a direct comparison between datasets and the real limit on the values $1/\nu$ can take is 10. The two Doppler bins that the moment $1/\nu$ values were greater than 10 were 17, $1/\nu = 21.8$, and 18, $1/\nu = 11.2$.

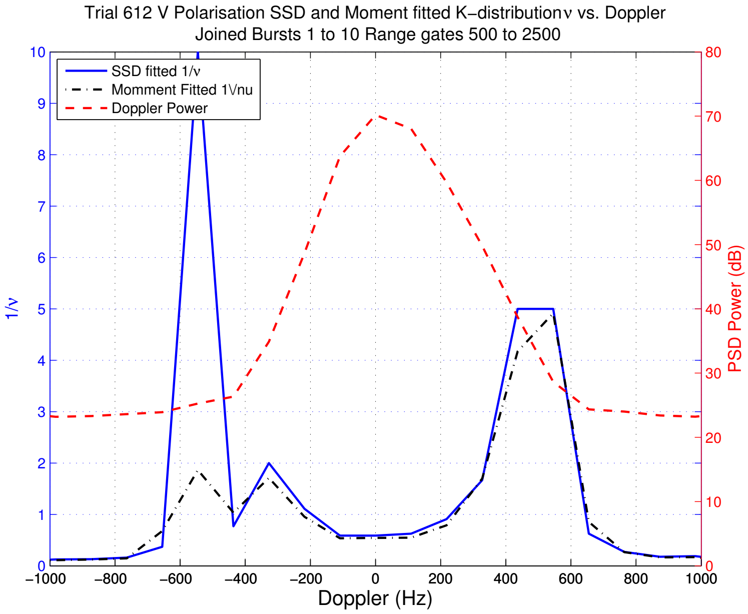

Figure 4.24: SW2000 data - trial 612 V pol - joint distribution Bursts 1 to 10 average PSD and SSD and moment fitted K-distribution vs. Doppler - top 5 samples removed

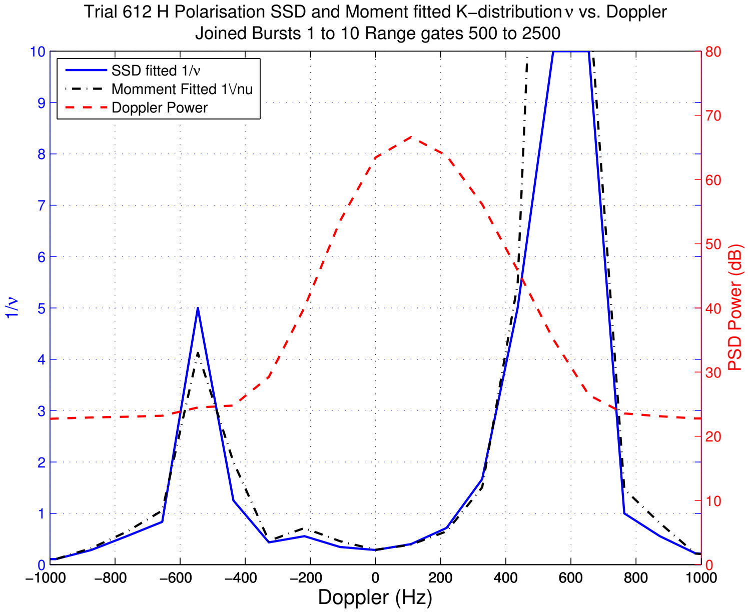

Figure 4.25: SW2000 Data - trial 612 H pol - joint distribution bursts 1 to 10 average PSD and SSD and moment fitted K-distribution vs. Doppler - top 5 samples removed

4.1.4 SW2000 Data Analysis Summary

The analysis of the SW2000 dataset has shown that the sea clutter present in the non-coherent time series domain is a good fit to the K-distribution. The shape parameter from adjacent pulses were shown to oscillate within a range of ± 2.5 in the vertical polarised data and ±4 for the horizontal polarised data with exception of outlier values. The vertically polarised dataset was shown to have more spiky (small ν) values than the horizontally polarised data. This disagrees with accepted prior research on the statistical comparison between the two polarisations which shows that the horizontal polarised data is on average more spiky. The reason for this may be due to the outlier values produced by a small subset of the pulses averaged.

It will be shown below that the for coherently-processed data, the clutter in individual Doppler bins is generally more spiky in horizontal than in vertical polarisation, the same as is seen with incoherent processing. Since the general values of the incoherent shape parameters and the clutter power levels are compatible with the values which would be expected, the ratios of the values observed with the coherently-processed data may be assumed to be statistical outliers

The fit of the Weibull distribution to the data was additionally tested, and was shown to fail to represent the data sufficiently well.

Both the histogram and single values CDF distribution methods have been used to produce discretely sampled log(P_{FA}) against threshold graphs. It has been shown that the single values CDF distribution methods produced more detailed quantitative representations of the data at the tail end of the distributions. Due to this all further analysis on the additional radar datasets uses only the single CDF method to represent the log(P_{FA}) curves of the data.

Once the very small number of examples or targets or interference have been removed, the coherent statistical analysis of the SW2000 data showed that the outer Doppler bins are noise limited. The Doppler bins with clutter present, from a low CNR to the peak CNR, fitted well to the K-distribution using both SSD and moment fitting methods which agreed closely with each other.

In the single burst analysis the characteristics of the variation of shape against Doppler bin was shown to be consistent from successive bursts. The variation showed a consistent increase in the inverse shape parameter on the leading positive Doppler edge of the clutter in both horizontal and vertical polarisation. The vertical polarisation exhibited fluctuating spiky statistics on the negative Doppler edge of the clutter spectrum at the location where the CNR entered the noise floor. In the case of the horizontally polarised data the spiky component fluctuated in its existence as well as location in negative Doppler.

The analysis of the coherent data using joint bursts was made possible because of the PRF resampling interpolations applied. This method ensured that it was viable to generate single distributions for each Doppler bin using multiple bursts of data. This allowed the tail of the distributions present to be evaluated at significantly lower P_{FA} levels. The results from the joint bursts distributions showed that the vertical polarisation was less spiky than the horizontal ($1/\nu = 5$ and $1/\nu = 10$ respectively) at the consistently spiky positive Doppler edge. Unlike the non-coherent statistical results this agrees with the prior research on the comparison of the average spikiness between vertical and horizontal polarisation.

The key result within the SW2000 data analysis is that a significant variation in statistics of the sea clutter across the Doppler spectrum exists. This variation has been shown to be consistent across multiple bursts of data, and present within two separately recorded and differently polarised datasets. This shows that the variation with Doppler is a real phenomena related to sea clutter, that is repeatable and possible to characterise. Without compensating for this variation detection algorithms using an assumed distribution will generate large numbers of false alarms potentially overloading any tracking processing. This is shown in the example comparing the fitted distributions from the peak CNR and peak $1/\nu$ distributions at a given false alarm, Fig. 4.19. This comparison produces a significant difference in threshold, -4.6 dB, for the given example false alarm level of $\log(P_{FA})$ = -2.

4.2 CSIR Results

This section details the analysis and results from the selected CSIR 2007 Signal Hill sea clutter datasets, 07, 10, 12 and 15, which are detailed in Section 3.1.2. The first part of the work discusses the non-coherent time series data analysis, which qualitatively compares each datasets Range Time Intensity (RTI) plots and investigates the temporal correlation properties of the time series data. This is followed by the Doppler analysis which reproduces the Doppler-time spectrograms from each dataset and goes on to quantify the amplitude statistics within each Doppler bin and how these vary with Doppler and dataset.

4.2.1 CSIR Non-Coherent Data Analysis

The data was initially investigated to establish whether sea clutter was present and the general statistical and temporal characteristics of the clutter, before further coherent analysis was completed. Figure 4.26 shows a flow diagram describing the key steps in the CSIR non-coherent data analysis.

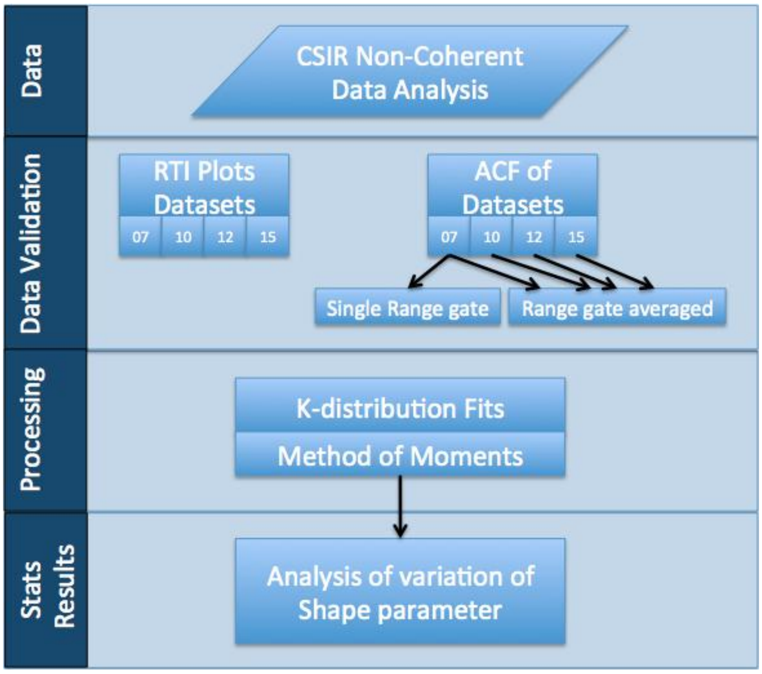

Figure 4.26: Non-coherent data analysis flow diagram

The RTI plots from the four selected datasets can be seen in Fig. 4.27, 4.28, 4.29 and 4.30. These figures show the clear large scale structure of the sea surface and the progression of waves through the range gates over the period of recording, ≈ 30 seconds.

Datasets 07 and 12 were recorded using an up-swell azimuth configuration, see Fig. 3.5 and 3.6, this produces RTI plots which clearly show the modulation of the swell structure produced by the presence of well developed waves, Fig. 4.27 and 4.29. Datasets 10 and 15 were recorded with a cross-swell configuration. At these azimuth angles coupling between the waves and the underlying modulation is less pronounced, Fig. 4.28 and 4.30. This is due to multiple individual waves existing within a single resolution cell; which is defined by the antenna azimuth beam width as well as the pulse width used. Despite this, clutter is qualitatively visible within these RTI plots but its periodic structure is not as significantly dominant in the image.

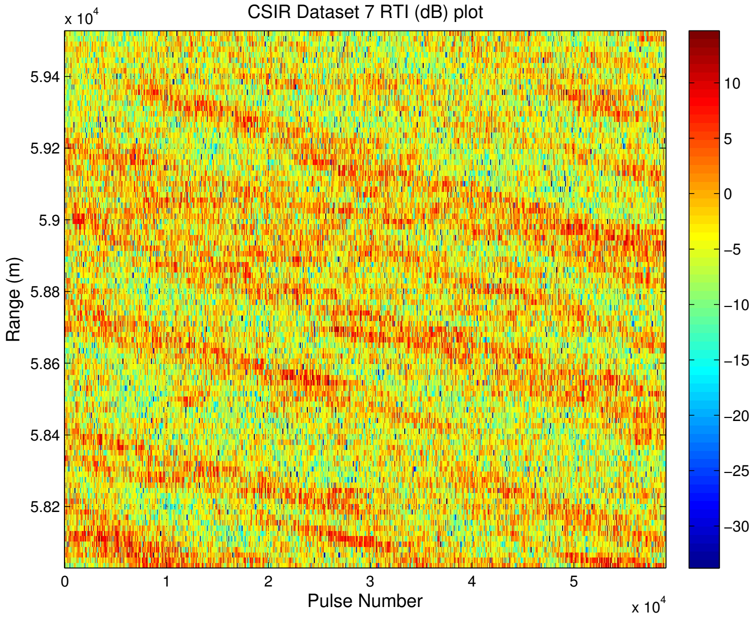

Figure 4.27: CSIR dataset 07 RTI

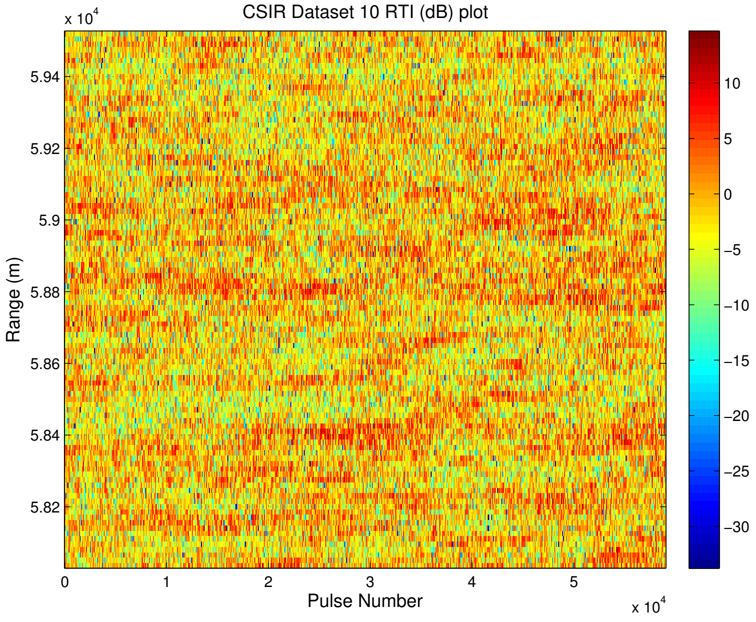

Figure 4.28: CSIR dataset 10 RTI

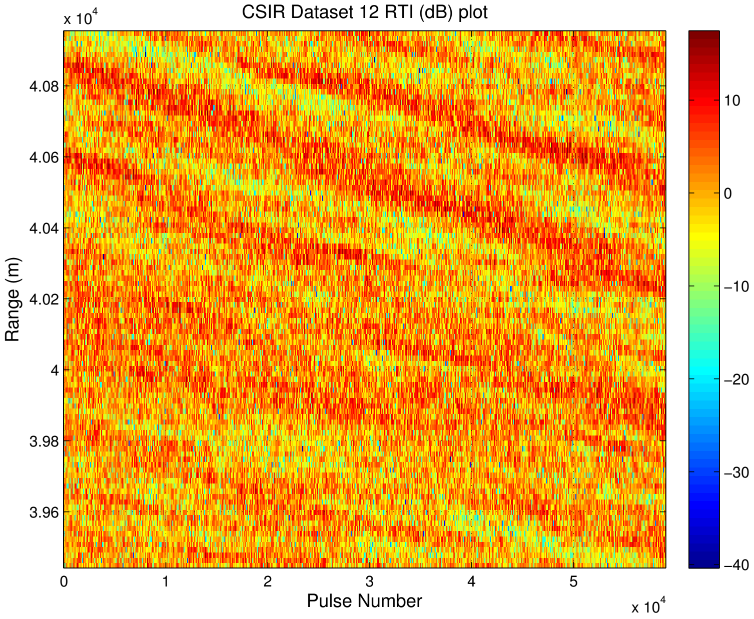

Figure 4.29: CSIR dataset 12 RTI

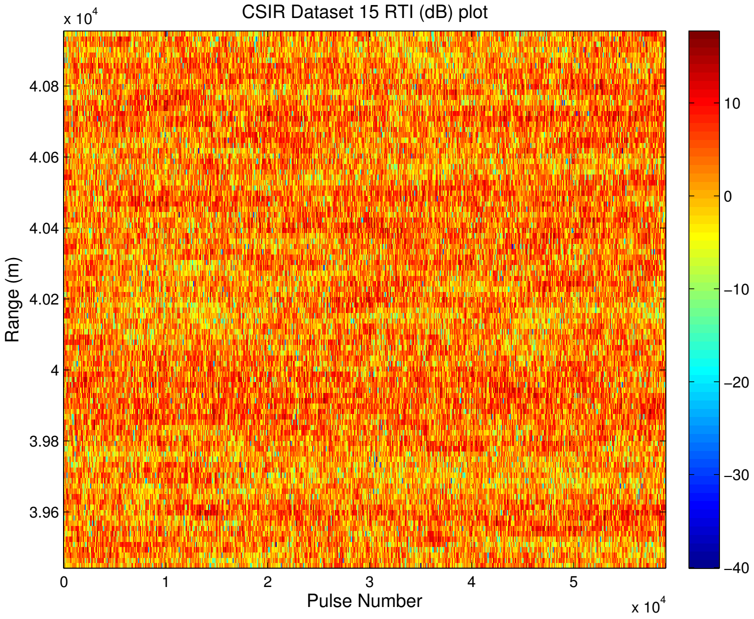

Figure 4.30: CSIR dataset 15 RTI

Following on from qualitatively establishing the existence of sea clutter within these selected datasets statistical characterisation was performed. As in the SW2000 non-coherent anaylsis, Section 4.1.1, the K-distribution shape parameters from the data were obtained. In this case the method of moments was used to evaluate the shape parameters from the time series data within each range gate. This has been completed for each datasets in turn and is shown in Fig. 4.31.

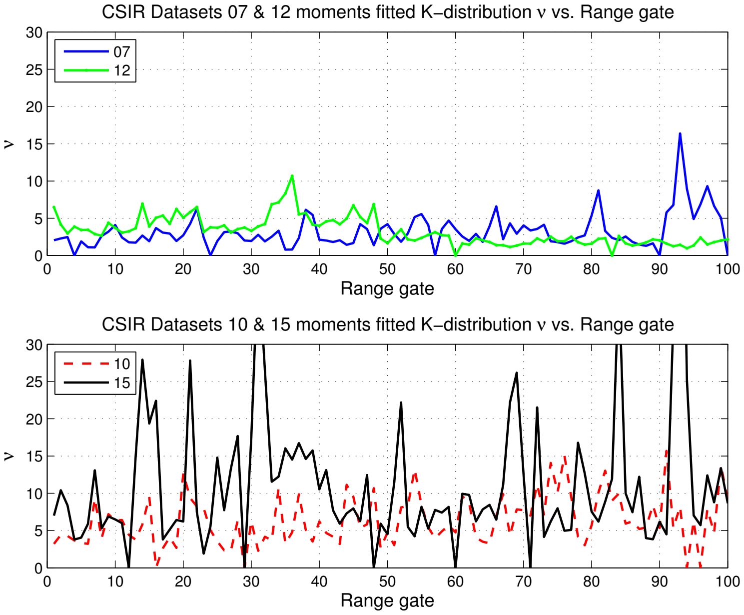

Figure 4.31: CSIR Non Coherent data Datasets 07, 10, 12 and 15 moment fitted shape parameter vs. range gate

There is no any overall increasing or deceasing trend in the shape parameters obtained as a function of range gate. Comparing between datasets it is clear that

Evaluating the temporal correlation properties of the times series data is an important component of sea clutter analysis. The following analysis reviews and compares the temporal correlation properties of the 4 CSIR datasets. To quantify the temporal correlation of the clutter the ACF from individual range gates was generated, an example plot from dataset 07 using data from range gates 10 to 15 is shown in Fig. 4.32.

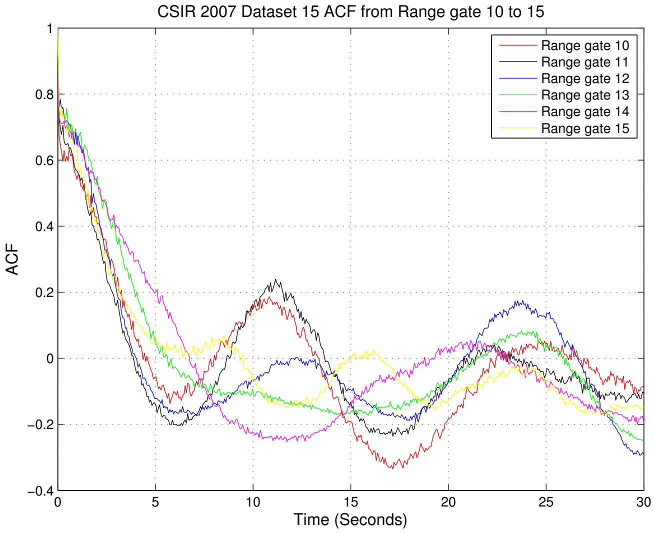

Figure 4.32: CSIR Dataset 07 ACF from range gates 10 to 15

The ACF was evaluated using Fourier analysis and is defined as,

$$ACF = IFFT[[FFT(X - \bar{X})]^2] \tag{4.1}$$

Where X is the dataset input. It has been normalised for the maximum to be equal to 1. The average ACF from all the range gates in each dataset was evaluated and plotted on the same axis to compare the average temporal correlation characteristics of the datasets, Fig. 4.33. The figure shows that dataset 07 and 12 have a strong long term periodic structure that exists after the averaging over all range gates. This means that the correlation of each range gate has a similar period in each range gate across the whole dataset. In contrast datasets 10 and 15 have a flat average long term temporal correlation with no periodic structure. All the datasets exhibit a large initial short time deccorelation. This is the decorrelation of the speckle component in contrast to the decorrelation of the texture component of the clutter present.

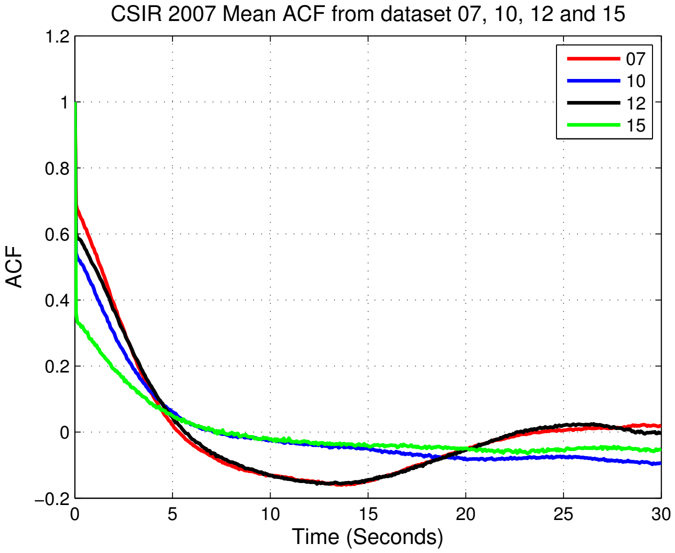

Figure 4.33: CSIR Datasets 07, 10, 12 and 15 ACF - Averaged over all range gates

4.2.2 CSIR Data Doppler Analysis

This section details the Doppler analysis performed on the CSIR datasets. The key processing stages are presented within the flow diagram seen in 4.34. The preprocessing applied to the data is described in section 3.2, where the Fourier analysis was applied in the short time domain to produce Doppler-time spectrograms for each individual range gate within a dataset. A 64 point short time FFT was used to obtain a higher Doppler resolution than the SW2000 data analysis, but maintain the short time frame over which the sea clutter Doppler spectra is evaluated. In addition to the change in Fourier transform window used an overlap of 50% was introduced when generating the Doppler spectra from the time series values. The reasoning for applying an overlap to the discrete samples that are input to the FFT processing is to reduce the artifacts that may be produced at the boundary between discrete sample groups. The use of a 50% overlap in the FFT processing does mean that there is a partial correlation between the adjacent blocks of Doppler-time data. Therefore when a PDF is produced using the data from a Doppler bin all the samples are not independent. This correlation issue is not considered to effect the resulting overall statistical trends that are shown within this research.

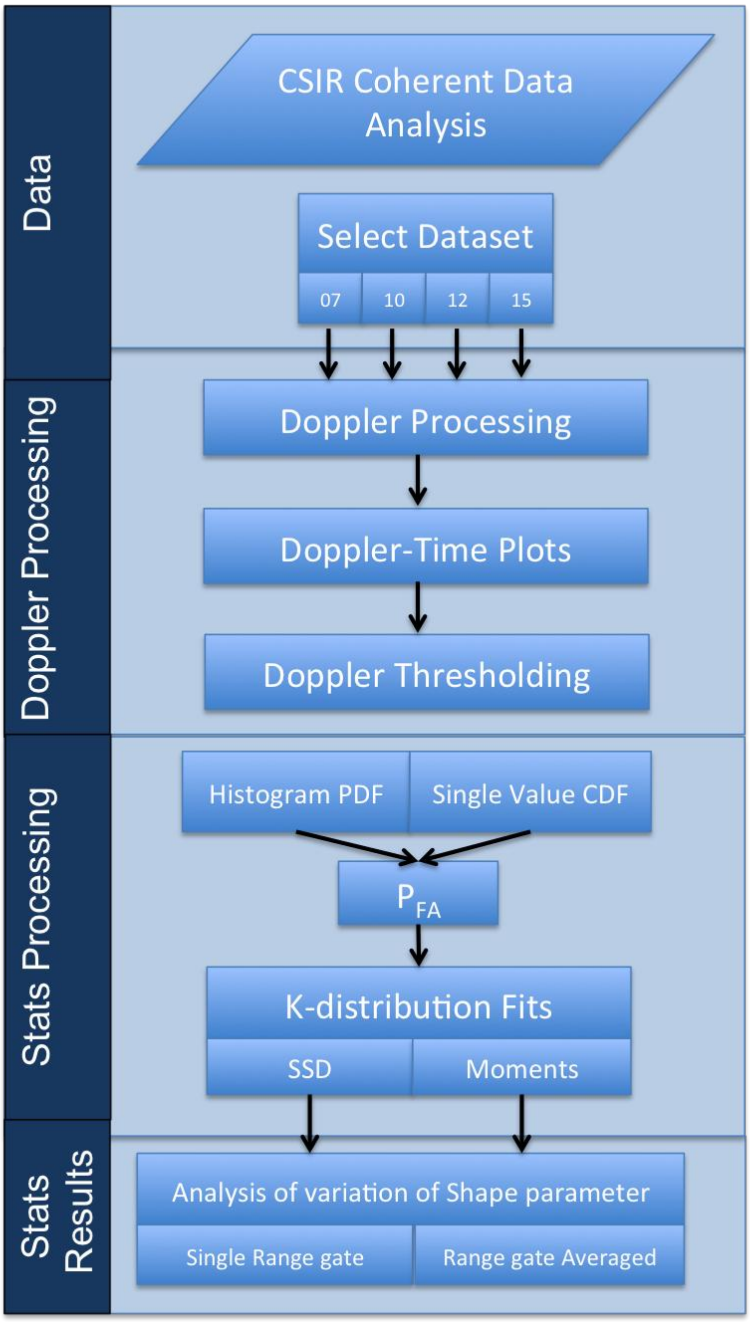

Figure 4.34: Coherent data analysis flow diagram

Doppler-time spectrograms from a example range gate within each dataset are shown in Fig. 4.35, 4.36, 4.37 and 4.38. Each spectrogram shows that sea clutter is present for the given range gate selected, with a CNR of $\approx$ 30 dB - 40 dB. The centre of gravity of the Gaussian spectra is shown to have a net positive shift for datasets 07, 12 and net negative shift for datasets 10 and 15. The Doppler resolution of the spectra gives more detail in comparison to the SW2000 Doppler spectra. This allows further extensive analysis on the behaviour of the sea clutter overall and how it develops/varies over time.

The width and centre of gravity of the spectra is shown to dynamically evolve with time as well as the CNR, which is known as non-stationarity. The *breathing* of the PSD width and shifting of its centre of gravity is a key affecting factor on the characteristics of the amplitude statistics variation with Doppler bins. This is defined by the temporary shift of the spectra into the boundary Doppler bins which are for the majority of the time thermally noise dominated, and for the other period clutter dominated when the spectra shifts or expands into that Doppler frequency. This shifting of the clutter into normally thermally noise dominated Doppler bins produces a more spiky distribution, due to the occasional existence of high CNR values in the Doppler bins.

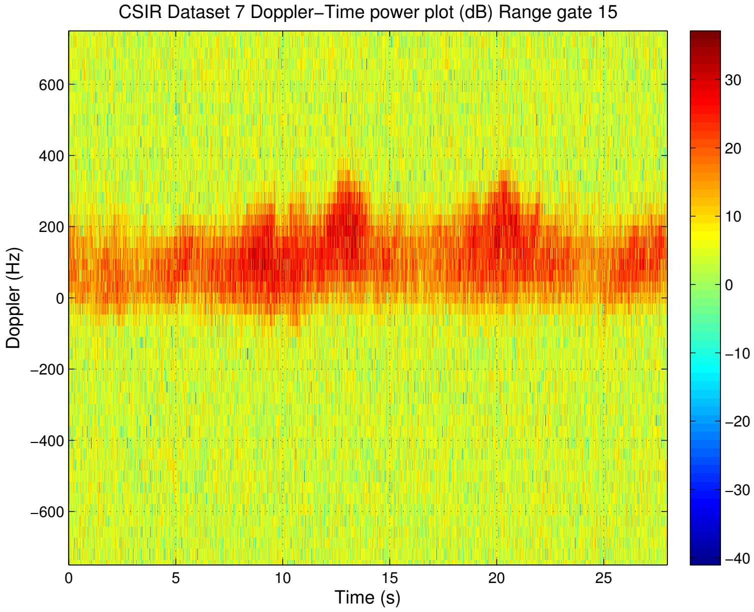

Figure 4.35: CSIR Dataset 07 Doppler-Time Spectrogram - Range gate 15

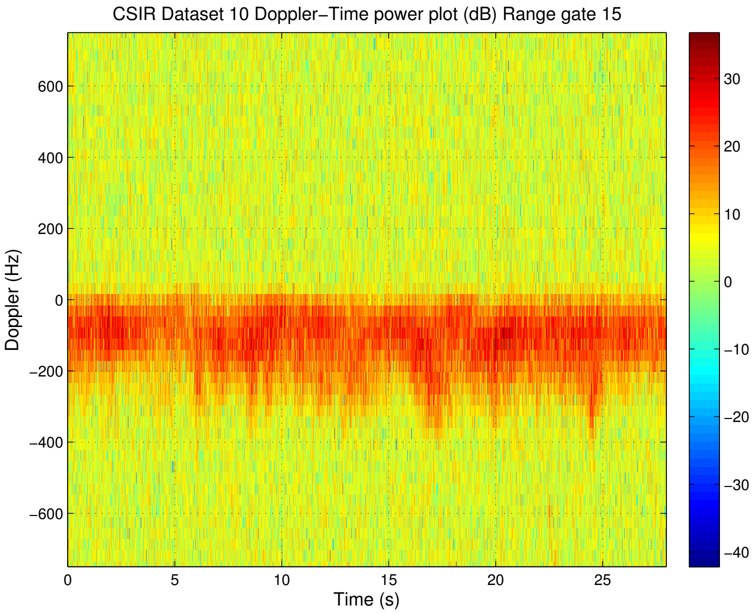

Figure 4.36: CSIR Dataset 10 Doppler-Time Spectrogram - Range gate 15

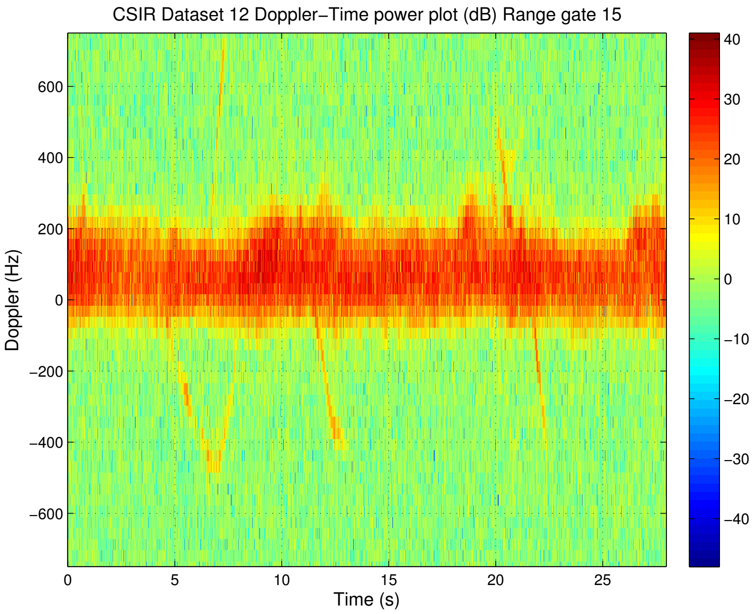

Figure 4.37: CSIR Dataset 12 Doppler-Time Spectrogram - Range gate 15

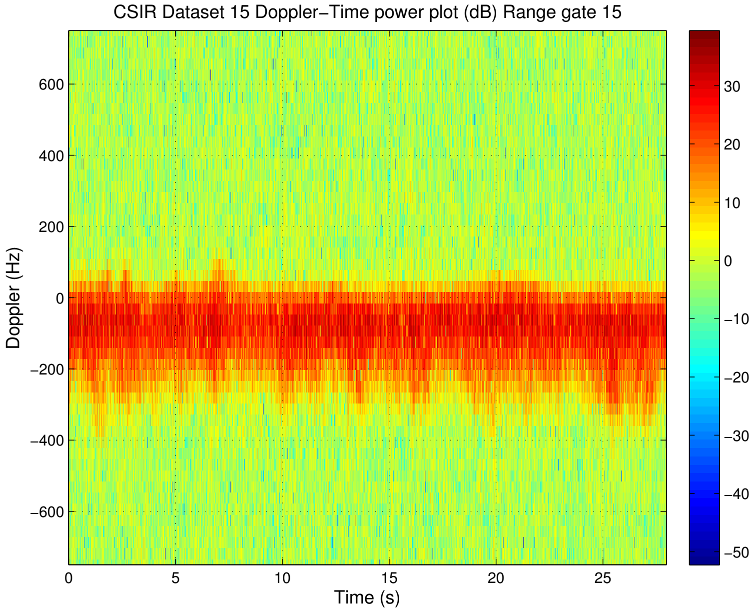

Figure 4.38: CSIR Dataset 15 Doppler-Time Spectrogram - Range gate 15

Further study of the Doppler spectra from all the ranges gates within each dataset revealed interference within the spectra. This was shown to occur only in individual specific range gates. Figure 4.39 (a) is a plot of each of the time averaged Doppler-time spectra against range gates. Five of the ranges gates have a significant increase in the averaged power across the whole Doppler spectrum. It is these range gates that therefore must include interference affecting the average power. The effect is seen more clearly when only the power from a single thermal noise limited Doppler bin is plotted. Figure 4.39 (b) shows a slice of Fig. 4.39 (a) at Doppler frequency -562.5Hz which is normally in the thermal noise floor area. The interference is ≈ 10 dB greater than the thermal noise floor and exists at ranges 58,081m, 58,381m, 58,875m, 59,370m and 59,520m.

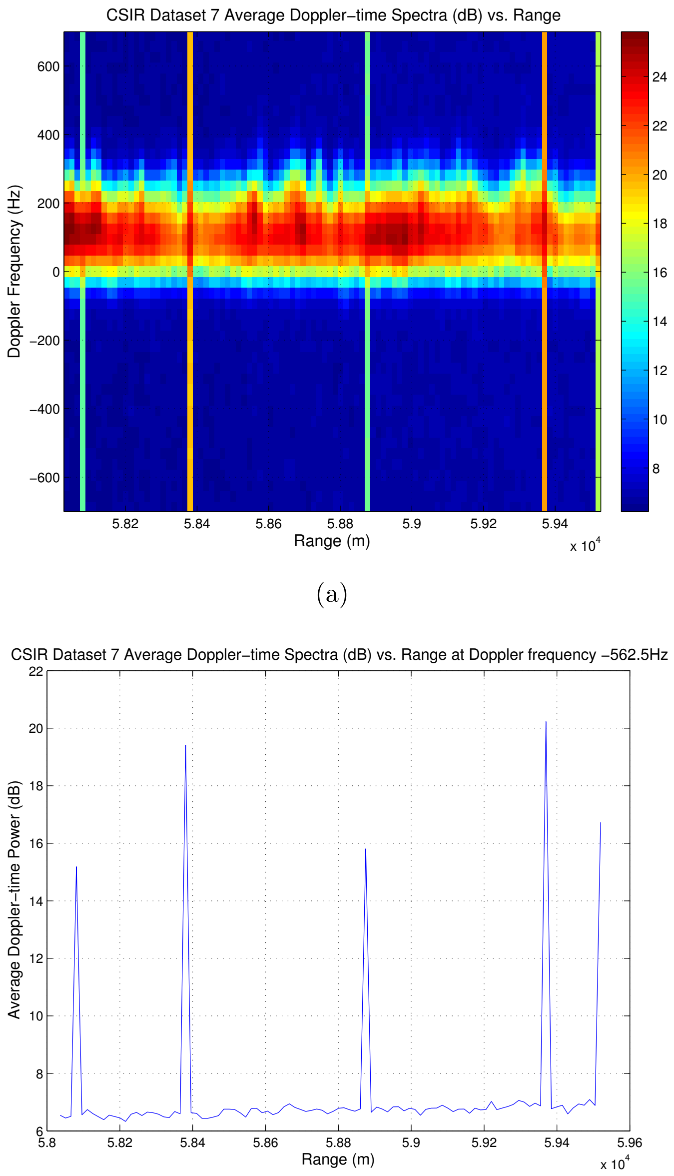

(a)

(b)

Figure 4.39: CSIR Dataset 07 Averaged Doppler-Time Spectrogram vs. Range (a) All Range gates (b) Slice of power profile at Doppler bin -562.5 Hz

This phenomenon is definitely not related to sea clutter and must have been caused by an external RF source active during the experiments. Therefore a thresholding technique was utilised to remove the individual Doppler PSD profiles in the Doppler-time spectrograms for the range gates that are highlighted in Fig. 4.39. Otherwise these high power interference signals would alter the evaluated statistical behaviour of the sea clutter as a function of Doppler. Figure 4.40 shows the Doppler-time spectra before (a) and after (b) this thresholding. Only a single Doppler spectra was removed during this process, located at ≈ 13 seconds, but by completing the thresholding the dynamic range to reduce from ≈ 45 dB to 30 dB. This process was repeated for all range gates that showed interference in the averaged Doppler-time spectra plots for all datasets prior to statistical analysis.

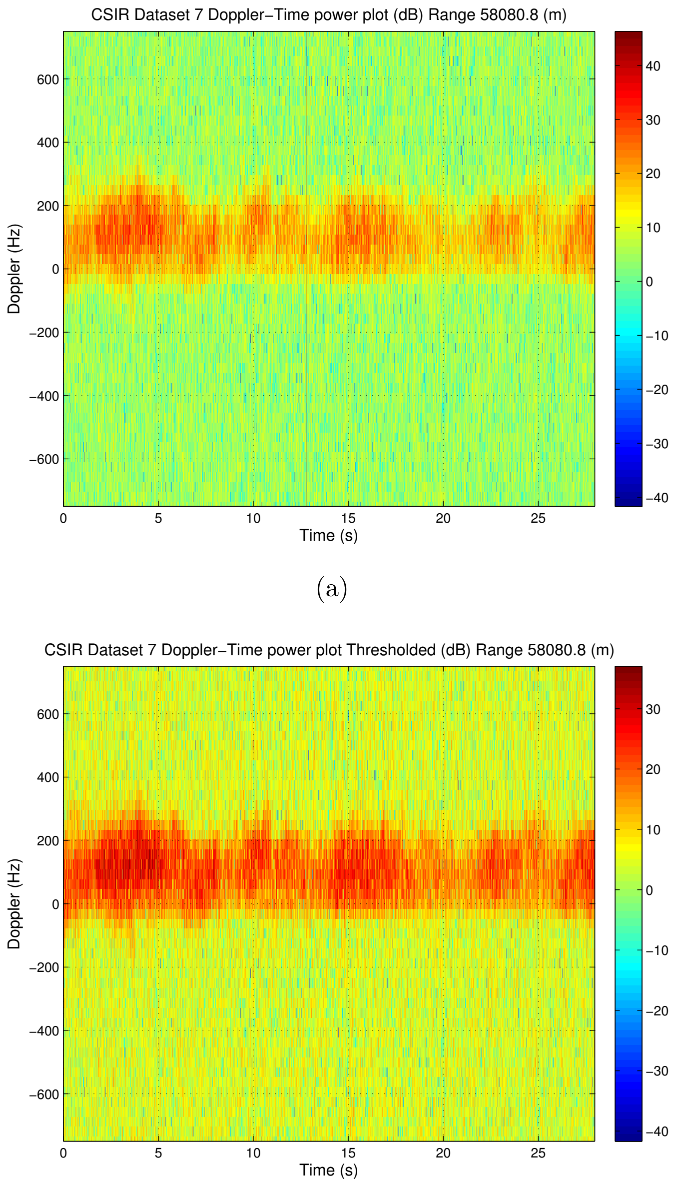

(a)

(b)

Figure 4.40: CSIR Dataset 07 Doppler-Time plot from Range 58,085m (a) Before Thresholding (b) After Thresholding

After the thresholding process was complete all datasets Doppler spectra was ready for statistical analysis. The SSD fitting method was then applied to the amplitude values within each Doppler bin, from the Doppler spectra of each range gates, this was repeated for all 4 datasets. Initial qualitative checks on the fittings were performed for each dataset to ensure that the data was well characterised by the K-distribution at high CNR Doppler frequencies and that the thermal noise floor was showing an expected Rayleigh distribution. Two examples plots from dataset 07, Fig. 4.41 (a) and (b), show the Log(P_{FA}) vs. Threshold curves for both the data and the SSD fitted K-distribution. The Doppler bin at -250 Hz is dominated by thermal noise and fits well to the highest shape parameter value, 100, as expected. The

187.5 Hz Doppler bin is clearly within the area that is dominated by a high CNR, $\approx$ 30 dB, see Fig. 4.35, and it seen to be well represented by the K-distribution. There is a discrepancy between the fitted K-distribution curve and the data curve at the 0dB threshold level. This is because the SSD fitting method used to select the best representative curve is applied to samples at threshold level of 0dB and greater. Data samples do exist at values less that 0dB but the aim of this work is to characterise the behaviour of the tail of the clutter distribution. The 0dB values on $\log P_{FA}$ vs. Threshold plots shown represents the mean value within the normalised dataset. Therefore this selected curve may not closely represent the data at 0dB in comparison to other potential K-distribution curves, but its is the over all best curve to represent the data when the emphasis is based on the tail of the distribution.

As well as these checks the mean SSD values for each fit performed was stored. This information can be used to check if individual range gates or datasets the goodness of fit for the K-distribution to the data and flag up any issues.

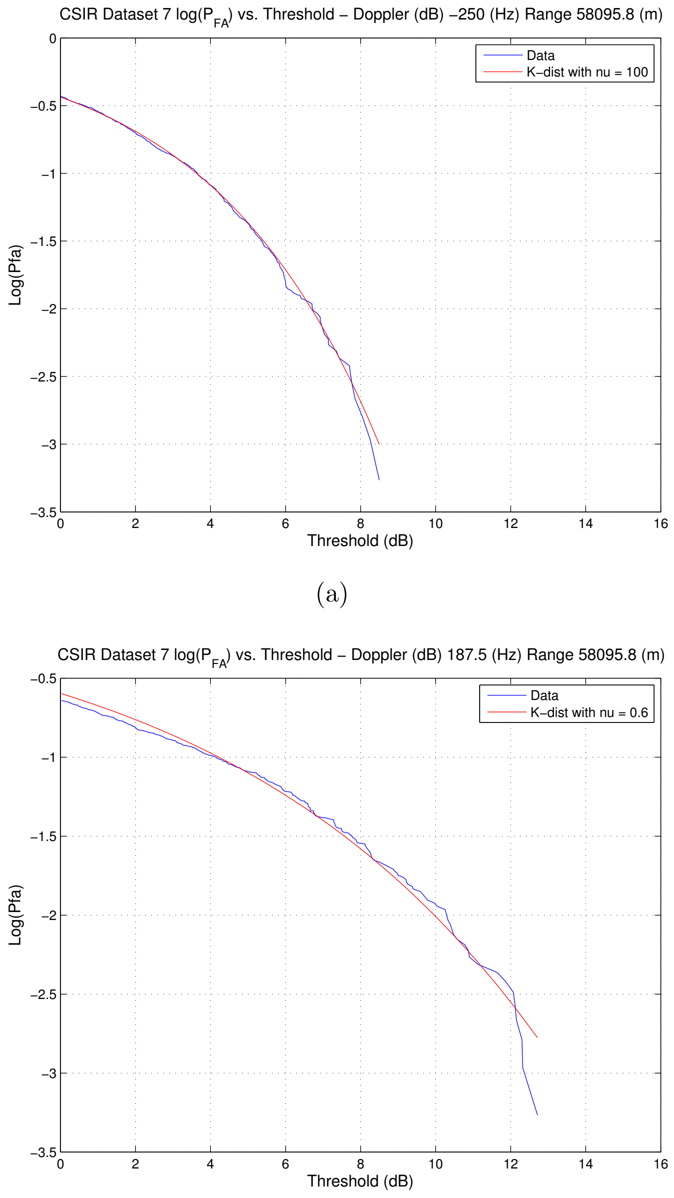

(a)

(b)

Figure 4.41: CSIR Dataset 07 Log(P_{FA}) vs. Threshold curve of data and SSD K-distribution curve - Range 58095.8 (m) (a) -250 Hz (b) 187.5 Hz

The shape parameter around the peak CNR was given as 0.7 which matched closely the SW2000 data result seen in Fig. 4.15 (b). This adds to credibility of the analysis of the sea clutter statistical behaviour as two separate radar system observing different seas both show similar results.

The SSD and moment fitted shape parameters from all Doppler bins within a single example range gate in dataset 07 have been plotted in Fig. 4.42. The $1/\nu$ values increase to a maximum on the leading edge of the clutter PSD, agreeing with the SW2000 analysis. The average PSD has a main Gaussian shape with an additional shoulder protrusion on the positive Doppler edge, where the statistics are most spiky. This structure may indicate a multiple Gaussian clutter spectra with a second lower amplitude Gaussian with a higher central Doppler frequency. Both the SSD and the moment fitted shape parameters are shown in the figure and agree closely with each other. The only separation between fitting results is seen in the most spiky result at Doppler frequency 281.2 Hz, where the SSD gave $1/\nu = 10$ and the moment $1/\nu = 9.53$. Even this is not a significant disagreement and amounts to very little realistic dB difference in threshold at the operational P_{FA} levels of a radar system.

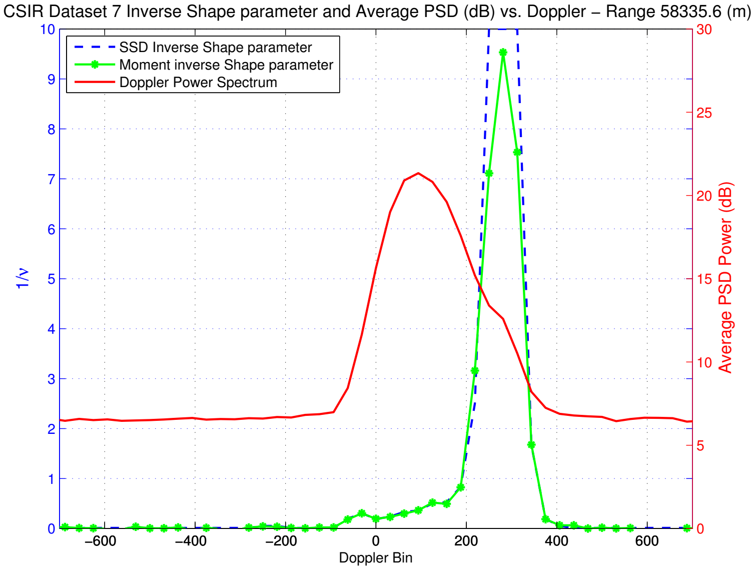

Figure 4.42: CSIR Dataset 07 SSD and moment fitted $1/\nu$ vs. Doppler (Hz) Range 58335.6 (m)

After verifying that the single range gate fits were giving comprehensible results the analysis focused on the variation of the fitted shape parameter with range gate. The SSD fit from all range gates have been plotted as a function of range and Doppler in Fig. 4.43, 4.44, 4.45 and 4.46 for datasets 07, 10, 12 and 15 respectively.

These plots show the variation of the shape parameter with both Doppler and range, giving a detailed insight into how the statistics are correlated. Within dataset 07 the most spiky component of the clutter is shown to consistently exist on the leading positive Doppler edge, as seen in the example Fig. 4.42. It varies in width from a single Doppler bin to covering an area of ≈ 200 Hz, and shifts its location from +375 Hz to +200 Hz. A second less spiky ridge between 0 Hz and -75 Hz also exists, this does not increase up to the maximum of $1/\nu = 10$, but peaks at $1/\nu \approx 5$ and is less consistent in its existence.

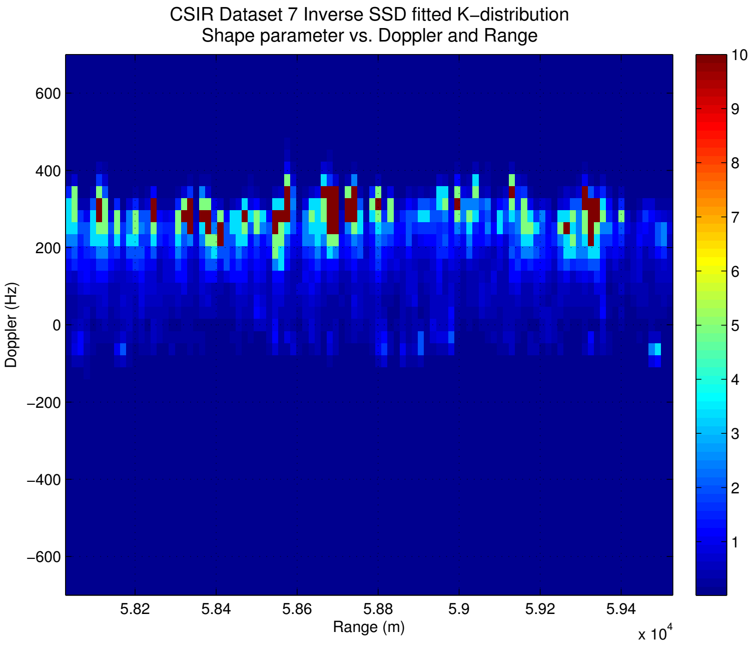

Figure 4.43: CSIR Dataset 07 SSD $1/\nu$ vs. Doppler (Hz) and Range (m)

The inverse shape parameter variation from dataset 10, Fig. 4.44, shows that the spiky section of the spectra has shifted to the negative side of the Doppler spectra following the shift in the CNR power within this dataset, see Fig 4.36. At ranges between 59,000 m and 59,200 m there is a significant increase in $1/\nu$ at greater negative Doppler that the body of the clutter, between -400 Hz and -700 Hz. This is most likely to be non-sea clutter related phenomena, and not discussed further in this comparative analysis. It is important to understand that other phenomena does occur during clutter measurements and to remove factors that can not be attributed to the clutter. As in Fig. 4.43 a two sided increase in $1/\nu$ is shown either side of the peak CNR, with a wider max $1/\nu$ on the negative side of the peak CNR.

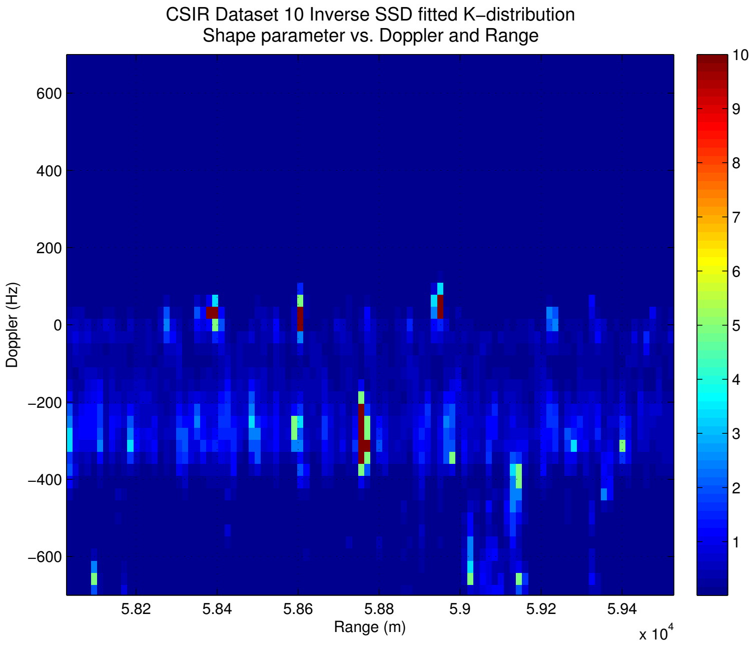

Figure 4.44: CSIR Dataset 10 SSD $1/\nu$ vs. Doppler (Hz) and Range (m)

Figure 4.45 shows the variation of $1/\nu$ for dataset 12, this has the most spiky statistics of all the CSIR datasets. Wide areas, $\approx$ 300 Hz, of maximum $1/\nu$ values exists across the spectra on both the negative and positive side of the peak CNR. As in Fig. 4.43 for dataset 07 the positive Doppler leading edge of the clutter is shown to have the most consistently spiky statistics. In addition to this large sections of the negative Doppler spectra, around ranges 39,400 m to 39,700 m, are also shown to have very spiky statistics.

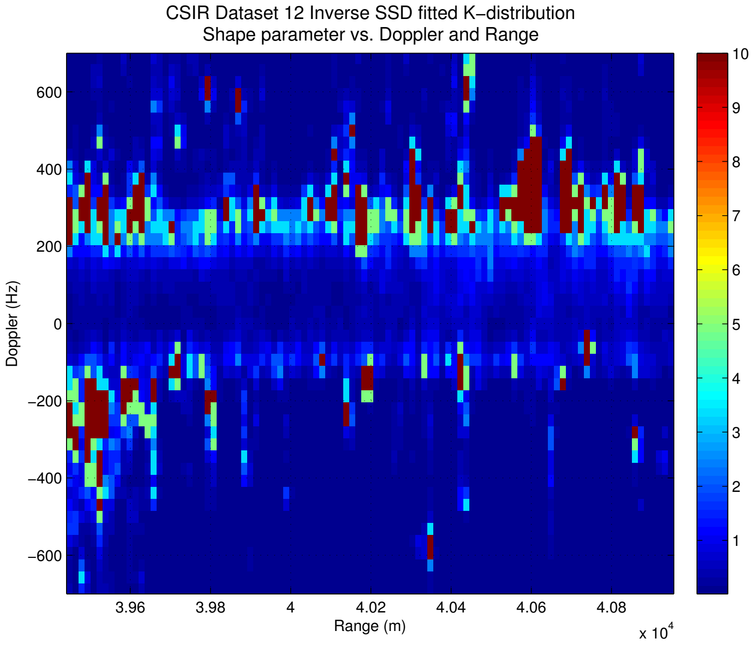

Figure 4.45: CSIR Dataset 12 SSD $1/\nu$ vs. Doppler (Hz) and Range (m)

The inverse shape parameter variation for dataset 15, Fig. 4.46, shows very similar characteristics to dataset 10. This is to be expected as they both have the same azimuth angle with respect to the swell. The peak $1/\nu$ values are focused at two points around 75 Hz and - 300 Hz, with the latter showing a wider increase in $1/\nu$ compared to the first ridge. A difference between the 10 and 15 datasets statistical behaviour is that dataset 15 has a more prominent spiky edge to the negative Doppler side of the spectra. Possibly an attribute of shifting closer to the radar. This may have increased the possibility of detection of the faster moving components of the clutter which contributed to the statistics within this region.

These results show that the cross swell configuration has a more consistent statistical variation behaviour that changes very little with changing elevation angle (and therefore grazing angle) and absolute range. Whereas the up swell azimuth results have a much greater variability in the statistical variations with Doppler.

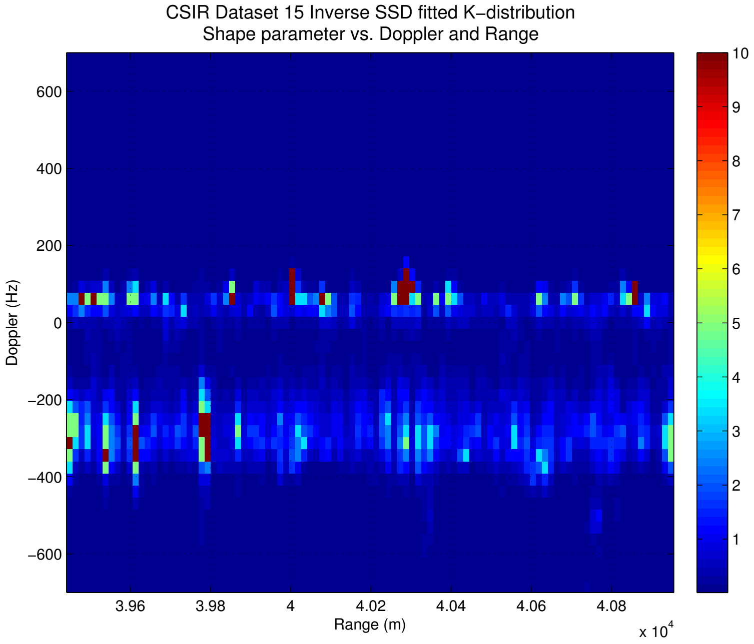

Figure 4.46: CSIR Dataset 15 SSD $1/\nu$ vs. Doppler (Hz) and Range (m)

To characterise the average variation of the statistics with Doppler the average SSD and moment fitted $1/\nu$ were evaluated. The moments fits were generated by averaging the moment values from each range gates then producing the averaged $1/\nu$ from this, while the SSD fits were completed by averaging the ν values directly to produce an average $1/\nu$ variation. The averaged spectra from all the range gates were also evaluated to plot along side the $1/\nu$ variation. The plots showing the average SSD fitted $1/\nu$, Moment $1/\nu$ and PSD for all datasets can be seen in Fig. 4.47, 4.48, 4.49 and 4.50.

Each averaged inverse shape parameter plot shows a good agreement between the SSD and moment fitted shape parameters, with the exception of dataset 12 which has the largest disagreement in the spiky areas of the PSD. All the averaged PSD spectra show general single Gaussian shape, that is slightly asymmetric with an elongated side on either the positive (datasets 07 and 12) or negative (datasets 10 and 15) Doppler edge. As discussed previously this may indicate that a secondary less powerful doppler component on the leading edge of the clutter is sometimes present. Although due to the averaging process it is shown as a extension to the side of the Gaussian shape.

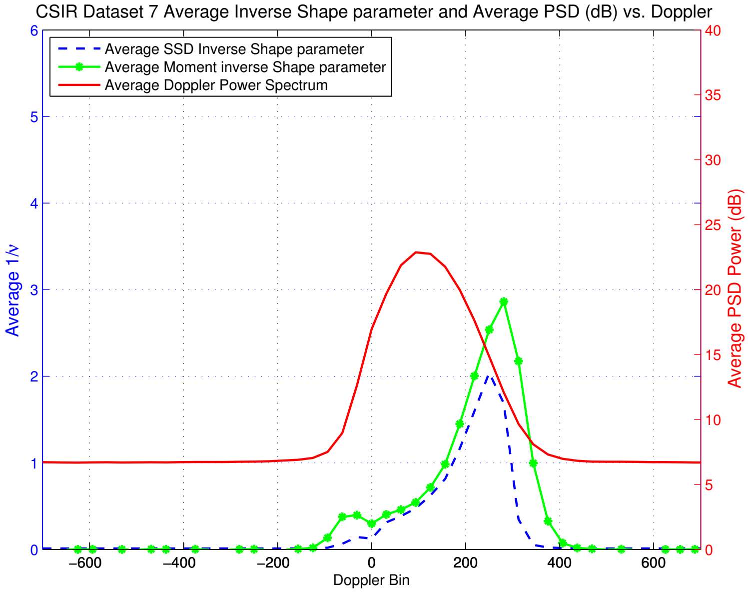

Figure 4.47: CSIR Dataset 07 Average SSD and Moment fitted $1/\nu$ vs. Doppler (Hz)

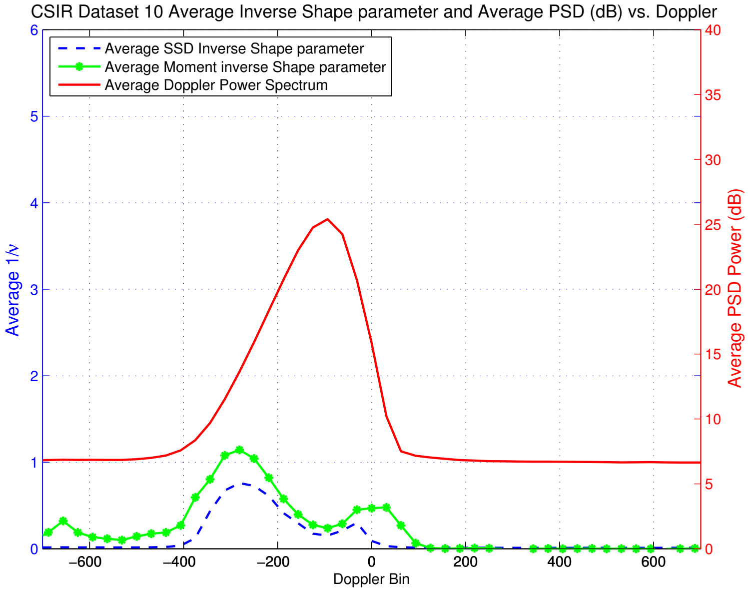

Figure 4.48: CSIR Dataset 10 Average SSD and Moment fitted $1/\nu$ vs. Doppler (Hz)

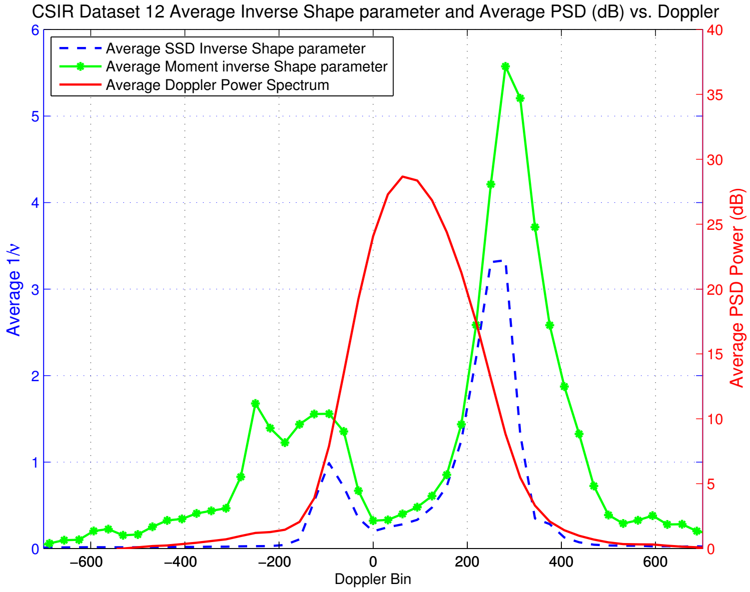

Figure 4.49: CSIR Dataset 12 Average SSD and Moment fitted $1/\nu$ vs. Doppler (Hz)

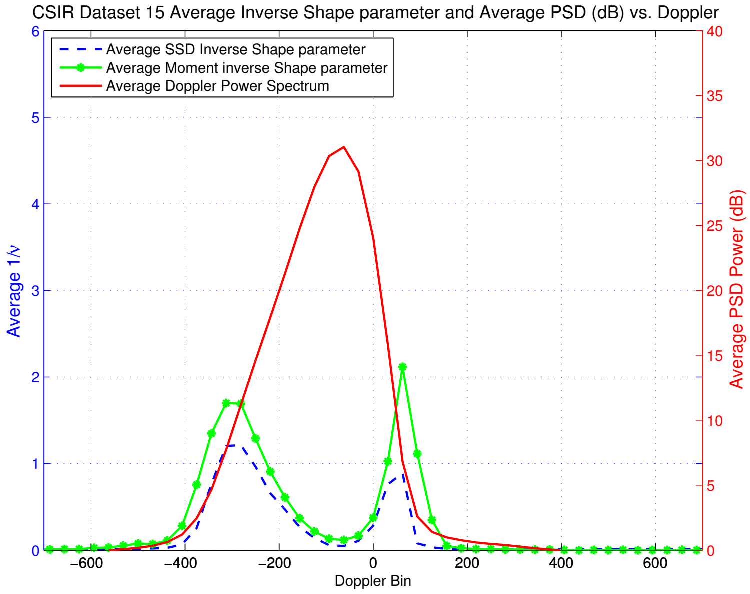

Figure 4.50: CSIR Dataset 15 Average SSD and Moment fitted $1/\nu$ vs. Doppler (Hz)

The main peak $1/\nu$ values from the datasets are shown in Table 4.2, along with $1/\nu$ for the secondary peak if a second local maxima existed within the $1/\nu$ values. The table shows a clear mirroring in the locations of the 1st primary peak between the two azimuth angles; with the exceptions of 07 (SSD) and 15 (Moment) peaks. Datasets 07 and 12 had the largest $1/\nu$ value as 281.2 Hz while datasets 10 and 15 have a peak at -281.2 Hz. The change in azimuth from 240° N to 307.5° N induced the exact same shift in $1/\nu$ at both ranges, which is reasonable to expect. The moment estimation of the shape parameter is shown to always estimate a larger values for the $1/\nu$. The closest agreement occurred in dataset 10, $\Delta 1/\nu = 0.38$, and the largest difference was found in dataset 12, $\Delta 1/\nu = 2.24$.

Table 4.2: CSIR Datasets Peak $1/\nu$ values

Dataset	1st Peak		2nd Peak	
	$1/\nu$ Value	Doppler Freq (Hz)	$1/\nu$ Value	Doppler Freq (Hz)
07 (SSD)	2.04	250	N/A	N/A
07 (Moment)	2.86	281.2	0.4	-31.25
10 (SSD)	0.76	-281.2	0.3	-31.25
10 (Moment)	1.14	-281.2	0.48	31.25
12 (SSD)	3.33	281.2	0.99	-93.75
12 (Moment)	5.57	281.2	1.56	-93.75
15 (SSD)	1.21	-281.2	0.89	62.5
15 (Moment)	1.70	-312.5	2.12	62.5

4.2.3 CSIR Data Analysis Summary

The analysis of the CSIR data successfully evaluated the variation of sea clutter with azimuth angle with respect to swell and wind direction. The four key datasets selected were found to be very suitable for sea clutter analysis and presented different characteristic behaviour in the non-coherent and coherent analysis. The key differences between the datasets was the azimuth and less so the range. All other parameters were maintained including the day of measurement, allowing the assumption of the sea being tested.

The non-coherent analysis showed that the average temporal correlation of the sea clutter was very dependent on look angle with respect to the swell. A long term (≈30 second) correlation in the clutter returns in datasets 07 and 12 demonstated was clearly present.

The coherent analysis showed that the clutter in all cases fitted well to the K-distribution at high CNR levels, after the removal of interference. The edge of the clutter spectra was also shown to be the location of the most spiky statistics, agreeing with the SW2000 results. The most spiky edge was the positive side for the up swell datasets 07 and 12, and the negative Doppler edge for the cross swell datasets 10 and 15.

The most spiky clutter was shown to exist in the up swell dataset 12, which was recorded at a range of 39448.7 m to 40947.7 m. With the main $1/\nu$ peak almost twice that of dataset 07 which has the same azimuth angle. The variability of the $1/\nu$ results within dataset 12 were shown the be the most in comparison to all the other dataset.

The cross swell $1/\nu$ fits with Doppler and range gate from datasets 10 and 15 were very consistent in Doppler location of the $1/\nu$ peak and width of the increase in $1/\nu$.

4.3 NetRAD Results

This section presents the analysis and results obtained from the NetRAD 2010 datasets which were defined in Section 3.1.3. The non-coherent time series data analysis is performed initially, investigating the amplitude statistics of the clutter present. This is followed by the Doppler amplitude statistical analysis and comparison between the 6 datasets. As well as comparing the monostatic and bistatic recordings within each dataset.

The data was recorded as .bin files in a 16 bit unsigned integers, uncompressed pulse form. This needed to be read in and manipulated to produce complex range-time data before analysis could begin. Header files are saved with each binary recording, these contain all waveform and configurable radar parameters. The ADC values were offset by 2_{n-1}, where n is the bits of the ADC, 14 in the case of NetRAD. In order to recover the complex components of the signal a Hilbert transform was used in the Matlab processing giving a complex array that is 1024 range gates by M pulses recorded.

NetRAD does not record the actual transmitted signal due to limitations of the system. Therefore a prior laboratory recorded version of the pulse transmitted, with the correct pulse length, was used to perform the matched filtering of the received signal. During this process the data was also passed through a low and high pass filter to remove spurious components.

As the main focus of the NetRAD data analysis is the comparison of monostatic and bistatic sea clutter at different bistatic angles it is important to address the specific issues relating to bistatic experiments prior to analysis. By evaluating these bistatic issues it is possible to confirm the validity of the results shown in Section 4.3.1 and 4.3.3.

A very important factor when evaluating bistatic data is to ensure that the data from the seperate nodes corresponds to the same physical geolocation. This depends on the reliability of the timing of the system and the correct selection of range gates within each dataset. In bistatic radar experiments the area of interest for analysis is bounded by the interaction between the transmitted and received beams. At these ranges the SNR is a maximum for the bistatic node. Regardless of the configuration the monostatic node data performs as a stand alone radar, so the data from all range gates is valid for analysis. Although to allow for effective scientific comparison between the phenomena observed by the two separate nodes only the monostatic data focused around the intersection area has been selected. The range of interest is defined in terms of the two way bistatic range for all NetRAD analysis, including the monostatic node. For the bistatic node this is the range from transmitter to intersection point plus the distance from intersection to receiver. For the monostatic node this is twice the normal accepted monostatic range of transmitter to target. The ranges selected were done so using both geometry calculation to evaluate the location of the intersection patch and qualitative analysis of CNR levels within the bistatic RTI data itself, they are shown in Table. 4.3. As the bistatic angle increased the number of overlapping range gates that could be used for analysis (due to having sufficient CNR) reduced from 130 at $\beta = 60°$ to 58 at $\beta = 120°$. Even at $\beta = 60°$ the number of range gates was still sufficient to allow for quantitative comparisons between the datasets. The selected range gates represented an absolute range extent of 342m and time duration of 40sec, which was adequate for characterisation of the clutter in this configuration.

Table 4.3: NetRAD Datasets range gates of interest

Dataset	Bistatic Angle	Two-way Range (m)	Number of Range gates
1233 & 1551	60°	3228 - 4002	130
1244 & 1603	90°	2310 - 2826	87
1253 & 1617	120°	1962 - 2304	58

Due to the 11° beamwidth of the antennas used the bistatic angle varied across the clutter cell. This means that each range gate within the bistatic data contains scattered returns from a range of bistatic angles. This was a physical limitation of the system, the beam widths were selected to be a reasonable size to ensure that the intersection area of the two beams was wide enough to allow for alignment.

4.3.1 NetRAD Non-Coherent data analysis

The following plots show the RTI from the range gates of interest in both the monostatic (a) and bistatic (b) nodes from all the datasets, Fig. 4.51, 4.52, 4.53, 4.54, 4.55 and 4.56.

Dataset 1233 in Fig. 4.51 shows clear large scale wave structure within both the monostatic and bistatic node. The CNR of the clutter in both cases is ≈ 40 dB, more than sufficient for analysis. The wave fronts are different relative angles with respect to the receiving antenna which is to be expected at the bistatic angle of 60°. A stationary line is shown in the bistatic data at ≈ 3250 m. This may be a fixed target within the scene and data from this range gate has been removed from statistical analysis of the sea clutter present.

The change in the angle of the wave front with bistatic angle can be seen by comparing the wave front angle in the bistatic results from dataset 1233 and 1244, Fig. 4.51 (b) and 4.52 (b). Dataset 1244 has a less steep incline in the wave fronts as the bistatic main beam has been altered to be directed closer to being perpendicular to the incoming waves.

This change in angle is important, as the CSIR results show the angle with respect to the swell changes the characteristics of the statistics significantly. The NetRAD data presents and opportunity to study this variation in greater detail as three bistatic angles are available in both polarisations.

The RTI plot from dataset 1253, Fig. 4.53 shows the wave structure within the monostatic node, and part of the bistatic node. The bistatic results clearly have additional phenomena occurring in the early range gates from 1900 m - 2100 m. This may be due to the configuration bringing the intersection patch closer to the shore line, or a spurious effect caused by switches within the radar.

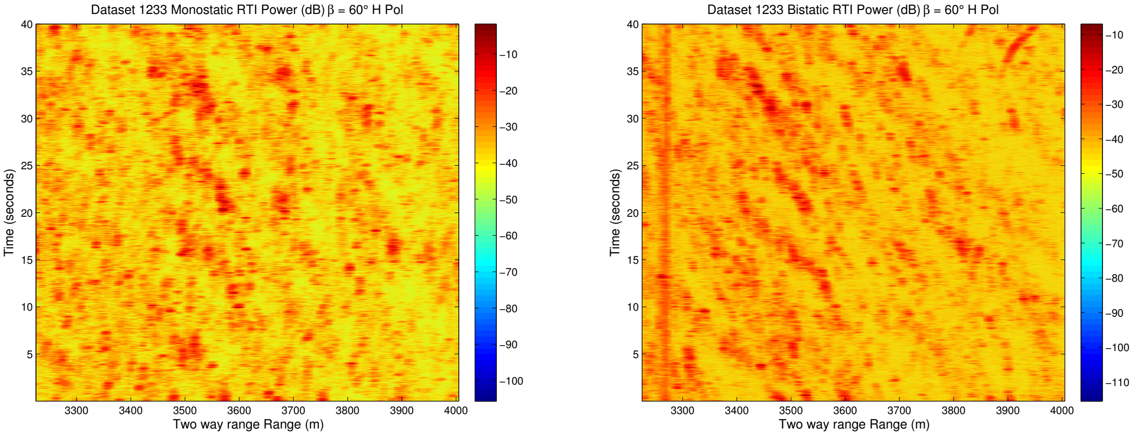

(a)

(b)

Figure 4.51: NetRAD Dataset 1233 Bistatic Angle 60° Horizontal Polarisation RTI plots (a) Monostatic (b) Bistatic

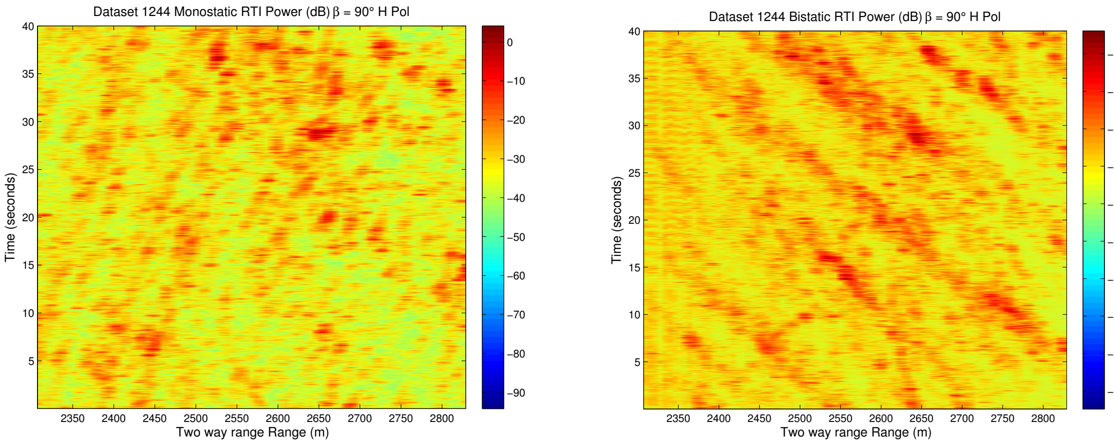

(a) (b)

Figure 4.52: NetRAD Dataset 1244 Bistatic Angle 90° Horizontal Polarisation RTI plots (a) Monostatic (b) Bistatic

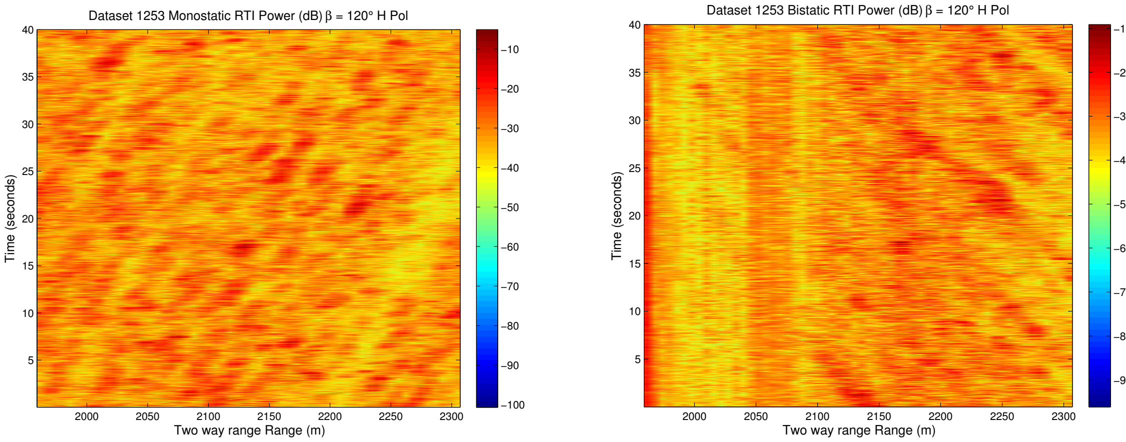

(a) (b)

Figure 4.53: NetRAD Dataset 1253 Bistatic Angle 120° Horizontal Polarisation RTI plots (a) Monostatic (b) Bistatic

The vertically polarised results in Fig. 4.54, 4.55 and 4.56 all clearly have clutter present within them. Wider wave fronts are seen in these RTI plots in comparison to the horizontally polarised data. This is accounted for by the difference in the interaction of the vertically polarised EM wave with the sea surface.

For parts of the bistatic results in datasets 1603 and 1617 a similar effect as seen in the beginning range gates bistatic 1253 data is shown. It is particularly prominent in dataset 1617, ranging from 1900 m to 2150 m. This effect has the same characteristics as seen in dataset 1253 and is assumed to have the same cause. It appears to be increase with increasing β angle and therefore a reduction in bistatic range. During the statistical analysis of the data these effected regions are not included to avoid corruption by this non-thermal noise component.

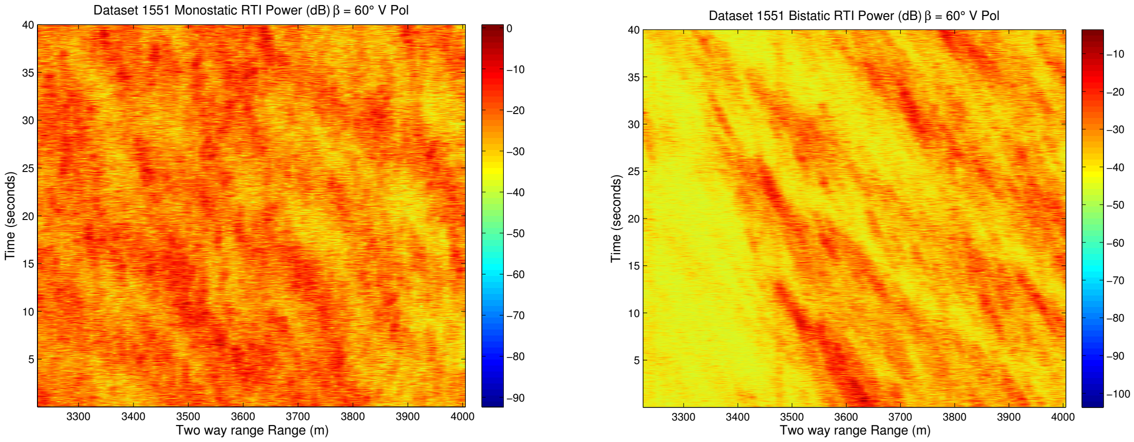

(a) (b)

Figure 4.54: NetRAD Dataset 1551 Bistatic Angle 60° Vertical Polarisation RTI plots (a) Monostatic (b) Bistatic

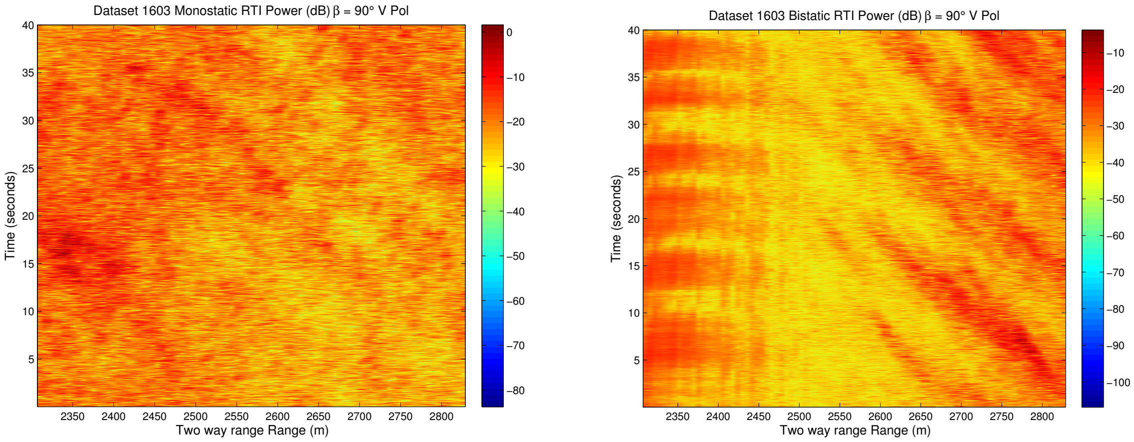

(a) (b)

Figure 4.55: NetRAD Dataset 1603 Bistatic Angle 90° Vertical Polarisation RTI plots (a) Monostatic (b) Bistatic

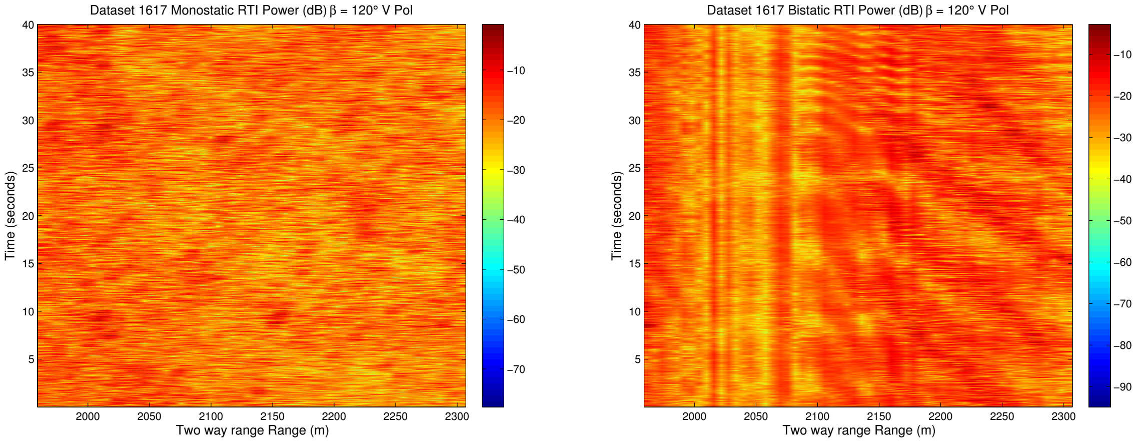

(a) (b)

Figure 4.56: NetRAD Dataset 1617 Bistatic Angle 120° Vertical Polarisation RTI plots (a) Monostatic (b) Bistatic

4.3.2 Phase Correction

The bistatic data recorded using NetRAD was affected by the issue of phase drift. This was introduced to the data by the GPSDOs timing equipment. The oscillators at each node are completely separate GPSDOs and due to imperfections on the synchronisation process they tend to drift in phase synchronisation. Hence there is a difference in the frequency of each clock. The main repercussion of this phenomena is the appearance of tramlines within the Doppler spectra.

The phase drifting issue has been rectified using Doppler post-processing on the bistatic data prior to qualitative and statistical analysis was performed. The phase of this direct breakthrough should be constant as the phase from a stationary target should remain constant, as long as no changing multipath effects are present. The phase of the direct breakthrough signal was extracted from the signal and used to correct the phase of all the data in the bistatic node.

During the transmission from the monostatic node part of the signal propagated directly into the sidelobe of the bistatic node. As the two nodes antennas were stationary during the experiments the relative distance between then should be constant, hence so should the phase. The phase of this break through was shown to drift, and it was this changing phase of the direct break through that was used to correct the phase of the rest of the bistatic data.

The side lobe direct breakthrough was easily detectable within the bistatic recording as it propagated along the shortest path to the bistatic node and hence stands out on its own as the first signal to arrive at the node. Figure 4.57 (a) shows RTI plot of all the 1024 range gates recorded from the first 2000 pulses within the bistatic node in dataset 1233. A clear solid line of increased power is present around range gate 350. This is the direct break through of monostatic signal that has travelled directly from node 3 into node 2 approximately along the baseline. The sharp increase caused by the break through can also be seen clearly in Fig. 4.57 (b) which is a range profile from a single pulse. This shows that only a single range gate contains the breakthrough. These phase values have been used to correct the phase within the rest of the data.

The sea clutter recorded in the bistatic node is shown to be visible between range gates 600 to 750 in this dataset. This signal has propagated to the intersection point and reflected towards the bistatic node, travelling significantly further.

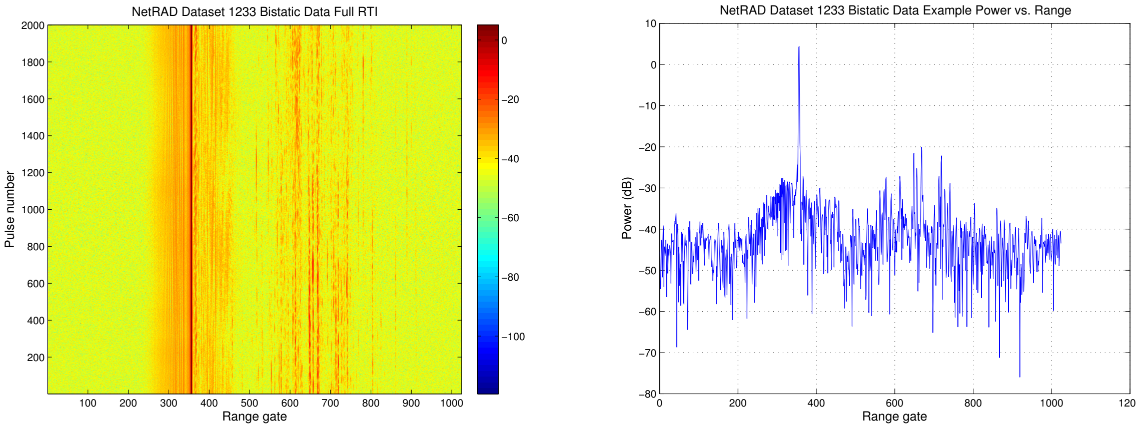

(a) (b)

Figure 4.57: NetRAD Dataset 1233 Bistatic Angle 60° Horizontal Polarisation (a) All range gate RTI (b) Single Pulse Power vs. Range

The phase taken from this single range gate from all pulses should show zero change if there was no relative drift between the two oscillators, but when analysed a drift is found. The phase from the direct break through range gate is shown within Fig. 4.58. The shift in phase has a clear trend that represents the difference in phase between the monostatic and bistatic node oscillators. By removing the phase change from the direct break through range gate from the rest of the data it is possible to compensate for this phenomena.

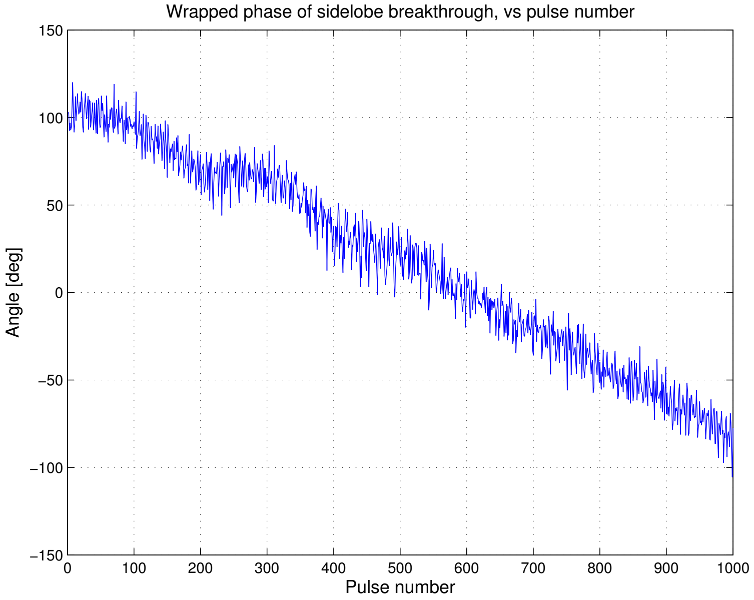

Figure 4.58: NetRAD Dataset 1233 Bistatic Angle 60° Horizontal Polarisation - Phase drift from direct break through signal

The before and after phase correction plot of Doppler-time from an example range gate within dataset 1233 is shown in Fig. 4.3.2. The tramlines that appear in (a) are removed completely by the phase compensation.

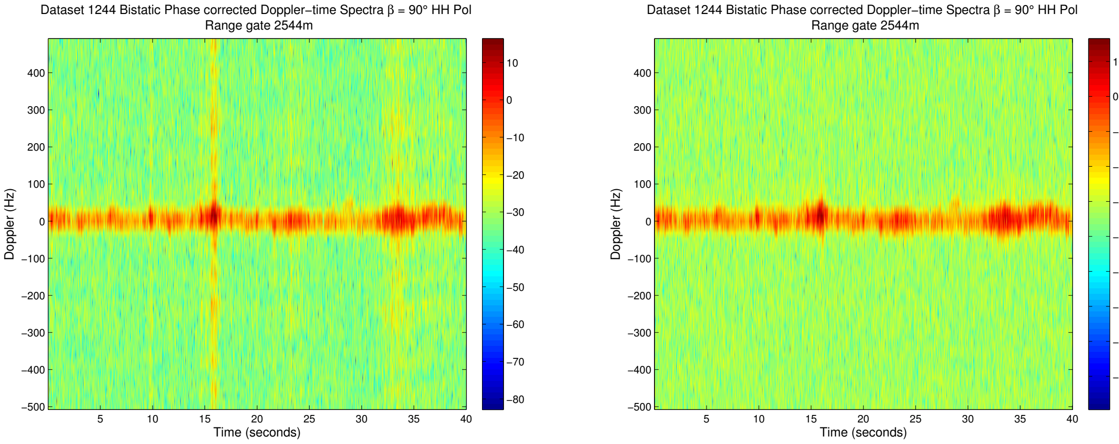

(a)

(b)

Figure 4.59: NetRAD Dataset 1244 Bistatic Angle 90° Horizontal Polarisation Example Doppler-Time spectra (a) Non-Corrected Phase (b) Corrected Phase

4.3.3 NetRAD Doppler data analysis

This section describes the processing results from the Doppler NetRAD data sets. The order of the processing and analysis steps are shown in the flow diagram shown in

Fig. 4.60. The pre-processing to obtain the Doppler data was the same as applied to the CSIR data described at the beginning of Section 4.2.2. The Doppler processing used a 64 point short-time -55 dB Dolph-Chebyshev weighted window with 50% overlap on all the time samples within each range gate.

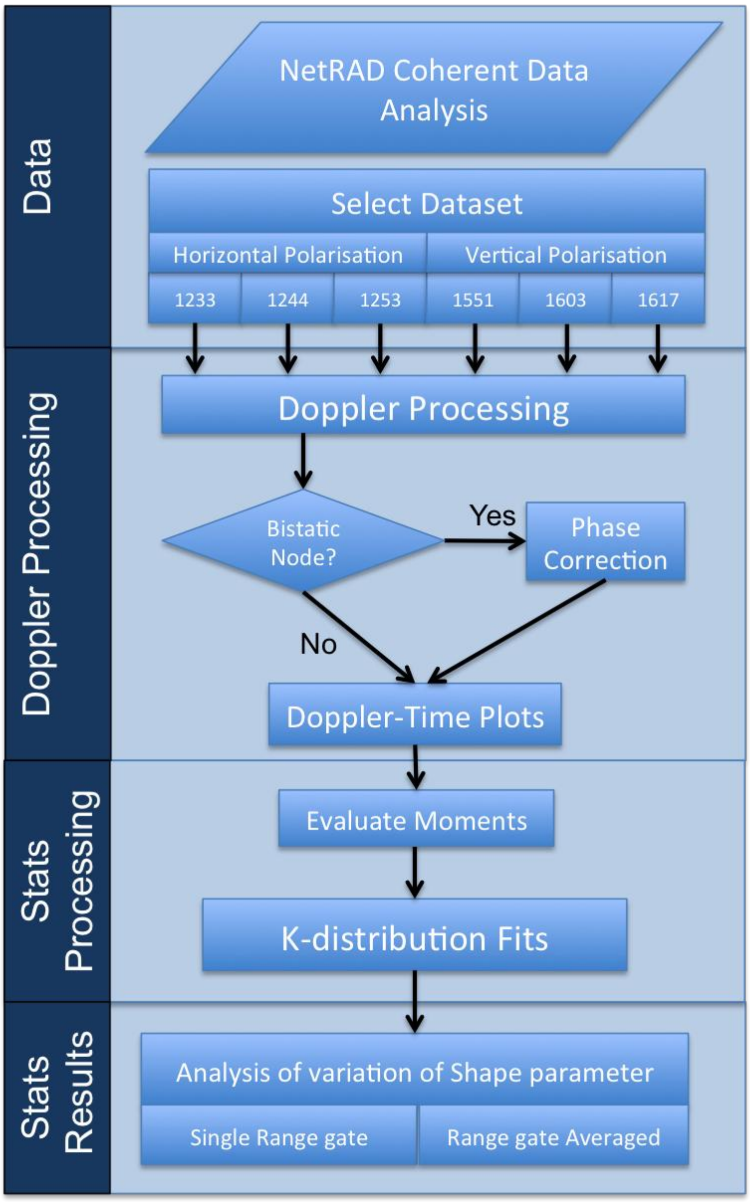

Figure 4.60: NetRAD Coherent data analysis flow diagram

The Doppler-time spectrogram from an example range gate in both the monostatic and bistatic nodes for datasets 1233, 1244, 1253, 1551, 1603 and 1617 respectively are shown in Fig. 4.61, 4.62, 4.63, 4.64, 4.65 and 4.66.

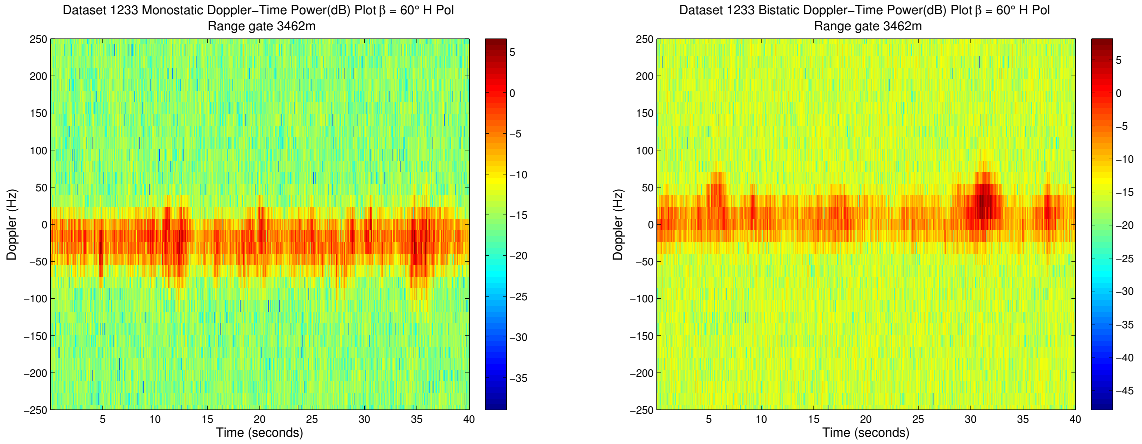

(a) (b)

Figure 4.61: NetRAD Dataset 1233 Bistatic Angle 60° Horizontal Polarisation Doppler Time plots from example range gate 3462 m (a) Monostatic (b) Bistatic

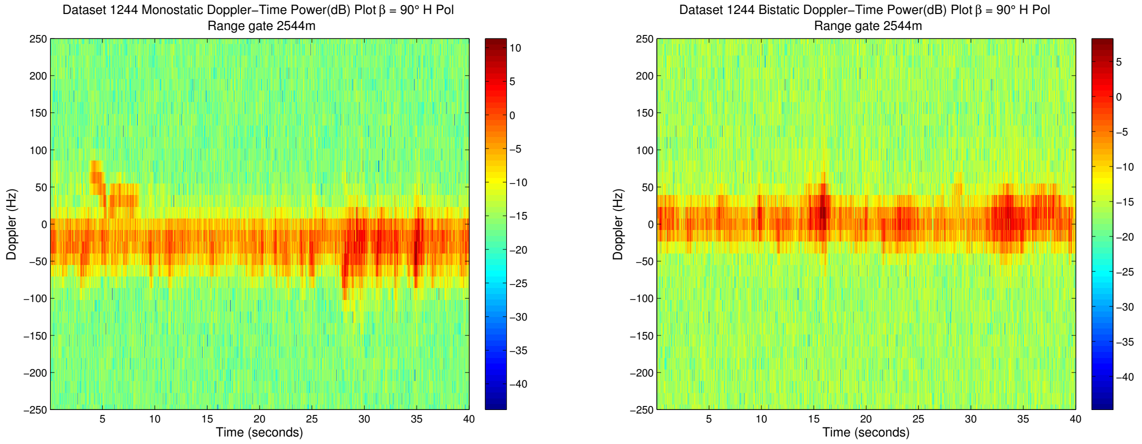

(a) (b)

Figure 4.62: NetRAD Dataset 1244 Bistatic Angle 90° Horizontal Polarisation Doppler Time plots from example range gate 2544 m (a) Monostatic (b) Bistatic

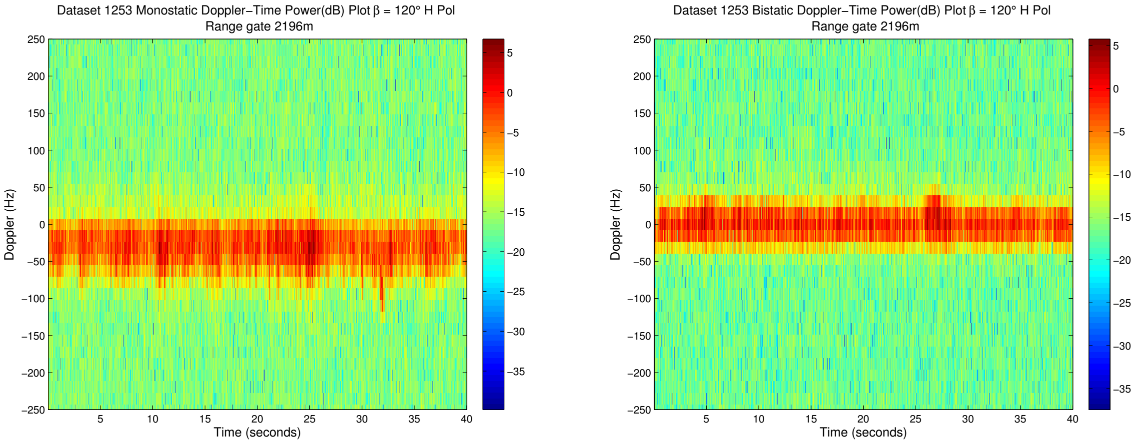

(a) (b)

Figure 4.63: NetRAD Dataset 1253 Bistatic Angle 120° Horizontal Polarisation Doppler Time plots from example range gate 2196 m (a) Monostatic (b) Bistatic

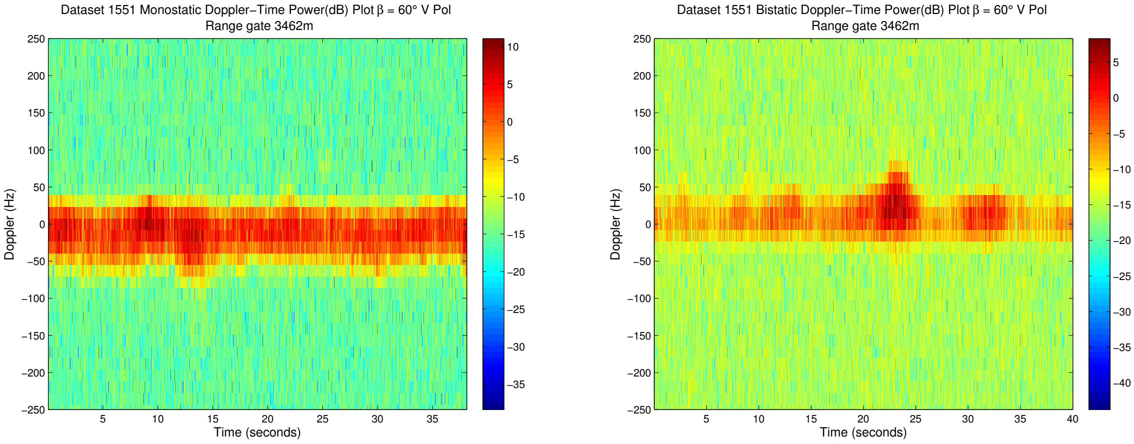

(a) (b)

Figure 4.64: NetRAD Dataset 1551 Bistatic Angle 60° Vertical Polarisation Doppler Time plots from example range gate 3462 m (a) Monostatic (b) Bistatic

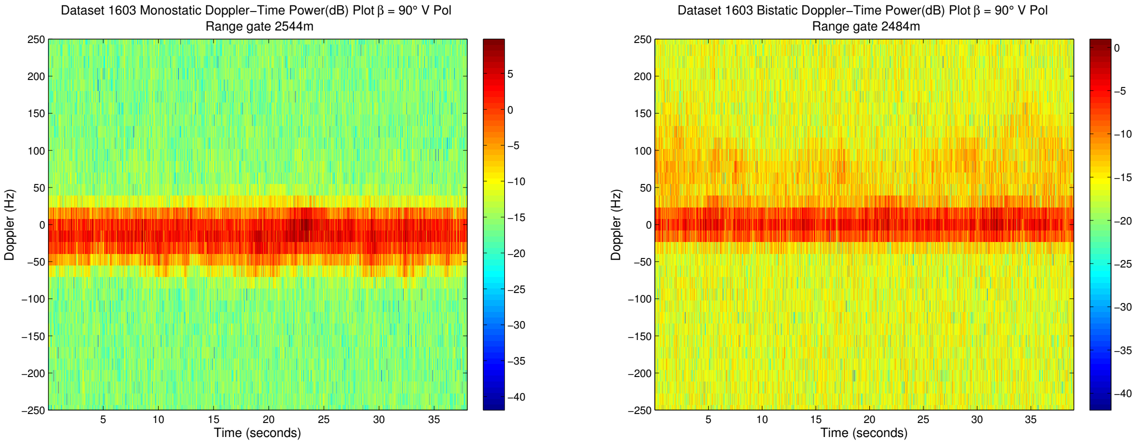

(a) (b)

Figure 4.65: NetRAD Dataset 1603 Bistatic Angle 90° Vertical Polarisation Doppler Time plots from example range gate 2484 m (a) Monostatic (b) Bistatic

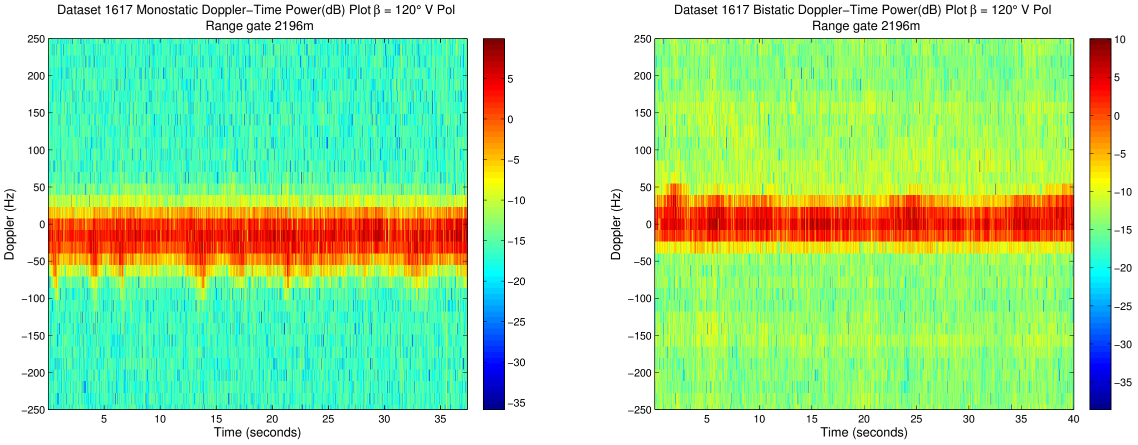

(a) (b)

Figure 4.66: NetRAD Dataset 1617 Bistatic Angle 120° Vertical Polarisation Doppler Time plots from example range gate 2196 m (a) Monostatic (b) Bistatic

The amplitude statistics from all the NetRAD datasets have been evaluated using the same methods applied to the CSIR dataset Doppler analysis, Section 4.2.2. An example SSD fitted log(P_{FA}) vs. threshold plot from in the outer thermally noise limited Doppler bin at -234.375 Hz for both monostatic and bistatic nodes in dataset 1233 are shown in Fig. 4.67. The distributions were both fitted to the highest possible K-distribution shape parameter allowable in the SSD fitting process. This shows that both the monostatic and bistatic data have a well behaved noise floor within the Doppler for dataset 1233. This check was repeated for all datasets to ensure that similar interference issues that were seen in the CSIR data did not exist. During this check it was clear that interference was present within the monostatic node data for datasets 1551, 1603 and 1617. A thresholding process similar to that used to remove the CSIR coherent data interference was also applied to the monostatic data in these datasets.

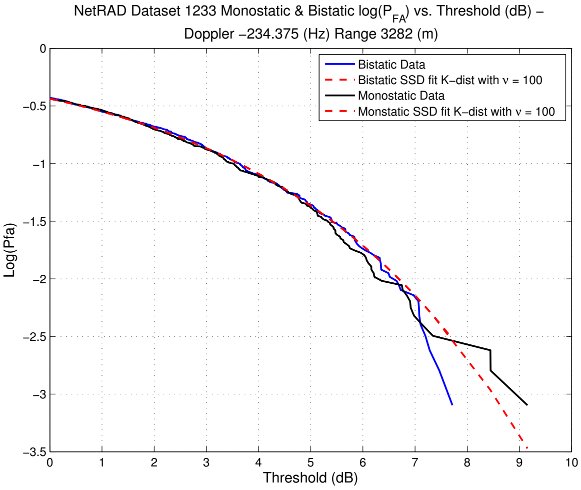

Figure 4.67: NetRAD Dataset 1233 - $\beta = 60°$ Horizontal Polarisation - Monostatic and Bistatic Log(P_{FA}) vs. Threshold data and SSD fitted K-distribution curve. Range 3282m, Doppler - 234.375 Hz

After thresholding of the monostatic data in datasets 1551, 1603 and 1617 the SSD and moment fittings methods were applied to all available data. The results of the moment fitted shape parameters plotted against the range gates of interest and Doppler bin are shown in Fig. 4.68, 4.69, 4.70, 4.71, 4.72, and 4.73. These show clear characteristic shapes in the variation of the amplitude statistics that vary with Doppler, as well as showing the variation that this behaviour has between monostatic and bistatic data and bistatic angle.

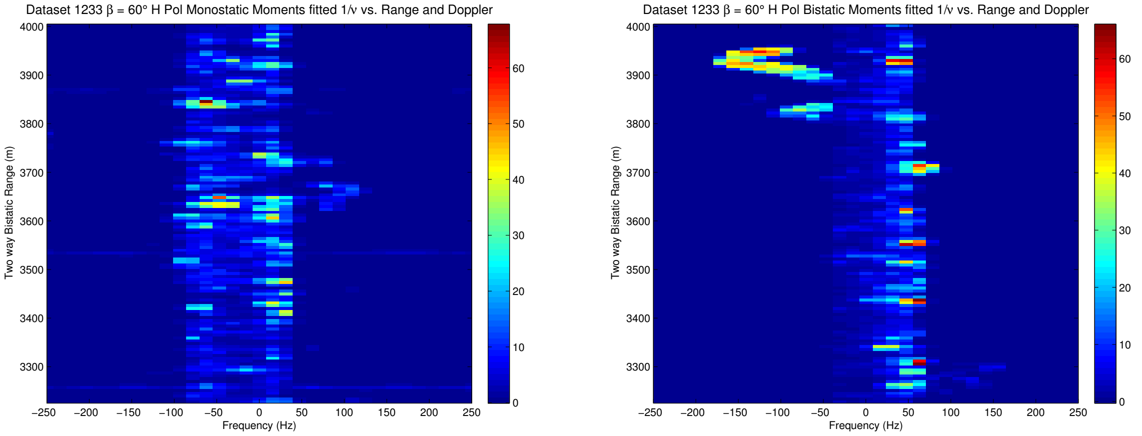

(a)

(b)

Figure 4.68: NetRAD Dataset 1233 Bistatic Angle 60° Horizontal Polarisation Moment fitted $1/\nu$ vs. Range and Doppler (a) Monostatic (b) Bistatic

The increased $1/\nu$ values in a curved shape within in Fig. 4.68, between range 3800 m and 4000 m at a Doppler frequency -50 Hz to -200 Hz, stand out from the bulk variation of ν. As it is at Doppler frequencies significantly separated from the main clutter spectra then it will be considered to be a feature that was not generated by sea clutter.

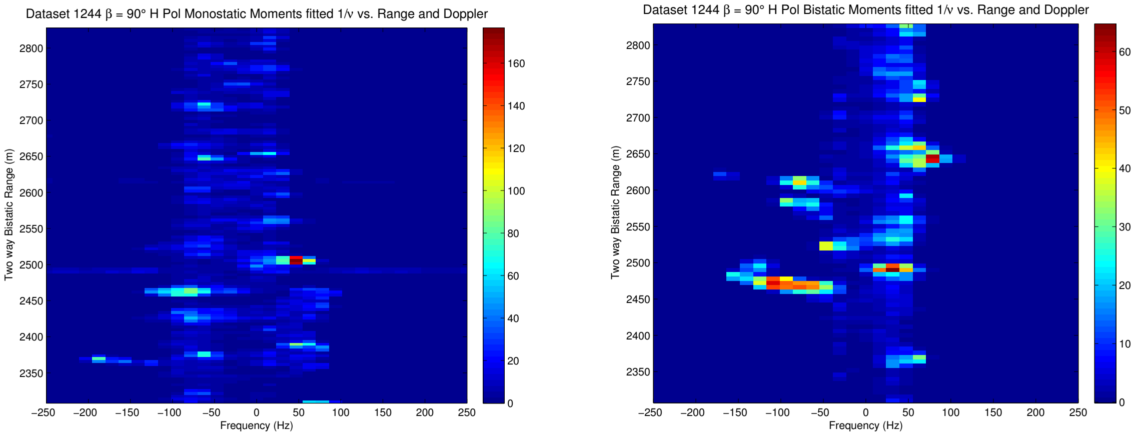

(a)

(b)

Figure 4.69: NetRAD Dataset 1244 Bistatic Angle 90° Horizontal Polarisation Moment fitted $1/\nu$ vs. Range and Doppler (a) Monostatic (b) Bistatic

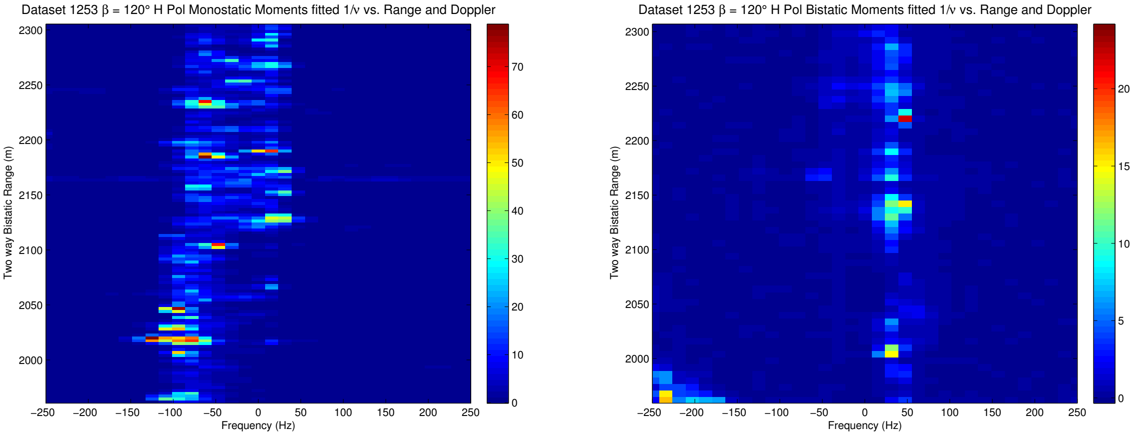

(a)

(b)

Figure 4.70: NetRAD Dataset 1253 Bistatic Angle 120° Horizontal Polarisation Moment fitted $1/\nu$ vs. Range and Doppler (a) Monostatic (b) Bistatic

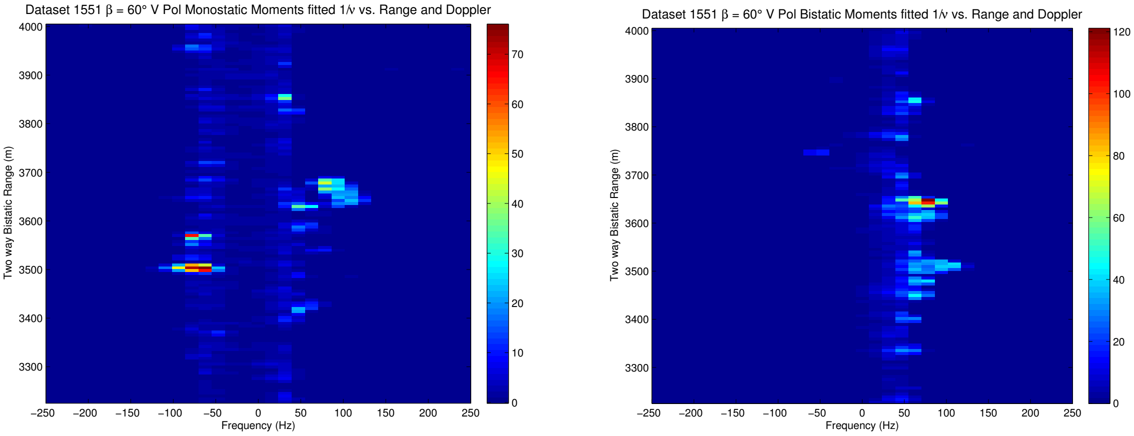

(a)

(b)

Figure 4.71: NetRAD Dataset 1551 Bistatic Angle 60° Vertical Polarisation Moment fitted $1/\nu$ vs. Range and Doppler (a) Monostatic (b) Bistatic

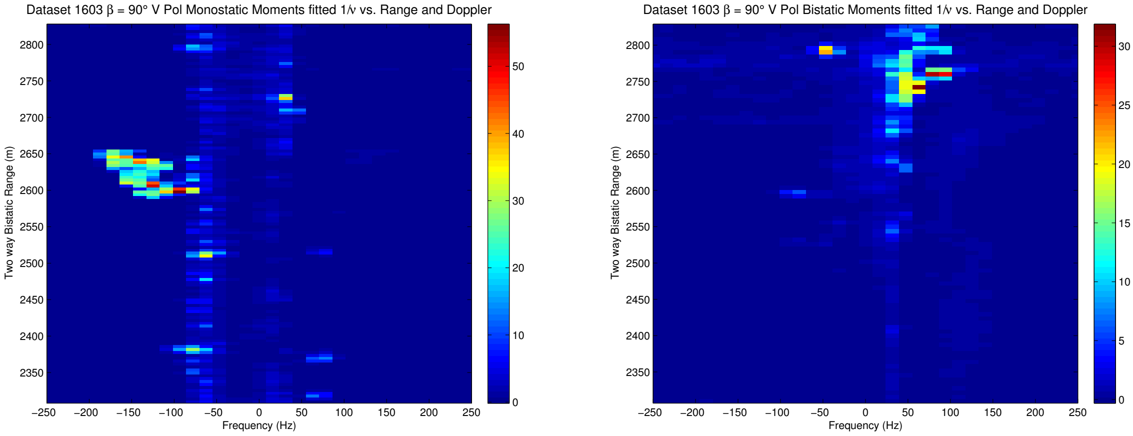

(a) (b)

Figure 4.72: NetRAD Dataset 1603 Bistatic Angle 90° Vertical Polarisation Moment fitted $1/\nu$ vs. Range and Doppler (a) Monostatic (b) Bistatic

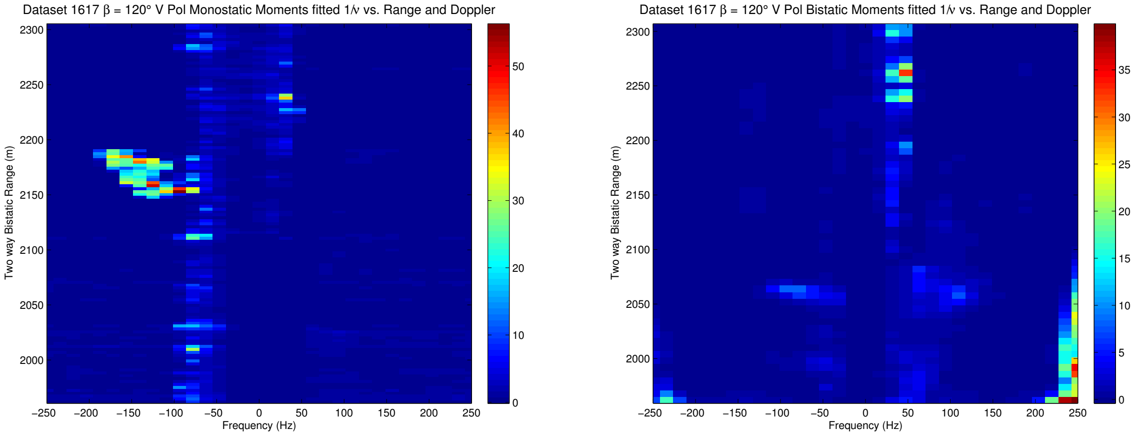

(a) (b)

Figure 4.73: NetRAD Dataset 1617 Bistatic Angle 120° Vertical Polarisation Moment fitted $1/\nu$ vs. Range and Doppler (a) Monostatic (b) Bistatic

For the two datasets 1603 and 1617, Fig. 4.72 and 4.73, the $1/\nu$ values are shown to decrease significantly at shorter ranges. For dataset 1603 this occurs at ranges $<$ 2650 m and for 1617 reduced values are seen for ranges $<$ 2200 m. This significant reduction in shape parameter is linked to the changes seen in the RTI plots for both of these datasets, Fig. 4.55 and 4.56 respectively. At these reduced range for these two datasets non-sea clutter affects are shown to dominate the RTI plots, and hence the statistics of the data is also shown to change. In the further range averaged analysis of these datasets these component of the data has been removed.

The significant amount of information that is shown in the shape parameter vs. range and Doppler has been further summarised using averaged shape parameter values from selected range gates. The average SSD and moment fitted shape parameters for datasets 1233, 1244, 1253, 1551, 1603 and 1617 are plotted in Fig. 4.74, 4.75, 4.76, 4.77, 4.78 and 4.79 respectively.

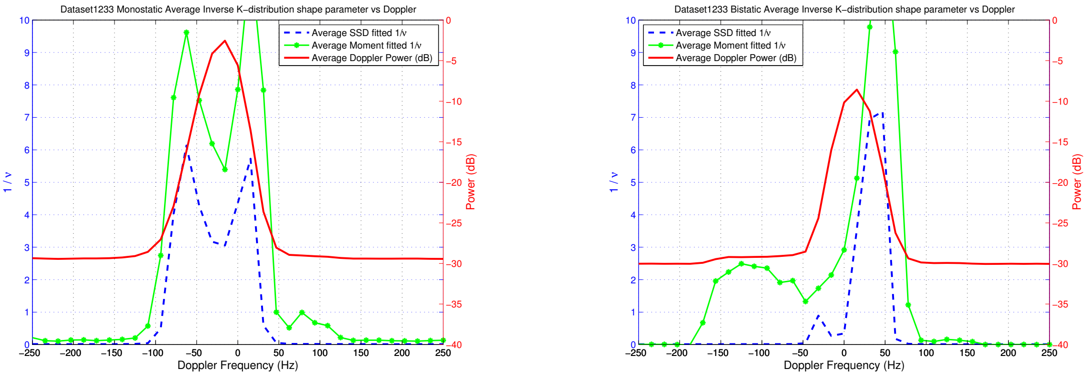

(a)

(b)

Figure 4.74: NetRAD Dataset 1233 Bistatic Angle 60° Horizontal Polarisation Average SSD and Moment fitted $1/\nu$ vs.Doppler (a) Monostatic (b) Bistatic

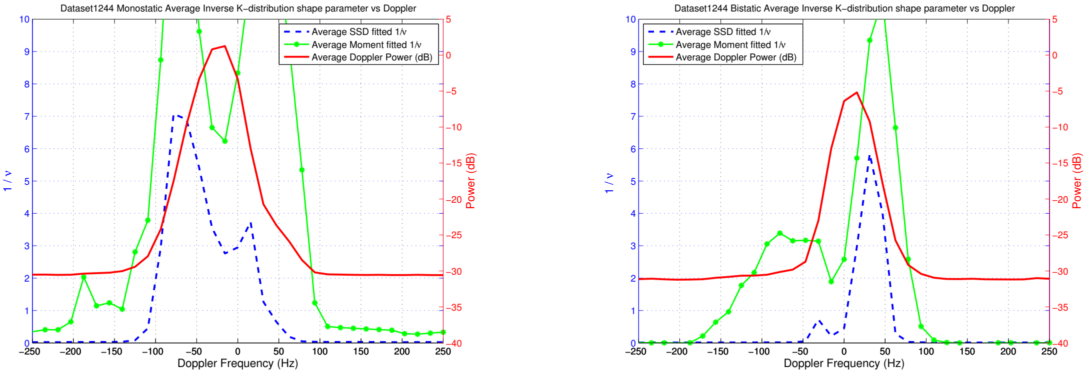

(a)

(b)

Figure 4.75: NetRAD Dataset 1244 Bistatic Angle 90° Horizontal Polarisation Average SSD and Moment fitted $1/\nu$ vs.Doppler (a) Monostatic (b) Bistatic

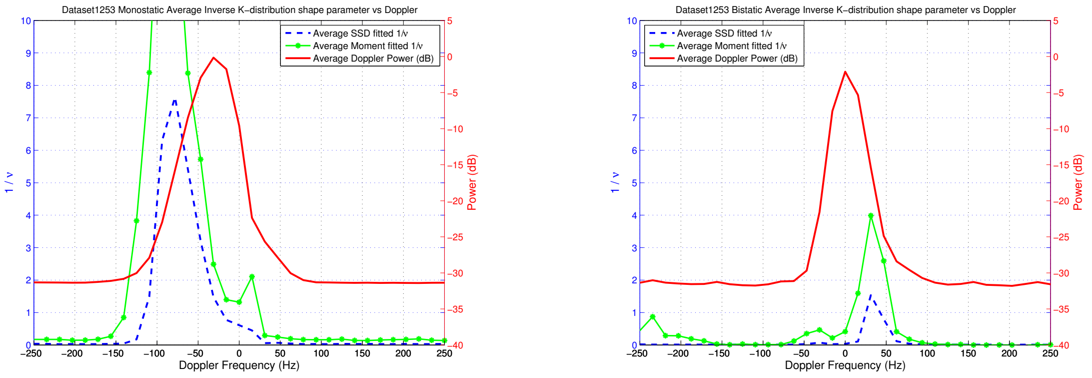

(a)

(b)

Figure 4.76: NetRAD Dataset 1253 Bistatic Angle 120° Horizontal Polarisation Average SSD and Moment fitted $1/\nu$ vs.Doppler (a) Monostatic (b) Bistatic

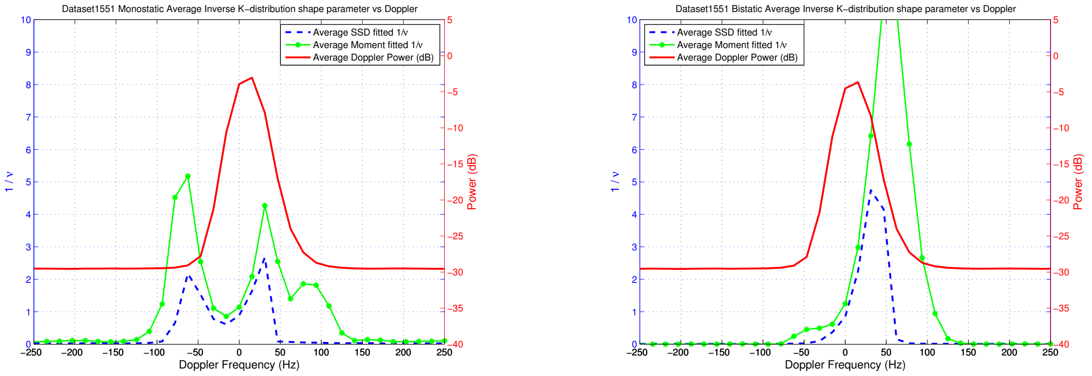

(a)

(b)

Figure 4.77: NetRAD Dataset 1551 Bistatic Angle 60° Vertical Polarisation Average SSD and Moment fitted $1/\nu$ vs.Doppler (a) Monostatic (b) Bistatic

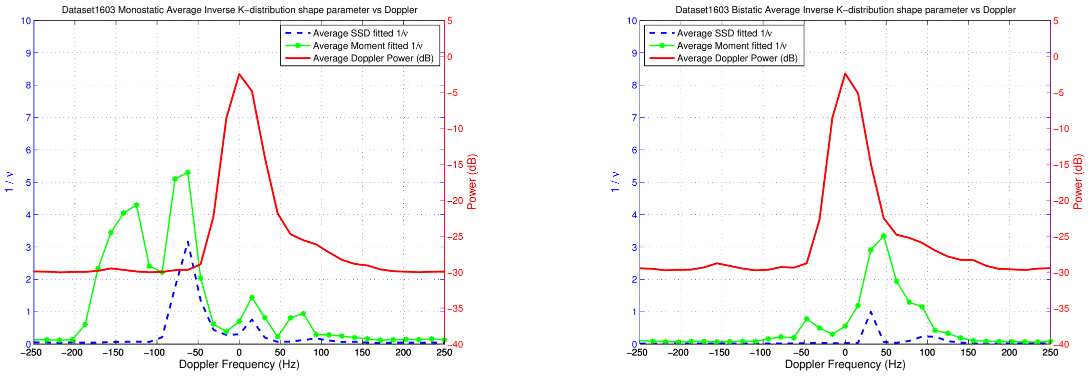

(a) (b)

Figure 4.78: NetRAD Dataset 1603 Bistatic Angle 90° Vertical Polarisation Average SSD and Moment fitted $1/\nu$ vs.Doppler (a) Monostatic (b) Bistatic

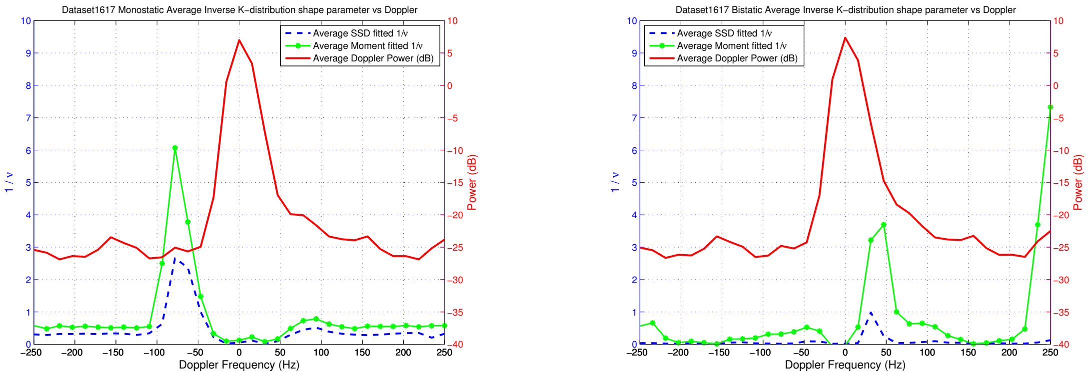

(a) (b)

Figure 4.79: NetRAD Dataset 1617 Bistatic Angle 120° Vertical Polarisation Average SSD and Moment fitted $1/\nu$ vs.Doppler (a) Monostatic (b) Bistatic

A key characteristic that is obvious when comparing the monostatic and bistatic result, in the majority of cases, is that the monostatic $1/\nu$ variation shows a double peak, whereas the bistatic result has a single peak. This comparison is clearest in datasets 1233, 1244, 1551 & 1603 where both SSD and moment fitted $1/\nu$ values show a double peak in the monostatic case and single in bistatic.

In datasets 1233 and 1244 there is a wide increase in the moment $1/\nu$ values in the bistatic case to the left of the single peak, ≈-175 Hz to -50 Hz for 1233 and ≈-125 Hz to -25 Hz for 1244, but this has a very different characteristic in comparison to the clear double peak seen in the monostatic case.

The two datasets that do not have double peaks in the monostatic are 1253 and 1617. Dataset 1253 shows single peak in the SSD $1/\nu$ values, the moment fitted $1/\nu$

values do have a secondary peak that is very low relative the to main peak. In the case of the 1617 dataset a single peak is shown in both the SSD and moment fitted values. The loss of the second peak was not due to a reduction in CNR as both datasets have CNR levels that are comparable to the other datasets. A reason for this change could be that at the geometries used to generate these datasets the sea conditions are altered. As the bistatic angle increases from 60° to 120° the patch of sea illuminated is shifted towards the shore. This shift may be causing the change in the 120° datasets 1253 and 1617 as the sea clutter is now very much in the littoral environment.

When comparing the SSD fitted peak $1/\nu$ values between monostatic and bistatic datasets the bistatic data is shown to be less spiky for $\beta = 90°$ & $120°$, but more spiky for the $\beta = 60°$ case in both polarisations.

4.3.4 NetRAD Data Analysis Conclusions

The analysis showed a direct comparison of how spiky the clutter distributions were as a function of Doppler for both the monostatic and bistatic case. As the datasets were measured on the same day within hours of each other the assumption is made that the same sea state is maintained between datasets. This is assumption is reinforced by the meteorological measurements, seen in Table. 3.12, which show the conditions remained $\approx$ the same between measurements. This is of significant importance as understanding how the amplitude distributions vary with β will enable radar engineers to design systems that can use this information to operate at β angles that minimise the spiky clutter. Therefore allowing a reduction in the threshold level set for the same P_{FA} which will make the system more sensitive to detections of targets within the clutter.

Chapter 5

Modelling and Simulation of Sea Clutter

This chapter looks at a technique developed by S. Watts to model and then simulate coherent sea clutter spectra. It describes an implementation of that model and shows its application to a wider range of clutter data than that used by S. Watts. This work is able to show connections between some of the parameters which is a step towards reducing the number of required parameters.

The model is based on a Gamma distributed coherent texture with a Gaussian shape PSD that varies in location and width in time. The Gamma distributed texture links to the K-distribution which uses a Gamma texture and a Rayleigh speckle component, Section 2.3.4.

As has been described previously it is an important scientific and radar engineering based objective to classify the behaviour of sea clutter. This knowledge can then feed into developing models that can represent both the quantitative and qualitative qualities of sea clutter. These models can be used to simulate sea clutter samples under a number of input conditions. By simulating sea clutter in different conditions it is possible to test new algorithms or radar hardware, therefore minimising the time consuming and expensive process of real world trials, [5]. These results from using simulated sea clutter data can give predicted performance results or allow for testing of new algorithms, which is vital when evaluating a maritime radar.

The model, applied in this work, uses a number of input parameters taken from real sea clutter Doppler spectra to simulate coherent clutter which aims to replicate the statistics of the original data. The simulated clutter is well representative of both the qualitative shape, the amplitude values, correlation and variation in statistical characteristics with Doppler.

To characterise the model the input parameters required will first be defined. The mathematical techniques used to simulate the coherent clutter are then detailed, in Section 5.1. Once the model is fully described real sea clutter data is used to extract the relevant characteristic parameters needed as inputs (Section 5.2). The methods of extraction of each input is detailed, demonstrating example parameter values for each component. The variation of the input parameters within and between datasets is also a key point of discussion in this section. Finally the simulation process is explained and the resulting simulated sea clutter spectra are compared to the original input Doppler spectra, in Section 5.3. Both the real values and the statistical nature of both data and simulation are compared.

The key strength of this model it is that is capable of reproducing the key features that are observed within real sea clutter datasets, as well as the behaviour of the statistical variation with Doppler. The key features extracted include :

- Asymmetric shape observed within the Doppler PSD.
- The variation of the clutter spectra with time due to its non-stationarity. Which is seen via the widening, shifting in centre of gravity and contracting of the spectra in time.
- The variation in amplitude statistics behaviour with Doppler observed in real data. See Section 4.2.2.

Additional recent work on modelling sea clutter was developed within [94]. This does also allow for the generation of k-distributed sea clutter, but does not create continuous coherent sea clutter samples that are directly comparable to real observed spectra.

5.1 Coherent sea clutter model description

The model applied in chapter was first proposed by S. Watts in [11] and later more fully defined within [123]. It was originally based on qualitative and quantitative analysis of the structure of temporal variation of sea clutter Doppler spectra within an individual range gate. The computer code to execute the simulation model for this work was generated independently from the original work. A thorough understanding of the method had to be achieved in order to be able to reproduce it, so this chapter contains some more explanations of some parts of the process than is found in the references. The model was then was applied to further datasets than those in [11] to analyse the effectiveness of the model under a wide range of conditions.

The first set of data originally used in [11] was taken from the CSIR 2006 database (CFC17-001). For the work shown in this thesis the data was selected from the CSIR 2007 sea clutter database, which was described in Section 3.1.2. Both the key four datasets extensively analysed in Section 3.1.2 as well as the additional three secondary datasets defined in Table 3.4 are used in this section. This data is well suited to this modelling process as the 2007 CSIR datasets selected were recorded specifically for sea clutter analysis and they have similar properties to the 2006 dataset which has been proved to be suitable for this task. A key advantage is that further testing of the model and its effectiveness with varying datasets can be completed.

By using all eight datasets it is possible to compare the performance of the simulation model as a function of both range and azimuth. In particular the secondary datasets give an additional three sample location in azimuth, and therefore bearing with respect to wind and swell directions. The azimuth of each measurement as well as the wind and wave directions are shown in Fig. 5.1. The wind and swell bearings for the 2007 data were 157.5° N and 235° N respectively. The wind parameters were measured at the radar site itself, while the swell azimuthal direction was measured at $-33.8648°$ S Latitude and $18.3302°$ E Longitude, which is approximately 20km south along the coast from the radar location. Note that the figure does not show the range swath extent to scale, only a unit length is used for each marker. This is because the purpose is only to demonstrate the azimuth of the datasets with respect to the wind and sea direction.

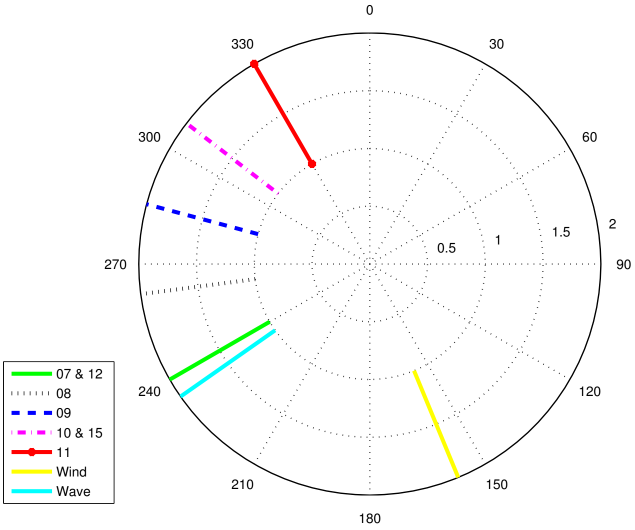

Figure 5.1: CSIR datasets azimuth direction as well as wind and wave azimuth directions

The construction of the model is based on the following components:

- The texture of the sea surface.
- The correlation of the texture.
- The speckle.
- The behaviour of the individual Doppler spectra with time.

Both the non-coherent and coherent properties of the real sea clutter data are required as inputs to the model. Using the compound K-distribution as the basis for the model, the sea clutter texture is defined as a correlated Gamma distribution with a given shape parameter. The Doppler component of the clutter is defined as a Gaussian with a defined location in Doppler and width. This Doppler spectra is then combined with a Rayleigh distributed speckle component producing a joint texture plus speckle Gaussian shaped Doppler spectrogram.

One of the fundamental components that this clutter model introduces is the linking between the centre of gravity of the Gaussian Doppler spectra and the intensity values of the Gamma texture. As the intensity of the Gamma texture increases so does the centre of gravity of the Gaussian PSD. Prior to this model no proposed linked between these two characteristics existed.

In the process of constructing the model the texture of the simulated clutter is produced first. To do this the following inputs are required: number of samples needed, the Gamma texture shape parameter of the texture and correlation. For each time-series of PSD which is simulated, a single sequence of properly-correlated Gamma distributed samples is required. These samples will then be weighted by a Doppler spectrum window. To produce correlated Gamma samples a Memoryless Non-Linear Transform (MNLT) has been used, in a similar approach described in [96]. This method uses an input of normally distributed samples and outputs Gamma distributed values with a desired shape parameter. The key relationship use for converting to a Gamma distribution is,

$$\int_{\eta}^{\infty} P_{dist}(\eta')d\eta' = \frac{1}{\sqrt{2\pi}}\int_{x}^{\infty}\exp(\frac{-x'^2}{2})dx' = \frac{1}{2}erfc(\frac{x}{\sqrt{2}}) \tag{5.1}$$

where the PDF of the values η is the required distribution PDF $P_{dist}(\eta)$. The second equality shows the complimentary error function, *erfc*. This means that the complementary quantile function of the desired distribution must be,

$$\int_{Q_{dist(\xi)}}^{\infty} P_{dist}(\eta)d\eta = \xi \tag{5.2}$$

where $Q_{dist}(X)$ is the complementary quantile function. Using this an MNLT can be defined that uses an input of Gaussian distribution random samples and produces samples with the desired distribution, Gamma in this case.

$$\eta(x) = Q_{dist}(\frac{\mathrm{erfc}(\frac{x}{\sqrt{2}})}{2}) \tag{5.3}$$

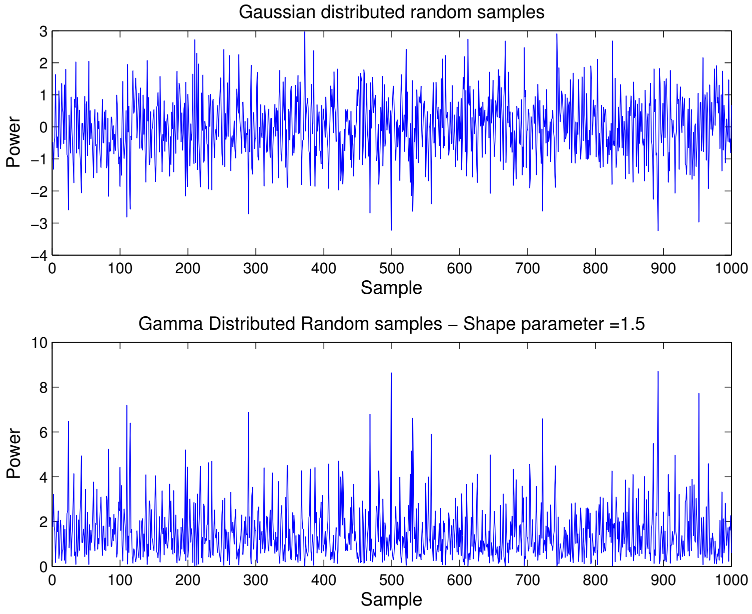

Figure 5.2: Example input Gaussian samples and resulting output Gamma samples with given shape parameter

Using this transform the output samples will be Gamma distributed with a given shape parameter. Figure 5.2 shows the Gaussian samples used to generate Gamma samples with a shape parameter of 1.5. The accuracy of this method of simulating Gamma distributed samples was tested by generating 1x10^5 samples with a range of shape parameters and using method of moments to compare the estimated shape parameter with the input desired shape parameter. This was repeated 100 times for each shape parameter and the average difference between input and estimated shape parameter was evaluated as a function on input shape parameter, see Fig. 5.3. This shows that the difference is <0.003 for all shape parameters between 0.1 and 5.

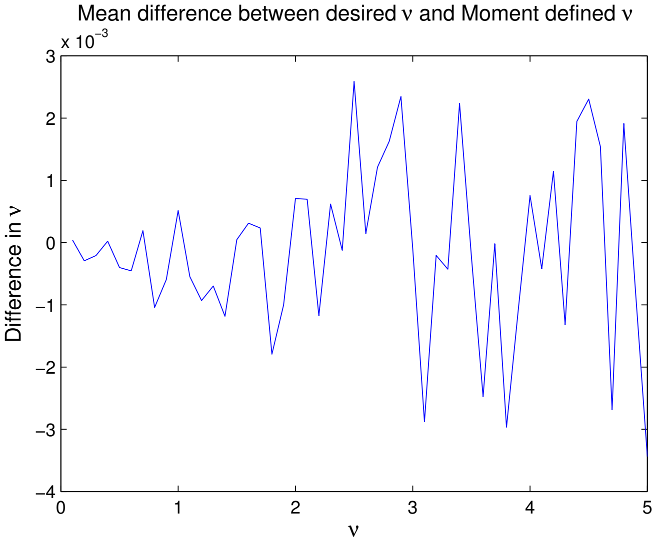

Figure 5.3: Average difference between input shape parameter and estimated shape parameter of Gamma distributed samples

An important issue is that the generated Gamma distributed samples do not have the same correlation as the input Gaussian samples used to generate them. The MNLT process of converting the samples from Gaussian to Gamma distributed does not maintain the correlation. The method used to overcome this is to apply a modified correlation to the input normal distributed samples prior to their conversion to Gamma distributed samples. A transfer function from the input correlation to output correlation was used to map the relationship between the desired ACF and the required input modified ACF prior to MNLT. This was defined in [96] as the following,

$$< \eta(0)\eta(t) >= \frac{1}{\pi}\sum_{n=0}^{\infty}\frac{R_G(t)^n}{2^n n!}\left(\int_{-\infty}^{\infty}dx\,\exp(-x^2)H_n(x)Q_{dist}\left(\frac{\mathrm{erfc}(x)}{2}\right)\right)^2 \tag{5.4}$$

where $R_G(t)$ is the ACF value at a given lag (t) and H_n is the Hermite polynomial. This integral was evaluated numerically in Matlab to produce a lookup table for correlation values relating an input ACF to the output ACF after MNLT processing. The numerical evaluation was completed for increasing values of n, as the series is rapidly convergent, especially when $\nu > 1$, only a few increments of n are required obtain a very accurate solution. It is stated that for $\nu = 2$ the first two terms of this series contain 92% of the output correlation function [23]. The relationship evaluated for a series of shape parameters (0.1, 0.2, 0.3, 0.5,1, 2, 3, 5 & 10) can be seen in Fig. 5.4.

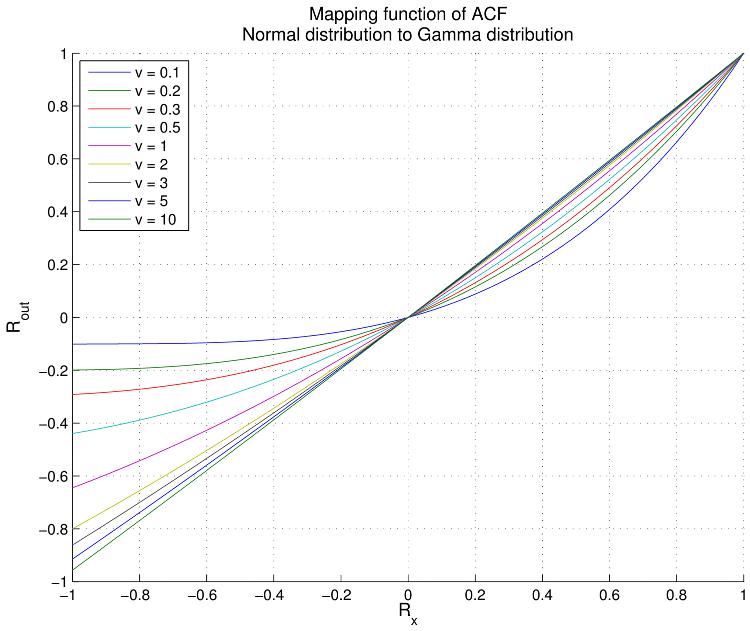

Figure 5.4: ACF conversion function between input ACF and output ACF from a MNLT transform - Using a range of shape parameters

An initial test produced Gamma samples from input correlated normal distributed samples. The correlation applied was modified from the actual desired correlation using the mapping function seen in Fig. 5.4. A comparison of the desired ACF, the modified input ACF and the output ACF after MNLT processing can be seen in Fig. 5.5. The desired correlation was defined as a exponentially decaying cosine function,

$$ACF_{Desired} = \cos(\frac{x}{100})\exp(-\frac{x}{400}) \tag{5.5}$$

This is because qualitatively sea clutter correlation is reasonably represented by a this function. The desired and actual output ACF in Fig. 5.5 are very similar showing that the process is successfully able to produce correlated Gamma samples.

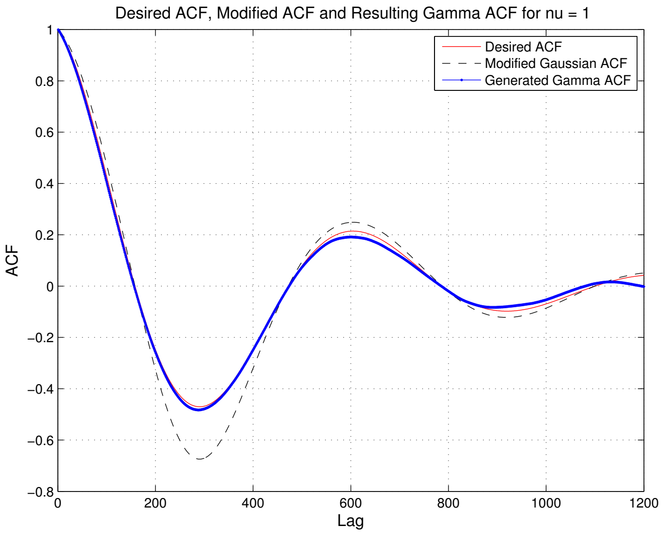

Figure 5.5: Example simulated Gamma samples ACF. Showing desired ACF, modified ACF and actual samples ACF

The actual input Gaussian correlated samples and the output Gamma correlated texture samples are shown in Fig. 5.6. The Gamma samples in this figure represent typical texture amplitude values that would be used in this model to simulate the clutter.

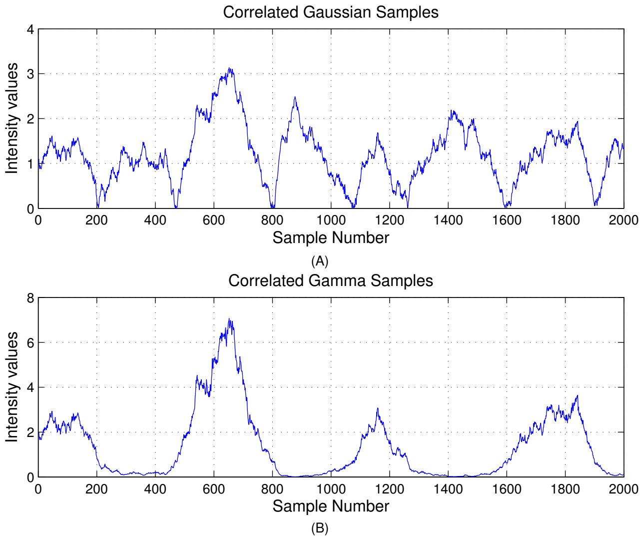

Figure 5.6: (A) Example simulated correlated Gaussian samples with modified ACF and (B) Gamma samples with $\nu = 1$ and desired ACF

To generate individual short time spectra from the extracted parameters the M texture samples were weighted using a varying Gaussian PSD defined over N points. This produces a set of Doppler spectra of size M x N where N is the number of Doppler bins present.

Each of the Gaussian PSDs is random with defined mean width and centre of gravity. The width of the Gaussian is obtained from normally distributed randomly varying value with a set mean and variance. The mean and variance are set by the input data that is being simulated. The model applies a correlation to the width values to ensure a smooth transition of spectra widths from each subsequent spectra. This is achieved by under sampling the required spectra width values, M, and interpolating between them. In this case every tenth width value was generated and then interpolation was applied to produce the intermediate values.

In the sea clutter model the centre of gravity of each Doppler spectrum is linearly related to the intensity of the spectrum. This was defined from qualitative observations of the spectra's relationship with intensity, where a trend was observed in the time domain of an increase in the PSD intensity this was linked directly to an increased shift in the PSD centre of gravity away from its long term mean value. The linear relationship is generated from using a straight line fit to intensity vs. centre of gravity samples. The Gamma intensity value for the given PSD being simulated is then used to define its centre of gravity using the linear relationship.

All these values are linked together to produce a simulation of a shifting breathing correlated Doppler spectrum. As noted above, the shape of the spectrum of the texture is assumed to be Gaussian. This is mathematically represented by,

$$G_{sim}(f,x,s) = \frac{x}{\sqrt{2\pi}s}\exp[-\frac{(f-m_f(x))^2}{2s^2}] \tag{5.6}$$

where G_{sim} is the simulated intensity of the texture within a given Doppler bin, x is the mean intensity (defined by the texture), f is the Doppler bin frequency, m_f is the centre of gravity of the Gaussian spectra and s is the standard deviation width of the spectra. The m_f value is related to the intensity through the linearly fitted parameters,

$$m_f = A.x + B \tag{5.7}$$

where A and B are defined from fits to the input data values. The spectrum width itself is a random variable with a Gaussian distribution and with a given PDF,

$$p(s) = \frac{1}{\sqrt{2\pi}\sigma_s}\exp[-\frac{(s-m_s)^2}{2\sigma_s^2}] \tag{5.8}$$

where m_s is the mean spectrum width and σ_s^2 is the variance of the spectrum width. Both of which are obtained from analysing the input clutter spectra that is being simulated, see Section 5.2.

The speckle component was then applied to the values of G_{sim} to ensure both texture and speckle components are present as defined by the K-distribution model. The speckle is represented by a complex independent normally distributed I and Q values. To include the speckle the product of the G_{sim} array and this I and Q component speckle was used.

As in a real radar system added thermal noise was introduced to the resulting texture plus speckle array. This was done at a level that gave the desired CNR for the simulated clutter. The thermal noise was summed with the texture and speckle array to produce the final resulting fully simulated spectra.

5.2 Extraction of parameters from real sea clutter

As defined in the model description, [123], the required parameters for simulation include non-coherent time series values as well as inputs generated from the Doppler analysis. The full list of each parameter needed are listed as follows:

- Non-coherent data parameters:
    - Gamma shape parameter
    - Temporal ACF of texture
- Doppler data parameters:
    - Centre of gravity of the PSD
    - The 3dB widths of each spectrum:
        - Average of the width values
        - Variance of the width values
    - Linear relationship between PSD Centre of Gravity and Amplitude
    - CNR of spectra
        - Relative CNR can be used. It is also possible to correct for absolute signal levels to model the correct levels for a particular radar system.

The following Sections, 5.2.1 and 5.2.2, show examples of each of these parameters in the order defined here. The example dataset selected is 07 from the CSIR 2007 dataset, each of the parameters has example plots using this dataset. In addition to showing examples plots of the parameters the methods used to generate them have been described.

5.2.1 Non-coherent data parameters

The first parameter defined was the non-coherent data texture Gamma shape parameter and the ACF of the texture, for a given range cell. To ensure that the texture component of the data was the focus of this analysis block averaging was imposed on the data with a window of length 64. This removed any speckle component from the time series data leaving only the texture component, as speckle is substantially removed via averaging. An example of the range gate amplitude profile before and after block averaging can be seen in Fig. 5.7. This shows an average shape parameter of 2.17 over all range gates. Some marked increase from this average is seen at range gate ≈ 90 where the values increase up to a maximum of 6. This is unexpected as the data recording is sufficiently long for a number of wave fronts to propagate through each range gate over its duration. Meaning that the same wave fronts would have propagated through successive range gates and should not have induced any markedly different statistics while passing through each range gate. The increase at range gate 90 onwards has been noted and the simulation process for these range gates will be monitored later.

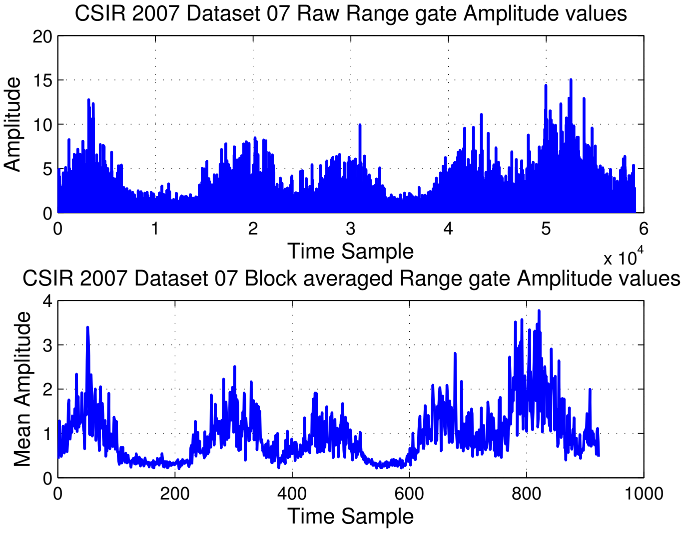

Figure 5.7: CSIR dataset 07 range gate profile before and after block averaging

The Gamma shape parameter values are then obtained from this texture component using moment analysis, which is defined in Section 2.3.4. The relationship between the Gamma shape parameter and the moments of the data is seen in Eqn. 3.9. Using this the moments of the each range gate of data were used to define the Gamma distribution shape parameters. The defined Gamma shape parameters from all range gates within dataset 07 are shown in Fig. 5.8.

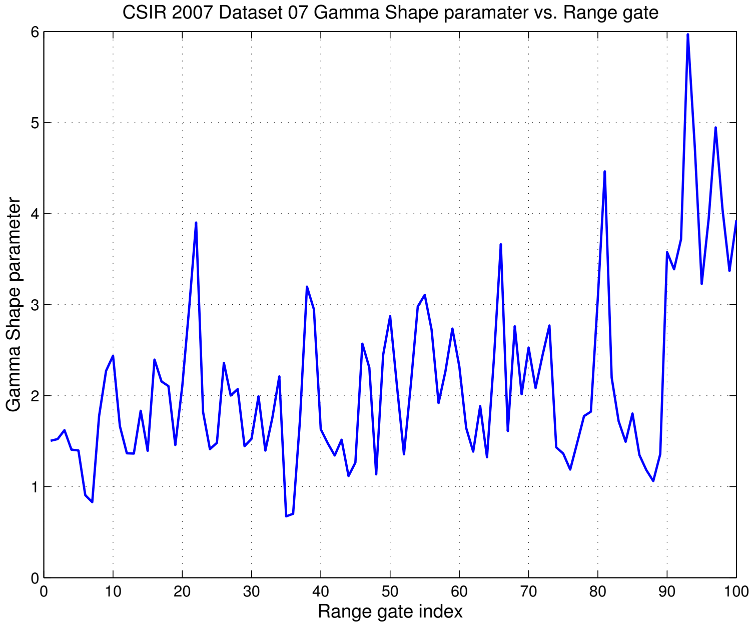

Figure 5.8: CSIR dataset 07 Gamma shape parameter vs. range gate

The number of samples within each range gate that were used to estimate these Gamma shape parameters was 1845. To evaluate a predicted error in this measurement a Monte Carlo simulation was used to estimate the predicted error in the moment estimated shape parameter as a function of shape parameter. 1845 Gamma simulated samples with a defined shape parameter were input to a moment estimator. This process was repeated 1000 times for each shape parameter. Shape parameters between 0.1 and 6 were tested as all the results within Fig. 5.8 reside within this range. The results from the estimation in error are shown in Fig. 5.9. This shows that the estimation error increases with shape parameter, but for the same size sample set all errors should be below 0.18.

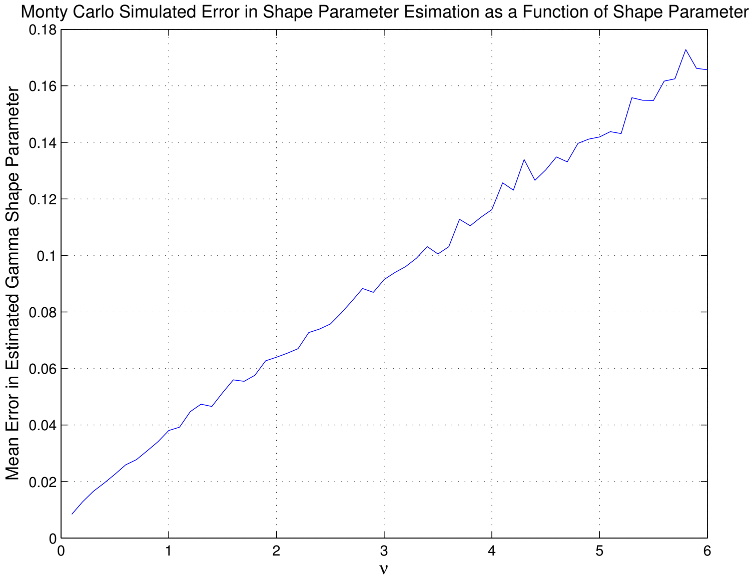

Figure 5.9: Monte Carlo estimated error in moment shape parameter estimation

These shape parameters were then used as inputs for simulating the Gamma distributed correlated components. As described in Section 5.1 the Gamma texture samples also need to be correlated. The ACF of the texture was defined using the same techniques applied in Section 4.2.1. An example ACF from the texture samples within a single range gate in dataset 07 is shown in Fig. 5.10.

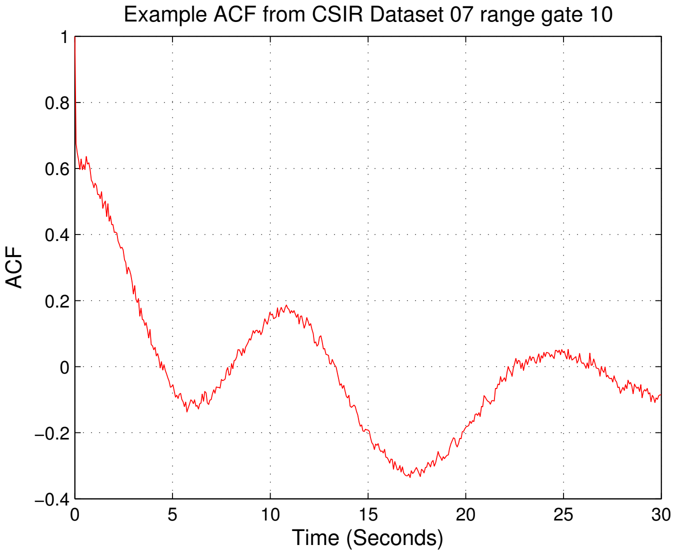

Figure 5.10: CSIR dataset 07 ACF of texture component from range gate 10

The ACF shows a typical two component structure as predicted by previous empirical results, [23]. The fast reduction after the first few lag shifts is the decorrelation of the residual speckle component, while the long scale sinusoidal variation is due to the texture component. The tested artificially generated ACF applied, Eqn. 5.5

in Section 5.1, has a similar decaying sinusoidal structure. Therefore the methods applied should be able to replicate the real clutter correlation without any problems.

5.2.2 Doppler data parameters

The input Doppler spectra used was exactly the same as that used in the previous Doppler analysis in Section 4.2.2. The Doppler data is represented by a 64 Doppler bin by $\approx$ 1845 individual PSDs for each range gate. For this analysis prior to obtaining parameters the Doppler spectra was averaged using a window size of 10 consecutive Doppler spectra. This reduced the originally amount of 1845 individual PSDs for each range down to 184. This method was also applied in the work seen in [11]. The averaging was completed because each spectrum is generated from 64 consecutive samples, with 50% overlap at a PRF of 2 KHz, meaning it covers $\approx$ 16ms in the time domain. This makes each spectra a noisy representation of the actual local spectrum. Therefore by averaging over 10 successive spectra, 128ms in time, a more stable representation of the clutter spectrum is obtained. An example of the short time Doppler spectra before and after the block averaging can be seen in Fig. 5.2.2 (a) and (b) from range gate 10 taken from dataset 07.

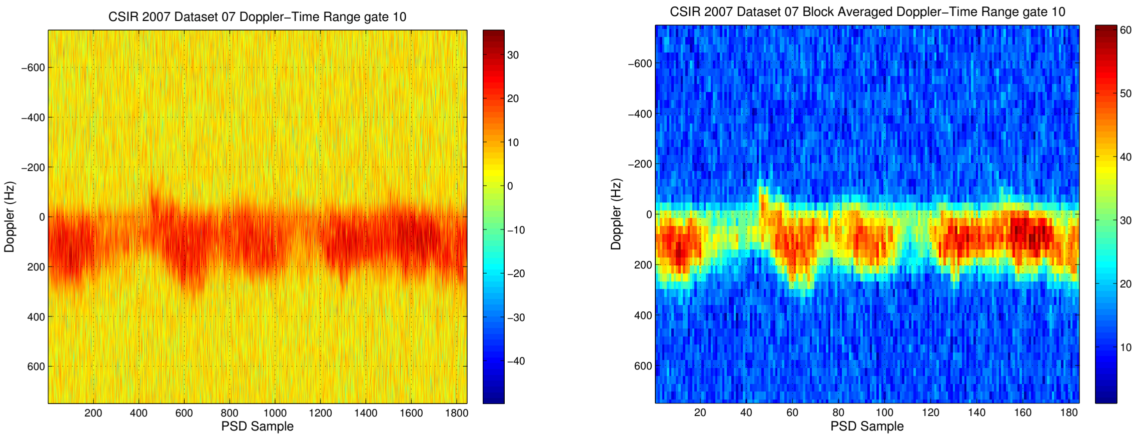

(a)

(b)

Figure 5.11: CSIR dataset 07 Doppler-time spectra (a) Before averaging (b) After block averaging

The averaged spectra from each range gate was then analysed to obtain the centre of gravity as a function variation across all the spectra from a given range gate. This centre of gravity was evaluated using the following equation,

$$x_{CoG} = \frac{\sum_{i=1}^{n} (PSD_i.F_i)}{\sum_{i=1}^{n} PSD_i} \tag{5.9}$$

where x_{CoG} is the frequency value of the PSD centre of gravity, PSD_i is the PSD power value for Doppler bin i and F_i is the Doppler frequency of Doppler bin i. The results from multiple range gates within the CSIR 2007 dataset 07 can be seen in Fig. 5.12.

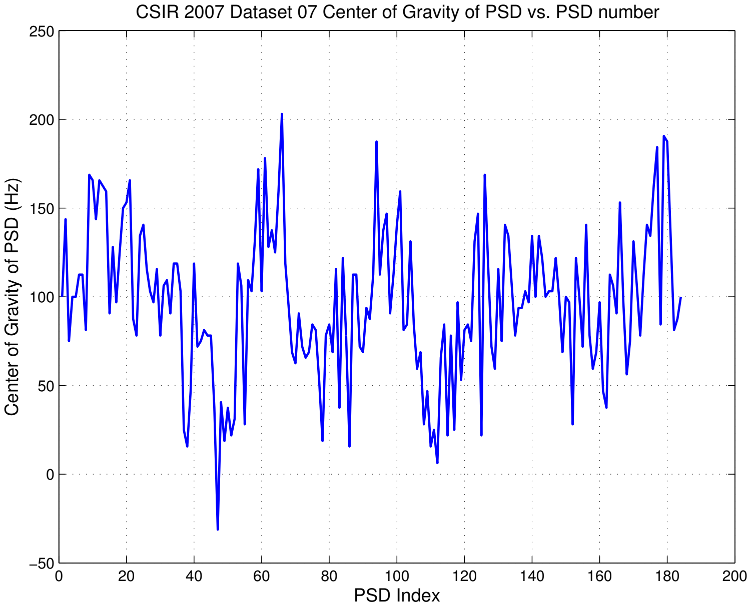

Figure 5.12: CSIR dataset 07 averaged PSD spectra centre of gravity vs. PSD index from single range gate

The model assumes a linear relationship between the centre of gravity and the intensity of each spectra. This was first proposed by S. Watts within [11] and has been shown to be valid in further publications [123, 124]. The values shown in Fig. 5.12 were plotted against the intensity of the PSDs and a standard linear regression fit [?] was applied, see Fig. 5.13. The scaling of each axis within Fig. 5.13 is different to allow the whole dataset to be clearly shown within the plot. The linear fit, y = A + B.x, for range gate 20 was found to be y = 16.6x + 34.2.

The apparent perception that some extreme values are being neglected in the fit within Fig. 5.13 is resolved when we appreciate that there is actually a high density of point clustered near the line. This is particularly true for intensity values between 2 - 4 and Doppler shifts between 50 - 150 Hz. The confidence in the fits applied is further enhance when observing the consistence within the averaged fitted parameter values shown later within Fig. 5.19 and Fig. 5.20.

The samples within Fig. 5.13 show a large standard deviation from this linear relationship, particularly at lower intensity values. It is shown that for the larger intensity values a more direct linear relationship is apparent in the few large intensity values. This shows that at the lower intensity values of the texture the clutter is likely to have a larger standard deviation from the averaged offset in Doppler. As the intensity increases it is the fewer high intensity texture events that produce a clearer change in the spectra centre of gravity that results in the main body of the sea clutter shifting out in Doppler from its mean location. The importance should therefore be place on ensuring the linear fit follows the trend of the few large intensity values while being centrally located within the bulk of the numerous lower intensity values.

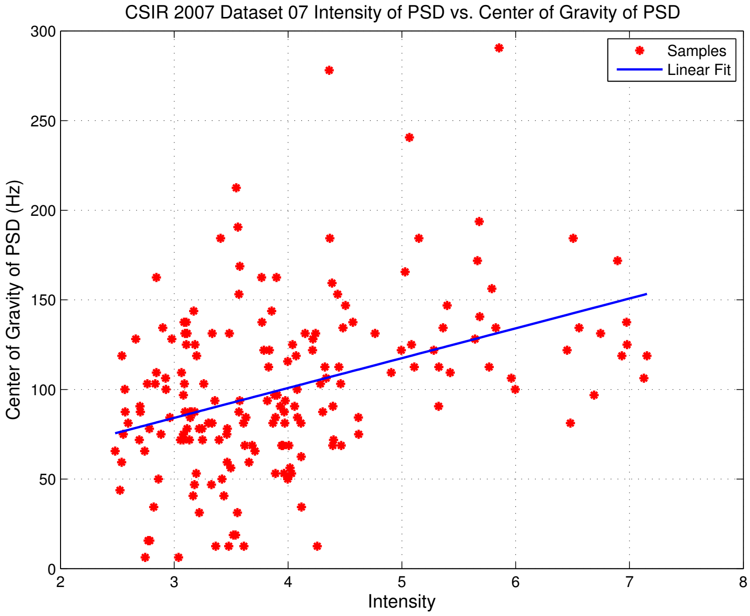

Figure 5.13: CSIR dataset 07 PSD intensity vs. centre of gravity

Both of the fitted linear parameters A and B have been plotted as a function of range gate in Fig. 5.14 from dataset 07. The mean and standard deviation values of A are 62, and 23.3, for B the same values were 11.1 and 5.6 respectively. The gradient of the fit (B) is consistently positive for all range gates. This shows that the linear fit was always found to have the same positive sloping value which validates that the major axis of the cluster of points is always in the same positively sloping direction.

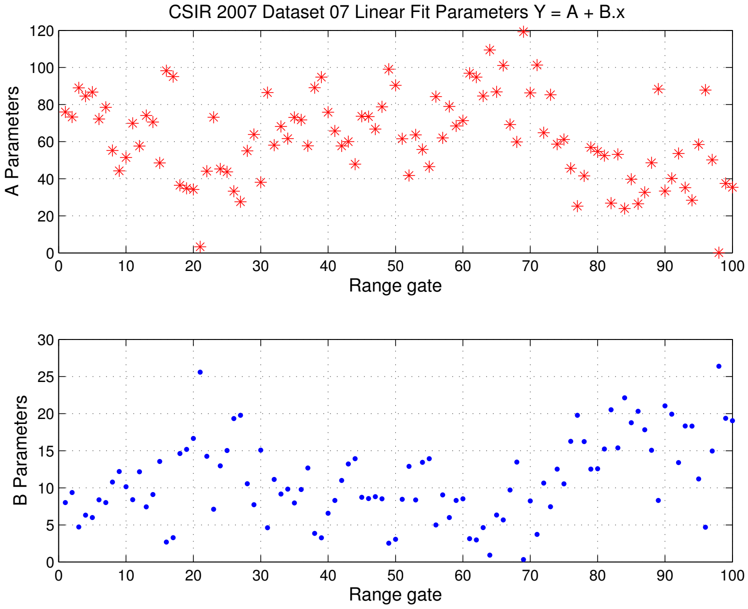

Figure 5.14: CSIR dataset 07 Linear fit parameters A and B vs. range gate

The linear fit process was then completed on all four CSIR datasets. The first comparison is between the plots of intensity vs. centre of gravity plots from individual example range gates, as in Fig. 5.12 for dataset 07. The plots for datasets 10, 12 and 15 are seen in Fig. 5.2.2 (a) (b) and (c). Similar to the dataset 07 result, Fig. 5.13, these example plots all show a large dispersion in the data points, in particularly for the lower intensity results. Again the confidence in the validity of these fits is reinforced when the overall averaged values are compared with the bearing used when the data was recorded. The clear trends between datasets show that the assumption that a linear fit can be effectively applied to the data is legitimate.

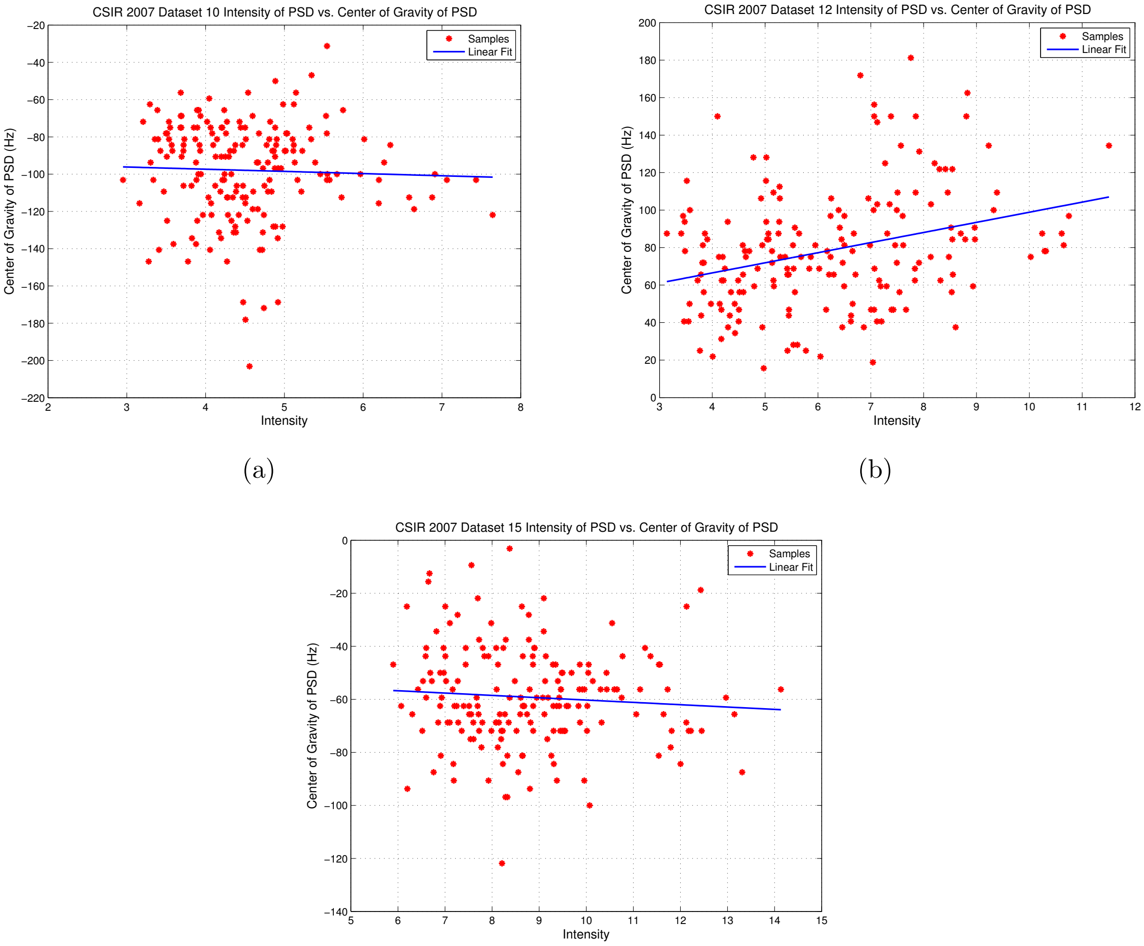

(a) (b)

(c)

Figure 5.15: CSIR datasets centre of gravity of PSD plotted against intensity with linear fit applied (a) Dataset 10, (b) Dataset 12, (c) Dataset 15

The linear fits as a function of range gate from dataset 10, 12 and 15 can be seen in Fig. 5.16, 5.17 and 5.18 respectively. The additional datasets 08, 09 and 11 have not been plotted here as do not give any additional information that can not already be seen within these figures. All datasets show a similar trend in parameter fits across range, with no net mean increase of decrease shown as a function of range. In some cases it is apparent that consecutive range gates show a correlation in parameters are a function of range over a short number of range gates. An example of this is the A and B parameters in range gates 2 to 6 in Fig. 5.16. The A parameters are shown to increase from $\approx$ -100 to $\approx$-55, while the B parameters decrease from $\approx$ 1 to $\approx$ -8. This correlation shows that, over short ranges, there is a relationship between the Doppler spectra of consecutive range gates that results in a trend in the fitted parameters. The sinusoidal shape of parts of Fig. 5.14 also agree that a correlation exists between the fitted linear parameters.

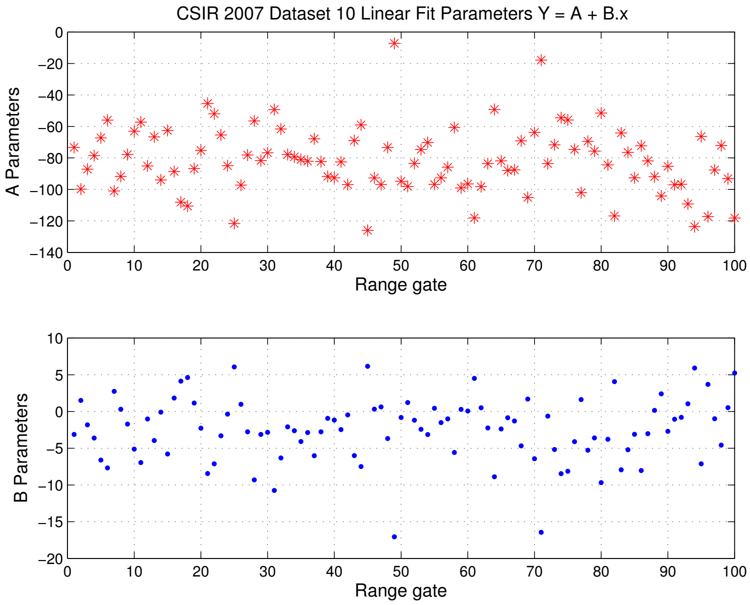

Figure 5.16: CSIR datasets Linear fit parameters A and B vs. range gate - dataset 10

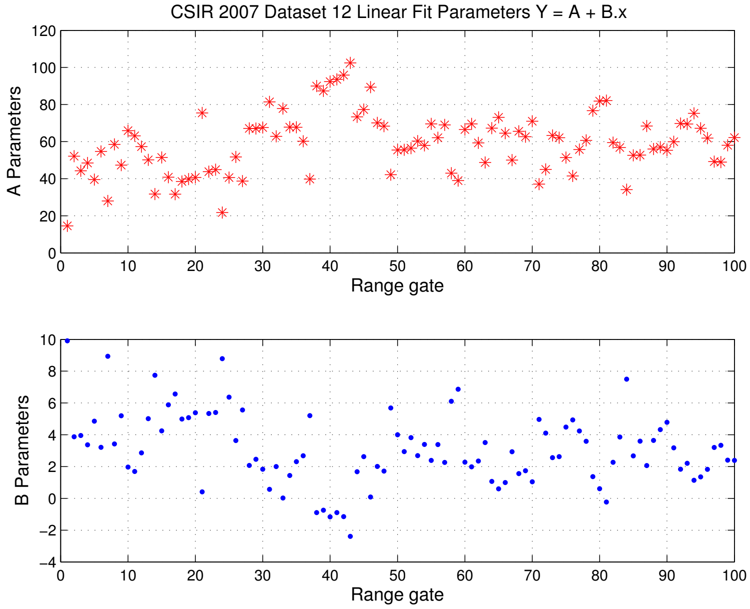

Figure 5.17: CSIR datasets Linear fit parameters A and B vs. range gate - dataset 12

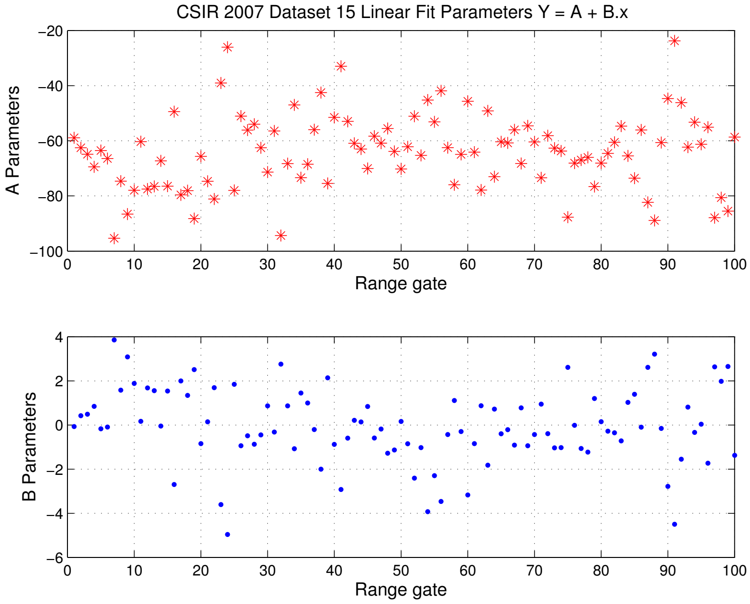

Figure 5.18: CSIR datasets Linear fit parameters A and B vs. range gate - dataset 15

The averaged values from all the linear fits in each dataset, including the additional datasets 08, 09, and 11, were evaluated and the results are shown in Table 5.1. The mean A parameter values are shown to decrease with range, seen from the direct comparison of same azimuth datasets 07 & 12 and datasets 10 & 15. The fractional change in A being 4.5% for datasets 07 to 12 and 21.57% for datasets 10 to 15. This shows that the change in A parameter is more significant for the cross swell measurements than the up swell configurations.

The contrast between B values at the same azimuth shows a different behaviour in comparison to the variation in A. Dataset 07 and 12 have a difference of -72% and datasets 10 & 15 have a difference of -97%. These are much more significant percentage changes showing a greater sensitivity of the B parameter to a change in range.

Table 5.1: CSIR 2007 Datasets mean fitted linear parameters

Dataset	Mean B Parameter Value	Mean A Parameter Value
07	11.1140	61.9905
08	9.5792	-6.5870
09	1.3851	-48.7758
10	-2.5290	-81.6609
11	-3.7338	-95.8923
12	3.0944	58.9520
15	-0.0672	-64.0470

The relationship between the mean parameters shown in Table. 5.1 and the bearing used for each given dataset was then investigated. Figure. 5.19 and 5.20

show the A and B parameters respectively, plotted against the bearing of antenna during the recording of that dataset.

The average A parameter fits, Fig. 5.19, from all datasets show a close agreement for the two pairs of datasets at matching bearing angles (07 & 12) and (10 & 15). As well as a definite trend in relationship between A and bearing. To quantify the relationship with bearing a quadratic fit was applied to the parameters A vs. bearing data points. The results of this fitting gave the following relationship,

$$A = 0.0148B_{earing}^2 - 10.13B_{earing} + 1636 \tag{5.10}$$

Where B_{earing} is the azimuth bearing value in degrees. This fitted curve was found to have a root mean square error (RMSE) of 7.79. This shows a reasonable agreement to the trend present and shows a clear quantified relationship between A and bearing. As the bearing from the radar is a circularly wrapped metric the relationship itself will alter if evaluated over a large enough azimuth variation. With expectation that at the inverse angle, 180° from the original, the linear relationship would have the same values but negative (or positive if they were originally negative). The samples in between these opposite angles would presumably produce a sinusoidal variation. This is not covered here as data was not available at any further azimuth measurements.

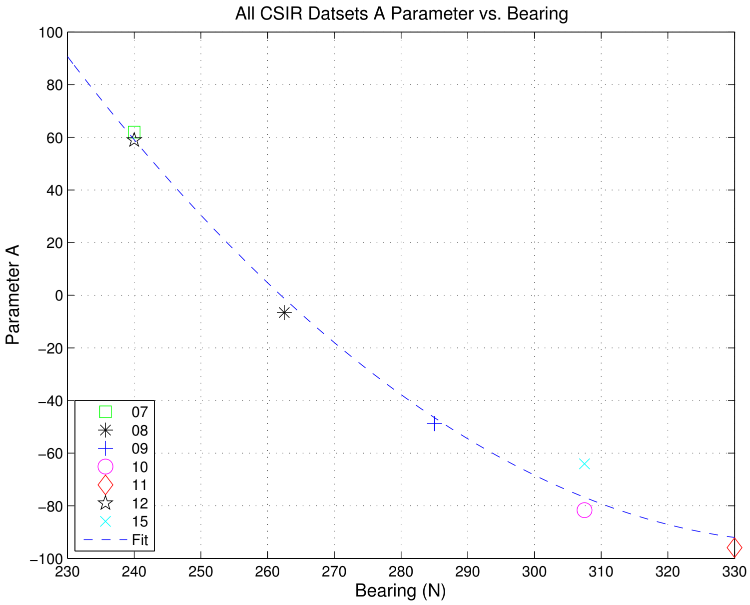

Figure 5.19: All CSIR Datasets average linear fit parameter A vs. bearing

For the B parameter values, Fig. 5.20, the variation in average value for the at the same azimuth is much greater. For datasets 10 and 15 they both appear to still lie within a quadratic trend, but datasets 07 and 12 have a significant variation. It appears that the average B parameters from dataset 12 do not fit the trend set by all the other datasets. The reason for dataset 12 not adhering to the trends seen in the other datasets may be due to a missing unknown parameter that has not been included within this model.

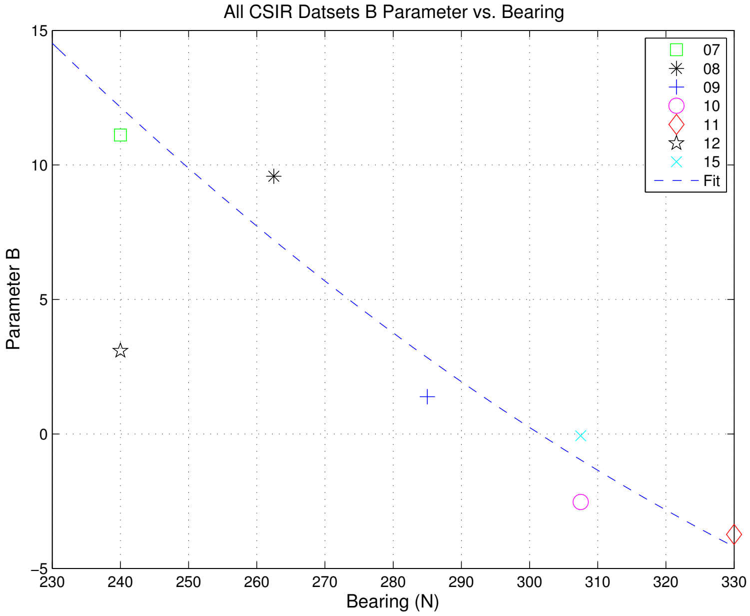

Figure 5.20: All CSIR Datasets average linear fit parameter B vs. bearing

The same method was used to fit to the B parameter values, but the outlying odd result from dataset 12 was removed from the fit. This gave the following relationship,

$$B = 0.0005629B_{earing}^2 - 0.5024B_{earing} + 100.3 \tag{5.11}$$

The fit was found to have a RMSE of 2.02 mean sum square difference from the least squared fit method. To directly compare both fits the R^2 values were evaluated and found to be 0.99 and 0.937 for the A and B parameters respectively. This shows a better fit to the quadratic shape was found for A parameters, although both fits are very good, therefore a clearer relationship between bearing and this parameter is present.

These two figures, 5.19 and 5.20, clearly show that the parameters are bearing dependent. As the bearing of the antenna increased from 240° (N) to close to 330° (N) both parameters reduce. These parameters will be dependent directly on the wave and wind directions, hence will have a peak when the wind and wave force the sea Doppler to have a maximum shift in the PSD centre of gravity will large intensity spectra. Datasets 07 and 12 are measured with an azimuth facing into the swell direction, hence the Doppler will be larger in comparison to the cross swell azimuth used for datasets 10 and 15. The results found from these mean linear fits agree with this hypothesis.

The mean linear fit values from all seven CSIR datasets have been plotted against each other to visually compare the parameters as a function of dataset, Fig. 5.21.

When comparing parameters generated from the same azimuth measurements it is clear that the average A and B from datasets 10 and 15 show a much closer agreement in comparison to datasets 07 and 12. These parameters have similar average A values and markedly different B values. Highlighting that the potential error in defined parameters or disagreement to this proposed quadratic link between the A and B parameters comes from the B values.

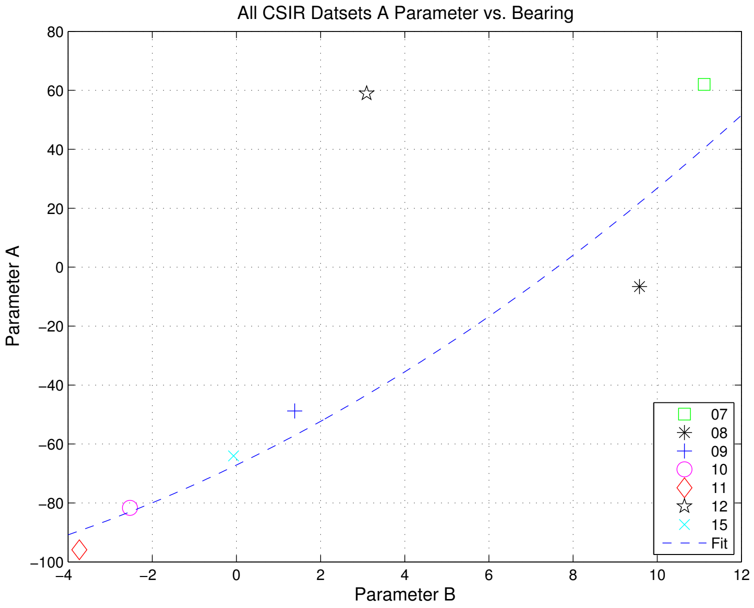

Figure 5.21: All CSIR Datasets Average linear fit parameters A and B vs. range gate

As seen from the B parameter fits the dataset 12 was an odd result. Therefore for this A vs. B plot a quadratic fit was applied to all the datasets except this one. The relationship was found to be,

$$A = 0.248B^2 + 6.91B - 67.13 \tag{5.12}$$

The fit was found to have an RSME of 21.62. The relationship between A and B reduces the complexity of the model as they are no longer independent parameters but a defined by the single relationship seen in Eqn. 5.12. This is a positive improvement for the simulation model as it allows the clutter to be described with one less independent component, improving the efficiency of the model.

It is also theorised that the relationship between A and B is probably related to the sea conditions. With emphasise based particularly on wind speed as this has a significant influence on the Doppler spectra of the sea. As the data used for this research was all collected on the same day using the assumption of the same sea state for all datasets this can not be tested. Further investigations into the variation of A and B with sea conditions would certainly be a worth while expansion to this work.

The next parameter extracted from the data was the 3 dB width of each PSD as well as the variance of this width. This was achieved by interpolating the averaged spectra in the Doppler domain by a factor of 10. A spline interpolation was used, with the general Gaussian shape of the PSD this was assumed to represent the data sufficiently. The interpolation gave a much higher resolution in Doppler, thus allowing the width of the assumed Gaussian PSD to be defined with greater accuracy. The width of a Gaussian at the half power point, equivalent to -3dB, in the linear domain is:

$$\Delta x = 2\sigma_s\sqrt{2\ln 2} \tag{5.13}$$

Where Δx is the full width of the Gaussian and σ_s is the variance of the Gaussian curve shape. The relationship for the $1/\sqrt{10}$, equivalent to -5dB, point below the peak power of the Gaussian PSD in the linear domain is,

$$\Delta x = 2\sigma_s\sqrt{2\ln(\sqrt{10})} \tag{5.14}$$

By obtaining the width of the spectra and these equations it was possible to define the σ_s values for each PSD. Both the half power and $1/\sqrt{10}$ thresholds were used to obtain an averaged sigma value with higher degree of accuracy. If the CNR ratio was too low to use a $1/\sqrt{10}$ threshold on the data then only the half power threshold was performed. Figure 5.22 shows an example of a -3dB and -5dB threshold being performed on a PSD. A dB scale was used to plot the figure for clarity of the thresholding, in reality the analysis Eqn. 5.13 and 5.14 refer to the linear power domain. Where the equivalent linear threshold levels of 1/2 and $1/\sqrt{10}$ were used.

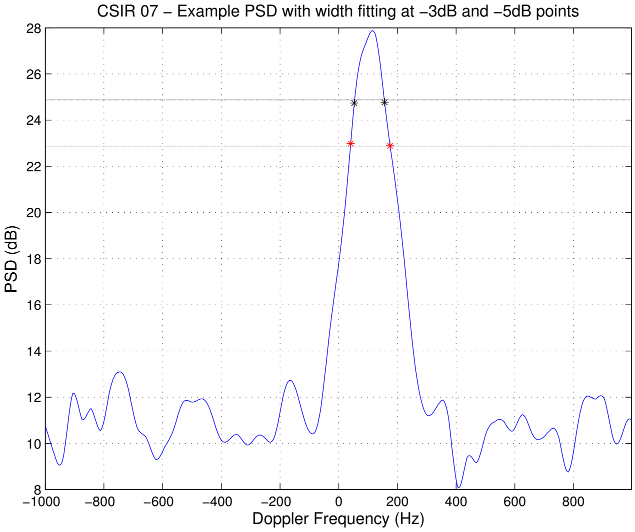

Figure 5.22: CSIR Dataset 07 interpolated PSD spectra thresholded at -3 dB and -5 dB

The obtained width values from a single example range gate within the CSIR 07 dataset are shown in Fig. 5.23. The 184 width values were generated from the 184 averaged PSD spectra within a single example range gate. Both -3dB (1/2) and -5dB ($1/\sqrt{10}$) threshold values are shown.

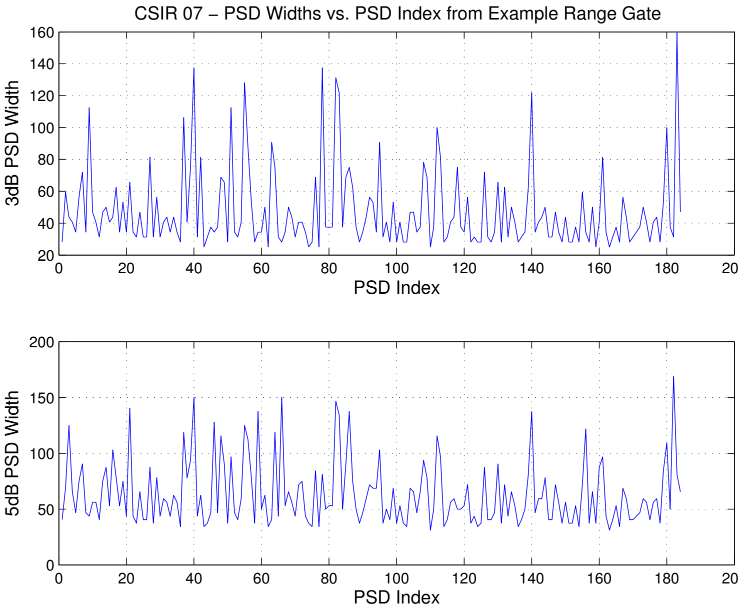

Figure 5.23: CSIR Dataset 07 PSD width values from thresholding at -3 dB and -5 dB

These values were then obtained from each range gate in each dataset, Fig. 5.24. The mean PSD width values for both the 3 dB and 5 dB thresholds are shown to be consistent with each other as well as over range. Using an average of both results should produce a PSD spectra that is very similar to the real data.

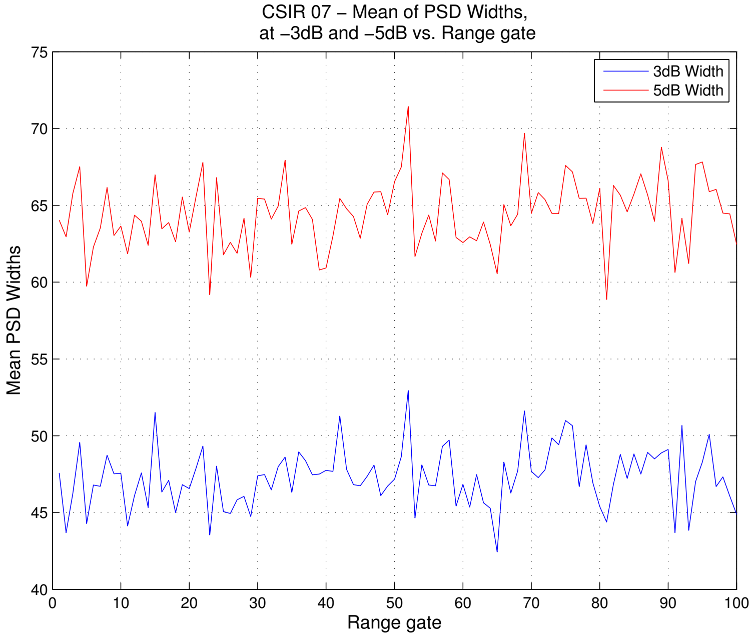

Figure 5.24: CSIR dataset 07 mean of PSD widths -3 dB and -5 dB

Table 5.2: CSIR datasets mean fitted full width values

Dataset	Mean 3dB Gaussian full width (Hz)	Mean 5 dB Gaussian full width (Hz)
07	47.3	64.4
08	46.2	62.5
09	44.2	59.2
10	43.8	58.8
11	45.0	60.8
12	45.0	60.4
15	40.4	53.6

The mean full width values over all range gates from each dataset are recorded in Table. 5.2. The into swell datasets 07 and 12 show the larger average PSD Gaussian width values in comparison to the equivalent cross swell measurements of 10 and 15. The direct comparison of datasets at the same azimuth shows dataset 07 is 5.1% and 6.6% larger than 12 (3dB and 5dB measurements respectively), and dataset 10 is 8.4% and 9.7% larger than dataset 15. In addition to this the data recorded at longer ranges, 07 and 10, at both azimuths shows a wider PSD shape.

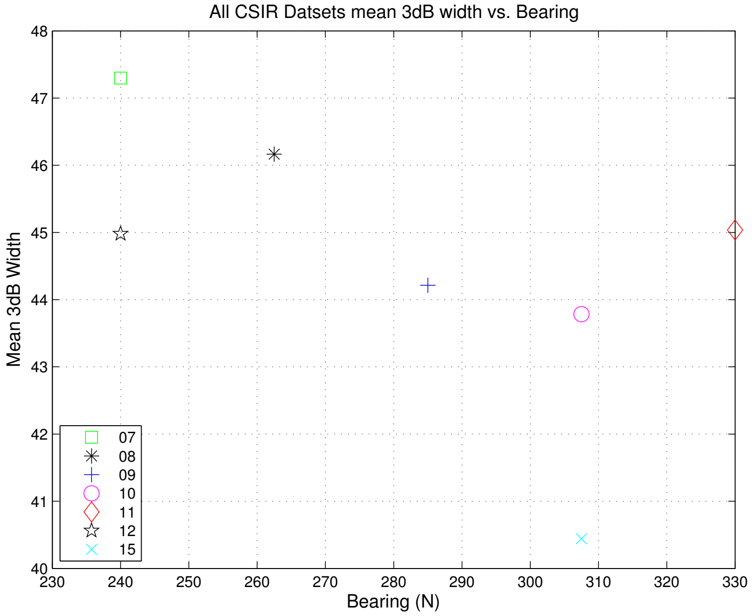

Figure 5.25: All CSIR datasets mean -3dB widths vs. bearing

These mean width values from each dataset has been plotted against azimuth in Fig. 5.25. This shows a trend in a reduction of 3 dB width with an increase in bearing up to 310° for datasets 07, 08, 09 and 10 all at the same range. Dataset 11 has an increase 3 dB width that does not fit with the reducing values of the previous datasets.

As described when evaluating the PSD centre of gravity linear fits the parameters fitted will have a sinusoidal relationship with bearing. This is due to the circular wrapping of the azimuth as the antenna rotates. In the case of the PSD width it is predicted that bearings separated by 180° will have the same PSD width values. This is not possible to verify with the datasets available as the radar would point in land for a large section of the possible bearings. Therefore the increase shown in dataset 11 may be an indicator of the beginning of this sinusoidal relationship with bearing. To indicate this behaviour datasets 07 to 11 have been plotted against a summed sinusoidal curve in Fig. 5.26.

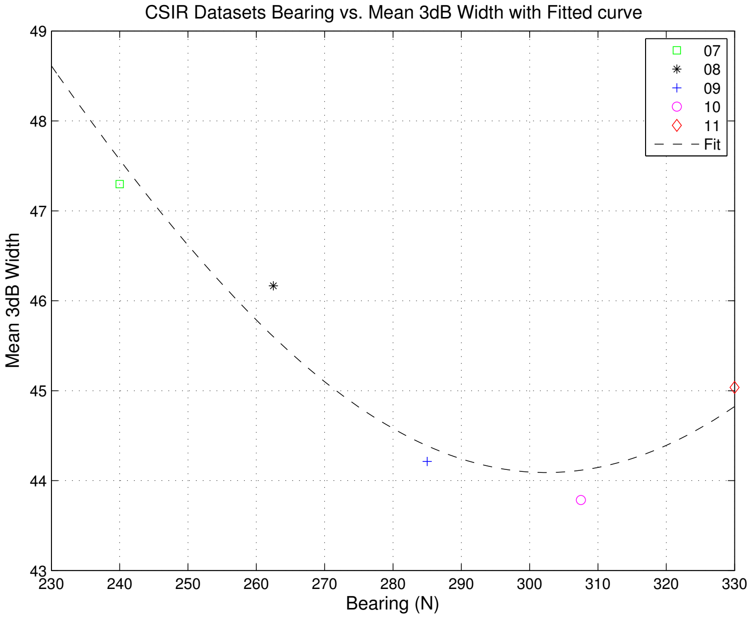

Figure 5.26: CSIR datasets 07 to 11 mean -3dB widths vs. bearing with fitted curve

This fitted summed sinusoidal curve was found to be,

$$\text{3dB Width} = 50.57 - 3.47\cos\left(0.0017458B_{earing}\right) + 5.473\sin\left(0.0017458B_{earing}\right) \tag{5.15}$$

The curve itself has been shown to have a reasonable agreement with the mean data points. It would be possible to further validate this proposed relationship with datasets with bearings outside of the range of 230° to 330° or inter-sampled locations between the selected bearings shown.

The final parameter extracted from the data was the CNR as a function of range gate. The mean CNR for each range gate was recorded to be used to simulate the correct CNR within the modelled data. An example plot of all the mean CNR values from dataset 07 is shown in Fig. 5.27. The CNR values are shown to vary ±3 dB across all the range gates, all of the values are significant clutter CNR levels which confirms that the data is suitable for this analysis.

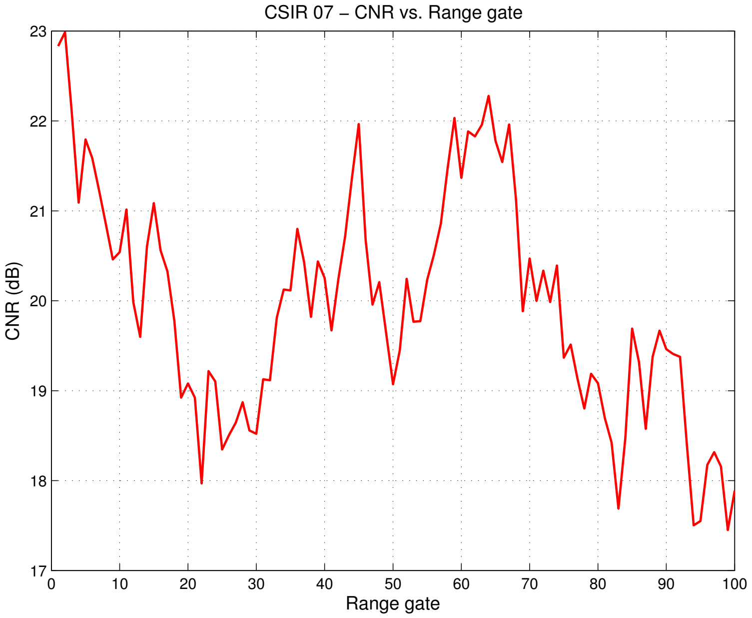

Figure 5.27: CSIR dataset 07 mean CNR vs. range gate

5.2.3 Extraction of parameters conclusions

This section has provided clear examples of all the input parameters required for the simulation model to replicate the datasets properties. As with the characterisation process of any dataset the more samples available the better it can be defined. In the case of the CSIR data used even when starting with $\approx 6\text{x}10^4$ samples this was reduced to only 184 averaged spectra to extract width and centre of gravity measurements. Despite this each step has shown:

- The suitability of the data for this analysis:
  - The significant CNR levels.
  - Well characterised Gamma texture
- Established new trends:
  - Between different proposed parameters. For example the relationship between A and B.
  - Or between the defined parameters and the azimuth of the dataset.

A very important component of the analysis was the establishment of the link between the A and B parameters. This new discovery gives an insight into the relationship of the linear fit between intensity and the centre of gravity of the Doppler spectra. As well as this the parameters individually were shown to be closely linked to the bearing angle used.

A partial limitation of the parameters extraction process was the number of datasets avaliable. Further analysis over more azimuth angles and ranges would improve the fits of individual parameters against bearing. In addition if recordings were made during a variety of sea states and wind conditions this would expand the knowledge into how the spectra relates to these important environmental factors.

5.3 Simulation Results

The practical and mathematical methods behind creating the model have been defined, as well as this real values for the input parameters and figures showing their variation have all been shown. All of this is now applied to generate correlated Doppler spectra from individual range gates within a single dataset, then from all range gates within a dataset and finally from additional datasets. Example real and simulated range gate spectra are shown, then the statistics of the simulated and real clutter as a function of Doppler are compared. The effectiveness of the model in replicating the data and comparisons between different datasets are then made.

The simulated Doppler spectra as well as the original real data spectra from dataset 07 range gate 30 can be seen in Fig. 5.28.

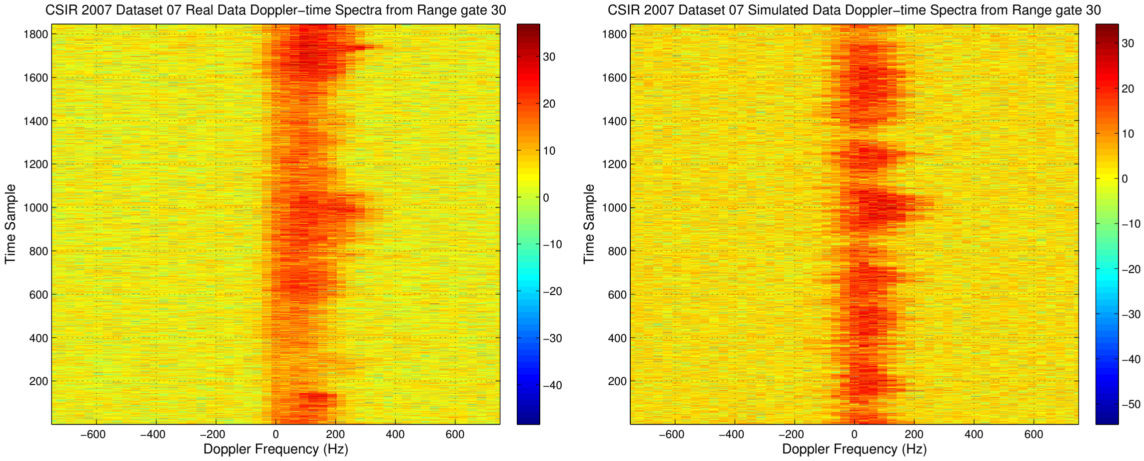

(a)

(b)

Figure 5.28: CSIR dataset 07 Doppler time spectra - (a) Real data (b) Simulated data

The two spectra show very similar shape and distributions of the amplitude values in both frequency and time. The simulation has successfully replicated the periods of increased intensity and spectral width along with sections that have lower intensity and centre of gravity. The CNR on average is seen to be comparable.

Once the data was simulated statistical analysis was performed on the amplitude statistics within each Doppler bin. The same methods were applied as seen in the analysis of the real CSIR data in Section 4.2. The amplitude moments of the data were used to generate the K-distribution shape parameter variation as a function of Doppler bin. Once this was complete it was possible to directly compare the statistics of the simulated data and the real original data that it was based upon.

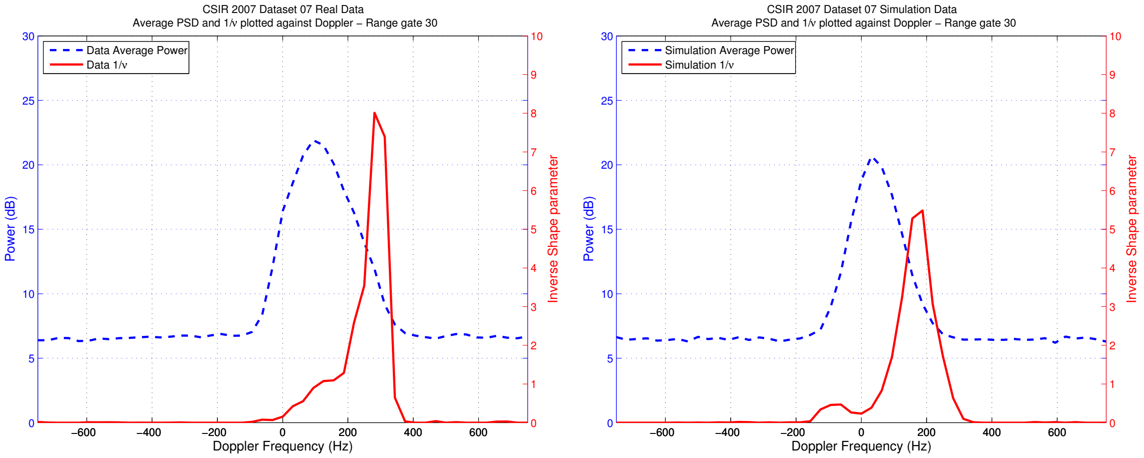

(a) (b)

Figure 5.29: CSIR dataset 07 single range gate average PSD power (dB) and inverse K-distribution shape parameter vs. Doppler - (a) Real data (b) Simulated data

Figure 5.29 shows the results from a single range gate, 30, of the average Doppler spectra power over time and the inverse K-distribution shape parameter variation as a function of Doppler frequency, for the real data (a) and the simulated data (b). This comparison shows how effective the simulation is are replicating the not only the qualitative behaviour of the sea clutter but also the variation of amplitude statistics across the Doppler spectra. Both $1/\nu$ variations have their peak, 9.3 for the simulated data and 8 for the real data, on the leading positive edge of the Doppler spectra. The width of the increased spiky area within the Doppler spectra is directly comparable between the data and simulation results, with the simulation being fractionally wider. The most significant difference is that the simulation statistics show an increased inverse shape parameter value at the centre of the average PSD peak in comparison to the real data. Although this is the clearest difference between the results it is only a small difference and the close agreement in the key leading edge area shows the simulation has successfully replicated the important aspects of the real sea clutter.

The inverse shape parameter values from all the simulated range gates are shown in Fig. 5.30 (a) along with the real data values in Fig. 5.30 (b). The figures have the colour regime limited bounded between 0 and 20. This is due to single irregular $1/\nu$ values within the simulated results.

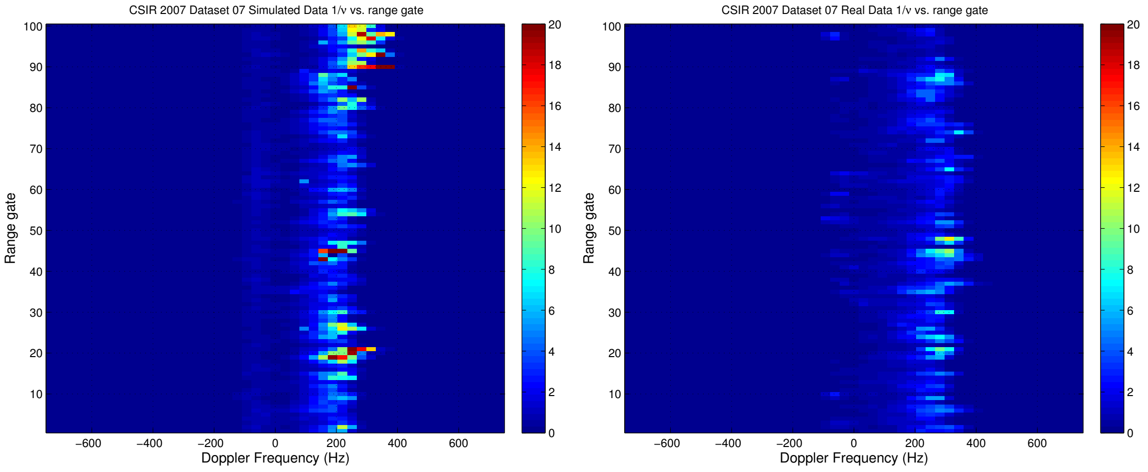

(a) (b)

Figure 5.30: CSIR Dataset 07 $1/\nu$ vs. Range and Doppler - (a) Simulated Data (b) Real Data

The average moment fitted shape parameters from all the range gate generated values in the simulated data and from real data are shown in, Fig 5.31.

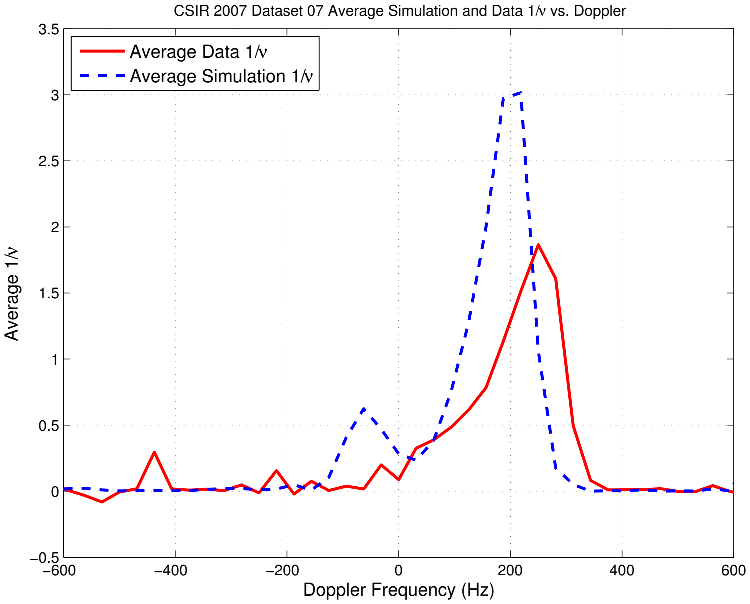

Figure 5.31: CSIR Dataset 07 Average Real and Simulation $1/\nu$ vs. Range and Doppler

This shows that over the 100 range gates that were input the simulation is well representative of the data on average. The simulation is shown to over-estimate how spiky the distributions are on average. Over estimating this parameter will make assumptions about false alarms more conservative which can be seen as being safe as long at the difference is not significant. The peak values for the simulation and data

$1/\nu$ parameter are 3.0 and 1.87 respectively. At a log(P$_{FA}$) of -4 this represents a difference of only 0.9 dB in threshold, as seen in Fig. 5.32.

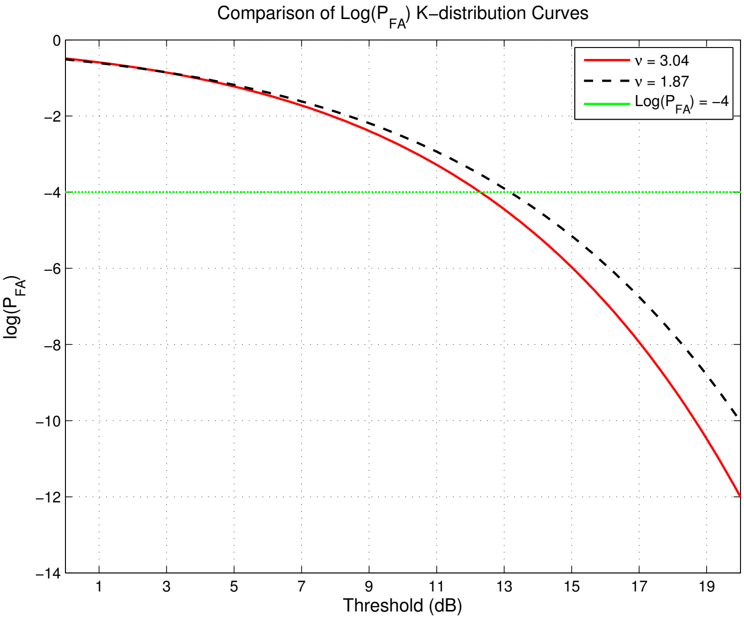

Figure 5.32: CSIR Dataset 07 Data and Simulation peak $1/\nu$ average comparison K-distribution Log(P$_{FA}$) Curves

Further CSIR datasets were then also used as inputs for simulation. Each dataset was analysed and the required parameters defined in Section 5.2 were recorded. These parameters were used in the simulation process using the same methods applied to produce the 07 dataset simulation results. Example Doppler time spectra from a single range gate from datasets 10, 12 and 15 can be seen in Fig. 5.33, 5.34 and 5.35 respectively.

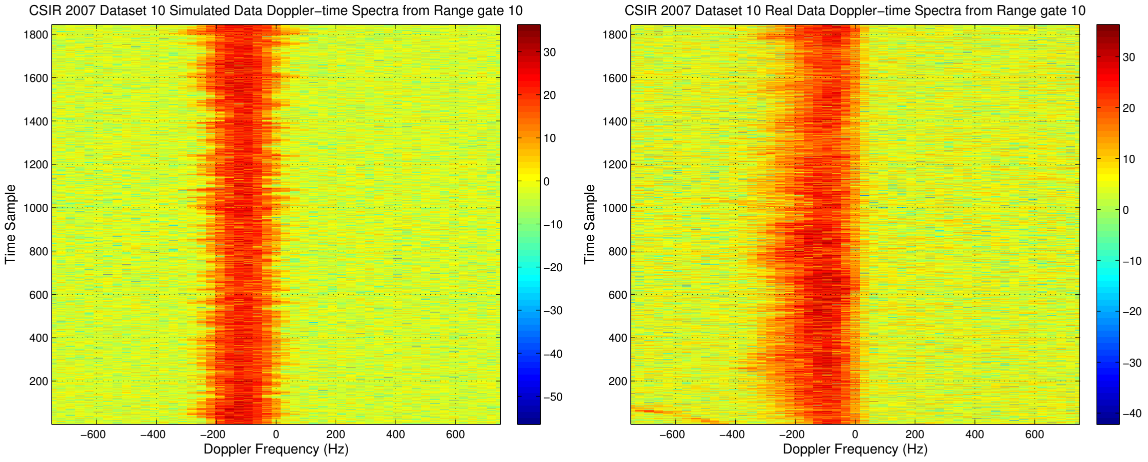

(a) (b)

Figure 5.33: CSIR dataset 10 Doppler-time spectrum from example range gate - (a) Simulated data (b) Real data

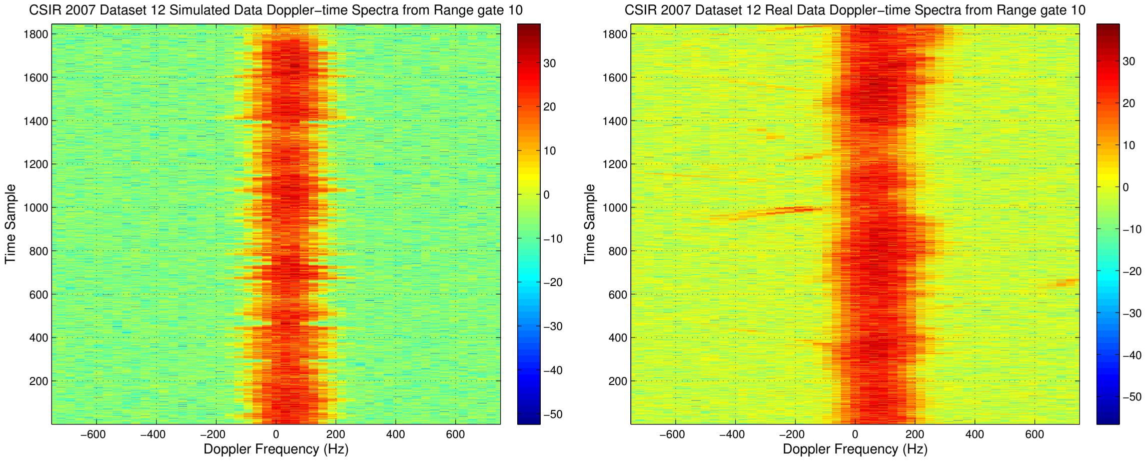

(a) (b)

Figure 5.34: CSIR dataset 12 Doppler-time spectrum from example range gate - (a) Simulated data (b) Real data

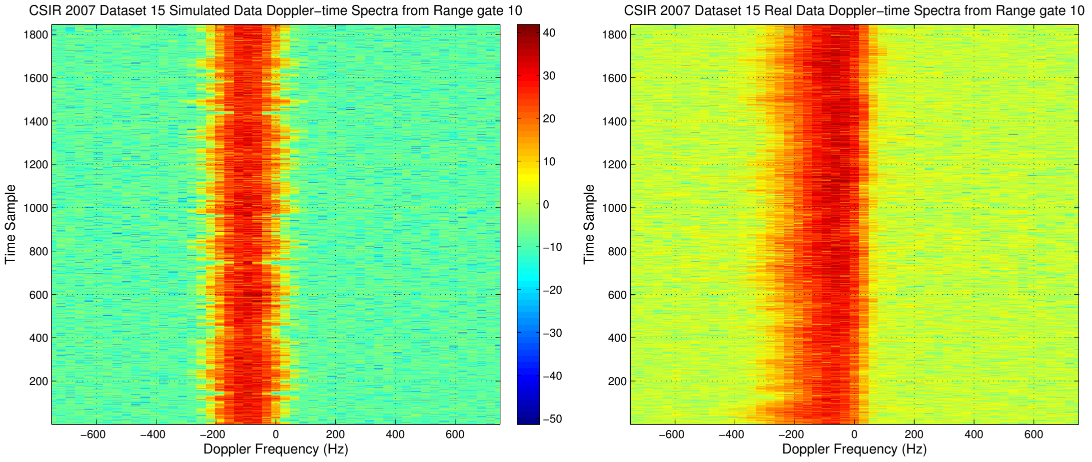

(a) (b)

Figure 5.35: CSIR dataset 15 Doppler-time spectrum from example range gate - (a) Simulated data (b) Real data

The same moment analysis was applied to generate the K-distribution shape parameters from the data and simulated samples. This was completed on each range gate, see Fig. 5.36, 5.37 and 5.38.

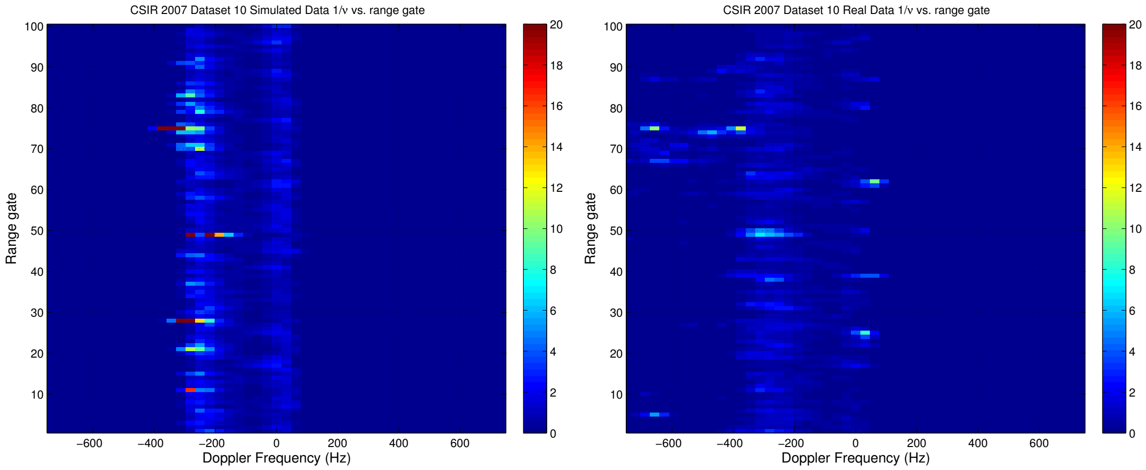

(a) (b)

Figure 5.36: CSIR dataset 10 $1/\nu$ vs. range and Doppler - (a) Simulated data (b) Real data

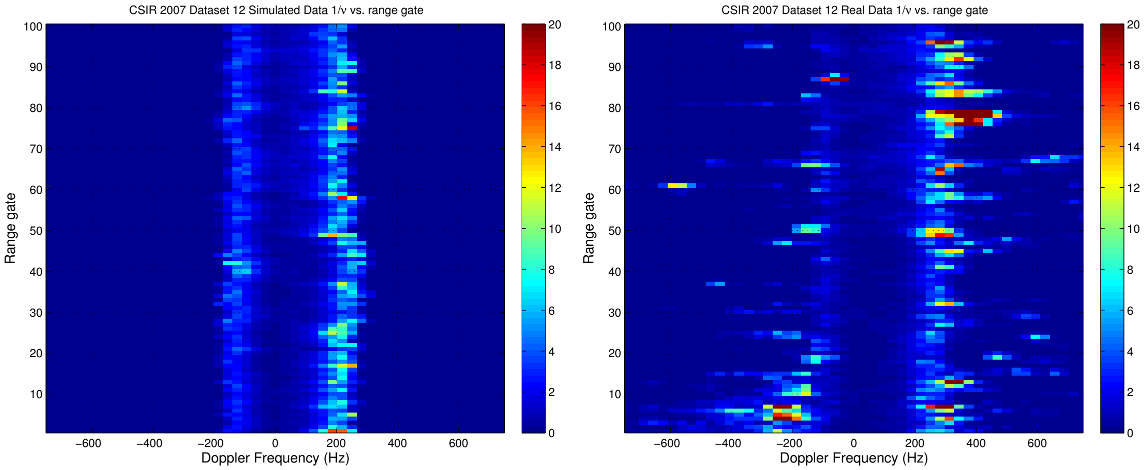

(a) (b)

Figure 5.37: CSIR dataset 12 $1/\nu$ vs. range and Doppler - (a) Simulated data (b) Real data

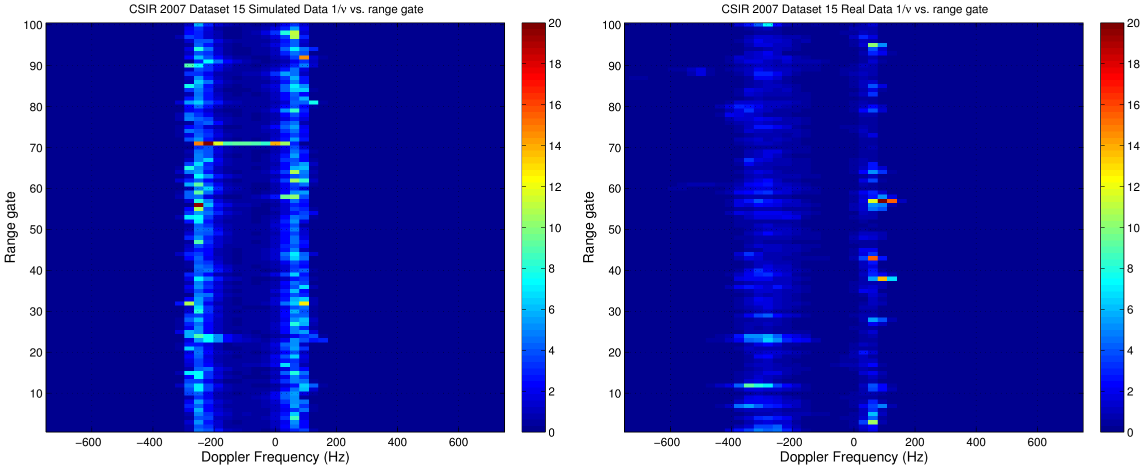

(a) (b)

Figure 5.38: CSIR dataset 15 $1/\nu$ vs. range and Doppler - (a) Simulated data (b) Real data

When comparing the ν variation between data and simulation there are some qualitative differences. The simulation results show the lines with the highest $1/\nu$ values more consistently with range, and the spiky *trailing edge* is also qualitatively more prominent. These comparisons are reinforce by the quantitative results in Table 5.3 and 5.4.

The averaged values of all the moment defined shape parameters from each dataset are plotted in 5.39, 5.40 and 5.41. These figures show a direct comparison for each dataset of how effectively, on average the simulation was replicating the statistics of the real data. In all occasions the simulation and data shows two key peaks in the inverse shape parameter variation. These peaks reside either side of the peak in the PSD power, as discussed in Section 4.2.

Within Fig. 5.39 a clear spike in the data and simulation averaged $1/\nu$ values is shown at $\approx +550$ Hz. This is considered to be unrelated to the sea clutter due to its significant separation from the bulk of the clutter.

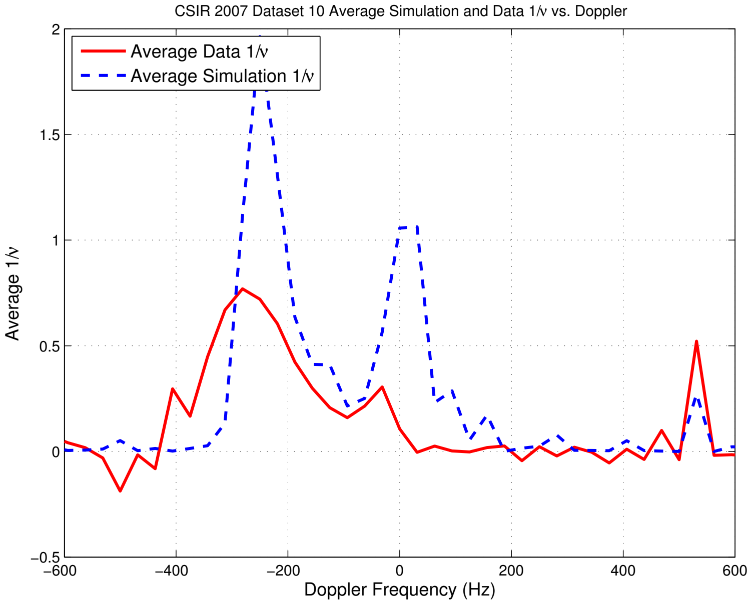

Figure 5.39: CSIR Dataset 10 Average Real and Simulation $1/\nu$ vs. Range and Doppler

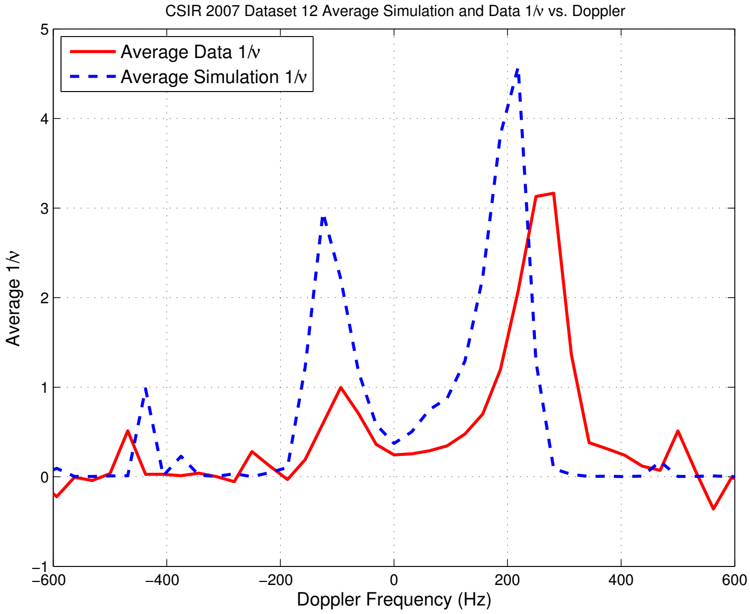

Figure 5.40: CSIR Dataset 12 average real and simulation $1/\nu$ vs. range and Doppler

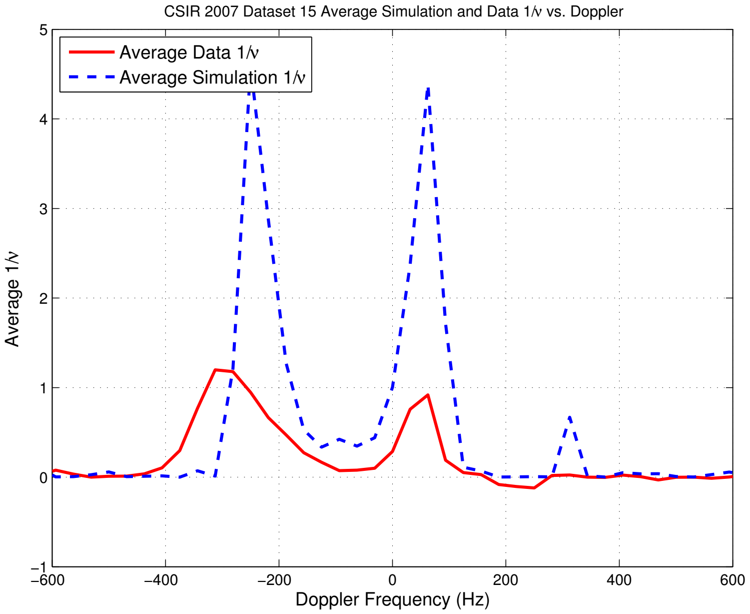

Figure 5.41: CSIR Dataset 15 average real and simulation $1/\nu$ vs. range and Doppler

The peak values of the inverse shape parameter curves on either side of the peak in the PSD power have been recorded in Table. 5.3 and 5.4. These tables show that the location of the peaks in the inverse shape parameter are typically within one Doppler bin range, 32.25 Hz, although the right hand peak in dataset 10 is separated by two Doppler bins. It is important that these locations show a good agreement in order for the model to successfully represent the behaviour of the data statistics. As the processed Doppler data has a relatively crude resolution the results shown in Tables. 5.3 and 5.4 can be considered to be acceptable.

Table 5.3: CSIR Simulated Data Peak $1/\nu$ values and Frequencies

Dataset	Left hand peak $1/\nu$		Right hand peak $1/\nu$	
	Freq (Hz)	Value	Freq (Hz)	Value
07	-62.5	0.62	218.8	3.0
10	-250	1.96	31.25	1.06
12	-125	2.95	218.8	4.58
15	-250	4.59	62.5	4.38

Table 5.4: CSIR Real Data Peak $1/\nu$ values and Frequencies

Dataset	Left hand peak $1/\nu$		Right hand peak $1/\nu$	
	Freq (Hz)	Value	Freq (Hz)	Value
07	-31.25	0.2	250	1.87
10	-281.3	0.77	-31.25	0.31
12	-93.75	1.0	281.3	3.17
15	-281.3	1.21	62.5	0.98

Along with the peak values and locations the difference in threshold, ΔT, at a set false alarm rate level of log(P_{FA}) = -4 has also been evaluated, Table. 5.5. The difference in threshold values is an important comparison between simulation and data as it shows how the assumed modelled distribution compares to the real data distribution at these crucial locations. The values have been generated by evaluating a K-distribution log(P_{FA}) vs. Threshold curve for the simulated and real $1/\nu$ values and comparing the difference in threshold at the level of log(P_{FA}) = -4. On average dataset 12 has the lowest difference in threshold between the two

Table 5.5: CSIR Threshold Difference Between Simulation and Real data Peak Value Shape Parameters

Dataset	Left hand peak ΔT (dB)	Right hand peak ΔT(dB)
07	3.2	0.9
10	2.1	3.2
12	2.2	0.5
15	2.4	2.9

After reproducing the simulated spectra for all four CSIR datasets the difference of the simulated data shape parameters and the real data were investigated. To show a clear comparison between the datasets the difference between the real data shape parameter and the simulated shape parameters was first evaluated.

The number of samples that had a difference less than a given value was calculated for a range of $\Delta 1/\nu$ values from 0.1 to 10 in steps of 0.1. This has been shown as a percentage of samples with a difference less than the selected $\Delta 1/\nu$, for all datasets in Fig. 5.42.

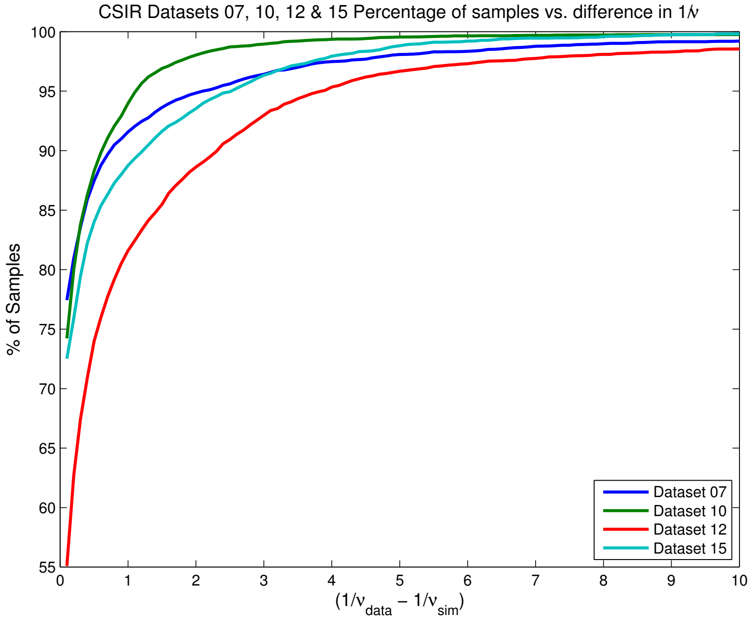

Figure 5.42: CSIR Datasets 07, 10, 12 & 15 Percentage of samples vs. Difference in $1/\nu$

The results show that all datasets produced 90% of samples with a difference in $1/\nu$ of 1.3 or less, except dataset 12. Dataset 10 shows the closest agreement, having the height percentage matching over all $\Delta 1/\nu$. Dataset 07 also shows a good agreement but becomes less. Relating this to the dataset parameters it is clear that the cross swell datasets 10 and 15 shown a better matching to the model. With the further ranged, 58,036m, dataset 10 performing better than the same azimuth shorter range, 39,449m, dataset 15.

In comparison the two up swell configuration datasets, 07 and 12, showed the largest percentage of samples over a given threshold, dataset 12 performing the worst. This shows that the model is better suited to simulating sea clutter Doppler spectra in a cross swell scenario.

A potential reason for the closer matching of data to model for the shorter range dataset in both cases is potentially because at the reduced range the data is recorded in an increasingly littoral which will produced different Doppler behaviour in comparison to open sea characteristics. This could be further tested through observing if there is a degradation in the percentage of samples that match by a given difference as the range is decreased.

5.4 Modelling and Simulation conclusions

The application of the coherent Doppler spectrum modelling method has been discussed from introduction of its background and theory to the comparison of input real sea clutter data and the produced simulated data. The methods used by S. Watts to produce simulated samples were described, in particular the production of correlated Gamma texture samples and the reproduction of a Gaussian shape PSD with a randomly varying width and a linearly proportional centre of gravity to intensity were both described in detail and the model has been implemented. A systematic description of all the input parameters required was given, showing examples of all input parameters and comparisons of key parameters between all four of the CSIR datasets described in Section 3.1.2.

Key parameters such as the mean linear fit A and B from the intensity and centre of gravity of the PSD as well as the mean 3dB width have been related to the experimental geometry in which the dataset was obtained. Particularly the true bearing of the radar antenna. All 7 datasets were used to relate these parameters to maximise the amount of bearing sampled available. This showed that the A and B values were themselves related to each other as well as exhibiting a smooth relationship with bearing. The 3dB width values exhibited a consitent decrease with range at the same azimuth angle and a steady decrease as the bearing was increased from 240°N to 310°N at a given range.

The resulting simulated data was well representative of the input data from all of the selected datasets. Qualitatively the spectra showed directly comparable CNR in all Doppler bins, thermal noise levels, mean width and correlation in the texture. All of these properties gave the simulated data very close characteristics to the input data and verifying that this method is suitable for use in testing of detection algorithms within radar systems testbeds. In addition to being well representative of many of the qualitative properties of sea clutter as discussed so far in this thesis the ability of the simulated clutter to replicate the statistics of the input sea clutter was also quantitatively tested. The results from the moment analysis of each range gate and the averaged range gate values again demonstrated that the simulated clutter closely match the real data. The inverse shape parameters matched well at the peak of the PSD power as well as at the important peak $1/\nu$ locations.

The limitations of the model have also been investigated during the processing. The structure of real sea clutter has been well replicated by the model. The real sea clutter often shows a more asymmetrical shape in its departure from its mean centre of gravity. These shifts in frequency are generally seen on the leading edge of the clutter. This is the positive Doppler side if there is a mean positive Doppler shift (datasets 07 and 12) and the negative Doppler side if the spectra has a mean negative Doppler shift (datasets 10 and 15). This behaviour has not quite been recreated by the model. Despite these limitations the simulated clutter is still closely representative of the vast majority of the real clutter properties.

In all cases that have been tested it was shown that this model is well suited to reproducing real sea clutter characteristics. This expands the initially hypothesised model from the single range gate and dataset it was initially tested with. The model can now be accepted to be more generally applicable to sea clutter over a variety of conditions. Importantly even recorded using a different radar system on different occasions.

This work has linked closely to all the prior analysis of the many aspects of sea clutter completed in Chapter 4. It then goes on to compliment this work through applying the qualitative and quantitative methods used to define the clutter to allow it to be reproduced through these simulation techniques. The result of which allows sea clutter Doppler to be simulated for given input parameters, which could then be used to evaluate a radars ability to operate within a sea clutter environment.

Chapter 6

Application of Information Theory to Sea Clutter Analysis

This chapter introduces the application of information theory concepts to the area of sea clutter statistical analysis. The aim of this work was to propose and then test a link between the established metrics used in information theory research and sea clutter analysis. The chapter begins by introducing and characterising the components of information theory applied to the sea clutter data. It then goes on to detail initial practical example tests of the theory. Finally real data and established sea clutter models are compared against each other using this novel metric. The work contained within this chapter is based upon the original published paper, [6], that first introduced the application of this concept.

In Chapters 4 & 5 sea clutter was characterised using its PDF and P_{FA}, which was then compared to theoretical models which have a defined PDF and P_{FA}. Through these comparisons it was judged whether the model was representative of the real data. In addition to this the variation of the shape parameters of the distributions were defined as a function of selected parameters such as Doppler frequency or range gate.

Prior analysis comparisons between the real and modelled distributions were completed using either a sum square difference between data and simulation or using a method of moments estimate. By using the field of information theory a novel method of quantifying how effectively models represent real sea clutter was tested. The metric that has been applied was the Kullback-Leibler divergence (KLD). As defined in Section 2.4 the KLD quantifies the divergence between two input PDFs. It was shown to be defined as,

$$D(p||q) = \sum_{x \epsilon \chi} p(x) \log \frac{p(x)}{q(x)} \tag{6.1}$$

where $p(x)$ and $q(x)$ are the two input PDFs that are compared. For this work the $q(x)$ distribution has been assigned to be the assumed distribution. This is the model

PDF that a radar uses to make assumptions for the behaviour of the clutter, and therefore set the threshold for detection. The $p(x)$ distribution is the actual real sea clutter distribution. The properties of the KLD means that it:

- Will always take non-negative values
- Is asymmetric
- Is non-commutative
- Gives the result 0 when $p(x) = q(x)$.

The connection of the KLD to radar signal processing can be seen through the use of log likelihood ratio. In the area of radar detection, as well as statistical tests in general, a likelihood ratio test is a common method of defining if a target is present or not. This uses the test,

$$\Lambda = \ln\left(\frac{P_T(z)}{P_A(z)}\right) \tag{6.2}$$

When Λ is greater than a set threshold λ_t a target is deemed to exist, and if $\Lambda < \lambda_t$ then no target is present. This same ratio of PDFs exists within the KLD, Eqn. 6.1 hence the two values are directly related.

When completing the detection process it is critical to consider carefully the assumed clutter component that is input to the test. This is because when applying this detection test the null hypothesis is that the cell under test contains clutter of a given distribution. If this assumed distribution is incorrect the resulting predicted and actual false alarm rate may be dramatically different for a given defined detection threshold. The probability of a Type I error (of incorrectly rejecting this null hypothesis) which equates to the probability of false alarm, (P_{FA}), is represented by the symbol α,

$$\alpha = \int_{\theta}^{\infty} f_N(z)dz = P_N(\theta) \tag{6.3}$$

where $f_N(z)$ is the probability distribution of the clutter. In a practical radar system the threshold value θ will be set by inverting Eqn. 6.3, and evaluating it at the desired false alarm probability using a given background distribution f_N. In the case that an incorrect distribution is assumed, f_Q, this will produce an incorrect threshold value θ'. When this incorrect threshold is applied to the actual distribution the resulting false alarm rate, α' is no longer the expected desired value.

$$\alpha' = \int_{\theta'}^{\infty} f_N(z)dz \tag{6.4}$$

Due to the lack of perfect knowledge and as real clutter distributions are always only at best *well represented* by models this misestimation will always occur. The application of the KLD to this area of radar processing allows for this error to be quantified in different scenarios from real datasets. The result of which is the quantification of the performance of the selected assumed distribution models, or the application of the metric as a fitting mechanism itself.

A potential reason for why the KLD has as of yet not been applied to radar signal processing in a practical way is its requirement for a full defined PDF. When analysing the output clutter distributions an empirical discretely sampled PDF can be produced, but it is not the *true* representative distribution of the clutter. The KLD therefore lends itself to the comparative analysis of theoretic distributions well, but is not as suited to the analysis of real data. This work investigates the application of the KLD to both theoretic and real data distributions and discusses the results for both cases.

In addition to testing the application of the KLD metric in sea clutter analysis another distribution comparison technique is applied. The Kolmogorov-Smirnov (KS) two sample test is often used to compare two sets of samples and evaluate if they have the same distribution [125, 126]. The KS test has been applied to sea clutter analysis previously, [34, 127] to confirm that the fitted theoretical distribution curves well represent the actual data.

The two sample KS test evaluates the max absolute difference between the CDFs of the two sample sets. This is defined as

$$D^* = max\left(|F_1(x) - F_2(x)|\right) \tag{6.5}$$

where $F_1(x)$ is the proportion of x_1 values less than or equal to x and $F_2(x)$ is the proportion of x_2 values less than or equal to x. The null hypothesis is that the two sample sets have the same distribution. This is rejected at a level α_{KS} if,

$$D^* > c(\alpha_{KS})\left[\frac{n+n'}{nn'}\right]^{1/2} \tag{6.6}$$

Where α_{KS} is the defined significant level. The variable c relationship with α_{KS} is defined from a lookup table, for example $\alpha_{KS} = 0.05 \rightarrow c = 1.36$.

6.1 Application to Theoretical Distributions

The initial tests of the application of the KLD were completed using an exact theoretic PDF solution for both the assumed and *real* clutter distributions. For these theoretic tests a K-distribution with varying shape parameters was used for both of the input

PDFs. This allows testing on expected KLD values as well as the behaviour of the KLD as the distribution is altered.

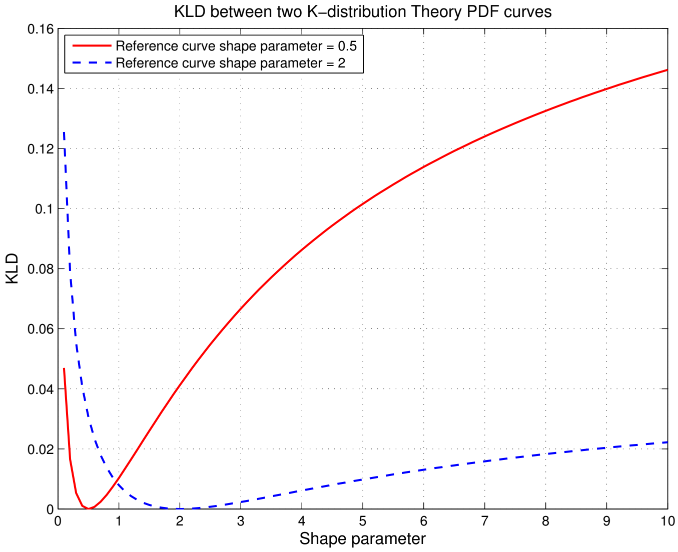

Figure 6.1: KLD between two example single K-distribution PDF curves and an array of other PDF curves with shape parameters between 0.1 and 10

The PDF of the K-distribution has previously been defined, Eqn. 2.33, this was used to generate input PDF curves to the KLD calculation. An array of K-distribution PDF curves were generated for a range of shape parameters from 0.1 to 10 in steps of 0.1. Each of these curves were evaluated numerically over a range of intensity values from 0 to 30 in increments of 0.01.

To evaluate the summation component of the KLD equation a numerical solution was applied to these finite and discretely sampled theoretic PDF curves. The first experiment evaluated the KLD between a fixed selected K-distribution and all the possible K-distribution curves. This process was repeated for two separate fixed reference PDFs to produce Fig. 6.1. In this case the reference distributions represent the *actual*, i.e. $p(x)$ in Eqn. 6.1, distribution while each of the other distributions tested against it are defined as the *assumed* distributions.

Figure 6.1 demonstrates clearly the non-commutability of the KLD. When the actual distribution was 0.5 it gave a KLD of 0.031 against the assumed distribution of 2. While in the reverse situation when the actual distribution was 2 a KLD of 0.041 was found between it and the assumed distribution of 0.5. The increased KLD value shows that there is an increased loss of information when interpreting the spikiness as $\nu = 0.5$ when the actual distribution is 2 that the reverse scenario. An important result from this is that under or over estimating the actual distribution by the same amount will produce different degrees of loss in detection power. In particular a greater loss occurs when the assumed shape parameter is higher than the actual value.

The obtained KLD values can be compared to other metrics that have been previously used to define the difference between two given distributions. This allows a direct comparison between known metrics and the newly proposed KLD technique. The metrics that have been compared are:

- Difference between the desired and achieved P$_{FA}$ for a given threshold level.
- Error in the threshold, and consequent reduction in radar sensitivity, due to deriving it from the incorrect distribution.
- The mean sum square difference (MSSD) between pairs of PDF and P$_{FA}$ curves.

The first comparison made is the difference between the desired and obtained P$_{FA}$ levels between two distributions. A reference level of log(P$_{FA}$)= -6 for the input actual distribution was used. Therefore the difference in P$_{FA}$ was evaluated from this point to the P$_{FA}$ of the selected assumed shape parameter distribution curve. An example of the difference in P$_{FA}$ between two distributions is shown in Fig. 6.2. The vertical line in this plot shows the threshold location where the reference curve, ν = 2, has a log(P$_{FA}$) = -6. The difference in P$_{FA}$ is evaluated vertically between the two curves at this point.

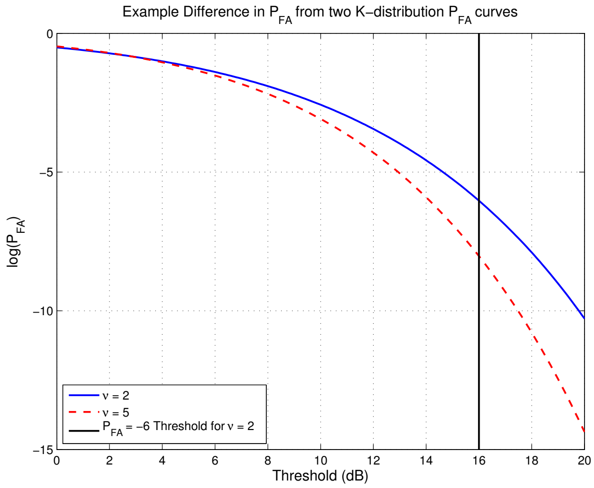

Figure 6.2: Example difference in P$_{FA}$ between two K-distribution P$_{FA}$ curves

This was then repeated between for two reference shape parameters curves of 0.5 and 2, against all other shape parameter curves between 0.1 and 10, Fig. 6.3. To establish the variation in P$_{FA}$ as a function of the reference and assumed distributions.

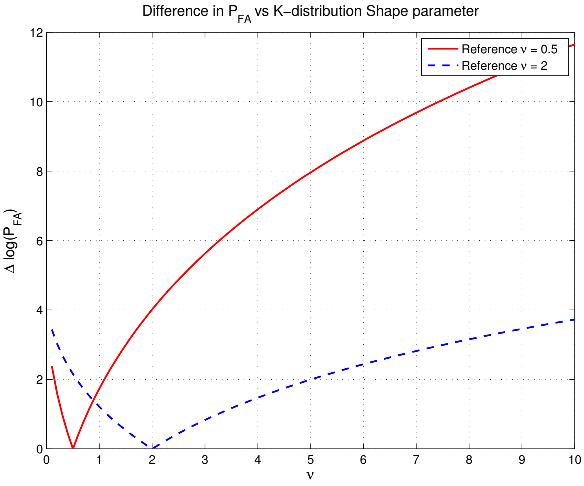

Figure 6.3: Difference in P_{FA} between two example single K-distribution P_{FA} curves and an array of other PDF curves with shape parameters between 0.1 and 10

The changing shape parameter on the abscissa of Fig. 6.3 is the shape parameter of the assumed distribution, as in Fig. 6.1. The difference reduces to zero when the assumed and actual distributions are exactly the same, which is to be expected. The steeper curves to the left of the matched shape parameters show that a larger difference in P_{FA} is obtained when the actual clutter has a relatively smaller shape parameter in comparison to the same equivalent increase in shape parameter, agreeing with the trends shown in KLD variation.

The next parameter evaluated for comparison to the KLD was the difference in threshold, for a given expected P_{FA}. The threshold difference between two example curves is seen in Fig. 6.4. It is a measure of the horizontal separation of the two curves at a fixed log(P_{FA}), which was again -6.

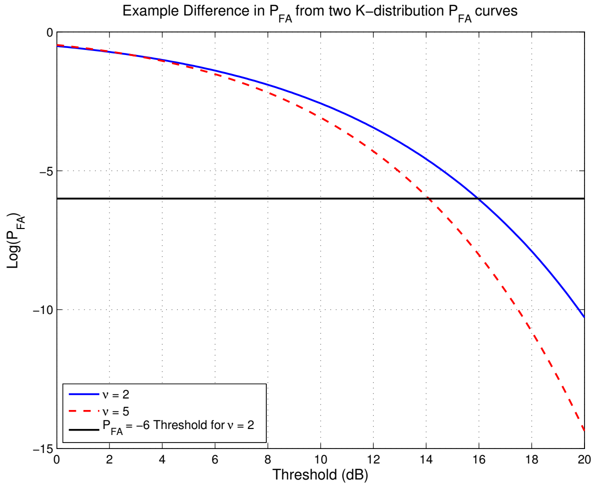

Figure 6.4: Example difference in Threshold for a fixed P_{FA} between two K-distribution P_{FA} curves

The threshold difference as a function of assumed shape parameter was then evaluated and is shown in Fig. 6.5. Each value on the curve in this figure corresponds to the difference shown in Fig. 6.4, but for different distributions. This shows real values for the cost of misestimating the distribution of the clutter present. A loss of 3dB sensitivity was obtained, when using the reference distribution of $\nu = 0.5$, at $\nu = 0.2$ & 1.4. Therefore underestimating the shape parameter by 0.3 gave the same loss as overestimating it by 0.9, when the actual value was 0.5. In comparison when the actual distribution was equal to 2 the threshold difference was only greater than 3dB for $\nu \leq 0.6$. In this case none of the $\nu > 2$ curves gave a threshold difference greater than 3dB. The two example curves both again are shown to have a steeper side to the left of the reference ν value, agreeing with the KLD and $\log(\mathrm{P}_{FA})$ differences.

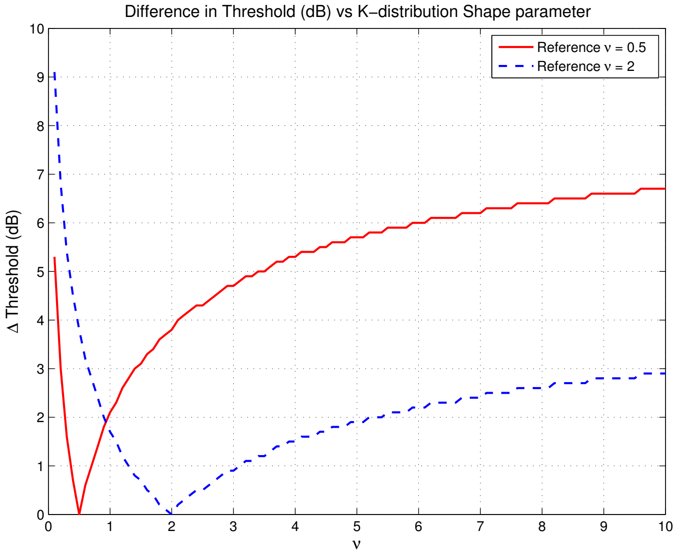

Figure 6.5: Difference in Threshold (dB) between two example single K-distribution P_{FA} curves and an array of other PDF curves with shape parameters between 0.1 and 10

The final comparative metric is the SSD between the assumed and actual distributions. The SSD between the same pairs of curves used to generate Fig. 6.1 is shown in Fig. 6.6. The nature of the SSD curves shows a similar shape to the KLD curves. This is a positive result as it reinforces the previous analysis used within this thesis. The KLD has a sound information-theoretical background and has been shown to agree with the variation given by the SSD evaluation. This therefore supports the assumption used previously in this thesis that the SSD is an effective method to fit theoretical distributions to the data.

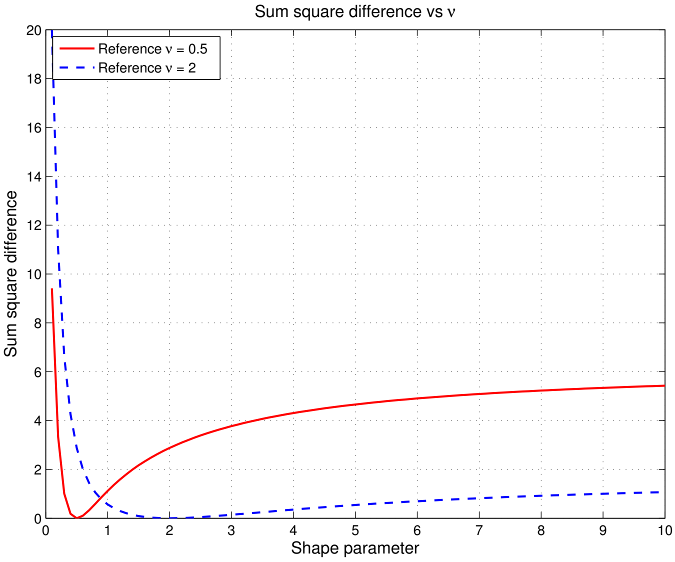

Figure 6.6: SSD between two example single K-distribution PDF curves and an array of other PDF curves with shape parameters between 0.1 and 10

The next step was to expand the investigation from using analytic solutions for the theoretical K-distribution PDF as inputs to the KLD. To achieve this Monte-Carlo simulation have been used as a way of showing that the distinctions shown previously are still apparent when using finite datasets of the sizes typical to clutter datasets. The modelling techniques used in Chapter 5 were applied to generate K-distributed samples with a given shape parameter. The PDF of these discrete sample sets was then evaluated and the resulting KLD between pairs of distributions was produced. The processing steps completed were:

- Simulate 10^5 samples of K-distributed variates with a given shape parameter.
- Define discrete PDF from the samples using a kernel density estimator. An in-built Matlab function was used for this.
- Evaluate KLD between pairs PDFs defined from the samples.
- Repeat process for all combinations of shape parameter pairs between 0.1 and 10.

The kernel density estimator applied was the“*ksdensity*” function within Matlab and used was applied by fixing the solutions to positive values, and used a fixed bandwidth for the kernel smoothing window of 0.01. The output kernel density PDF samples were evaluated over a range of 0.01 to 50 in steps of 0.01.

The resulting variation of KLD and difference in threshold (dB) between pairs of PDFs can be seen in Fig. 6.7 and 6.8 respectively. The KLD is shown as a function of the ν of p(z) and the ν of q(z) which are denoted as ν_1 and ν_2 in Fig. 6.7. The threshold difference has been evaluated at a fixed log(P$_{FA}$) of -4. The logarithm of the KLD has been plotted, as it allows for the whole dynamic range of values to be visualised. A logarithmic scale was also used because when comparing the result to the difference in threshold (dB) to allow a clearer comparison to be made.

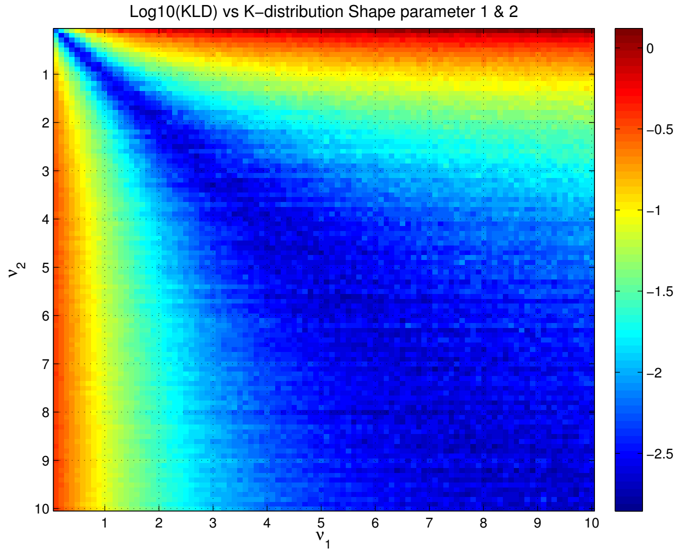

Figure 6.7: KLD between pairs of PDF curves generated using simulated samples

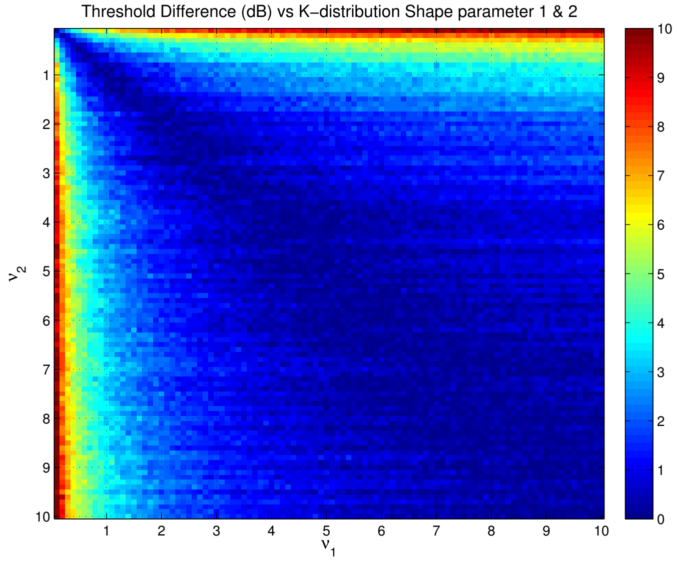

Figure 6.8: Threshold difference, at a set log(P$_{FA}$) = - 4, between pairs of PDF curves generated using simulated samples

The two figures showing the KLD and difference in threshold (dB) between pairs of curves clearly have a close relationship. In both cases the most significant errors occur in the region where either the actual data has a very low shape parameter or the assumed shape parameters has a low shape parameter (< 1). This emphasises the requirement of interpreting clutter with high accuracy when spiky (low shape parameter) clutter is present. While the cost of misestimation is much reduced in larger shape parameter scenarios.

The analysis performed to produce Fig. 6.7 was then applied to the KS two sample test. The K-distributed samples generated with a range of shape parameters were used to compare the KS test result. A fixed shape parameter distribution was compared to a range of varying shape parameter distribution samples. The result from the KS test is either 0 when the null hypothesis is accepted, which is the two sets of samples have the same distribution, or 1 when the null hypothesis is rejected. Figure 6.9 shows the KS test output from comparing a set of K-distribution samples with a $\nu = 1$ to multiple other sets of K-distribution samples with varying ν values. The significant level used for this KS test analysis was 0.05.

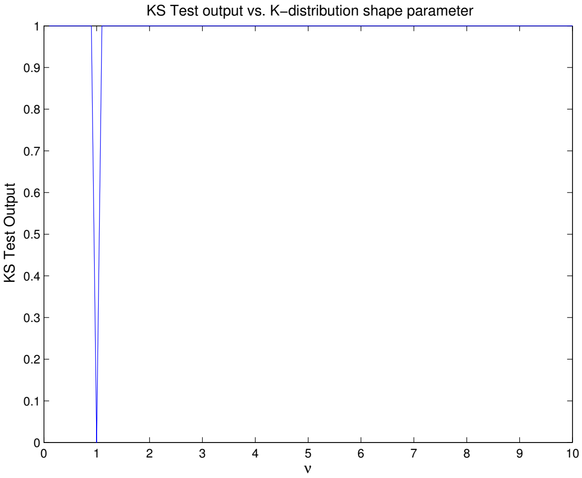

Figure 6.9: KS Test between generated samples of a fixed K-distribution $\nu = 1$ and varying other K-distribution ν values

The output values clearly show that the test accepted the null hypothesis only for one shape parameter, $\nu = 1$ which was the only distribution generated with the same shape parameter value. This binary result does allow for a verification when comparing data the proposed representative distribution.

This process was then repeated by varying both ν values of the two sample sets that are input into the test, see Fig. 6.10. The significant level used for this analysis was 0.05. In this figure all the KS test 0 values are shown in blue and all the KS test 1 values are shown in red. This method is comparable to that used to generate the KLD values in Fig. 6.7 when comparing two K-distribution datasets. The results here show that at low shape parameters only the exact distributions were shown to pass the null hypothesis. As the shape parameters increase a wider array of samples were shown to pass the test despite being generated with a different intended ν. This shows the importance of assessing the shape parameters correctly at low values,

$\nu < 2$, as they are clearly very different and a small misestimation clearly fails the KS test. Whereas in the case of $\nu > 6$ the difference between K-distributions reduces and the KS test can not differentiate them successfully.

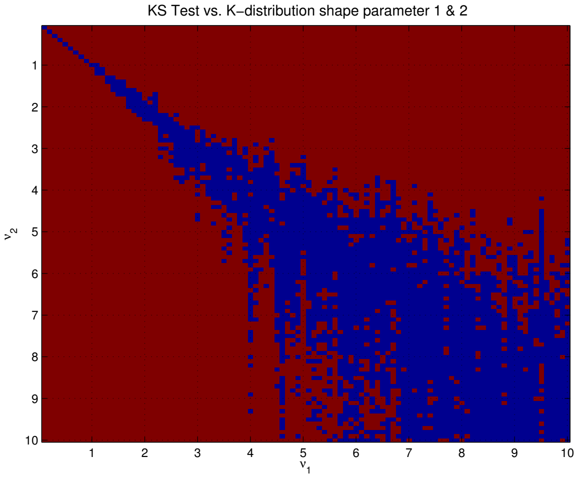

Figure 6.10: KS Test between generated samples with varying K-distribution ν

6.2 Application to Real Sea clutter

This section applies the KLD metric to the assessment of how well theoretical distributions represent real sea clutter data. Initially the K-distribution and a thermal noise distribution (negative exponential) were tested against the selected real sea clutter distributions. The data used for this analysis was taken from the CSIR 2007 dataset, see Section 3.1.2, specifically dataset 07. The Doppler data from this individual dataset has been selected and the distributions within each Doppler bin were defined. Each Doppler bin contains 1845 samples, which are then used to generate a PDF that represents the statistics within that individual Doppler bin.

As the real clutter data is finite and discretely sampled an approximate PDF representation is required. In order to produce the representative PDF for the data the same methods used in Section 6.1 were applied. A kernel density estimate was used to produce a smoothed PDF estimate from the discrete data samples. The same kernel density estimate methodology was used as that described in the KLD theoretical analysis Section 6.1. This method can be considered to provide the best possible non-parametric density estimate possible for the input data. Although in addition to the kernel density estimate a basic histogram estimate for the PDF was also tested to obtain comparative results. The resulting PDF is then used as the actual clutter distribution and the assumed distributions were a range of K-distribution curves, with the same range of shapes used in Section 6.1.

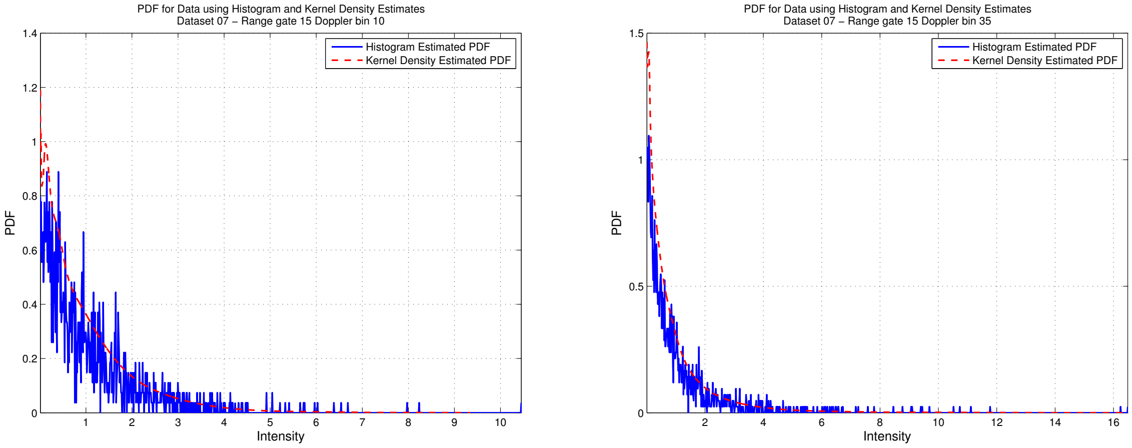

(a) (b)

Figure 6.11: CSIR Dataset 07 Histogram and Kernel Density Estimate PDFs from individual Doppler bins data (a) Doppler bin 10 (b) Doppler bin 35

Two example plots of the estimated PDFs from separate Doppler bins are shown in Fig. 6.11 (a) Doppler bin 10 and (b) Doppler bin 35. In the case of Doppler bin 10 the data is thermal noise limited with no clutter present. For Doppler bin 35 the CNR is $\approx$ 20dB, meaning that the distribution will be dominated by sea clutter amplitude statistics. This is seen by the significantly longer tail of the distribution which increases intensity to ≈ 16 where as Doppler bin 10 only goes to ≈ 6.

The data distributions were then used to evaluate the KLD between real sea clutter and selected theoretical distributions. A varying array of K-distribution curves evaluated with the PDF (evaluated at the same locations in the intensity), were used. The shape parameters varied from 0.1 to 10 in steps of 0.1, as well as having an additional shape parameter 100 curve. This was used as the data itself was fitted to this range of shape parameters using a SSD fit shown in Section 4.2.2. The scale parameter was normalised with respect to the mean of the dataset in all cases.

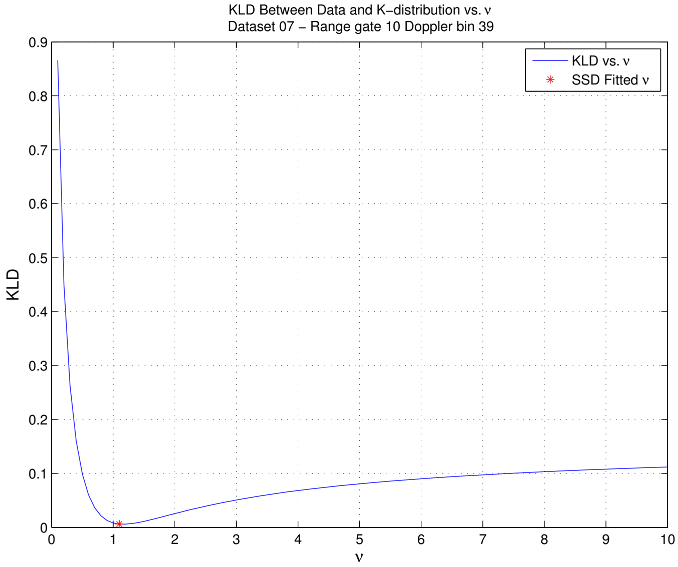

Figure 6.12: KLD between Data and Theoretical K-distribution curve vs. Shape parameter - Dataset 07 Doppler bin 39 Range gate 10

The result of this analysis from a single Doppler bin is shown in Fig. 6.12. where the set of shape parameters used is plotted against the resulting KLD between the data and the K-distribution curve with that given shape parameter. The K-distribution shape parameter PDF that was found to have the minimum KLD was 1.2, while the SSD fitted and moment shape parameters for this Doppler bin were 1.1 and 1.13 respectively. These results show a very close agreement as to which K-distribution curve best represented the data.

The difference that does exist between the fitted results has a number of possible explanations. In attempting to represent the discretely sampled data points as a continuous PDF, using the kernel density estimate, errors will be introduced. The actual PDF distribution of these samples is difficult to characterise as it has not absolutely correct solution. This could possibly lead to a misestimation in the resulting KLD as to which K-distribution curve best represents the data. Another possibility is that the SSD method is itself failing to select the *best* representative distribution and the KLD is in fact an improved method for fitting a distribution to the data.

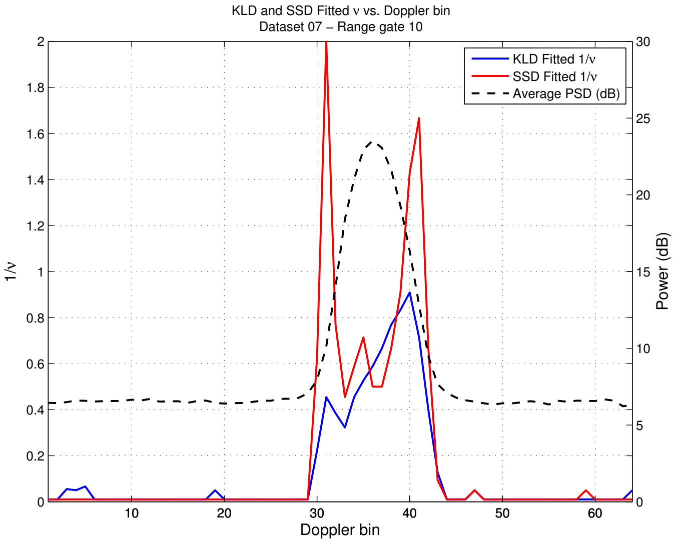

Figure 6.13: KLD and SSD fitted $1/\nu$ values vs. Doppler bin - Dataset 07 Range gate 10

The analysis was then extended to all Doppler bins within a selected range gate. In each case the data distribution within the selected Doppler bin was represented by a PDF defined using the kernel density estimate. This PDF was then input to a KLD evaluation between itself and a range of K-distribution shape parameter curves. The K-distribution that gave the smallest KLD value was defined as the KLD fitted K-distribution curve. This gave the variation of K-distribution shape parameter from both methods seen in Fig. 6.13. It can be seen that in the outer thermally noise dominated Doppler bins (1 to 28 and 45 to 64) the two fitting methods agree very closely. It is also shown that the two peaks in the inverse shape parameter, which were first noted in Section 4.1.3, exist for both fitting methods at the same location in Doppler.

The next step in the analysis was to compare the KLD values as a function of Doppler. The KLD was evaluated between the SSD fitted K-distribution and the data, as well as the minimum KLD value K-distribution (see Fig. 6.12) and the data. This is a direct comparison of the minimum of the curve in Fig. 6.12 to the KLD value from the SSD fitted curve, the red data point, as a function of Doppler bin.

The KLD fitting method shows lower inverse shape parameters of 0.456 and 0.909 for the left and right peaks respectively. While the SSD fitted inverse shape parameter peak values were shown to be 2 and 1.67. Even though the shape parameter values do not agree exactly both methods are therefore demonstrating that it is at this section of the Doppler spectra that the sea clutter definitely changes its statistical behaviour. The KLD and SSD show that the distribution shifts and becomes an increasingly longer tail distribution.

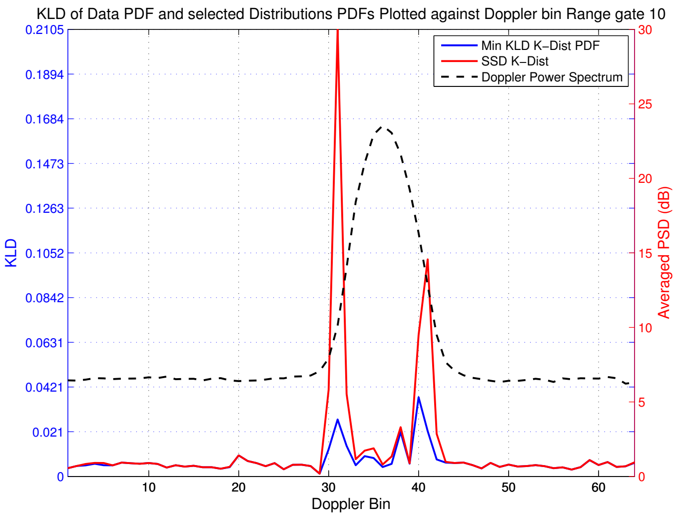

Figure 6.14: KLD vs. Doppler of KLD and SSD fitted K-Distribution Curves - Dataset 07 - Range gate 10

The KLD was then evaluated between a fixed distribution PDF and the data PDF for each Doppler bin. The fixed distributions selected were a thermal noise distribution (defined by the Rayleigh distribution) and a K-distribution with a fixed shape parameter of 2.

By using a Rayleigh distribution for each Doppler bin it is possible to evaluate the cost in misestimation when using a thermal noise distribution to represent the data in all Doppler bins. The KLD between the data PDF and a Rayleigh distribution evaluated at the same intensity locations is shown in Fig. 6.15.

The thermal noise KLD comparison shows that the outer Doppler bins have relatively very low KLD values. Meaning that they were a good fit to the thermal noise distribution suggesting they contain only noise, i.e. the clutter spectrum is narrower than the available unambiguous Doppler range. Over the region where the clutter is present the KLD values increase dramatically. The peak value is shown to increase up to ≈ 0.3, in comparison the KLD fitted curve in Fig. 6.14 and has a peak value of ≈ 0.04. This quantifies how ineffective the assumption of Rayleigh noise is at representing real sea clutter in the Doppler domain. There are two peaks in the KLD values that exist at the leading (Doppler bin 40) and trailing (Doppler bin 31) Doppler edge of the clutter PSD. It is therefore at these points that the clutter deviates most significantly from a thermal noise distribution, which is also seen in the K-distribution KLD evaluations. This shows that both distributions are least effective at representing the real data at these location, but to different extents.

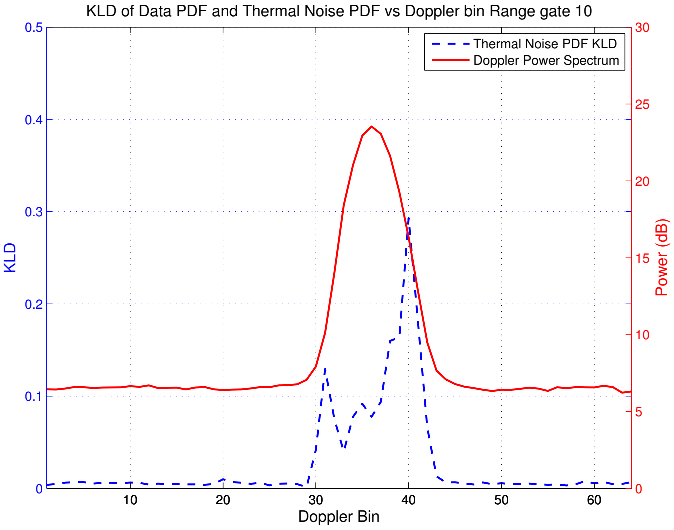

Figure 6.15: KLD between Data and Thermal Noise PDFs vs. Doppler - Dataset 07 - Range gate 10

The second KLD evaluation between the data and a fixed distribution is shown in Fig. 6.16. The KLD between the data PDF and a K-distribution with $\nu = 2$ was used to produce this figure. This shape parameter was selected due to it being the SSD fitted ν at the peak in CNR. This compares the divergence between the data and the closest fitting distribution where the clutter is at it's peak power. It represents the potential mistake of using the simple assumption that the clutter is always distributed the same way it is at its peak power. By evaluating the KLD between the fitted K-distribution at the CNR and the distribution in each Doppler bin the cost associated with this simple assumption is shown.

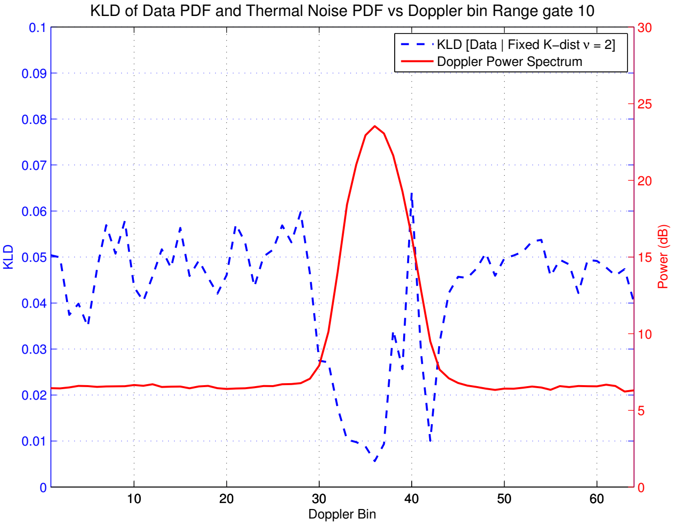

Figure 6.16: KLD between Data and Fixed K-distribution with $\nu = 2$ vs. Doppler - Dataset 07 - Range gate 10

The KLD values produced using a fixed K-distribution are much less than those seen in Fig. 6.15 within the clutter dominated region, but much greater over the rest of the Doppler spectrum. The fixed K-distribution best represented the data at the peak CNR Doppler bin, which is expected as it was selected using the SSD fitted ν value from this Doppler bin. Over the CNR dominated region the KLD values are shown to be lowest around the peak of the CNR and at the very leading edge of the Doppler spectra before the CNR reduces to its minimum. The peak in the KLD values is found on the rising edge of the spectra at Doppler bin 40. This is the same location in Doppler that the peak in the KLD has been shown for both the thermal noise and fitted K-distribution KLD values, Fig. 6.15 and 6.14. This makes this Doppler bin the least well represented by all tested distributions. It is important to note the difference in scale of the KLD values between Fig. 6.15 and 6.16. The thermal noise was found to have a KLD of 0.29 while the K-distribution $\nu = 2$ had a KLD of 0.06. Hence the thermal noise had a divergence of ≈ 5 times more than the selected K-distribution.

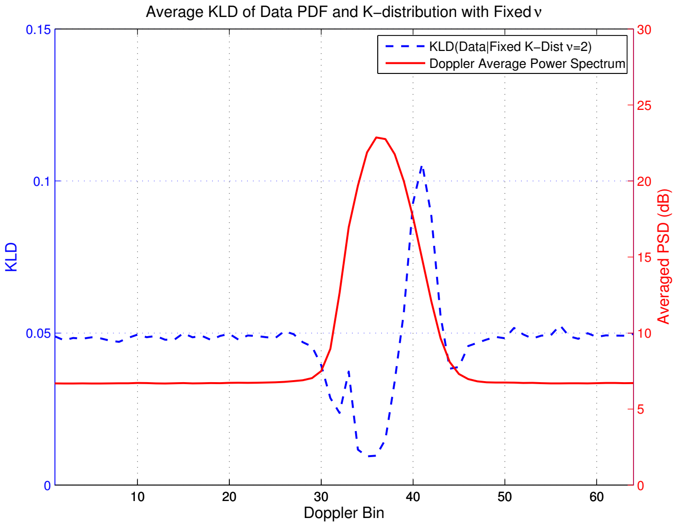

Figure 6.17: Averaged KLD between data and fixed K-distribution with $\nu = 2$ vs. Doppler - Dataset 07

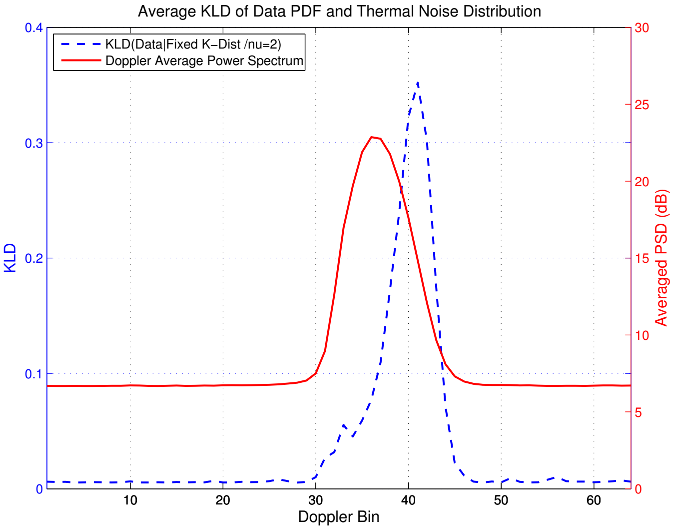

Figure 6.18: Averaged KLD between data and thermal noise vs. Doppler - Dataset 07

The process of KLD evaluation between a fixed K-distribution or thermal distribution and the data was then repeated within all the range gates of dataset 07, in Fig. 6.17 and 6.18 respectively. The fixed K-distribution used was $\nu = 2$ for all the range gates. The averaged values reinforce the key results seen within the single range gate figures. The fixed K-distribution was most effective at the peak of the CNR while failing on the leading edge of the clutter. The thermal noise distribution failed to represent clutter distributions over the clutter dominated region of the Doppler spectrum, particularly on the leading edge of the clutter.

6.3 Information Theory Conclusions

This chapter has introduced the KLD as an effective quantitative measure for comparing the divergence of two distributions in the application of sea clutter analysis. The principles behind the KLD as well as its mathematical background were first defined. These principals were applied using theoretical distributions to model the difference between K-distribution PDFs with varying shape parameters. This demonstrated the loss relating to the misestimation of a parameter within a fitted distribution. The KLD was shown to produce results that were comparable to relative values found when using other ad hoc measures of difference, such as the SSD. The use of the KLD in the application of distribution fitting and quantification was further validated by this, as well as reinforcing methods that have been used throughout previous analysis. The non-commutability of the KLD represents the consequences of mis-interpreting the background clutter distribution as more or less spiky than it actually is, which is not accounted for by metrics such as the SSD.

The KLD was then applied using real sea clutter distributions generated from

Doppler data taken from the CSIR 2007 database. The analysis demonstrated the novel use of the KLD as an effective analytic tool for fitting distribution models to real sea clutter data. As well as the ability to fit distributions to real data the KLD also gave a quantitative measurement of the effectiveness of the models in representing the data. In the analysis shown this was demonstrated as a function of Doppler. The K-distribution was shown to well represent the clutter at the peak CNR location in Doppler, but was not as effective on the leading and trailing edges of the clutter.

The next processing stage involved evaluating the KLD between the data and fixed distributions as a function of Doppler. The two distributions, a K-distribution with a fixed ν and the thermal noise distribution, were compared to the data distribution with each Doppler bin. The results from this processing showed the cost of assuming a basic thermal noise distribution for the clutter, or assuming an unchanging K-distribution. This relates well with the work described in this thesis that characterised the variation of the amplitude statistics with Doppler. This strengthens the argument behind adapting for the changing amplitude statistics of the sea clutter as a function of Doppler.

The KS test results showed that is can successfully differentiate between sets of K-distribution samples and will validate if a theoretical distribution fits to the input data. The difference between the KS test and the KLD is that the KLD produced a metric not a binary result, this is importance because it means that more information is contained within the KLD output in comparison to the KS test.

Fundamentally the KS test has a null hypothesis that the two distributions are the same, and tests whether the test results disproves this. Using the KLD the assumption is that the two input distributions are different and we are analysing how different they are, as we want to ask is model A closer to the data than model B?. The theory behind the KLD can also be related closely to the problem of radar detection and background misestimation.

Considering the analysis performed there are some issues with the application of the KLD, a key issue being that an approximation of the *real* sea clutter must be made. This issue does not affect the theoretical analysis, which observes the variation of the KLD between relative K-distributions PDF curves. For real data the approximation is difficult and in this analysis it was limited by the ability of the kernel density estimate to generate the *correct* PDF. To achieve this a kernel density estimate was applied to the discrete finite samples, it is considered to be an effective solution. The KS test uses the CDF of the data samples and therefore does not require this estimation which is a source of error.

In summary it is important to consider that within real world scenarios the sea clutter is beyond the control of the radar engineer and its *actual* distribution remains undefinable. The models used here will never exactly represent the clutter distribution but can be considered to be successful if they will effectively represent the clutter effectively in the majority of scenarios. The KLD metric, which is base on clear mathematical reasoning, has been presented as a measure of how effective the models are at achieving this goal. In this application is has been shown to be suitable and should therefore become a more commonly used analytic measure for defining the success of further models in their application to additional datasets.

Chapter 7

Conclusions

This chapter summarises the key conclusions, novel contributions and achievements of this research. Future potential research areas related to the material that has been presented within this thesis are also discussed. The key conclusions discussion, Section 7.1, progresses in line with the analysis that was performed in Chapters 4 to 6. The novel contributions are then clearly presented in Section 7.2, highlighting where this research has contributed to the current scientific understanding. Finally potential areas where the research could now be expanded are highlighted in Section 7.3.

Sea clutter research is an important topic within the radar research community. Despite this, novel contributions to the global knowledge and understanding of this phenomena have been demonstrated within this work. As the analysis progressed it has been shown that each dataset provided incremental understanding of sea clutter statistical variations. At each stage more detailed and deeper relationships of sea clutter to additional parameters have been revealed.

It was shown that that little information exists on the specific characteristics of the amplitude distributions of sea clutter in the Doppler domain. This specific area of sea clutter work hence clearly showed good potential for further investigation. By researching into this domain the resulting conclusions have both contributed to the scientific research community, as well as provide practical radar engineering advantages gained from the knowledge of how the statistics of the sea clutter behave. By furthering the understanding of the phenomena this research has direct implications for quantifying the effectiveness of detection algorithms that are used for Doppler signal processing applied in any radar system.

7.1 Summary

7.1.1 SW2000 Data analysis

The first dataset that was made available for analysis was from the Thales UK SW2000 AEW radar system. This data analysis was on recordings from an operational radar system. Therefore the results from this study are not only scientifically important but they also are of practical radar engineering relevance. The practical engineering aspect is linked to the improvement of radar performance in the sea clutter environment. The information shown will enable future enhancement of detection algorithms to more successfully adapt to the clutter environment.

Through statistical analysis of the amplitude distributions within individual Doppler bins it was possible to show a clear variation in the statistical behaviour. The variation was shown by fitting a widely accepted sea clutter model, the K-distribution, to the data using SSD and moment fitting methods. These results are the first to quantify a variation with sea clutter data of the K-distribution shape parameter as a function of Doppler. The variations shown were clear, were shown to have a characteristic shape and were consistent. A comparison between the vertical and horizontal polarised datasets showed the largest increase in the moment fitted $1/\nu$ values on the leading edge of the PSD within both datasets and a secondary increase on the trailing edge. The horizontally polarised data demonstrated the largest increase in inverse shape parameter, which is consistent with prior literature on the time domain statistics of vertical and horizontal polarised data.

The SW2000 datasets were not ideal for pure sea clutter analysis due to the PRF agility of the radar with complicates the analysis. There was also the limited meteorological information avaliable. Despite this it was still possible to achieve this first quantification the variation of the sea amplitude statistics with Doppler, and compare these results between two polarisations. This work could then be expanded upon, though characterising the variation with azimuth angle or in the bistatic case, via the analysis of the two datasets reviewed below.

7.1.2 CSIR Data analysis

Following the SW2000 data analysis the focus of the research moved to the analysis of the CSIR 2007 data. As this dataset was generated specifically for sea clutter measurements and included carefully measured meteorological and geometric parameters. The RF parameters were also well characterised. The potential of furthering the understanding of the variations of observed phenomena with these parameters was therefore significant. Four key datasets were selected for analysis that were shown to be best suited to characterise the behaviour of the statistical distributions as a function of azimuth angle and range.

The first analysis completed was on the non-coherent data from each measurement. The temporal ACF was produced for each range gate within each dataset, and by averaging these it was possible gain an understanding of how consistent was the long term temporal correlation. This showed a clear sinusoidal structure within the upswell geometry datasets, and a flat long term correlation profile within the cross swell data. This information would later prove very valuable when applying the Doppler model to simulate individual datasets.

The results from the statistical variation of the amplitude of the sea clutter with Doppler showed that it was most spiky in two key Doppler locations, except in the 07 dataset. These locations in Doppler were on the leading and trailing edge of the clutter PSD, which were dependent on wind and swell direction. The highest peak inverse shape parameter values were shown to be the leading positive Doppler edge on the upswell datasets and the leading negative Doppler edge in the cross swell datasets. This is related to the downwind side of the Doppler spectra showing a more spiky distribution. This is potentially linked to the wind blowing spray from the white cap waves, which resulting is numerous high amplitude returns. Overall the results showed that the upswell measurements produced the most spiky statistics, in particular the closer range upswell dataset (Dataset 12).

These results of statistical variation reinforced the top level conclusions from the SW2000 data. By confirming this characteristic behaviour this analysis therefore demonstrated that the initial discoveries shown using the SW2000 data were neither unique to that radar system nor the particular environment that it was measuring.

7.1.3 NetRAD Data analysis

The NetRAD sea clutter data analysis represents very novel using a unique dataset. This radar system is an S-band system in comparison to the two prior datasets, which allows the previous X-band results to be compared to S-band sea clutter amplitude statistics demonstrating if they are still valid. The data was generated by the research group at UCL specifically to obtain the first coherent simultaneous measurements of bistatic and monostatic sea clutter. I was personally involved in the generation of this data and was therefore able to use my insights from this to progress the data from a raw state all the way to the high level statistical comparisons that have been made.

The South African trials campaign produced a number of sea clutter datasets over a period of weeks. The initial task in the analysis was to select which were the most relevant to the goals of my research. The six datasets that were selected were generated at three bistatic angles (60°, 90° & 120°) at two polarisations (vertical and horizontal). The results of the variation of both the monostatic azimuth angle and the resulting comparative bistatic angle could be observed in each of the datasets. This connects the results to the CSIR data analysis as well and producing completely novel results pertaining to the equivalent bistatic measurement.

The complexities of generating bistatic data and analysing the results were a major issue when undertaking the analysis of the data. These had to be overcome in order to allow effective direct comparisons between monostatic and bistatic data. The phase correction processing was a very important step when comparing Doppler spectra of the two radar nodes, with this no comparison could be made between the monostatic and bistatic results.

When comparing the monostatic results with the previous work completed on the SW2000 and CSIR datasets it is clear that these established characteristic variations are again repeated within the NetRAD data. The horizontal monostatic statistics are shown to be more spiky than the vertically polarised, a double peak in the $1/\nu$ values is frequently seen in the variation with Doppler, not in all cases though. As well as this the location of the PSD and the peak in $1/\nu$ shift with the moving β, and therefore azimuth, angle.

When comparing the simultaneous monostatic and bistatic data it was shown that both datasets were a good fit to the K-distribution, the first time that this has been shown in the bistatic case. The PSD shape and absolute power were shown to be comparable between the monostatic and bistatic data, the significant differences were shown in the statistical behaviour of the data. The bistatic data was on average shown to be less spiky than the equivalent monostatic data. In all cases the range gate averaged K-distribution SSD fitted $1/\nu$ values were less in the bistatic case, except for both H and V polarisation datasets at $\beta = 60°$. In the $\beta = 60°$ datasets the bistatic data was shown to be more spiky at it's peak, but this increase in the spiky behaviour of the clutter was over a small range within the Doppler spectrum. This relationship agrees with other data analysis using SAR data recorded over land in a semi-urban environment in [128], but has not yet been shown with sea clutter Doppler spectra prior to this research. These key results were published within [129], which was the first publication to describe the Doppler bistatic sea clutter statistical variations.

When considering these results in the context of the task of detecting targets in clutter the bistatic geometry has been shown to be potentially more favourable. This is because on average the clutter is less spiky, and hence has a shorter tailed distribution. It is considered that the bistatic geometry avoids the frequent high amplitude returns due to the change in scattering angle with respect to the wave surface. For the same given desired P_{FA} a bistatic system would have a greater sensitivity to target signals because of this. Even in the $\beta = 60°$ datasets where the peak $1/\nu$ was larger in the bistatic data, this was over a smaller area within Doppler. Hence the bistatic system would still more effective within the majority of Doppler spectrum. In terms detection processing this means that a lower threshold could be set across the Doppler spectra allowing for the detection of lower RCS targets within the clutter.

7.1.4 Simulation and Modelling

The simulation and modelling research completed within this thesis follows on directly from the sea clutter analysis. It relates directly to the analysis previously discussed as it represents a direct application of the knowledge obtained from the analysis of real data.

The first step of this work was the independent algorithm development of the recently established Doppler spectra model, that was first proposed by S. Watts. In its initial presentation the model itself was tested on a single range gate within one dataset. This research applied the model to significantly more data, from the CSIR 2007 dataset, which varied over a variety of azimuth angles.

By characterising the required input properties it was possible to simulate the Doppler spectra of each dataset. The successful simulation of the data both represented the observed qualitative properties of the PSD but also replicated the statistical variation which has been shown to be a key feature throughout this thesis.

A novel aspect of the simulation processing was the link discovered between the centre of gravity of the PSD and the intensity values. Using multiple datasets generated at different azimuth angles it was shown that the linear fit parameters A and B were related to each other as well as being a function of azimuth, with respect to wind/swell direction. This discovery enhances the model as the number of independent variables required is reduced.

The results shown within the simulation and modelling research have been submitted for publication in [124]. This represents the first large scale application of the proposed model and further establishes it as an effective method of simulated sea clutter Doppler spectra.

7.1.5 Information Theory Analysis

Through the application of the KLD metric it was possible link the fields of sea clutter analysis and information theory. The metric was first shown to be suitable for the area of distribution comparisons as well as begin directly related to detection likelihood tests used in radar detection theory.

The initial tests using the KLD evaluated the divergence between two theoretical distributions. The resulting values were then compared to other metrics that have been used previously as well as quantitative values such as P_{FA} and difference in threshold (dB) to put the divergence variation in context. This gave a valuable insight into the theoretic values that would be obtained if *real* sea clutter was represented exactly by a K-distribution with a given ν, and the assumed distribution used a different ν.

The KLD was then applied to real sea clutter data from multiple Doppler bins taken from the CSIR 2007 database. The real sea clutter PDFs were successfully replicated using kernel density estimates to allow a KLD evaluation between data and theoretic distribution. The analysis demonstrated that the KLD was able to capture the varying divergence between data and K-distribution as a function of ν. This information could then be used as a new form of fitting of the K-distribution to the data.

The processing was then expanded to all Doppler bins to fit the K-distribution to the data as well as quantify the divergence as a function of Doppler. The KLD was found to give divergence values that matched the characteristic variation in $1/\nu$ with Doppler, therefore strengthening the prior research within the thesis that initially defined these variations.

Fixed distributions were then input to the KLD for each Doppler bin to evaluate the cost of assuming the same distribution across all Doppler bins. The distributions used were a K-distribution with the ν values obtained from the peak CNR Doppler bin and a thermal noise distribution. This analysis showed that significant divergence values were obtained if the peak CNR ν was used across the clutter dominate sections away from the CNR peak. The largest divergence values were found on the leading edge of the clutter PSD.

By relating the KLD to sea clutter analysis a link has been developed between the established area of optimisation information extraction from signals and the area of sea clutter distribution analysis. The conclusions of this work are supported by the publication of parts of the analysis in [6]. The results within this chapter clearly showed that the KLD is an applicable and effective metric that has the potential to be a widely used method of quantifying the misestimation of model against real clutter.

7.2 Achievements and Contributions of Research

The wide ranging analysis that has been completed has added significantly to the knowledge base of the area of sea clutter research. The key contributions of this research are as follows:

- The research relating to the analysis completed on the SW2000 data is the first demonstration of the variation of sea clutter statistics with Doppler using the K-distribution. This work also demonstrated for the first time a direct comparison between the vertical and horizontal sea clutter amplitude statistic variation as a function of Doppler. The results of analysis performed from my research were published in [130]. All the analysis results shown within this publication were generated by myself from software that I wrote. The paper was then co-authored with A. Stove and K. Woodbridge.

- The analysis completed on the CSIR dataset enhanced the understanding of how amplitude statistics altered with azimuth angle in relation to swell and wind direction. The expansion of the initial results confirmed that the characteristic behaviour, an increase $1/\nu$ at the leading and trailing edge of the clutter, was consistent with the SW2000 results as well as showing a strong dependence on look angle.

- The analysis of the NetRAD simultaneous bistatic and monostatic sea clutter is a very novel area of research. The S-band monostatic sea clutter data is shown for the first time to be well represented by the K-distribution. The coherent monostatic and bistatic comparisons the statistical variation of the sea clutter as a function of Doppler also have never been shown within prior literature. This work has provided the first insight into the comparative behaviour of the coherent clutter in these two scenarios. This work represents a clear step forward in this area allowing opening the area of research up for further experimental campaigns to compliment the samples of the multi-dimensional problem that have been analysed.

- The modelling and simulation work demonstrated the effectiveness of a newly proposed model, as well as begin able to further reduce its complexity. The initial analysis showed that the model was applicable to a much wider set of data that it had been previously tested with. This strengthened the confidence in this model as a practical and effective representation of sea clutter Doppler over a wide range of conditions. The latter analysis within this work demonstrated a new connection between variables within the model, which hence reduced the number of variables required to simulate the clutter. This was shown through the direct connection of PSD centre of gravity and the azimuth angle of the recording.

- The information theory research is the first application of the KLD to the study of sea clutter analysis. It was demonstrated that the KLD metric was a relevant quantifiable value that can be used to estimate the cost of misestimation between two theoretic models with varying parameters, or between distribution models and real sea clutter distributions. In addition to this it was used to determine the cost of assuming a uniform distribution across all Doppler bins.

7.3 Future Work

Leading on from this research there are a number of potential avenues that could be explored, the most significant of which are discussed below.

The research in this thesis has focused on furthering the understanding of the statistical variation of sea clutter. There has been no specific analysis using targets within the sea clutter itself. An obvious future extension of the work would be to analyse targets within sea clutter data to observe the influence sea clutter has on targets and vice versa. It may be potentially possible to detect targets not only from their reflections but from the changes to the Doppler distributions of the observed sea clutter. As well as this the new understanding that has been demonstrated within this thesis could then be taken forward by the detection and tracking community to optimise the efficiency of their algorithms using this a priori knowledge of the environment as a whole.

The modelling and simulation theory work is an area that is clearly opened to further expansion. The model itself has only be shown to effectively represent sea clutter at X-band frequencies. No experiments have been completed at and alternative frequencies, such as the S-band NetRAD data, modelling analysis on further frequency bands would be of great value to the research community.

The observations made when completing the simulation and modelling work all used data recorded on the same day, over assumed constant conditions. By testing the model further using data generated over a variety of sea conditions it would be possible to determine if the Doppler spectra is still well represented by the model. As well as understanding how the input parameters of the model change with variables such as sea conditions, wind speed / direction and grazing angle.

The KLD analysis only represented the first application of this metric to the area of sea clutter analysis. Prior work has been completed on the use of the KLD in ATR in the presence of land clutter, in [131]. The work shown within this thesis could be developed further towards targets detection sea clutter. By relating the KLD directly to the difference in threshold averaged over all false alarm rates it would be possible to gain a directly relevant understanding of how the metric relates to radar performance. A concise relationship between these two parameters would be of significant practical use to radar engineers.

Bibliography

[1] G. W. Stimson. *Introduction to airborne radar.* SciTech Publishing, 2nd edition, 1998.

[2] S. Watts. Radar sea clutter : recent progress and future challenges. In *Proc International Radar Conference*, pages 10–16, 2008.

[3] N. J Willis and H.D. Griffiths. *Advances in bistatic radar.* SciTech Publishing, 2007.

[4] S. Kingsley and S. Quegan. *Understanding radar systems.* McGraw Hill, 1992.

[5] K.D. Ward and S. Watts. Use of sea clutter models in radar design and development. *IET Radar, Sonar & Navigation*, 4(2):146, 2010.

[6] M. A. Ritchie, A. Charlish, and K. Woodbridge. Use of the Kullback-Leibler Divergence in Estimating Clutter Distributions. In *Proc. IEEE Radar Conference*, pages 751–756, May.

[7] V. J. Phillips. The Telemobiloscope an Edwardian Radar. *Wireless World*, page 68, July 1978.

[8] B. Wade. SharpEye A 'New Technology' marine radar. In *Proc. IET International Conference on Radar Systems*, August 2007.

[9] T. R. Kronhamn. AEW performance improvements with the ERIEYE phased array radar. In *Proc. IEEE Radar Conference*, pages 34–39, 1993.

[10] M. Heed. The ERIEYE phased array antenna-from a systems viewpoint. In *Proc. IEEE International Conference on Phased Array Systems and Technology*, pages 391–394, 2000.

[11] S. Watts. A new method for the simulation of coherent sea clutter. In *in Proc. IEEE Radar Conference*, pages 52–57, 2011.

[12] M. Skolnik. *Radar Handbook.* McGraw Hill, New York, 3rd edition, 2008.

[13] N. C. Currie. *Principles of Modern Radar: Basic Principles.* SciTech Publishing, 2010.

[14] N. J Willis. *Bistatic Radar.* SciTech Publishing, 2005.

[15] R. Blockley and W. Shyy. *Aerospace Encyclopedia.* Wiley & Son, 2010.

[16] M. Cherniakov. *Bistatic Radars - Emerging Technology.* John Wiley & Sons, 2008.

[17] L. R. Moyer, C.J. Morgan, and D.A. Rugger. An exact expression for resolution cell area in special case of bistatic radar systems. *IEEE Transactions on Aerospace And Electronic Systems*, 25(4):584–587, 1989.

[18] J.W. Crispin, R.F. Goodrich, and K.M. Siegel. A Theoretical Method for the Calculation of the Radar Cross Sections of Aircraft and Missiles. Technical report, University of Michigan Radiation Lab Report. 2591-1-H, 1959.

[19] K. M. Siegel and J. J. Bowman. RCS Calculation of Simple Shapes - Bistatic. In *Methods of Radar Cross-Section Analysis*, chapter 5. Academic Press, New York, 1968.

[20] G. Ewell and S. Zehner. Bistatic radar cross section of ship targets. *IEEE Journal of Oceanic Engineering*, 5(4):211–215, October 1980.

[21] T. Lamont-Smith, K. D. Ward, and D. Walker. A comparison of EM scattering results and radar sea clutter. *RADAR 2002*, 2002.

[22] D. Walker. Experimentally motivated model for low grazing angle radar Doppler spectra of the sea surface. *IEE Proc. Radar, Sonar and Navigation*, 147(3):114–120, June 2000.

[23] K. D. Ward, R. J. A. Tough, and S. Watts. *Sea clutter: scattering, the K distribution and radar performance.* IET Radar, Sonar and Navigation Series 20, 2006.

[24] D. Walker. Doppler modelling of radar sea clutter. *IEE Proc. Radar, Sonar and Navigation*, 148(2):73–80, April 2001.

[25] A. T. Jessup, W. C. Keller, and W. K. Melville. Measurements of sea spikes in microwave backscatter at moderate incidence. *Journal of Geophysical Research*, 95:9679–9688, 1990.

[26] Y. Liu and S. J. Frasier. Measurement and classification of low-grazing-angle radar sea spikes. *IEEE Transactions on Antennas and Propagation*, 46(1):27–40, 1998.

[27] D. B. Trizna, J. P. Hansen, and P. Hwang. Laboratory studies of radar sea spikes at low grazing angles. *Journal of Geophysical Research*, 96(91):529–537, 1991.

[28] W. Weibull. A statistical theory of strength of materials. *IVA-Handl*, 151, 1939.

[29] R. R. Boothe. The Weibull Distribution Applied to the Ground Clutter Backscatter Coefficient. Technical report, No. RE-69-15, AD 691109, U.S Army Missile Command, Redstone Arsenal, AL, 1969.

[30] M. Sekine and Y. Mao. *Weibull radar clutter.* Institution of Engineering and Technology, 1990.

[31] A. Farina, A. Russo, F. Scannapieco, and S. Barbarossa. Theory of radar detection in coherent Weibull clutter. *IEE Proc. F Communications, Radar and Signal Processing*, 134(2):174, 1987.

[32] G. Li and K.B. Yu. Modelling and simulation of coherent Weibull clutter. *IEE Proc. Radar and Signal Processing*, 136(1), 1989.

[33] G. V. Trunk and S. F. George. Detection of Targets in Non-Gaussian Sea Clutter. *IEEE Transactions on Aerospace and Electronic Systems*, AES-6(5), 1970.

[34] A. Farina, F. Gini, M.V. Greco, and L. Verrazzani. High resolution sea clutter data: statistical analysis of recorded live data. *IEE Proc. Radar, Sonar and Navigation*, 144(3):121, 1997.

[35] E. Jakeman and P. Pusey. A model for non-Rayleigh sea echo. *IEEE Transactions on Antennas and Propagation*, 24(6):806–814, November 1976.

[36] K. D. Ward. Compound representation of high resolution sea clutter. *Electronics Letters*, 17(16):561–563, 1981.

[37] K. D. Ward, C. J. Baker, and S. Watts. Maritime surveillance radar part 1 : Radar scattering from the ocean surface. *IEE Proc. F Radar and Signal Processing*, 137(2):51–62, 1990.

[38] D. Lewinski. Nonstationary probabilistic target and clutter scattering models. *IEEE Transactions on Antennas and Propagation*, 31(3):490–498, May 1983.

[39] T. M. Cover and J. A. Thomas. *Elements of information theory.* John Wiley & Sons, New Jersey, 2nd edition, 2006.

[40] C. E. Shannon. *Claude Elwood Shannon: Collected Papers.* IEEE Press, New York, 1993.

[41] C. E. Shannon and W. Weaver. *The mathematical theory of communication.* University of Illinois Press, 1962.

[42] C. E. Shannon. Communications in the Presence of Noise. *Proc. IRE*, 37(1):10–21, 1949.

[43] C.E. Shannon. Communication In The Presence Of Noise. *Proc. of the IEEE*, 86(2):447–457, February 1998.

[44] S. Kullback and R. A Leibler. On Information and Sufficiency. *Ann. Math. Statist.*, 22(1):79–86, 1951.

[45] S. Kullback. *Information theory and statistics.* John Wiley & Sons, New York, 1959.

[46] W. B. Davenport and W.L. Root. *Introduction to the Theory of Random Signals and Noise.* McGraw Hill, New York, 1958.

[47] S. M. Kay. *Fundamentals of Statistical Signal Processing, Vol. II: Detection Theory.* Prentice Hall, New Jersey, 1998.

[48] E. S. Pearson. *The Neyman-Pearson story: 1926-34.* John Wiley & Sons, 1966.

[49] J. W. Wright. Backscattering from Capillary Waves with Application. *IEEE Transactions on Antennas and Propagation*, 14(6):749–754, 1966.

[50] S. O. Rice. Reflection of Electromagnetic Waves from Slightly Rough Surfaces. *Communications on Pure and Applied Math*, 4:351–378, 1951.

[51] W. H. Peake. Theory of Radar return from Terrain. *IRE Convention Record*, 7(27-41), 1959.

[52] F. E. Nathanson. *Radar design principles.* McGraw Hill, New York, 1969.

[53] F. E. Nathanson, J. P. Reilly, and M. N. Cohen. *Radar Design Principles.* SciTech Publishing, New York, 2nd edition, 1999.

[54] M. M. Horst, F. B. Dyer, and M. T. Tuley. Radar Sea clutter model. *IEEE AP/S URSI Symp. Digest*, pages 6–10, 1978.

[55] J. W. Wright. New Model for Sea Clutter. *IEEE Trans. Antennas Propag.*, 16(2):217–223, 1968.

[56] N.W. Guinard and J.C. Daley. An experimental study of a sea clutter model. *Proc. of the IEEE*, 58(4):543–550, 1970.

[57] G. R. Valenzuela and M. B. Laing. On the Statistics of sea clutter. Technical Report Page I, Naval research lab, Tech. Rep. NRL Rept. 7349, 1971.

[58] G. V. Trunk. Radar Properties of Non-Rayleigh Sea Clutter. *IEEE Transactions on Aerospace and Electronic Systems*, AES-8(2), 1972.

[59] F. Fay, J. Clarke, and R. Peters. Weibull distribution applied to sea clutter. In *Proc. IEE Conference Radar '77*, pages 101–103, London, 1977.

[60] J. Hansen and V. Cavaleri. High-resolution radar sea scatter, experimental observations and discriminants. Technical report, Technical Report 8557, Naval Research Laboratory, Washington D.C, 1982.

[61] E. Jakeman and R. J. A. Tough. Non-Gaussian models for the statistics of scattered waves. *Advances in Physics*, 37(5):471–529, 1988.

[62] W. Stehwien. Statistics and correlation properties of high resolution X-band sea clutter. *Proc. IEEE Radar Conference*, pages 46–51, 1994.

[63] J. Carretero-Moya, J. Gismero-menoyo, A. Blanco-del campo, and A. Asensio-lópez. Statistical Analysis of a High-Resolution Sea-Clutter Database. *IEEE Transactions on Geoscience and Remote Sensing*, 48(4):2024–2037, 2010.

[64] J. Carretero-Moya, J. Gismero-Menoyo, A. Asensio-lópez, and A. Blanco-del campo. Experimental Validation of the Compound Gaussian Sea Clutter Model at Sub-Meter Range Resolution. In *Proc. IEEE International Radar Conference*, 2009.

[65] J. Carretero-Moya. Application of the radon transform to detect small-targets in sea clutter. *IET Radar, Sonar & Navigation*, 3(2), 2009.

[66] J. Carretero-Moya, A. De Maio, J. Gismero-Menoyo, and A. Asensio-Lopez. High resolution sea clutter and maritime target data: Experimental performance of distributed target coherent detectors. In *Proc. IEEE RadarCon (RADAR)*, pages 383–388, 2011.

[67] M. Farshchian and F. L. Posner. The Pareto distribution for low grazing angle and high resolution X-band sea clutter. In *Proc. IEEE Radar Conference*, pages 789–793, 2010.

[68] H. Leung and S. Haykin. Is there a radar clutter attractor? *Applied Physics Letters*, 56(6):593, 1990.

[69] S. Haykin, C. Krasnor, T.J. Nohara, B.W. Currie, and D. Hamburger. A coherent dual-polarized radar for studying the ocean environment. volume 29, pages 189–191, 1991.

[70] T. J. Nohara and S. Haykin. Canadian East Coast radar trials and the K-distribution. *IEE Radar and Signal Processing*, 1991.

[71] T.J. Nohara and S. Haykin. AR-based growler detection in sea clutter. *IEEE Transactions on Signal Processing*, 41(3):1259–1271, March 1993.

[72] T.J. Nohara and S. Haykin. Growler detection in sea clutter with coherent radars. *IEEE Transactions on Aerospace and Electronic Systems*, 30(3):836–847, July 1994.

[73] M.S. Seymour and S. Haykin. ISAR using Thomson's multiwindowed adaptive spectrum estimation method. *IEEE Transactions on Aerospace and Electronic Systems*, pages 1065–1070, 1993.

[74] T. Lo, H. Leung, J. Litva, and S. Haykin. Fractal characterisation of sea-scattered signals and detection of sea-surface targets. *IEE Proc. F Radar and Signal Processing*, 140(4):243, 1993.

[75] T.J. Nohara and S. Haykin. Growler detection in sea clutter using Gaussian spectrum models. *IEE Radar, Sonar and Navigation*, 1994.

[76] S. Haykin and X.B. Li. Detection of signals in chaos. *Proc. of the IEEE*, 83(1), 1995.

[77] G. Jones and S. Haykin. Higher-dimension detection of targets from scanned radar data. *IEE Radar, Sonar and Navigation*, 143(5), 1996.

[78] T.K. Bhattacharya and S Haykin. Neural Network-Based Radar Detection for an Ocean Environment. *IEEE Transactions on Aerospace and Electronic Systems*, 33(2), 1997.

[79] S. Haykin and T.K. Bhattacharya. Modular Learning Strategy for Signal Detection in a Nonstationary Environment. *IEEE Transactions on Signal Processing*, pages 1113–1116, 1997.

[80] Simon Haykin and DJ Thomson. Signal Detection in a Nonstationary Environment Reformulated as an Adaptive Pattern Classification Problem. *Proc. of the IEEE*, (1), 1998.

[81] F. Gini and J. H. Michels. Performance analysis of two covariance matrix estimators in compound-Gaussian clutter. *IEE Proc. Radar, Sonar and Navigation*, 146(3):133, 1999.

[82] F. Gini, M. Greco, and A. Farina. Clairvoyant and adaptive signal detection in non-Gaussian clutter: a data-dependent threshold interpretation. *IEEE Transactions on Signal Processing*, 47(6):1522–1531, 1999.

[83] S. Haykin. Radar clutter attractor: implications for physics, signal processing and control. *IEE Proc. Radar, Sonar and Navigation*, 146(4):177, 1999.

[84] F. Gini, M. Greco, M. Diani, and L. Verrazzani. Performance analysis of two adaptive radar detectors against non-Gaussian real sea clutter data. *IEEE Transactions on Aerospace and Electronic*, pages 1429–1439, 2000.

[85] P. L. Herselman and C. J. Baker. Analysis of calibrated sea clutter and boat reflectivity data at C- and X-Band in South African coastal waters. In *Proc. IET International Conference on Radar Systems*, pages 1–5, 2007.

[86] P. L. Herselman, C. J. Baker, and H. J. de Wind. An analysis of X-band calibrated sea clutter and small boat reflectivity at medium-to-low grazing angles. *International Journal of Navigation and Observation*, pages 1–14, 2008.

[87] P. L. Herselman and H.J. de Wind. Improved covariance matrix estimation in spectrally inhomogeneous sea clutter with application to adaptive small boat detection. In *International conference on Radar*, pages 1–6, 2008.

[88] M. Katzin. On the mechanisms of radar sea clutter. *Proc. of the IRE*, 101:209–214, 1957.

[89] M. Long. *Radar reflectivity of land and sea.* Artech House, 3rd edition, 2001.

[90] D. J. Mclaughlin, N. Allan, E. M. Twarog, , and D. B. Trizna. High Resolution Polarimetric Radar Scattering Measurements of Low Grazing Angle Sea Clutter. *IEEE J. Ocean. Eng.*, 20(3):166–178, 1995.

[91] K.J. Sangston and K.R. Gerlach. Coherent detection of radar targets in a non-gaussian background. *IEEE Transactions on Aerospace and Electronic Systems*, 30(2):330–340, April 1994.

[92] S. Watts. Radar detection prediction in K-distributed sea clutter and thermal noise. *IEEE Transactions on Aerospace and Electronic Systems*, (1), 1987.

[93] M. Greco, F. Gini, and M. Rangaswamy. Statistical analysis of measured polarimetric clutter data at different range resolutions. *IEE Proc. Radar, Sonar and Navigation*, 153(6), 2006.

[94] G. Davidson. Simulation of coherent clutter. *IET Seminar on Radar Clutter Modelling*, pages 33–39, 2008.

[95] G. Davidson. Simulation of coherent sea clutter. *IET Radar, Sonar & Navigation*, 4(2):168, 2010.

[96] R. J. A. Tough and K. D. Ward. The correlation properties of gamma and other non-Gaussian processes generated by memoryless nonlinear transformation. *Journal of Physics D: Applied Physics*, 32(23):3075, 1999.

[97] W. Pidgeon. Doppler Dependence of Radar Sea Return. *Journal of Geophysical Research*, 73(4), 1968.

[98] G. R. Valenzuela and M. B. Laing. Study of Doppler Spectra of Radar Sea Echo. *Journal of Geophysical Research*, 75(3):551–563, 1970.

[99] C.J. Baker. Spectral properties of radar sea clutter. *IEE Colloquium on Radar Clutter and Multipath Propagation*, 1989.

[100] C. J. Baker. K-distributed coherent sea clutter. *IEEE Proc. F Radar and Signal Processing*, 138(2):89–92, 1991.

[101] P. H. Y. Lee, J. D. Barter, K. L. Beach, C. L. Hindman, B. M. Lake, H. Rungaldier, J. C. Shelton, A. B. Williams, R. Yee, and H. C. Yuen. X band microwave backscattering from ocean waves. *Journal of Geophysical Research*, 100(C2):2591–2611, 1995.

[102] M. Greco, F. Bordoni, and F. Gini. X-Band Sea-Clutter Nonstationarity : Influence of Long Waves. *IEEE Journal of Oceanic Engineering*, 29(2):269–283, 2004.

[103] M. Greco, F. Gini, and M. Rangaswamy. Non-stationarity analysis of real X-Band clutter data at different resolutions. *IEEE Radar conference*, pages 44–50, 2006.

[104] M. Greco, P. Stinco, F. Gini, and M. Rangaswamy. Impact of Sea Clutter Nonstationarity on Disturbance Covariance Matrix Estimation and CFAR Detector Performance. *IEEE Transactions on Aerospace and Electronic Systems*, 46(3):1502–1513, July 2010.

[105] M. Greco, F. Gini, L. Verrazzani, and A. Balleri. Analysis of polarimetric marine scattering at different range resolutions. *Proc. IEEE International Geoscience and Remote Sensing Symposium*, 5:3096–3099, 2004.

[106] V. Pidgeon. Bistatic cross section of the sea. *IEEE Transactions on Antennas and Propagation*, 14(3):405–406, May 1966.

[107] A. R. Domville. The bistatic reflection from land and sea of X-band radio waves, part I. Technical report, GEC (Electronics) Ltd., Stanmore, England, Memorandum SLM1802, 1967.

[108] A. R. Domville. The bistatic reflection from land and sea of X-band radio waves, part II. Technical report, GEC (Electronics) Ltd, Stanmore, England, Memorandum SLM2116, 1968.

[109] T.P. Kochanski, M.J. Vanderhill, J.V. Zolotarevsky, and T. Fariss. Low Illumination Angle Bistatic Sea Clutter Measurements At X-band. *Proc. OCEANS '92*, 1:518–523, 1992.

[110] G. Ewell and S. Zehner. Bistatic Sea Clutter Returns Near Grazing Incidence. In *Proc. IEE Radar 82*, 1982.

[111] G. Ewell. Bistatic Radar Cross Section Measurements. In N.C. Currie, editor, *Techniques of Radar Reflectivity Measurement*, chapter 7. Artech House, 2nd edition, 1989.

[112] H.D. Griffiths, W. A. Al-Ashwal, K.D. Ward, R.J.A. Tough, C.J. Baker, and K. Woodbridge. Measurement and modelling of bistatic radar sea clutter. *IET Radar, Sonar & Navigation*, 4(2):280–292, 2010.

[113] W. A. Al-Ashwal, A. Balleri, H. D. Griffiths, W. J. Miceli, K. Woodbridge, C. J. Baker, R. Harmanny, M. Inggs, J. S. Sandenbergh, M. A. Ritchie, A. G. Stove, S. Watts, R. J. A. Tough, and K. D. Ward. Measurements of bistatic radar sea clutter. In *Proc. IEEE Radar Conference*, pages 217–221, May 2011.

[114] T. Derham, S. Doughty, K. Woodbridge, and C. J. Baker. Realisation and Evaluation of a Low Cost Netted Radar System. In *Proc. CIE International Conference on Radar*, Shanghai, 2006.

[115] T. E. Derham, S. Doughty, K. Woodbridge, and C. J. Baker. Design and evaluation of a low-cost multistatic netted radar system. *IET Radar, Sonar & Navigation*, 1(5):362–368, October 2007.

[116] S. Doughty. *Development and Performance Evaluation of a Multistatic Radar System.* PhD thesis, University College London, 2008.

[117] W. A. Al-Ashwal. *Measurement and modelling of bistatic sea clutter.* PhD thesis, University College London, UK, 2011.

[118] J.S. Sandenbergh and M. Inggs. A common view GPSDO to synchronize netted radar. pages 24–24, 2007.

[119] J. S. Sandenbergh, M. Inggs, and W. A. Al-Ashwal. Evaluation of coherent netted radar carrier stability while synchronised with GPS-disciplined oscillators. In *Radar Conference (RADAR), 2011 IEEE*, pages 1100–1105, May 2011.

[120] J. Cody. *An overview of software development for special functions.* Springer Verlag, Berlin, 1976.

[121] M. Abramowitz and I. A. Stegun. Handbook of Mathematical Functions. chapter sections 9. Dover Publications Inc., 1965.

[122] B. Dawber. The advanced radar technology integrated system testbed (ARTIST) and the need for cognitive radar management and control. In *DASP Workshop*, 2011.

[123] S. Watts. Modelling and Simulation of Coherent Sea Clutter. *IEEE Transactions on Aerospace and Electronic Systems*, 48(4):3303–3317, October 2012.

[124] M. A. Ritchie, A. G. Stove, S. Watts, K. Woodbridge, and H. D. Griffiths. Application of a New Sea Clutter Doppler Model. In *Accepted for publication in Proc. IEEE International Radar Conference*, 2013.

[125] A. Justel, D. Pea, and R. Zamar. A multivariate kolmogorov-smirnov test of goodness of fit. *Statistics and Probability Letters*, 35(3), 1997.

[126] F. J. Massey. The kolmogorov-smirnov test for goodness of fit. *Journal of the American Statistical Association*, 46(253), 1951.

[127] D.J. Crisp, L. Rosenberg, N.J. Stacy, and Yunhan Dong. Modelling x-band sea clutter with the k-distribution: Shape parameter variation. In *Proc. IEEE Radar Conference*, pages 1–6, 2009.

[128] G. A Yates. *Bistatic Synthetic Aperture Radar*. PhD thesis, University College London, 2005.

[129] M. A. Ritchie, W.A. Al-Ashwal, A.G. Stove, K. Woodbridge, and H.D. Griffiths. Statistical analysis of monostatic and bistatic sea clutter Doppler spectrum. *Proc. of 2011 IEEE CIE International Conference on Radar*, pages 816–820, October 2011.

[130] M. A. Ritchie, K. Woodbridge, and A. G. Stove. Analysis of sea clutter distribution variation with Doppler using the compound k-distribution. In *Proc. IEEE Radar Conference*, pages 495–499, Washington D.C, 2010.

[131] Aaron D. Lanterman, Joseph A. O'Sullivan, and Michael I. Miller. KLD for Quantifying clutter and models. *Optical Engineering*, 38(12):2134–2146, 1999.